PETROCHRONOLOGY AND STATISTICAL ANALYSIS TO INTEGRATE DIFFERENT TYPES OF DATA TO SOLVE COMPLEX EARTH SYSTEMS PROBLEMS

by

Claire Ostwald Harrigan

A dissertation

submitted in partial fulfillment

of the requirements for the degree of

Doctor of Philosophy in Geoscience

Boise State University

August 2022

BOISE STATE UNIVERSITY GRADUATE COLLEGE

DEFENSE COMMITTEE AND FINAL READING APPROVALS

of the dissertation submitted by

Claire Ostwald Harrigan

Dissertation Title: Petrochronology and Statistical Analysis to Integrate Different Types of Data to Solve Complex Earth Systems

Date of Final Oral Examination: 06 June 2022

The following individuals read and discussed the dissertation submitted by student Claire Ostwald Harrigan, and they evaluated the student's presentation and response to questions during the final oral examination. They found that the student passed the final oral examination.

Mark D. Schmitz, Ph.D.	Chair, Supervisory Committee
James L. Crowley, Ph.D.	Member, Supervisory Committee
Clyde J. Northrup, Ph.D.	Member, Supervisory Committee
V. Dorsey Wanless, Ph.D.	Member, Supervisory Committee

The final reading approval of the dissertation was granted by Mark D. Schmitz, Ph.D., Chair of the Supervisory Committee. The dissertation was approved by the Graduate College.

ACKNOWLEDGMENTS

Sincerest thanks to Mark Schmitz, my committee, my labmates and collaborators, Casey Harrigan and my family, and my friends for their support during my time in graduate school.

ABSTRACT

Complex Earth systems problems, like reconstructing orogens and calibrating the geologic time scale, require investigations that link time to geologic processes. To use time as a means of organizing geologic evidence, geochronometric dates must be contextualized by integrating with different data types. This is the work of petrochronology—linking mineral ages to geochemical, textural, or other geologic information. The U-Pb isotopic system as preserved in the minerals zircon ($ZrSiO_4$) and titanite ($CaTiSiO_5$) can be used in a petrochronological context to date geologic events including the age of granitoid pluton emplacement, the age of rock fabric formation in deformed granitoids, and the age of volcanic ash beds.

One focus of my dissertation was to use petrochronology to investigate high-temperature crustal strain partitioning and localization on the micro- to macro-scale using the western Idaho shear zone (WISZ), west-central Idaho. The WISZ is a crustal-scale structure that localized arc magmatic process and deformation related to terrane accretion and translation along the North American Cordillera. I used a WISZ orthogneiss to examine how fabric develops during high-temperature deformation on the micro-scale. By integrating the geochronometric, geochemical, and microstructural titanite record using statistical and petrologically-relevant visualizations, I document the local preservation of titanite related to magmatic and subsolidus processes. Importantly, this petrochronological workflow results in a date for the onset of deformation in the WISZ,

confirming tectonic interpretations of WISZ deformation as a separate event from local terrane suturing.

I expanded this work to the macro-scale with a suite of samples that transect the WISZ near McCall, Idaho to track the spatial-temporal patterns of pluton emplacement and deformation. My tandem zircon and titanite petrochronology results show that 1) the propensity of titanite to (re)crystallize in response to changes in pressure and temperature makes titanite petrochronology a useful approach for documenting subtle subsolidus fabric development, 2) strain localizes in time and space in response to local intrusions, and 3) WISZ fabric development is observed further east than previously mapped, causing the model of a west-to-east younging of pluton emplacement and deformation to be updated in favor of a model in which deformation focuses young magmatism within the center of the shear zone.

In a second focus of my dissertation work, I integrated geochronology and statistical modeling to recalibrate and refine the Devonian time scale. The Devonian is a period in Earth history with significant biologic, climatic, and tectonic events. I dated Devonian ash beds using high-precision zircon geochronology and used those dates with a Bayesian age-depth model as the statistical framework to relate geochronometric and astrochronologic data to biostratigraphic data. I produced an updated Devonian time scale with new stage boundary ages with robust uncertainty estimates. This integrated stratigraphic approach is broadly applicable to time scale modeling.

This work is united under a theme of using petrochronology and statistical modeling to link time to geologic processes including magmatism, deformation, and

stratigraphic accumulation. Time constraints on the initiation and duration of geologic processes can deepen our understanding of the evolution of complex Earth systems.

TABLE OF CONTENTS

LIST OF TABLES

LIST OF FIGURES

INTRODUCTION

My dissertation work integrates different types of geologic data to understand how the geochronologic ages we measure represent and describe geologic processes. Accessory mineral chronometers, like zircon and titanite, are used as proxies to date geologic processes. For example, the age of magmatic zircon from an ash bed is commonly used as a measure of when a volcano erupted. In other Earth systems like shear zones, accessory mineral dates can track multiple processes, and therefore, the link between a date and a geologic process can be less obvious. To strengthen how we as geochronologists link radioisotopic dates and the associated geologic processes, this dissertation develops new petrochronology methods focused on visualizing and statistically analyzing different types of data. With multiple datasets combined to contextualize ages, we can more effectively model complex Earth systems.

In the first and second chapters, I examined the western Idaho shear zone (WISZ) from west-central Idaho to understand how the rocks we observe today preserve a complex record of how the crust is created and deformed in collisional arc settings. For the first chapter, I dated a strongly deformed porphyritic orthogneiss with tandem zircon and titanite petrochronology and found an extended record of titanite crystallization. To differentiate between magmatic and subsolidus titanite growth, I integrated trace element geochemistry and microstructural analysis with titanite dates through statistically- and petrologically-informed visualizations. By connecting qualitative and quantitative datasets through coding and interactive geochemistry plots, I was able to find to find the

most compelling, informative way to represent the petrologic changes related to subsolidus rock fabric development and date the initiation of shear zone deformation.

For the second chapter, I used the WISZ as a natural laboratory for examination of how pluton emplacement and deformation processes manifest and interact on the map scale. This work relied on similar methods as Chapter One. This broader examination of titanite from plutons of different ages revealed a rich record of progressive temporal overprinting by progressive strain accumulation. I used tandem zircon and titanite petrochronology and the map patterns of plutons to disentangle the overprinted record and study the feedbacks between magmatism and deformation. This chapter represents the iterative process of developing hypotheses, collecting data, and refining hypotheses. Narrow, targeted questions like "when did this shear zone deform?" transformed into more compelling questions like "why did this shear zone deform at this time?" By exposing and highlighting complexity, petrochronology becomes a tool to help us ask more specific questions and develop more nuanced models of shear zone deformation.

In the third chapter, I applied and honed my coding and visualizing skills to a different complex system—the Devonian Period of the geologic time scale. This work relied on the application and development of code to contextualize astrochronologic and biostratigraphic data using zircon geochronology. I developed a novel method for integrating relative and absolute ages and durations into a statistical framework, leading to a new calibration of the Devonian time scale with robust uncertainty estimates on stage boundary ages.

This dissertation demonstrates the work I have done to generate, model, and visualize data. The petrochronological approaches detailed in this work allow me to more

efficiently use time as a means of organizing geologic information and demonstrate how seemingly disparate types of data can be coherently combined to address questions related to complex Earth systems.

CHAPTER ONE: DETERMINING THE INITIATION OF SHEAR ZONE DEFORMATION USING TITANITE PETROCHRONOLOGY

Abstract

We present an integrative petrochronological approach to dating the initiation of shear zone deformation in granitic rocks, using the mineral titanite ($CaTiSiO_5$). This method is suited to granitoid-hosted shear zones in continental arc settings, where the interplay between tectonics, magmatism, and deformation is actively debated. Microstructural observations including crystallographic misorientations, fabric context, and backscattered electron images were used to identify relict magmatic, partially to fully recrystallized, and neoblastic titanite crystals. Principal component analysis of trace element compositional variance in titanite was able to further distinguish and quantify the crystal chemical response to deformation. High-precision isotope dilution U-Pb geochronological measurements on relict magmatic, partially to fully recrystallized, and neoblastic titanite crystals was used to constrain the timing of shear zone initiation. For a sample of a porphyritic orthogneiss from the western Idaho shear zone of the northern U.S. Cordillera, U-Pb zircon geochronology dates emplacement of this unit to between ca. 105 and 103 Ma, whereas the age of partially recrystallized and neoblastic titanite grains constrain the initiation of the western Idaho shear zone to between ca. 98 and 96 Ma. The >5 Ma lag between pluton emplacement and the onset of deformation indicates that mid-Cretaceous deformation in the western Idaho shear zone is temporally distinct from Late Jurassic–Early Cretaceous accretionary tectonics. Our integrated

petrochronological investigation documents that: 1) deformation induces textural, chemical, and isotopic changes in titanite; 2) the geochemical properties of primary magmatic titanite collapse into a discernible trend of subsolidus syn-deformational titanite compositions; and 3) the onset of deformation and progression of strain accumulation are preserved in the U-Pb ages of these titanite crystals.

Introduction

High-temperature shear zones play a major role in partitioning oblique slip at transpressional and transtensional plate boundaries (e.g., Fitch, 1972) and have been called upon to solve the "room problem" of plutonism in dominantly contractional arc settings (e.g., Hutton et al., 1990). Much of the interplay between deformation and magmatism takes place in the roots of continental arcs at lower to mid-crustal depths, and the interaction of these processes can be explored using accessory mineral petrochronology in deformed granitoids. The timing of shear zone deformation in continental arc settings can be used to reconstruct ancient tectonic processes related to lithospheric assembly and modification, from changes in subduction geometry (e.g., Axen et al., 2018) to the mechanics of terrane accretion (e.g., Tikoff et al., 2022).

It is difficult to directly date high-temperature (>550°C) deformation in shear zones. Most geochronological methods used in continental arc settings date either igneous crystallization (e.g., U-Pb zircon) or a lower temperature cooling interval (e.g., $^{40}Ar/^{39}Ar$ biotite and hornblende) and while useful for broadly bracketing the timing of deformation, do not date high-temperature fabrics directly. Titanite ($CaTiSiO_5$), a mineral common in granitoid plutons, recrystallizes and grows in response to changes in pressure, temperature, and differential stress and thus can record evidence of fabric-forming events

(Kohn, 2017). The high diffusive closure temperature for Pb in titanite (>750°C; Hartnady et al., 2019 and references therein) makes titanite a useful U-Pb chronometer for high-temperature systems, albeit one necessitating correction for initial Pb incorporated during crystallization (Frost et al., 2000; Storey et al., 2006; Bonamici and Blum, 2020). When titanite (re)crystallization can be associated with deformation fabrics, the U-Pb age of titanite may be inferred to date shear zone deformation directly. Techniques such as electron backscattered diffraction (EBSD) that quantify intragrain crystallographic misorientation domains have been successfully used to associate the partial recrystallization of titanite with deformation (Bonamici et al., 2015; Gordon et al., 2021).

However, because titanite commonly crystalizes at magmatic through subsolidus temperatures, relict igneous, recrystallized, and neoblastic titanite can coexist in the same mesoscale volume of a deformed granitoid, complicating the association of titanite ages with a specific process (e.g., Getty and Gromet, 1992). This can be remedied by characterizing and dating titanite at the single crystal or intracrystalline scale. Numerous studies have: 1) documented a range of natural titanite compositions (e.g., Frost et al., 2000; El Korh et al., 2009); 2) attributed different morphologies to magmatic and metamorphic titanite crystals (e.g., Getty and Gromet, 1992; Resor et al., 1996); 3) leveraged those morphological differences to categorize titanite and extract chemical characteristics from those categories (e.g., Garber et al., 2017); and 4) used in situ titanite ages of metamorphic titanite to explore the relationship between magmatism and deformation (e.g., Papapavlou et al., 2017; Rossetti et al., 2017). Despite these and other efforts to use titanite petrochronology to date deformation, more work remains to apply

these techniques to settings of syntectonic plutonism where igneous titanite crystallization and deformation-related titanite (re)crystallization may differ in age by only a few million years and where titanite recrystallization and growth takes placed within a continuum of fabric development.

In the work that follows, we used integrated zircon and titanite petrochronology to date pluton emplacement and the initiation of shear zone deformation. We identified magmatic through subsolidus titanite growth by combining textural information from backscattered electron (BSE) imaging and electron backscatter diffraction (EBSD) crystallographic misorientation maps with trace element chemistry as measured by laser ablation inductively coupled plasma mass spectrometry (LA-ICPMS). Recent empirical calibration of tracer diffusion rates in titanite (Garber et al., 2017; Kohn, 2017; Holder et al., 2019; Gordon et al., 2021) suggest that crystal domains sufficiently recrystallized to modify Nb, Zr, and rare earth element (REE) concentrations will experience U-Pb isotopic resetting. Thus, the expulsion or incorporation of high field strength elements and REE can indicate crystal domains whose U-Pb ages reflect deformation-related recrystallization and neoblastic growth. Using tandem LA-ICPMS and intragrain microsampled isotope dilution–thermal ionization mass spectrometry (ID-TIMS) U-Pb geochronology, we targeted and analyzed recrystallized and neoblastic titanite domains to resolve the lag between pluton crystallization and the onset of shear zone initiation.

Geological Background

Coeval plutonism and deformation was a common occurrence during the Cretaceous construction of the North American Cordillera (e.g., Braudy et al., 2017; Bartley et al., 2018). In the Idaho section of the North American Cordillera, the

Cretaceous western Idaho shear zone (WISZ) is a crustal-scale, dextral transpressive, high-temperature shear zone that deformed syntectonic intrusive rocks (Figure 1.1.; Manduca et al., 1993; Tikoff et al., 2001; Giorgis et al., 2008). In the McCall, Idaho area, three plutonic complexes were deformed by the WISZ: the Hazard Creek complex, the Little Goose Creek complex, and the Payette River complex (Manduca et al., 1993). Previous work in the area constrained pluton emplacement to ca. 118 Ma (Hazard Creek complex), ca. 105 Ma (Little Goose Creek complex), and ca. 90 Ma (Payette River complex) and constrained deformation to older than ca. 90 Ma (Manduca et al., 1993; Giorgis et al., 2008).

The strongly deformed Little Goose Creek complex contains the $^{87}Sr/^{86}Sr = 0.706$ isopleth which delineates the boundary between accreted terranes to the west and the Idaho Batholith to the east (Fleck and Criss, 1985; Manduca et al., 1992). The WISZ lies within and is parallel to the Salmon River suture zone, a Late Jurassic to Early Cretaceous structure that encompasses the transition from Mesozoic accreted terranes to continental North America (McClelland et al., 2000). Terrane accretion along this suture was dated at 128 ± 3 Ma using a multi-mineral Sm-Nd isochron (Getty et al., 1993). It is debated whether the WISZ overprints the Jurassic terrane accretion episode as a distinct shearing event (McClelland et al., 2000) or if the WISZ is the expression of continuous deformation following terrane accretion (Gray et al., 2012). WISZ deformation that post-dates magmatism would support the hypothesis of Late Jurassic to Early Cretaceous suturing and mid-Cretaceous transpressional shearing as distinct events. Below we describe the detailed, contextualized accessory mineral petrochronology that allows us to distinguish between magmatism and solid-state deformation.

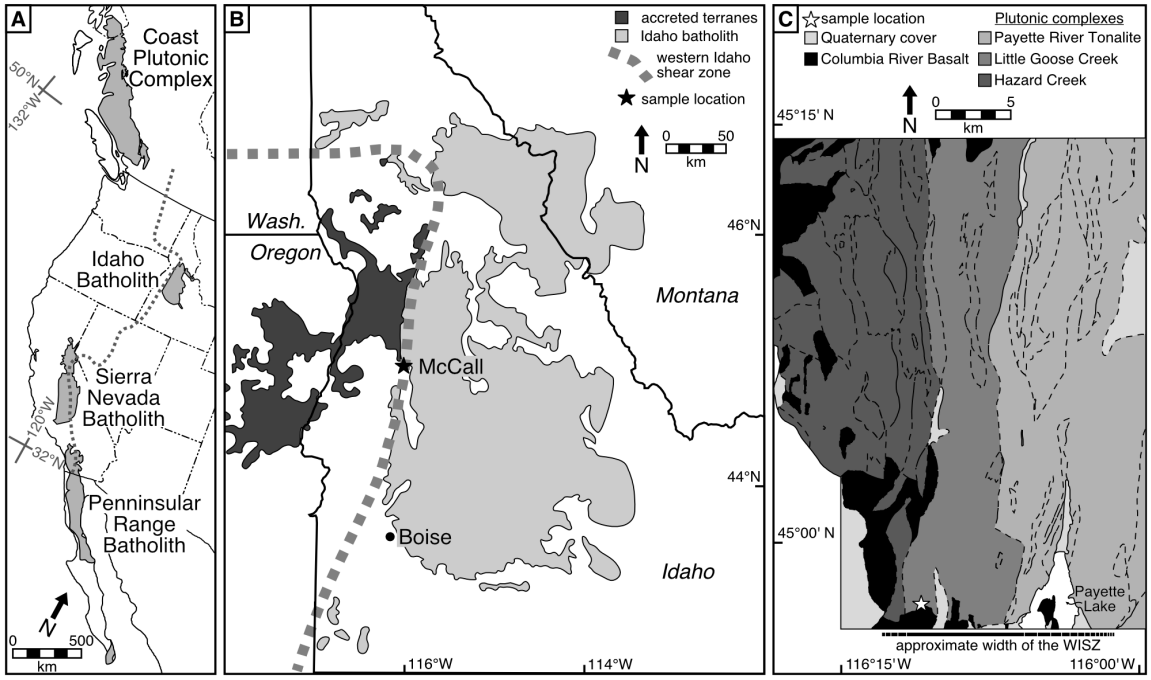

Figure 1.1. (A) Map of the North American Cordillera with Cretaceous batholiths (gray polygons) and the $^{87}Sr/^{86}Sr = 0.706$ isopleth (thick dashed line). Modified from Tikoff et al. (2022). (B) Map of the location of the western Idaho shear zone (dashed line) in relation to accreted terranes and the Idaho Batholith, modified from Lund (1995). Wash. – Washington. (C) Map of the plutonic complexes deformed by the western Idaho shear zone near McCall, Idaho. Contacts between mapped units within each plutonic complex are indicated with solid (observed) and dashed (interpreted) lines, modified from Manduca et al. (1993). WISZ – western Idaho shear zone.

Material and Methods

Sample Description

We examined a highly deformed porphyritic orthogneiss (14WZ3-2; 44.9669°N, 116.18085°W, WGS84) from the Little Goose Creek Complex of the Border Zone Suite of the Idaho Batholith near McCall, Idaho (Figure 1.1.; Manduca et al., 1993). Approximately 1 kg of sample was extracted for thin and thick sections and feldspar, zircon, and titanite mineral separates following standard petrographic and separation techniques.

Pb Isotopic Compositions of Feldspar

The isotopic composition of initial Pb in this sample was estimated from the measured Pb isotope composition of feldspar crystals, following methods modified from (Housh and Bowring, 1991). An approximately 8 cm^3 K-feldspar porphyroclast was isolated with a wafer saw from the hand sample and analyzed separately from matrix K-feldspar extracted during standard crushing and density separation of the geochronology sample. Fifty milligrams of each subsample of feldspar crystals were prepared by Frantz magnetic barrier separation (non-magnetic at 0.5 A magnet current, 10° side slope, 7° forward slope), lithium metatungstate density separation ($\rho < 2.64$ g/cm^3), and hand-picking for mineral clarity and lack of inclusions. Each subsample was sequentially leached in 6M HCl (30 min), 8M HNO_3 (30 min), 1M HF (1 hour) and again in 1M HF (1 hour), before collecting a series of three 1M HF (30 min) leaches that were processed through 1M HBr-based anion-exchange chromatography (Strelow and Toerien, 1966). Pb isotope ratios were measured by static multicollection on 1011 Ω resistor amplifiers on an IsotopX Phoenix X62 thermal ionization mass spectrometer. Instrumental mass bias was corrected using external calibration to repeated measurements of NBS981 at the same sample quantity and run temperature conditions.

Zircon Petrochronology

Zircon was separated, annealed at 900°C for 60 hours, mounted, imaged via cathodoluminescence, and dated at the Boise State University Isotope Geology Laboratory using methods detailed by Macdonald et al. (2018). LA-ICPMS analysis of >200 spots on approximately 47 zircon crystals resulted in age determinations and trace element concentrations (analytical parameters described in Table A1.1.; zircon LA-

ICPMS results in Tables A1.2. and A1.3.). We used LA-ICPMS ages and CL images to inform grain selection for ID-TIMS, targeting domains that represented the main phase of magmatic crystallization or subsequent metamorphism.

We subsampled 16 zircon crystals into 26 crystal fragments using a New Wave Research UP213 laserprobe as a cutting tool and treated the fragments with chemical abrasion at 180° or 190°C to mitigate Pb loss (modified from Mattinson, 2005). Samples were spiked with an in-house ^{205}Pb-^{233}U-^{235}U tracer (BSU-1B) calibrated to EARTHTIME gravimetric standards (Condon et al., 2015; McLean et al., 2015), dissolved, and processed for U and Pb separation by HCl-based anion-exchange chromatography (Krogh, 1973). Isotopic measurements were made on an IsotopX Isoprobe-T or Phoenix X62 multicollector TIMS with a Daly photomultiplier detector. U-Pb zircon dates by ID-TIMS are given in Table 1.1. Isotopic ratios and the details of instrumental fractionation, common Pb correction, and error propagation are given in Table A1.7.

Table 1.1. Zircon and titanite $^{206}Pb/^{238}U$ dates by ID-TIMS for sample 14WZ3-2 (Cretaceous only).

Sample (titanite)	Date ± 2σ uncertainty (Ma)	
t1	99.29	0.16
t2	95.67	0.12
t3	95.10	0.14
t4	95.93	0.11
t5	94.00	0.12
t7a	100.36	0.21
t9	104.98	0.14
t11	94.32	0.17
t12b	92.57	0.16
t13a	102.95	0.37
t14a	100.57	0.16
t14b	98.68	0.12
t15a	93.98	0.17
t15b	97.46	0.17
t15c	99.64	0.25
t15d	98.42	0.17
t16a	99.08	0.24
t16b	100.45	0.23
t17a	103.53	0.36
t17c	100.41	0.23
t106a	98.13	0.86
t106b	97.54	0.68
t117	89.86	0.38
t121	86.93	0.65
t516	86.8	1.1
t312	82.6	2.9
t336	86.7	1.4

Sample (zircon)	Date ± 2σ uncertainty (Ma)	
z1b	110.464	0.086
z1d	110.635	0.088
z2b	109.49	0.10
z2d	112.624	0.087
z3d	111.46	0.17
z6a	105.10	0.10
z6b	107.71	0.37
z6c	109.011	0.084
z8b	109.94	0.15
z10a	107.04	0.16
z10b	104.07	0.38
z11	134.13	0.11
z12	105.30	0.12
z14b	96.21	0.48
z15	97.71	0.44
z16b	108.233	0.083
z16c	108.18	0.11
z16d	106.59	0.12
z17	107.287	0.081
z18	105.155	0.086
z19b	134.93	0.10
z20a	103.20	0.13
z20b	104.15	0.12

Titanite Petrochronology

Microstructures

We analyzed XZ thick sections with BSE imaging and EBSD analysis at the University of Wisconsin–Madison using a Hitachi S3400 Variable Pressure scanning electron microscope fitted with a Hitachi High-Sensitivity BSE detector and an Oxford EBSD detector. Data was processed using Aztec software and the MTEX toolbox for MATLAB (Bachmann et al., 2010) with code modified from Michels et al. (2015). We identified the crystal phases present and measured the three-dimensional orientation of the crystallographic lattice at micron-scale resolution (Prior et al., 1999, 2002). Mineralogical phase maps were used to investigate the textural context of titanite within the rock fabric. Lattice misorientation maps were used to visualize the magnitude of the intracrystalline misorientation and the pattern of misorientation relative to the titanite grain boundaries.

Trace Element Geochemistry

All titanite trace element chemistry and geochronology analyses were performed at the Boise State University Isotope Geology Laboratory. BSE imaging was conducted on titanite separates at the Boise State University and on titanite in thick sections at the University of Wisconsin–Madison. We analyzed >700 spots on approximately 220 titanite crystals from separates and within thick sections to capture the full range of titanite trace element chemistry. Trace element measurements were made on a ThermoElectron X-Series II quadrupole ICPMS and New Wave Research UP213 Nd:YAG UV (213 nm) laser ablation system and followed the procedures described by

Schmitz et al. (2018; analytical parameters described in Table A1.4.; titanite LA-ICPMS results in Tables A1.5. and A1.6.).

To examine the trace element variability in titanite from this sample, we did principal component analysis in R (R Core Team, 2022) on a non-normalized suite of trace elements (Sr, Y, Zr, Nb, La, Ce, Pr, Nd, Sm, Eu, Gd, Tb, Dy, Ho, Er, Tm, Yb, Lu, Ta, Th, U, Hf) without any a priori categorization of the analyzed spots (i.e., microstructural characterization of titanite grains into magmatic, recrystallized, and neoblastic categories did not inform the principal component analysis).

Geochronology

Titanite crystals for ID-TIMS geochronology were selected based on texture, internal misorientation pattern, fabric context, and trace element chemistry with the aim of capturing the range of variability in the sample. BSE images of ID-TIMS-dated titanite crystals are given in Figure A1.1. Titanite crystals with sufficiently high U concentrations (greater than approximately 50 ppm) to yield measurable radiogenic Pb were subsampled by fracturing grains with a sharpened steel dental tool. To extract titanite from thick sections, the UP213 laserprobe was used to ablate material surrounding the titanite grain in a moat shape. Titanite grains were then plucked from thick sections using a sharpened steel dental tool, transferred to a glass vial filled with deionized water, and sonicated in 5 second bursts for 10 minutes to clean the titanite crystal faces.

In preparation for dissolution, titanite crystals or crystal fragments were sonicated with 3.5 M HNO_3 for 15 min and rinsed twice with ultra-pure H_2O. Samples were spiked with an in-house ^{205}Pb-^{233}U-^{235}U tracer (BSU-1B) calibrated to EARTHTIME gravimetric standards (Condon et al., 2015; McLean et al., 2015) and dissolved following

the methods described in Schmitz et al. (2018). Titanite was processed for U and Pb separation by HBr- and HCl-based anion-exchange chromatography (Strelow and Toerien, 1966; Krogh, 1973). Isotopic measurements were made with the same instrumentation and methods as zircon, except U and Pb were measured on separate filaments. U-Pb titanite dates by ID-TIMS are given in Table 1.1. Isotopic ratios and the details of instrumental fractionation, common Pb correction, and error propagation are given in Table A1.7.

Results

Pb Isotopic Compositions of Feldspar

The Pb isotopic compositions of matrix and porphyroclast K-feldspar are given in Table 1.2. Leachates 3-5 have reproducible compositions, suggesting that the initial acid leaches sufficiently eliminated reservoirs of surface-correlated or mineral inclusion Pb. For initial Pb estimates, we averaged the values of leachates 3-5 and found that the Pb isotopic composition of the porphyroclast was indistinguishable, within uncertainty, from matrix K-feldspar. As our matrix K-feldspar sample averages the full analytical volume from which zircon and titanite were extracted, we use its composition for the initial Pb correction of zircon and titanite dates for analyses that exceed the 0.4 pg of common Pb that we attribute to procedural blank (see Table A1.7 for blank composition).

Table 1.2. K-feldspar Pb isotopic data.

Analysis	$^{208}Pb/^{206}Pb$	$^{207}Pb/^{206}Pb$	$^{208}Pb/^{204}Pb$	$^{207}Pb/^{204}Pb$	$^{206}Pb/^{204}Pb$
14WZ3-2 matrix K-feldspar					
Leachate 3	2.045	0.828	38.608	15.634	18.8808
Leachate 4	2.045	0.828	38.610	15.634	18.8795
Leachate 5	2.046	0.828	38.625	15.639	18.8824
average	*2.045*	*0.828*	***38.614***	***15.636***	***18.8809***
± 1σ %	*0.018*	*0.011*	***0.024***	***0.017***	***0.0076***
14WZ3-2 porphyroclast K-feldspar					
Leachate 3	2.045	0.828	38.605	15.634	18.880
Leachate 4	2.044	0.828	38.585	15.629	18.877
Leachate 5	2.043	0.828	38.586	15.628	18.885
average	*2.044*	*0.828*	*38.592*	*15.630*	*18.880*
± 1σ %	*0.036*	*0.032*	*0.029*	*0.021*	*0.021*

Bold text indicates values used as an initial Pb isotopic composition for zircon and titanite isotope dilution thermal ionization mass spectrometry ages.

Isotope ratios include an external fractionation correction of 0.10 ± 0.02% (1σ) per atomic mass unit, based upon NBS981 measurements on similar sized ion beams at the same run temperatures. Fractionation uncertainty imposes the following minimum absolute uncertainties (1σ): $^{208}Pb/^{204}Pb$, 0.019; $^{207}Pb/^{204}Pb$, 0.007; $^{206}Pb/^{204}Pb$, 0.008; $^{208}Pb/^{206}Pb$, 0.0009; $^{207}Pb/^{206}Pb$, 0.0004.

Zircon Petrochronology

Excluding crystals with Jurassic and earliest Cretaceous dates, zircon dates range from 112.62 ± 0.09 Ma to 96.21 ± 0.48 Ma (Figure 1.2., Table 1.1.). CL imaging (Figure A1.1.) revealed inherited cores in nearly every zircon, and the subsampling of zircon crystals allowed us to largely, but not completely, avoid Jurassic and earliest Cretaceous inherited cores, as evidenced in some ID-TIMS dates (Table A1.7.). Six zircon crystals

were subsampled and yielded multiple dates. In some cases, crystal fragments from a single crystal were the same age within uncertainty (e.g., z1b: 110.464 ± 0.086 Ma; z1d: 110.635 ± 0.088 Ma), and in other cases, multiple fragments from a single crystal spanned >3 Ma (e.g., z6a: 105.10 ± 0.10 Ma; z6b: 107.71 ± 0.37 Ma; z6c: 109.01 ± 0.08 Ma). The dispersion in dates from a single crystal is strongly correlated with variation in CL texture of sampled domains. All zircon grains from this sample have a significant sector and oscillatory zoned volume (e.g., z16d: 106.59 ± 0.12 Ma), and we interpreted these portions of the crystals as crystallizing during the main period of super-solidus zircon saturation. Some zircon grains have dark-banded and sector-zoned rims (e.g., z6a, z10b, z12, z18, z20) which we interpreted to constrain the main phase of magmatic zircon growth in this sample (ca. 105 to 103 Ma). The two youngest zircon dates (z15: 97.71 ± 0.44 Ma, and z14b: 96.21 ± 0.48 Ma) are from crystal fragments microsampled from CL-bright rims truncating interior zoning, a texture commonly associated with metamorphic growth (Corfu et al., 2003). These dates reflect mixtures between magmatic (>103 Ma) and metamorphic (<98 Ma, after shear zone initiation, described below) zircon domains and thus were interpreted as maximum ages of zircon rim growth during metamorphism.

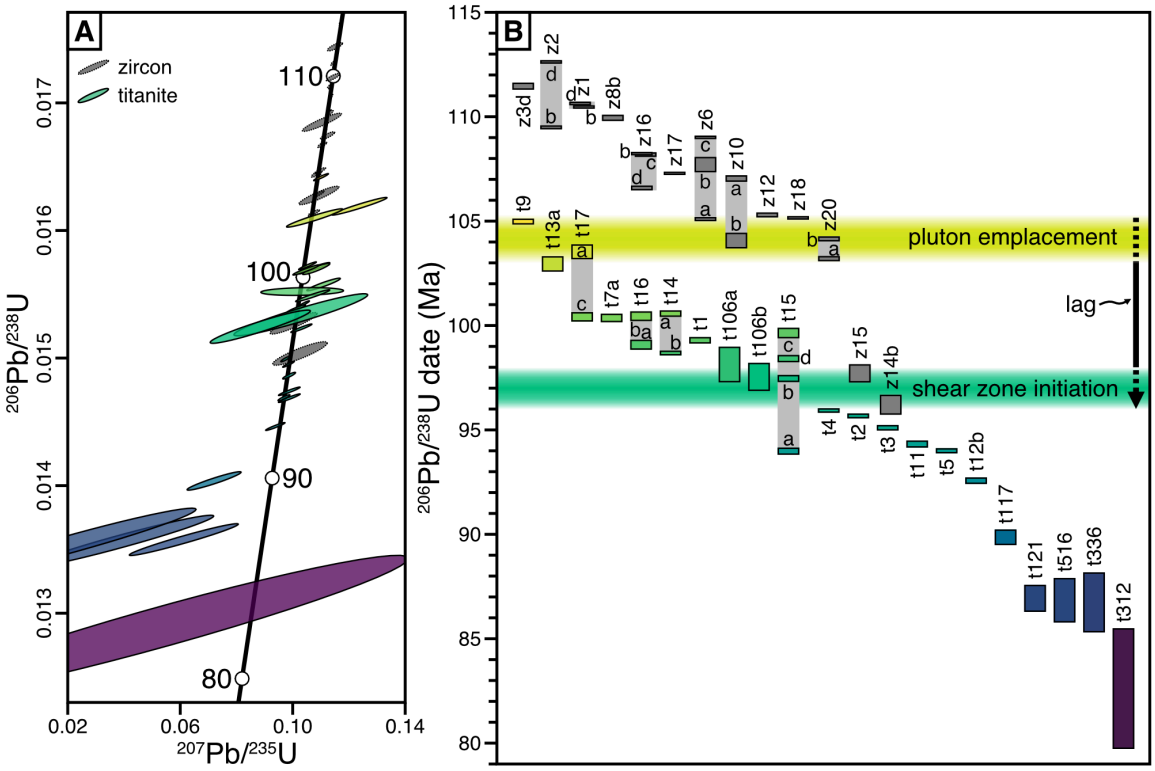

Figure 1.2. (A) Zircon (gray ellipses with dotted borders) and titanite (colored ellipses with solid borders) ID-TIMS dates in Wetherill concordia space. Titanite is colored according to $^{206}Pb/^{238}U$ date. (B) Ranked date plot of zircon (dark gray) and titanite (colored) ID-TIMS dates. The height of the rectangles is the 2σ uncertainty on the $^{206}Pb/^{238}U$ dates. Light gray bars connect fragments of the same crystal. Titanite symbols are colored according to $^{206}Pb/^{238}U$ date. The horizontal yellow band indicates the timing of pluton emplacement and crystallization, 105 to 103 Ma. The horizontal dark green band indicates the interval during which the shear zone initiated, 98 to 96 Ma. The vertical black arrow represents the time lag between pluton emplacement and the start of shear zone deformation.

Titanite Petrochronology

Microstructures

Titanite grains within oriented thick sections show a range of morphologies and degrees of crystallographic distortion because of both crystal plastic deformation and changes in crystallization conditions. Using internal zoning observed in BSE images, EBSD misorientation maps, and petrographic context, we recognized several distinct types of titanite grains (Figure 1.3.; Table 1.3.). Wedge-shaped titanite grains within K-

feldspar porphyroclasts have oscillatory zoning in BSE images and small degrees of misorientation (less than 1°) if the titanite c-axis is parallel to the lineation (e.g., t702). Subhedral, elongate titanite grains with little to no BSE zoning (e.g., t909) and with their c-axis parallel to the margin of K-feldspar porphyroclasts and ribboned quartz domains display the most significant misorientation gradient (0 to 5°) with the highest degrees of misorientation found at grain tips. Rounded and lenticular titanite grains characteristic of neoblastic growth are found within ribboned quartz and myrmekitic feldspar domains. These grains display minimal degrees of misorientation (less than 2°) despite commonly having elongate and boudinaged morphologies (e.g., t902). Some lenticular grains have no observable variations in composition (e.g., t902), while others display core and rim zones in BSE images (e.g., t903).

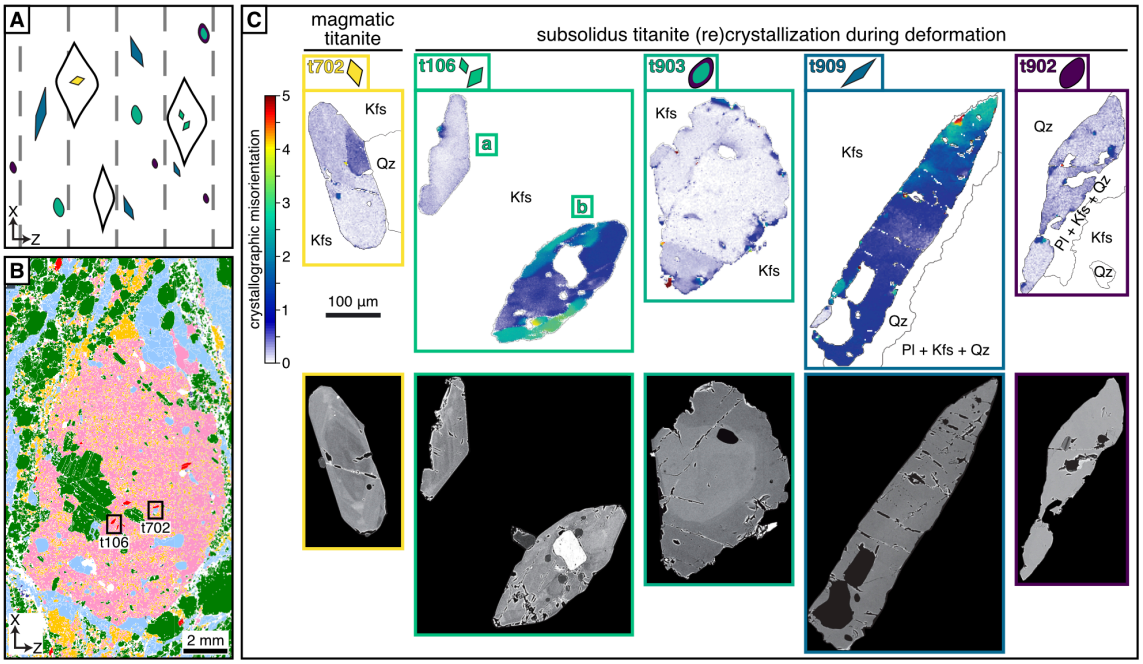

Figure 1.3. (A) Schematic XZ section (dashed lines parallel to lineation) with feldspar porphyroclasts (solid black lines) and titanite grains (colored shapes). The schematic highlights the different titanite populations: euhedral diamonds are magmatic or partially recrystallized grains; elongate, subhedral grains are recrystallized grains; and rounded grains are neoblastic grains. (B) EBSD phase map of an XZ section with a K-feldspar porphyroclast (pink) surrounded by ribboned quartz (blue) and calcic and sodic plagioclase (green and yellow, respectively). Titanite grains (red) can be observed within the porphyroclast and the fabric. Black boxes indicate titanite grains from this section that are highlighted in (C). (C) Schematic titanite grains paired with their representative grains. Boxes and labels are colored and ordered according to relative age based on position within geochemical trend (Figure 1.4.). Top row: titanite crystallographic misorientation maps for misorientations from 0-5°, with quartz (Qz), plagioclase (Pl), and K-feldspar (Kfs) labeled. Bottom row: BSE images for each grain.

Table 1.3. Summary of microstructural and textural titanite characteristics.

Example grain	t702	t106b	t903	t909	t902
Morphology	wedge-shaped	wedge-shaped	rounded and lenticular	subhedral, elongate	elongate and boudinaged
Fabric context	within K-feldspar porphyroclasts, titanite c-axis is parallel to the lineation	within K-feldspar porphyroclasts, titanite c-axis at high angle to the fabric	within ribboned quartz and myrmekitic feldspar domains	titanite c-axis parallel to the margin of K-feldspar porphyroclasts and ribboned quartz domains	within ribboned quartz and myrmekitic feldspar domains
Backscattered electron zoning	oscillatory	oscillatory	core and rim zones	minimal variation	minimal variation
Degree of misorientation	low (< 1°)	moderate to high (up to 4°)	low (< 2°)	high (up to 5°), highest misorientation at grain tips	low (< 2°)
Interpreted category	magmatic	partially recrystallized	neoblastic	fully recrystallized	neoblastic

Trace Element Geochemistry

We applied principal component analysis on a suite of trace element concentrations measured by LA-ICPMS to distinguish titanite compositional types and trends. The chemical variability reduced to three branches defined by divergence in Y + Nb, Th + light rare earth element concentrations, and U + heavy rare earth element concentrations (Figure 1.4.A.). When coded by Zr-in-titanite temperatures (Figure 1.4.A.; Hayden et al., 2008 with P = 0.44 GPa from Braudy et al., 2017) or age of ID-TIMS-dated crystals (Figure 1.4.B.; ages described below), systematic variations are observed between the branches of the principal component analysis score plot, with the coolest and youngest titanite crystals restricted to one branch of the data.

The dimensional reduction of principal component analysis efficiently highlights the trace elements most responsible for the chemical variance of titanite in this sample. However, by accentuating that variance through summing or ratioing certain geochemical parameters, we can more clearly visualize and interpret the differences between titanite compositional domains and their origins. By featuring geochemical parameters associated with the main titanite valence substitution groups (tri-, tetra-, and pentavalent), we examined the effect on different trace element substitution mechanisms during titanite (re)crystallization. A trivariate plot of rare earth elements (REE)–U–Nb/Th displays two "spurs" oblique to a main compositional trend of decreasing REE and high field strength elements (Figures 1.4.C. and 1.4.D.). The two spurs are distinctive because of their high Nb/Th and REE concentration, respectively. Titanite crystals that plot on the spurs commonly display sector (e.g., t1) or oscillatory zoning (e.g., t13a) in BSE images. Titanite in the spurs grew at high temperatures, up to about 770°C. By contrast, titanite

crystals in the main trend typically have a patchy or homogenous BSE response, and their temperatures decrease in a correlated fashion from about 725°C at high REE + U + Nb/Th to about 625°C at low REE + U + Nb/Th.

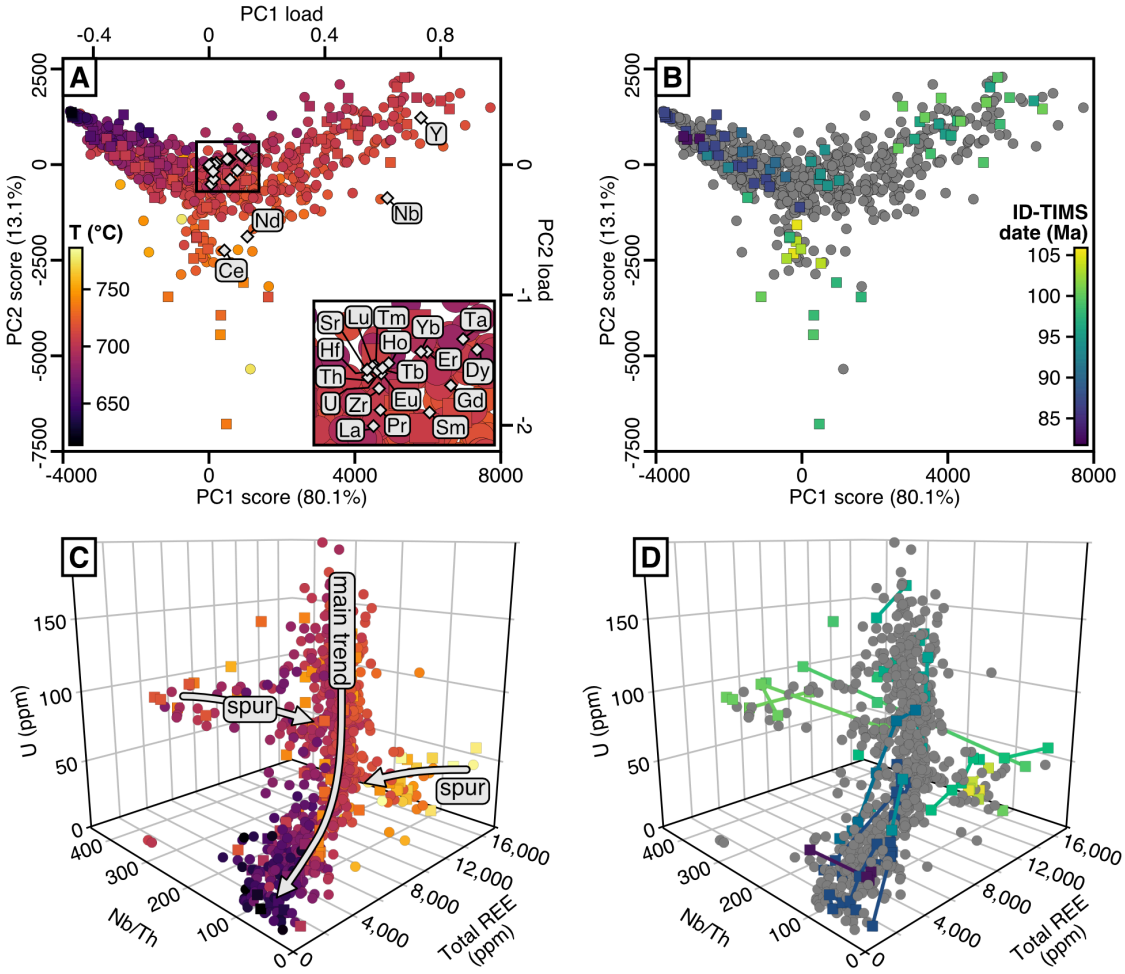

Figure 1.4. Trace element chemistry of titanite with ID-TIMS-dated crystals indicated by squares and undated crystals indicated by circles. Principal component analysis plots colored by (A) temperature and (B) ID-TIMS date. Principal component loads are shown as gray diamonds in (A). 80.1% and 13.1% are the percent contributions of principal components 1 and 2, respectively. Trivariate total REE–U–Nb/Th plots colored by (C) temperature and (D) ID-TIMS date. In (D), colored lines connect fragments of the same titanite crystal. Color bars in (A) and (B) also apply to (C) and (D), respectively. T – temperature, PC1 – principal component 1, PC2 – principal component 2.

Geochronology

We dated titanite grains sampled directly from various positions within thick sections as well as across chemical trends in grains from mineral separates to link textural and chemical indicators of titanite recrystallization and neoblastic growth to the time of deformation. Subsampling and dating intragrain titanite domains by ID-TIMS, including an initial Pb correction utilizing coexisting K-feldspar, achieved a median precision of 0.2% (2σ) on our individual crystal or crystal fragment titanite $^{206}Pb/^{238}U$ dates (Table 1.1.). A ^{204}Pb-based initial Pb correction of titanite data allowed us to plot titanite dates in the same Wetherill concordia space typically used for zircon dates, providing a graphical way to compare the ages and uncertainties of the different mineral chronometers. Apart from the four youngest, lowest U and least radiogenic reversely discordant titanite analyses, our ^{204}Pb-corrected titanite analyses are concordant, attesting to the accuracy of the K-feldspar based initial Pb correction strategy. In fact, our preferred initial Pb from K-feldspar is similar to modeled terrestrial Pb isotopic compositions from 100 to 80 Ma (Stacey and Kramers, 1975) and overlaps with the range of modern whole rock Pb from the Idaho Batholith (Figure 1.5.F., inset; Gaschnig et al., 2011).

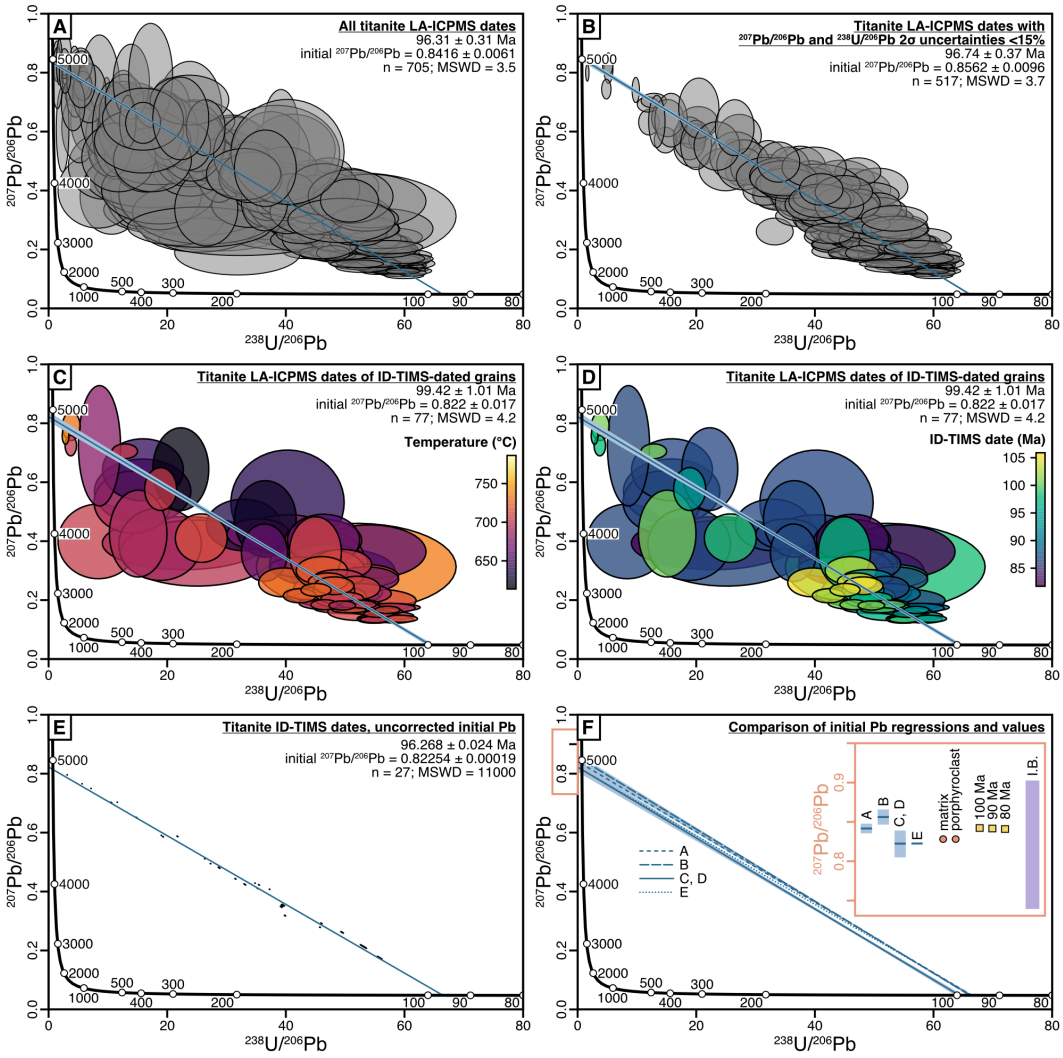

Figure 1.5. Comparison of titanite LA-ICPMS and ID-TIMS dates and regressions in Tera-Wasserburg concordia space. The concordia intercept age ± 95% confidence interval and the initial $^{207}Pb/^{206}Pb$ value ± 95% confidence interval are determined using the maximum likelihood algorithm of Ludwig (1998) and represented in the plots as dark blue lines in panels A-F with light blue error envelopes. Uncertainty in the isotopic measurements is shown as 95% confidence ellipses. (A) All titanite LA-ICPMS dates. (B) Titanite LA-ICPMS dates with $^{207}Pb/^{206}Pb$ and $^{238}U/^{206}Pb$ 2σ uncertainties <15%. (C, D) Titanite LA-ICPMS dates of spots on crystals or crystal fragments later dissolved for ID-TIMS colored by temperature (C) or ID-TIMS date (D). (E) Titanite ID-TIMS dates with no initial Pb correction applied. (F) Comparison of the regressions in panels A-E. (F, inset) Comparison of initial $^{207}Pb/^{206}Pb$ regression values and uncertainties from panels A-E (blue rectangles), measured $^{207}Pb/^{206}Pb$ values from matrix and porphyroclast K-feldspar (orange circles; 95% confidence interval analytical uncertainty is smaller than the size of the symbols), modeled $^{207}Pb/^{206}Pb$ using a two-stage isotope evolution model (Stacey and Kramers, 1975; yellow squares), and the range of modern whole rock $^{207}Pb/^{206}Pb$ values from the Idaho Batholith (Gaschnig et al., 2011; purple rectangle; I.B.–Idaho Batholith).

ID-TIMS dates from all titanite types range from 105.0 ± 0.1 Ma to 82.6 ± 2.9 Ma (Table 1.1.; Figure 1.2.). The three oldest dated titanite crystals or crystal fragments (104.98 ± 0.14 to 102.95 ± 0.37 Ma) located in the geochemical spurs (Figure 1.4.D.) are equivalent in age to the magmatic zircon fragments which constrain pluton emplacement in this sample (105.30 ± 0.12 to 103.20 ± 0.13 Ma), supporting inferences from textural and geochemical characteristics that magmatic titanite is locally preserved. Other subsampled titanite crystals from these geochemical spurs yield different dates for crystal fragments (e.g., four t15 fragments span from 99.64 ± 0.25 to 93.98 ± 0.17 Ma; Figure 1.2.B.), documenting subgrain isotopic resetting. Some titanite dates are thus likely averaging physical mixtures of different variably recrystallized titanite age domains. Several titanite crystals or crystal fragments (t106a, t106b, t15b, t4, t2) overlap within uncertainty with the dates of the metamorphic zircon rim fragments (z15, z14b), which links this minor sub-solidus zircon growth to the more substantial transformations occurring in titanite.

Within the higher-U portion of the main geochemical trend, titanite crystals like t4 and t2 are lenticular, a morphology associated with metamorphic titanite growth (Getty and Gromet, 1992). Thus, we interpret the dates of t4 and t2 (t4: 95.93 ± 0.11 Ma; t2: 95.67 ± 0.12 Ma) as relating to neoblastic growth during solid-state deformation. Consequently, we interpreted all titanite dates younger than t4 and t2 as dominantly reflecting neoblastic (re)crystallization during deformation. An inflection in the main geochemical trend corresponding to Zr-in-titanite temperatures <680°C, U concentrations <80 ppm, and total REE contents <5000 ppm corresponds to titanite crystals that return dates consistently <90 Ma.

Discussion

In Situ Versus Microsampled Isotope Dilution Geochronology

Multiple approaches exist for correcting titanite dates for the incorporation of initial Pb. A ^{204}Pb-based initial Pb correction is the standard approach for both ID-TIMS (Schmitz and Bowring, 2001) and SIMS titanite geochronology (Stern, 1997; Bonamici and Blum, 2020). The ^{204}Pb-based correction assumes an isotopic composition for initial Pb, either from a standard Earth Pb evolution model (Stacey and Kramers, 1975) or the measured isotopic composition of a co-existing low U phase (Frost et al., 2000), and allows the calculation of all three radiogenic ^{207}Pb*/^{206}Pb*, ^{207}Pb*/^{235}U and ^{206}Pb*/^{238}U chronometers to assess concordance. However, accurately measuring ^{204}Pb via LA-ICPMS is a challenge because of a ^{204}Hg isobaric interference related to contaminants in the Ar gas, and thus most LA-ICPMS titanite dates are computed with a ^{207}Pb-based initial Pb correction, whereby individual analyses are corrected based upon an estimated initial ^{207}Pb/^{206}Pb and assumed U-Pb isotope concordance, or groups of analyses are regressed in Tera-Wasserburg concordia space to return both an age and initial ^{207}Pb/^{206}Pb value from the concordia and ^{207}Pb/^{206}Pb axis intercepts (Storey et al., 2006; Bonamici and Blum, 2020).

The relatively young age, low U content, and close temporal spacing of the changes in titanite that we are attempting to resolve pose challenges for in situ LA-ICPMS geochronology. To assess the adequacy of a ^{207}Pb-based correction for both LA-ICPMS and ID-TIMS U-Pb dates, we regressed titanite data on Tera-Wasserburg plots to determine estimates for initial ^{207}Pb/^{206}Pb compositions and titanite ages in this sample (Figure 1.5.). When a subset of the LA-ICPMS isotopic data representing all portions of

the geochemical trivariate trends (Figure 1.4.D.) are plotted, no clear temperature- or age-defined populations emerge through which to regress the LA-ICPMS data to determine multiple initial $^{207}Pb/^{206}Pb$ values or dates corresponding to different titanite populations. This does not preclude the existence of multiple titanite populations in the sample; rather, the in situ isotopic data lacks the resolution to identify these populations. Single titanite grains with multiple LA-ICPMS spots only occasionally have sufficient spread in $^{207}Pb/^{206}Pb$ to produce robust intragrain regressions in Tera-Wasserburg space and do not reliably return reproducible initial $^{207}Pb/^{206}Pb$ estimates (Figure A1.2.). Regression of the ID-TIMS titanite data in Tera-Wasserburg space revealed significant over-dispersion from a linear fit (MSWD = 11000), discernible due to the high precision of ID-TIMS dates, strongly suggesting that these titanite crystals are not a single-age population and warning against indiscriminate grouping of analyses to define regression lines.

In ID-TIMS measurements, ^{204}Pb is the quantitative proxy for initial Pb. Measurements of ^{204}Pb can be used to subtract the initial Pb component from the total Pb budget and calculate radiogenic $^{207}Pb/^{235}U$ and $^{206}Pb/^{238}U$ dates using an estimate of the initial $^{207}Pb/^{204}Pb$ and $^{206}Pb/^{204}Pb$ ratios. A coeval low $^{238}U/^{204}Pb$ mineral, like K-feldspar, can provide the estimate of the pool of initial Pb incorporated into minerals that (re)crystallize during deformation (Frost et al., 2000). Notably, this technique for recovering radiogenic isotope ratios and corresponding dates does not rely on the grouping of multiple analyses to define regression lines, nor does it sacrifice the $^{207}Pb/^{235}U$ chronometer, like the commonly used "semi-total Pb" projection or "^{207}Pb-correction" technique in Tera-Wasserburg space (Stern, 1997; Ludwig, 1998; Storey et al., 2006). By using both the $^{206}Pb/^{238}U$ and $^{207}Pb/^{235}U$ chronometers, we can evaluate

concordance as well as confirm that individual titanite crystals and crystal subdomains can—and in this case, do—record distinct dates representing different stages of fabric development in a deformed rock (Figure 1.2.). Our concordant ID-TIMS dates document >22 Ma of magmatic and deformation-related titanite (re)crystallization, demonstrating that, for this sample, a single intercept age in Tera-Wasserburg space of all LA-ICPMS isotopic data is inadequate for making geological interpretations. Perhaps more importantly, within this larger range there are more rapid transitions in the evolution of deformation and crystal response, which are documented by the higher temporal resolution of ID-TIMS measurements on grain subdomains.

Bracketing Shear Zone Initiation: A Maximum Age from Titanite Recrystallization

Textural, geochemical, and age information can be used to ascribe a (re)crystallization process to different titanite crystal types within a single sample. It is apparent that titanite records multiple (re)crystallization processes within different fabric contexts. Specifically, EBSD phase and titanite crystallographic misorientation maps showed that most euhedral, wedge-shaped titanite grains are found included in K-feldspar porphyroclasts rather than the matrix. The inclusion of titanite within the core of K-feldspar porphyroclasts, a magmatic phase, indicates that some of the titanite within the rock formed during pluton emplacement and solidification. We interpreted these wedge-shaped titanite grains with low degrees of internal crystallographic misorientation as relict magmatic titanite, shielded from fully recrystallizing during shear zone deformation by the surrounding K-feldspar porphyroclast. However, some titanite grains included in K-feldspar porphyroclasts, particularly those grains whose c-axis is at a high angle to the rock fabric, do show crystallographic misorientation evidence of partial recrystallization.

We interpreted these wedge-shaped crystals with moderate to high crystallographic misorientation on titanite grain edges as partially recrystallized titanite that contains both relict magmatic and recrystallized domains. This shows that not all titanite grains included in porphyroclasts are shielded from and immune to deformation effects. Rather, even titanite grains within porphyroclasts respond to fabric-forming processes if their primary orientation is at a high angle to the developing solid-state fabric, which is, by inference, inducing local recrystallization of the K-feldspar porphyroclasts.

By integrating trace element chemistry and age on the trivariate plot, a more resolved correlation between chemistry and age is evident: the spurs are associated with older dates, while within the main trend, total REE, U, and Nb/Th decrease with time (Figure 1.4.D.). The spurs represent different magmatic compositions probably related to sector zoning (e.g., t1 LA-ICPMS spots were placed on different sector zones (Figure A1.1.) and plot on both spurs). The trivariate plot colored by temperature (Figure 1.4.C.) supports this interpretation with the hottest, magmatic temperatures generally restricted to the spurs. Intragrain geochemistry variations, commonly associated with high crystallographic misorientation, confirm that some crystals are physical mixtures of relict magmatic and newly recrystallized domains. On the trivariate REE–U–Nb/Th plot, LA-ICPMS spots on partially recrystallized titanite grains plot in a trend along the spurs. The spurs collapse from the two magmatic compositions of high Nb/Th and REE, respectively, into the main trend at intermediate REE + U + Nb/Th, presumably through REE and high field strength element expulsion during partial to full recrystallization. For example, two individual crystals approximately 200 μm from each other within a feldspar porphyroclast (Figure 1.3.) yield dates that overlap within uncertainty (t106a: 98.13 ±

0.86 Ma; t106b: 97.54 ± 0.68 Ma). The backscattered oscillatory zoning and the homogenous low degrees of misorientation in t106a (the small area of 1-2° of misorientation along the edge of t106a is likely an artifact of polishing) seemingly suggest that t106a is a relict magmatic grain, though its date (t106a: 98.13 ± 0.86 Ma) is a few million years younger than the pluton emplacement age as determined by zircon (ca. 105 to 103 Ma). This younger-than-expected date for t106a is explained by the space it occupies in the low-U spur of the trivariate REE–U–Nb/Th plot (Figure 1.4.D.). When the trivariate plot is rotated to highlight the spur visible in REE versus U space (Figure 1.6.), it is evident that grains t106a and t106b plot in an array between the high-REE end of the spur toward the main trend. One LA-ICPMS spot from t106a is a magmatic composition at the end of the spur, and another spot with a lower REE concentration indicates that some domains recrystallized, expelling trace elements, and therefore also resetting the U-Pb isotopic systematics in the recrystallized domains. This recrystallization is not obvious in the BSE image or the crystallographic misorientation map of t106a, possibly because of recrystallization below the polished surface of the grain.

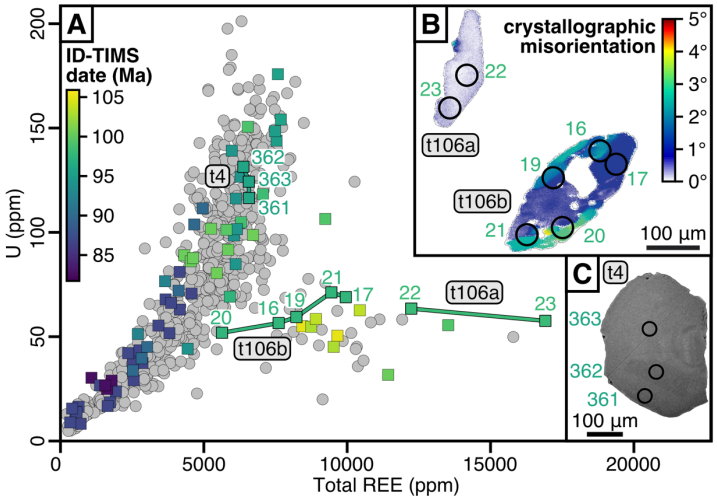

Figure 1.6. (A) Rotated view of the trivariate REE–U–Nb/Th plot (symbols as in Figure 4D) showing the main trend and lower U spur in total REE vs. U space. LA-ICPMS spot numbers for key titanite grains (t4, t106a, t106b) are highlighted in the geochemistry plot and mapped on (B) crystallographic misorientation maps of t106a and t106b and (C) a BSE image of t4.

The moderate to high degrees of the crystallographic misorientation along the edges of t106b, as well as its widely varying REE concentrations that plot along the spur and towards the main trend, are both indicative of deformation-induced recrystallization. Since the chemistry of t106b plots closer to the main trend than t106a, it has recrystallized more than t106a, and its date of (97.54 ± 0.68 Ma) provides an upper limit for the age of deformation initiation: ca. 98 Ma. Similarly, titanite grains older than ca. 98 Ma also plot in the spurs of the trivariate REE–U–Nb/Th plot and are interpreted as partially recrystallized, though to a lesser degree than t106b. In another example of subgrains tracking of recrystallization, fragments of grain t15 are older, equivalent in age to, and younger than t106a and t106b (Figure 1.2.). Grain t15 plots within the other high-Nb/Th spur and toward main trend on the REE–U–Nb/Th plot, consistent with the interpretation that magmatic to subsolidus titanite compositions will plot along the spurs and intersect with the main trend through partial recrystallization.

Bracketing Shear Zone Initiation: A Minimum Age from Titanite Neoblastic Growth

In addition to within K-feldspar porphyroclasts, titanite recrystallization is observed in the ribboned quartz and myrmekitic domains of the rock fabric. Quartz dynamic recrystallization features such as grain size reduction and grain boundary migration are consistent with strain localizing in these portions of the fabric. Titanite grains in these fabric domains tend to be highly to completely recrystallized with patchy crystallographic misorientation patterns, consistent with the strong reactivity of titanite to changes in differential stress (Kohn, 2017). These fabric domains also contain neoblastic titanite grains with a lenticular morphology and low degrees of crystallographic misorientation.

The interpretation of some titanite grains as neoblastic is consistent with their geochemical character. In the trivariate REE–U–Nb/Th plot, the lenticular or elongate and boudinaged titanite grains located within the ribboned quartz and myrmekitic feldspar fabric domains plot in the main trend of the data (Figures 1.4.C. and 1.4.D.). Critically, the spurs of magmatic and partially recrystallized titanite intersect the main trend at intermediate REE + U + Nb/Th, which means that titanite crystals with higher REE + U + Nb/Th grew with access to a trace element reservoir separate from the relict magmatic titanite. Nucleation of neoblasts was likely in response to an increase in available titanite-forming elements due to the local breakdown of magmatic phases, including calcic plagioclase into sodic plagioclase during solid state-deformation. Matrix titanite is spatially associated with biotite aggregations (Figure A1.3.), and the orientation of biotite defines the solid-state foliation in this sample. Therefore, the oldest neoblastic titanite date that plots within the high REE + U + Nb/Th portion of the main trend (t4:

95.93 ± 0.11 Ma; Figure 1.6.), above the spurs, reflects crystal nucleation during deformation and thus provides a minimum age for shear zone initiation: ca. 96 Ma.

Additionally, some crystals contain intragrain domains that plot in an array along the main trend, suggesting progressive growth and/or recrystallization with decreasing temperature. Some lenticular grains have distinct core and rim zones in BSE images, suggestive of multiple generations of neoblastic growth (e.g., t903; Figure 1.3.). The neoblastic and recrystallized titanite grains that plot in the mid to lower REE + U + Nb/Th portions of the main trend reflect continued deformation until at least 82.6 ± 2.9 Ma (t312). We interpreted the U-Pb dates of these titanite crystals as (re)crystallization ages rather than cooling ages because the Pb closure temperature in titanite is >750°C (Hartnady et al., 2019 and references therein). Titanite dates will record shear zone deformation until the pressure, temperature, and differential stress that control titanite reactivity diminishes to the point where titanite stops (re)crystallizing. Therefore, titanite likely does not capture the coolest end stages of shearing and is a poor constraint on the end of deformation. The Little Goose Creek complex was rapidly exhumed through hornblende and biotite $^{40}Ar/^{39}Ar$ closure temperatures (550°C and 325°C, respectively) between 85 and 70 Ma (Giorgis et al., 2008).

Mid-Cretaceous WISZ

The new petrochronological data show that WISZ deformation initiated between 98 and 96 Ma at this location within the Little Goose Creek complex. The solid-state deformation occurred >5 Ma after crystallization of the pluton between ca. 105 and 103 Ma. Because deformation in this sample was not ongoing during and immediately after pluton emplacement, the implication is that the dextral transpressional deformation

recorded in the WISZ is distinct from the suturing events in the Late Jurassic and Early Cretaeous (e.g., McClelland et al., 2000). Both the timing and the style of deformation is consistent with the growing recognition of a ca. 100 Ma event in which the oblique collision of the Insular superterrane with continental North America caused dextral transpressional deformation within the magmatic arcs of the central Cordillera (Tikoff et al., 2022 and references therein).

The titanite dates younger than 96 Ma indicate continued, protracted WISZ deformation. These results suggest that the WISZ was actively deforming during the intrusion of the ca. 90 Ma Payette River complex (Manduca et al., 1993; Giorgis et al., 2008). However, some WISZ studies have concluded that ca. 90 Ma is the end of WISZ deformation based on zircon U-Pb ages of non-deformed dikes and plutons (Giorgis et al., 2008; Braudy et al., 2017). These findings apparently contradict our youngest titanite dates that indicate that the shear zone was active until at least 82.6 ± 2.9 Ma. We suggest that this discrepancy is due to strain localizing in different lithologies across the shear zone and causing deformation to appear to cease at different times in different locations. Further titanite petrochronology throughout the WISZ, including the dating of non-deformed dikes and plutons, could evaluate this interpretation.

Conclusions

Tandem zircon and titanite petrochronology can determine when shear zone deformation initiated. Coexisting relict magmatic, recrystallized, and neoblastic titanite were distinguished by BSE images, EBSD microstructures, and trace element geochemistry. Age-integrated principal component analysis and geochemical trends document the changes induced by progressive fabric development at high temperatures.

A trivariate plot of REE–U–Nb/Th resolves a main geochemical trend of neoblastic and fully recrystallized titanite compositions and contrasting spurs of magmatic and partially recrystallized titanite compositions. Magmatic and partially recrystallized grains within K-feldspar porphyroclasts constrain deformation to younger than ca. 98 Ma. Neoblastic titanite grains defining a continuum of subsolidus geochemical and temperature variation are ca. 96 Ma and younger and represent nucleation and growth during active deformation. Thus, the shear zone thus initiated between 98 and 96 Ma. Systematic correlations between U-Pb age, crystallographic misorientation trends, and changing trace element geochemistry indicate that titanite deformation ages are robust.

The precision of titanite ID-TIMS geochronology is necessary to distinguish between near-synchronous magmatism and deformation. In the Little Goose Creek Complex of the western Idaho shear zone, Idaho, deformation lagged pluton emplacement by >5 Ma. This result indicates that WISZ shearing is a distinct event from Late Jurassic–Early Cretaceous terrane accretion. WISZ deformation beginning between 98 and 96 Ma is consistent with a major ca. 100 Ma event within the North American Cordillera related to the oblique collision of the Insular superterrane.

The presented approach is broadly applicable to any range of titanite compositions. The combination of statistical tools and enhanced petrological visualizations can be used to identify key components of the geochemical variance that isolate titanite response to strain and fabric development. This petrochronological workflow complements and extends diffusion-based thermochronometers to higher temperature deformation processes and may become a valuable tool for tectonics research in granitoid-hosted shear zones.

CHAPTER TWO: TANDEM ZIRCON AND TITANITE PETROCHRONOLOGY REVEALS SPATIAL-TEMPORAL PATTERNS OF MAGMATISM AND STRAIN LOCALIZATION IN THE WESTERN IDAHO SHEAR ZONE

Introduction

Magmatism and deformation are fundamental processes controlling the evolution of convergent plate margins and the formation and modification of continental lithosphere. In continental magmatic arcs, strain is commonly accommodated in high-temperature (>550°C) arc-axis shear zones hosted in granitoid plutonic rocks (e.g., de Saint Blanquat et al., 1998). In these settings, magmatism and deformation are interrelated processes, with deformation facilitating pluton emplacement in some settings (e.g., Titus et al., 2005) and with magmatism localizing deformation in others (e.g., Pennacchioni and Zucchi, 2013). Understanding the interplay between magmatism and deformation in shear zones will help in modeling how strain is partitioned at convergent margins.

One such structure that accommodated strain in an ancient convergent margin arc is the crustal-scale western Idaho shear zone (WISZ) of the northern U.S. Cordillera. The WISZ is a Late Cretaceous dextral transpressive shear zone on the western border of the Idaho batholith, proximal to the Salmon River suture zone, the boundary between accreted terranes and continental North America (Hamilton, 1963; Taubeneck, 1971; Fleck and Criss, 1988; McClelland et al., 2000). The WISZ has been interpreted to act as both a magmatic conduit for the emplacement of a variety of granitoid lithologies and a

high-strain zone of transpressional deformation (Manduca et al., 1993; McClelland et al., 2000), making this shear zone of interest for examining how magmatic and solid-state deformation processes interact.

In sheared granitoid plutons, the record of deformation manifests as a rock fabric that integrates strain over the lifetime of the shear zone. This accumulation of strain can begin during suprasolidus conditions of magma emplacement and extend to subsolidus, solid-state deformation of the crystallized rock mass (e.g., de Saint Blanquat et al., 1997). Syntectonic plutons may thus carry magmatic fabrics with the same orientation at which solid-state fabrics later develop. This integrated record can make identifying significant phases in the evolution of a shear zone challenging unless precise time constraints can be ascribed to different stages of fabric formation. Traditionally, bracketing constraints on the timing of deformation have been made by determining the age of magma emplacement using U-Pb zircon geochronology and by determining cooling ages related to exhumation, typically with the $^{40}Ar/^{39}Ar$ system.

As is common with other shear zones, the timing of WISZ deformation has been constrained by crosscutting relationships and dates of igneous plutons and dikes that have variable solid-state fabric development (e.g., Giorgis et al., 2008; Braudy et al., 2017). However, relying on crosscutting relationships is problematic if strain localizes in different lithologies and areas, with one area within the shear zone actively deforming while another area not accumulating strain is being crosscut by apparently weakly deformed dikes. In such cases, the solid-state fabrics (or lack thereof) do not sufficiently describe the shear zone activity. To move beyond a model of shear zone deformation in

which a broad area is assumed to be actively deforming at the same time, we need to assign ages to different stages of fabric development from the outcrop to map scale.

Through the tandem use of zircon ($ZrSiO_4$) and titanite ($CaTiSiO_5$) petrochronology, we can date magmatic and subsolidus processes. U-Pb zircon geochronology is commonly used to date granitoid pluton emplacement as well as high-grade metamorphic events (Davis et al., 2003 and references therein). U-Pb titanite geochronology can also be used to date the magmatic phase of granitoid plutons and has additional utility as a deformation chronometer (Getty and Gromet, 1992; Resor et al., 1996; Torvela et al., 2008; Rossetti et al., 2017; Papapavlou et al., 2017). To a greater degree than zircon, titanite responds to high temperature deformation by (re)crystallizing, and deformation-related titanite crystals or crystal domains can be distinguished from magmatic titanite by trace element geochemistry and the amount of intracrystalline lattice misorientation (Bonamici et al., 2015; Garber et al., 2017; Gordon et al., 2021). By recording processes spanning from pluton emplacement to solid state deformation, tandem zircon and titanite petrochronology can track a granitoid pluton through multiple stages of fabric development.

Directly dating the timing of fabric development allows us to ascribe a sequence and tempo to the strain events that accumulate as rock fabric with better resolution than relative dating methods. Here, we examine the spatial-temporal patterns of strain accumulation in the WISZ using tandem zircon and titanite petrochronology. We examine a variety of granitoid lithologies of varying emplacement and deformation depths, today exposed in an east-west transect near McCall, Idaho. We test the hypothesis that the WISZ did not deform across its width and depth simultaneously and instead

partitioned strain into localized areas of deformation, with different domains of the shear zone active at different times. We use backscattered electron (BSE) and cathodoluminescence (CL) imaging and trace element chemistry measured by in situ laser ablation–inductively coupled plasma mass spectrometry (LA-ICPMS) to characterize the zircon and titanite in our samples, and we use isotope dilution–thermal ionization mass spectrometry (ID-TIMS) on single crystals or crystal fragments to precisely reconstruct the record of pluton emplacement and shear zone evolution.

Geologic Background

The mid- to Late Cretaceous WISZ is a major structure that manifests as foliated granitoids on the western border of the Idaho batholith (Hamilton, 1963; Taubeneck, 1971; Fleck and Criss, 1988; McClelland et al., 2000), and its tectonic significance relates to its spatial association with the margin of North American continental crust. The WISZ spatially overlaps, modified, and is temporally distinct from the Salmon River suture zone, an Early Cretaceous structure that formed as island arc terranes obliquely converged with the margin of the North American continent (see Chapter One; Lund and Snee, 1988; McClelland et al., 2000; Montz and Kruckenberg, 2017). The Sr isotopic composition of Mesozoic plutons in Idaho has been used to differentiate between areas associated with accreted terranes ($^{87}Sr/^{86}Sr < 0.704$) and areas associated with Precambrian continental crust ($^{87}Sr/^{86}Sr > 0.708$), and in west-central Idaho this transition from low to high $^{87}Sr/^{86}Sr$ occurs over a restricted area, only 5-20 km wide (Armstrong et al., 1977; Fleck and Criss, 1985; Criss and Fleck, 1987; Lund and Snee, 1988; Manduca et al., 1992). Tracing the $^{87}Sr/^{86}Sr = 0.706$ isopleth, the WISZ strikes approximately N020° through southwestern Idaho and approximately N000° through west-central Idaho

and bends approximately 90° towards and into Washington near Orofino, Idaho (Figure 2.1; Fleck and Criss, 1985; Criss and Fleck, 1987; Manduca et al., 1993; Benford et al., 2010). Sr isotopes, along with other sharp geochemical gradients across the shear zone, including $\delta^{18}O$ isotopic values, support a subvertical arc-continent transition (Fleck and Criss, 1985; Criss and Fleck, 1987; Manduca et al., 1992). This spatially abrupt isotopic transition is the result of the transpressional component of WISZ deformation modifying a moderately-dipping accretionary boundary through tens of kilometers of east-west shortening (McClelland et al., 2000; Giorgis et al., 2005), though more recent work suggests more a more modest shortening estimate (Davis and Giorgis, 2014). Seismic data confirms that the WISZ is a crustal-scale structure with a subvertical orientation (Davenport et al., 2017).

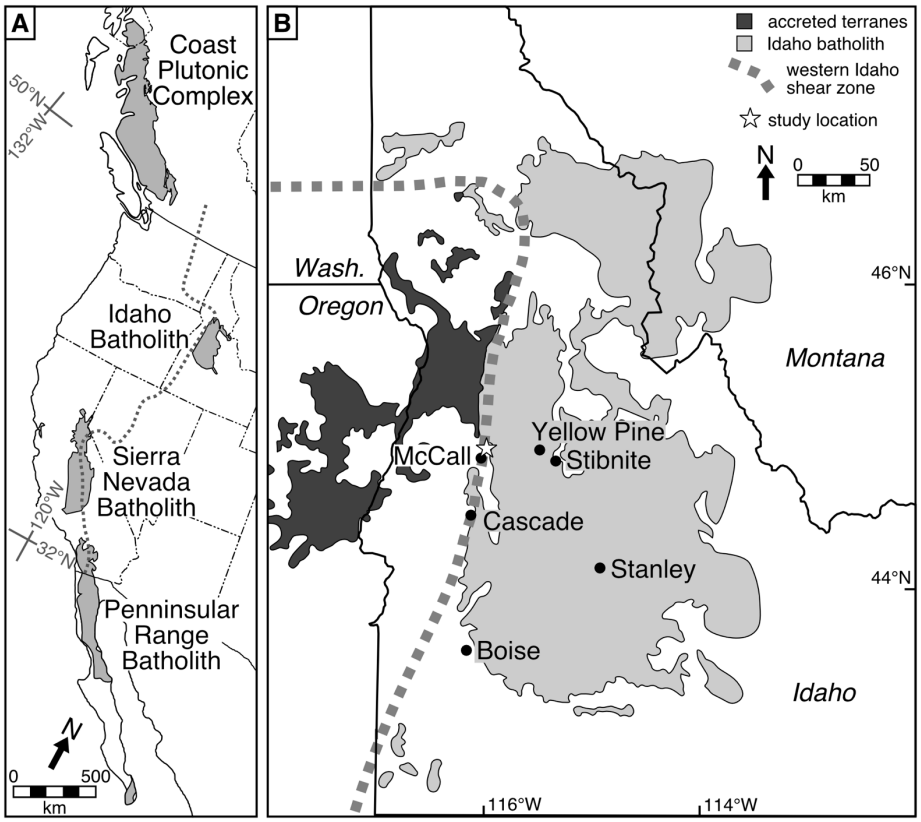

Figure 2.1. (A) Map of Cretaceous batholiths (gray polygons) of the North American Cordillera and the $^{87}Sr/^{86}Sr = 0.706$ isopleth (gray dashed line). (B) Map of the location of the$^{87}Sr/^{86}Sr = 0.706$ isopleth (gray dashed line) as a proxy for the location of the western Idaho shear zone and its relationship to Idaho batholith granitoids (light gray polygons) and accreted terrane rocks (dark gray polygons).

In addition to isotopic gradients and a seismic velocity model of the crust marking the location of the WISZ, the shear zone is identified by a strong solid-state fabric with a steeply dipping foliation and down-dip stretching lineations that record dextral transpressional kinematics (Lund and Snee, 1988; Manduca et al., 1993; McClelland et al., 2000; Giorgis and Tikoff, 2004; Michels et al., 2015). Miocene Basin and Range extensional tectonics modified the orientation of Late Cretaceous WISZ fabrics through normal faulting, and when the extensional effects are removed, the WISZ fabric is restored to a subvertical orientation (Tikoff et al., 2001). In addition to a broad, 5-20 km wide zone of foliated orthogneisses, deformation is also observed on the decimeter-scale

in the WISZ in north-south trending areas of localized strain (Manduca, 1988; McClelland et al., 2000). Furthermore, field and petrographic observations of a magmatic fabric parallel to the solid-state fabric have been used to infer that some of the granitoids were emplaced into an actively deforming shear zone, with the WISZ serving as a conduit for magma (Manduca et al., 1993).

In west-central Idaho, the WISZ has been mapped in three tabular plutonic complexes: the Hazard Creek complex (HCC), the Little Goose Creek complex (LGCC), and the Payette River complex (PRC; Figure 2.2.; Manduca, 1988; Manduca et al., 1993). Due to the dextral transpressive movement of the WISZ, today's surface exposure of the border zone west of the Idaho batholith reveals a gradient of deeply to shallowly emplaced plutons (Lund and Snee, 1988). The westernmost complex, the HCC, is composed of variably deformed tonalites, trondjhemites, granodiorite, and granites that commonly contain magmatic epidote (Taubeneck, 1971; Manduca et al., 1993), which signifies pluton emplacement depths of at least 25 km (Zen and Hammarstrom, 1984). East and inboard of the HCC, the tonalites, granodiorite, and granites of the LGCC have pervasive solid-state fabric development and contain the $^{87}Sr/^{86}Sr = 0.706$ isopleth. Based on the wall rocks and screens preserved in the three complexes, the transition from oceanic arc and continentally derived material is within the Little Goose Creek complex, and the transition occurs over less than 2 km (Manduca, 1988). Stepping further to the east, the tonalites, granodiorite, and granites of the PRC grade from strong solid-state fabric development on the west side of the complex near the contact with the LGCC to weak solid-state or magmatic fabric development on the easternmost side of the PRC. Both the LGCC and the PRC lack magmatic epidote and therefore were emplaced at

depths of less than 25 km (Zen and Hammarstrom, 1984; Manduca, 1988; Manduca et al., 1993). Amphibolite facies metasedimentary screens in the PRC record pressures of 3-6 kbar (Kuntz, 2007; Braudy et al., 2017), suggesting emplacement of the PRC at mid-crustal depths. A granodiorite complex with a weak, steep foliation is east and inboard of the PRC and has been associated broadly with the Border Zone suite of the Idaho batholith (Gaschnig et al., 2010) and more specifically referred to as the granodiorite of Box Lake (Kuntz, 2007). Continuing to the east, the Idaho batholith manifests as biotite granodiorite and muscovite-biotite granite and granodiorite of the Atlanta peraluminous suite (Lewis et al., 1987; Gaschnig et al., 2010).

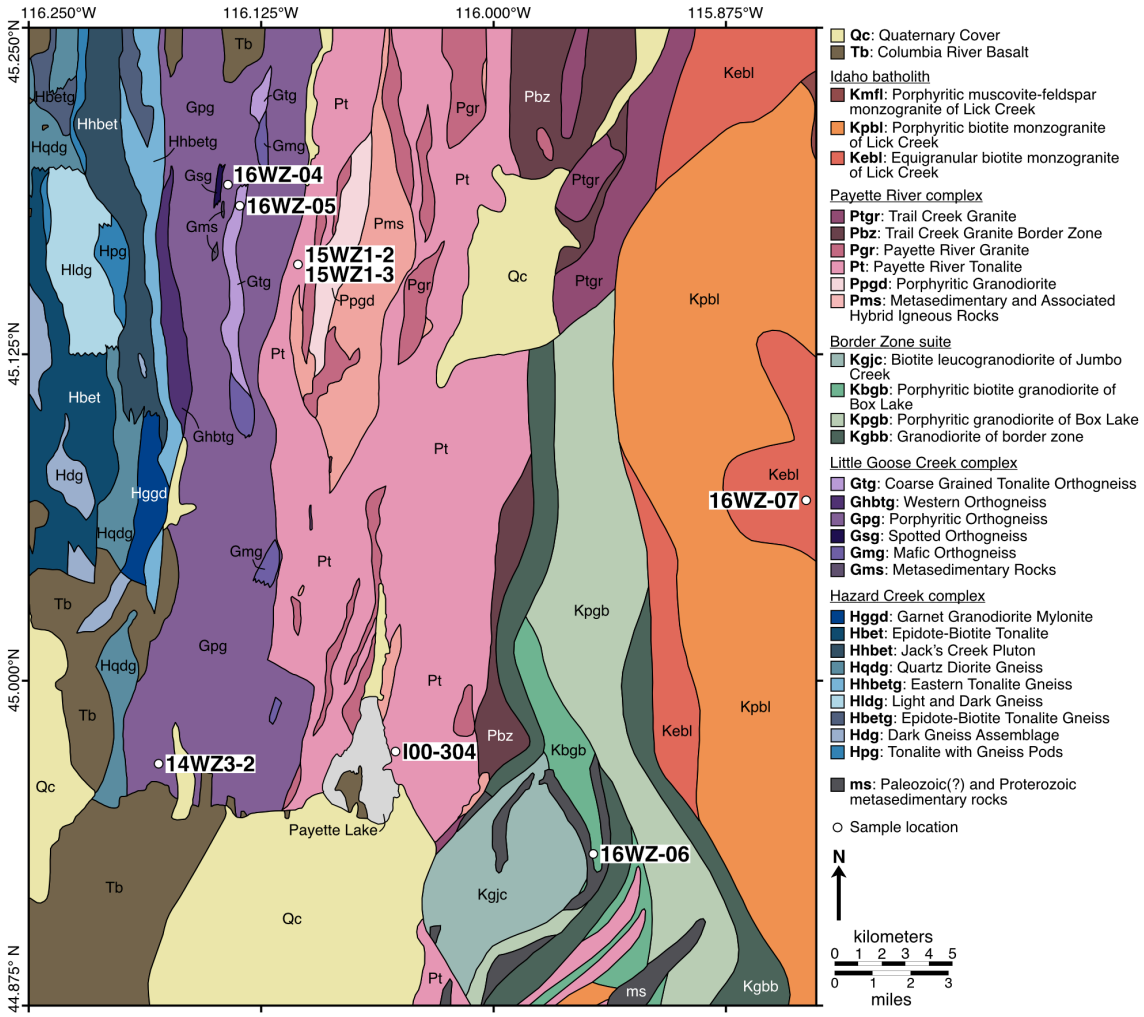

Figure 2.2. Map of plutonic and metasedimentary rocks within or proximal to the western Idaho shear zone near McCall, Idaho, with sample locations indicated. Modified from Manduca (1988) and Kuntz (2007).

Previous relative and absolute dating of the igneous rocks at the western margin of the Idaho batholith have tested hypotheses about synemplacement deformation and a general eastward younging of magmatism within the plutonic complexes deformed by and adjacent to the WISZ. In the McCall, Idaho area, Manduca et al. (1993) argued for synemplacement deformation of the LGCC and parts of the HCC based on contact relationships between older gneissic fabric or folded blocks cut by younger intrusions with weaker fabric development as well as tabular pluton geometry parallel to the solid-

state fabric. Manduca et al. (1993) dated members of each of the plutonic complexes deformed by the WISZ with U-Pb zircon geochronology and determined pluton emplacement ages of 118 ± 5 Ma for the HCC, 110 ± 5 Ma for the LGCC, and 90 ± 5 Ma for the PRC. Giorgis et al. (2008) determined consistent U-Pb zircon ages for the LGCC (105.2 ± 1.5 Ma) and the PRC (91.5 ± 1.1 and 89.7 ± 1.2 Ma). They also dated a mylonitic granodiorite gneiss that cross-cuts the LGCC fabric and found an age consistent with PRC ages: 90.0 ± 1.4 Ma. These fabric and geochronologic relationships have been used to argue that deformation in the WISZ was concurrent with LGCC pluton emplacement and ended during PRC emplacement. Our results from Chapter One contradict this narrative and instead place the beginning of WISZ deformation at 98 to 96 Ma, after the emplacement of the K-feldspar porphyritic granodiorite of the LGCC, while titanite dates as young as 85 Ma suggest continued fabric development in the LGCC after PRC emplacement. Kuntz (2007) used field relationships and U-Pb and $^{40}Ar/^{39}Ar$ geochronology to determine that the Granodiorite of Box Lake intruded into the tonalite of the PRC and was emplaced prior to Idaho batholith monzogranite emplacement, though they did not date zircon from the Granodiorite of Box Lake and do not have an absolute age for the emplacement of the Granodiorite of Box Lake unit. $^{40}Ar/^{39}Ar$ cooling ages in biotite and hornblende ranging from ca. 87 to 70 Ma support rapid exhumation and cooling during WISZ transpression (Kuntz, 2007; Giorgis et al., 2008).

Similar age relationships are documented elsewhere in the WISZ. In the West Mountain area, approximately 60 km south-southwest from McCall, Idaho, the western, weakly deformed tonalite unit yields a U-Pb zircon age of 100.9 ± 3.0 Ma which was interpreted as being emplaced prior to, and thus constraining, WISZ deformation (Braudy

et al., 2017). Orthogneisses from the West Mountain area range in U-Pb zircon age from 111 to 91 Ma and are interpreted to represent emplacement prior to and during deformation (Braudy et al., 2017). The youngest pluton in the West Mountain area is not foliated and yields a U-Pb zircon age of 88.2 ± 3.3 Ma and was interpreted to constrain the end of WISZ deformation (Braudy et al., 2017). Other U-Pb zircon ages from metaluminous plutons of the Border Zone and Atlanta lobe of the Idaho Batholith range from 98.2 ± 2.1 Ma to 86.7 ± 2.8 Ma (Gaschnig et al., 2010).

Sample Descriptions

We sampled the WISZ and related rocks near McCall, Idaho across a 28 km wide transect, from a highly deformed portion of the WISZ in the west to a non-deformed sample of the Idaho batholith in the east (Figure 2.2.; Table 2.1.).

Table 2.1. Sample locations and descriptions.

Sample	Sample Description	Latitude, Longitude†	Foliation	Lineation
Little Goose Creek complex				
14WZ3-2	K-feldspar porphyritic granodiorite orthogneiss	44.9669°N, 116.1809°W	N002, 60°E	59/076
16WZ-04	K-feldspar porphyritic granodiorite orthogneiss	45.1902°N, 116.1446°W	N.R.	N.R.
16WZ-05	coarse-grained tonalite orthogneiss	45.1822°N, 116.1380°W	N010, 85°E	85/089
Payette River complex				
15WZ1-2	tonalite orthogneiss	45.1596°N, 116.1072°W	N029, 70°E	44/026
15WZ1-3	leucocratic dike	45.1596°N, 116.1072°W	N.A.	N.A.
I00-304	tonalite	44.9720°N, 116.0548°W	N196, 61°W	N.R.
Border Zone suite and Idaho batholith				
16WZ-06	K-feldspar porphyritic granodiorite orthogneiss	44.9336°N, 115.9455°W	N184, 78°W	N.R.
16WZ-07	monzogranite	45.0686°N, 115.8330°W	N.A.	N.A.

†World Geodetic System 1984 (WGS84).
N.A.–not applicable; N.R.–not recorded.

Little Goose Creek Complex

We examined three samples from the Little Goose Creek complex to investigate how different lithologies influence strain localization in the WISZ. The lithological complexity in the LGCC includes orthogneisses with compositions of pyroxenite, gabbro, tonalite, and granodiorite (Manduca, 1988). The Porphyritic Orthogneiss (Gpg) unit of Manduca (1988) is a distinctive K-feldspar porphyritic orthogneiss, and this unit dominates the LGCC near McCall, Idaho. The intrusive contact relationships between Gpg and the other, interlayered orthogneisses of the LGCC have been obscured by deformation, and as such, the temporal relationships between different lithologies of the LGCC is somewhat unconstrained (Manduca, 1988).

We sampled the Porphyritic Orthogneiss (Gpg) unit in two locations as a first-order assessment of the temporal homogeneity of emplacement and deformation throughout the unit. One sample was taken from the southern area of the McCall segment of the WISZ, and a second sample was taken from 25 km north-northeast of the first sample. In the southern area along Highway 55, sample 14WZ3-2 of Gpg is a medium- to coarse-grained, mylonitic, porphyritic granodiorite with a strong, steep foliation and down-dip lineation and K-feldspar porphyroclasts up to 6 cm long. In the northern section of the McCall segment of the WISZ, near Upper Hazard Lake, sample 16WZ-04 of Gpg is a similarly medium- to coarse-grained, mylonitic, porphyritic granodiorite orthogneiss with K-feldspar porphyroclasts.

Despite contact relationships obscured by deformation, some WISZ units near McCall can be relatively dated by their association with the different plutonic complexes. Based on mineralogy, mafic mineral textures, and major element chemistry, Manduca

(1988) hypothesized that the Coarse-Grained Tonalite Orthogneiss (Gtg) unit was a sheet of PRC tonalite that intruded into the LGCC prior to mylonitic deformation. To test the emplacement and deformation age relationships between units Gpg and Gtg, we sampled the Gtg unit 1 km southeast of the 16WZ-04 sample of Gpg. Sample 16WZ-05 is a coarse-grained, non-porphyritic, compositionally banded, tonalite orthogneiss with abundant hornblende and titanite.

Payette River Complex

The Payette River complex is predominantly tonalite with some granodiorite and included metasedimentary screens (Manduca, 1988). The mapped solid-state fabrics decrease in strength towards the eastern margin of the PRC (Manduca, 1988), and some have proposed that only the western PRC, and not the eastern PRC, was deformed by the WISZ (Tikoff et al., 2001; Giorgis et al., 2008). The PRC has been compared to the tonalite sill along the eastern, inboard side of the Coast shear zone in Alaska and British Columbia, an intra-arc structure that, like the WISZ, records terrane accretion and then later transpressional kinematics (McClelland et al., 2000 and references therein). The magmatic and sub-solidus fabrics of the tonalite sill of the Coast shear zone, as in the tonalite of the PRC, are parallel to the solid-state fabric of the shear zone and thus these tonalite sheet complexes have been interpreted to have been syntectonically emplaced at shallow crustal depths (McClelland et al., 2000 and references therein). We tested the hypothesis that the tonalities of the PRC were emplaced during active WISZ deformation by dating the pluton emplacement and deformation ages of various samples of the PRC. We would expect both the pluton emplacement ages and the deformation ages to be

consistent with the LGCC deformation ages if the PRC intrusion was concurrent with WISZ deformation.

For this experiment we selected a strongly foliated sample from Fisher Creek Saddle near the LGCC–PRC contact. Sample 15WZ1-2 is a medium-grained tonalite orthogneiss mapped as Payette River Tonalite (Pt) by Manduca (1988). Its foliation is defined by hornblende phenocrysts and mafic enclaves. From the same outcrop, we sampled a non-foliated, relatively coarse-grained leuocratic dike (sample 15WZ1-3) that crosscuts the WISZ solid-state fabric and may be part of the collection of pegmatite and aplite dikes associated with Idaho batholith intrusion (Manduca, 1988). Previous studies have used weakly to non-foliated dikes and plutons to constrain the end of deformation in the WISZ (Giorgis et al., 2008; Braudy et al., 2017). This sample allowed us to examine the relationship between dike emplacement ages and the age of titanite associated with the WISZ foliation which is cross-cut by the dike.

We also examined a PRC sample with a weak foliation to test if the subsolidus deformation of the WISZ, as recorded by titanite, extended through the whole plutonic complex or whether the weaker fabrics on the east side of the PRC were the result of WISZ deformation ending during the emplacement of the eastern edge of the PRC. Manduca (1988) observed only weak subsolidus fabric development with recrystallized quartz west of the Payette River and concluded that the weak fabrics east of the Payette River and Payette Lake were likely magmatic and non-deformed. However, Manduca et al. (1993) determined that there was evidence of deformation that post-dated some or all PRC emplacement. To clarify whether the weakly developed fabric in parts of the PRC is magmatic or subsolidus and whether this part of the PRC was deformed by the WISZ, we

sampled a medium-grained tonalite from the east side of Payette Lake, McCall, Idaho. This sample, I00-304, is mapped as Payette River Tonalite (Pt) by Manduca (1988), and in outcrop, we observed equigranular quartz and a weak foliation defined by the alignment of mafic minerals.

Border Zone Suite and Idaho Batholith

The term "border zone" has been used to refer to gneissic tonalites to granodiorites along the margin of the Idaho batholith, distinct from the typically non-foliated, cross-cutting two-mica granites of the Idaho batholith (Hamilton, 1963; Taubeneck, 1971). We sampled from the Border Zone suite east of the PRC and west of the Idaho batholith two-mica granites to test the hypothesis that WISZ deformation extends further to the east than is currently mapped. The minor solid-state fabric on the east side of the Border Zone suite has been used in support of a model of the WISZ where pluton emplacement age and degree of strain grade from older, higher strain rocks in the west to younger, low- to no-strain rocks in the east (Lund and Snee, 1988; Manduca et al., 1993; Tikoff et al., 2001; Kuntz, 2007), though this model was suspected to be overly simplistic by some (Taubeneck, 1971). The mapped eastward extent of WISZ deformation near McCall is, in part, a product of where detailed mapping studies have been done (Manduca, 1988). We hypothesize that the low- to no-strain PRC rocks are a consequence of strain localization and not a reflection of the eastern edge of WISZ deformation. Constraining the spatial boundaries of the WISZ is critical for producing tectonic models of the WISZ that accurately represent the entirety of deformation across the structure.

Of the Border Zone suite, we sampled a strongly foliated granodiorite similar in character to the Gpg unit of the LGCC. Sample 16WZ-06 is a medium-grained, porphyritic granodiorite orthogneiss with 2-3 cm long K-feldspar porphyroclasts. The foliation is defined by the alignment of K-feldspar porphyroblasts, biotite books, ribboned quartz, and elongate mafic inclusions. Although our sample comes from outcrops mapped by Kuntz (2007) as the porphyritic biotite granodiorite of Box Lake (Kpgb), this sample was observed to have notably less biotite than the lithologies closer to Box Lake. The granodiorite of Box Lake is lithologically variable and has volumetrically and spatially significant inclusions of metasedimentary rocks and tonalite (Kuntz, 2007), but given that the area from which 16WZ-06 was sampled has significant lithological variation and little detailed mapping, we refer to this sample more generally as a K-feldspar porphyritic granodiorite orthogneiss of the Border Zone suite rather than the granodiorite of Box Lake.

A few kilometers east of where we sampled 16WZ-06, the Border Zone suite is in contact with the Idaho batholith (Kuntz, 2007), so to continue exploring the eastern extent of the WISZ, we sampled a non-foliated monzogranite characteristic of the Idaho batholith. Sample 16WZ-07 is a light-colored, medium- to coarse-grained equigranular granite mapped by Kuntz (2007) as the equigranular biotite monzogranite (Kebl) of Lick Creek.

Methods

Zircon Petrochronology

We used zircon petrochronology to date pluton emplacement and, in some cases, metamorphic zircon rim growth during deformation. Zircon petrochronology included

crystal imaging by cathodoluminescence (CL; Figure 2.3.; Appendix B), trace element geochemical analysis by laser ablation – inductively coupled plasma mass spectrometry (LA-ICPMS), initial Pb characterization through the measurement of Pb isotopes in coexisting feldspar, and high precision age determination through chemical abrasion – isotope dilution thermal ionization mass spectrometry (CA-ID-TIMS). Methods are detailed in Chapter One.

Figure 2.3. CL images of zircon crystals dated by LA-ICPMS (white circles and white numbers indicate LA-ICPMS spots) and CA-ID-TIMS (dated fragments are outlined with white dashed lines, otherwise entire crystal was dissolved and dated).

Titanite Petrochronology

We used titanite petrochronology to characterize and date magmatic through sub-solidus titanite to date pluton emplacement, when possible, and high-temperature deformation. Titanite petrochronology entailed backscattered electron (BSE) imaging (Figures 2.4. and 2.5.; Appendix B), trace element geochemical analysis by LA-ICPMS, initial Pb characterization through the measurement of Pb isotopes in coexisting feldspar, and high precision age determination through isotope dilution – thermal ionization mass spectrometry (ID-TIMS). Methods are detailed in Chapter One.

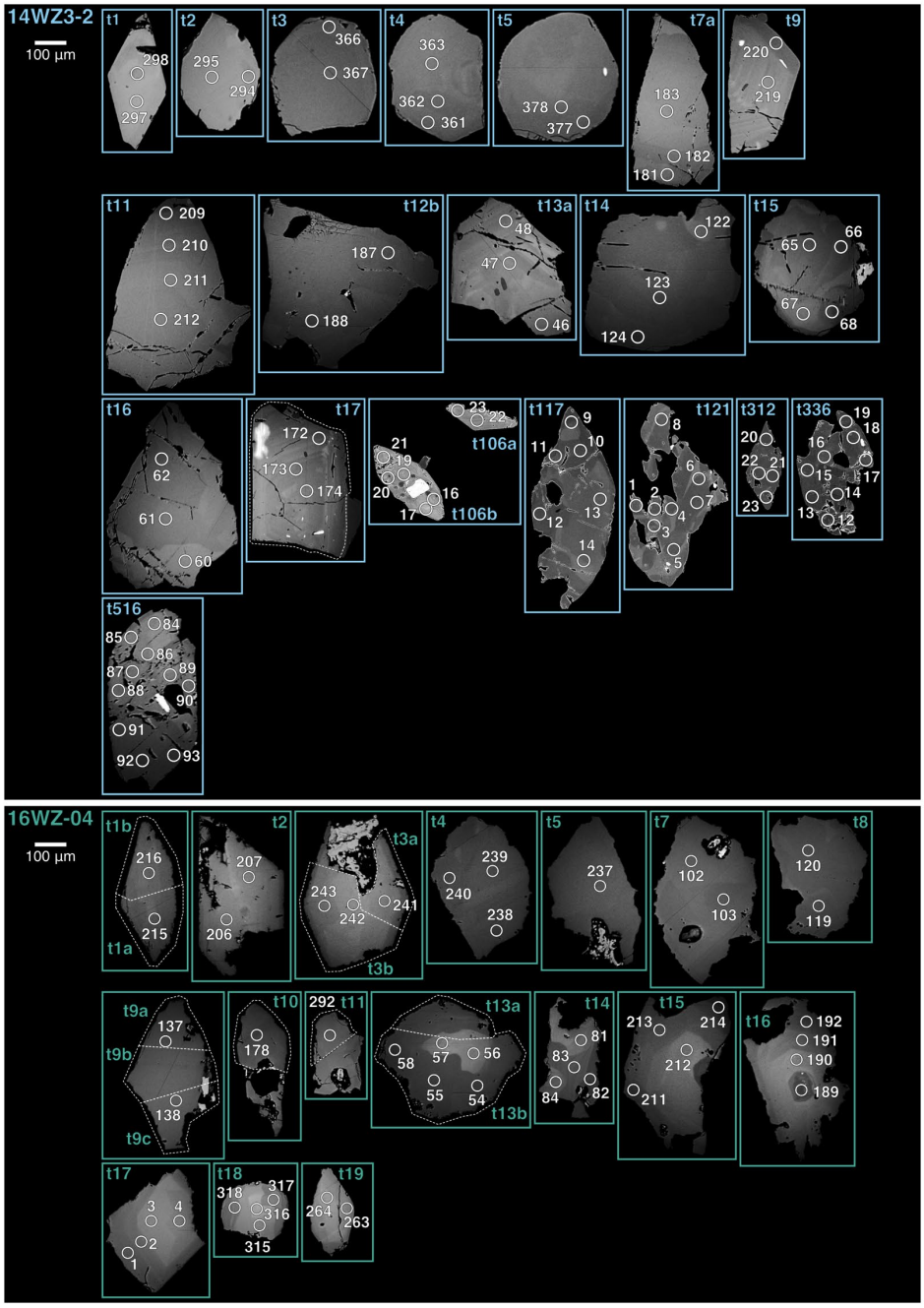

Figure 2.4. BSE images of titanite crystals dated by LA-ICPMS (white circles and white numbers indicate LA-ICPMS spots) and CA-ID-TIMS (dated fragments are outlined with white dashed lines, otherwise entire crystal was dissolved and dated) for samples 14WZ3-2 and 16WZ-04.

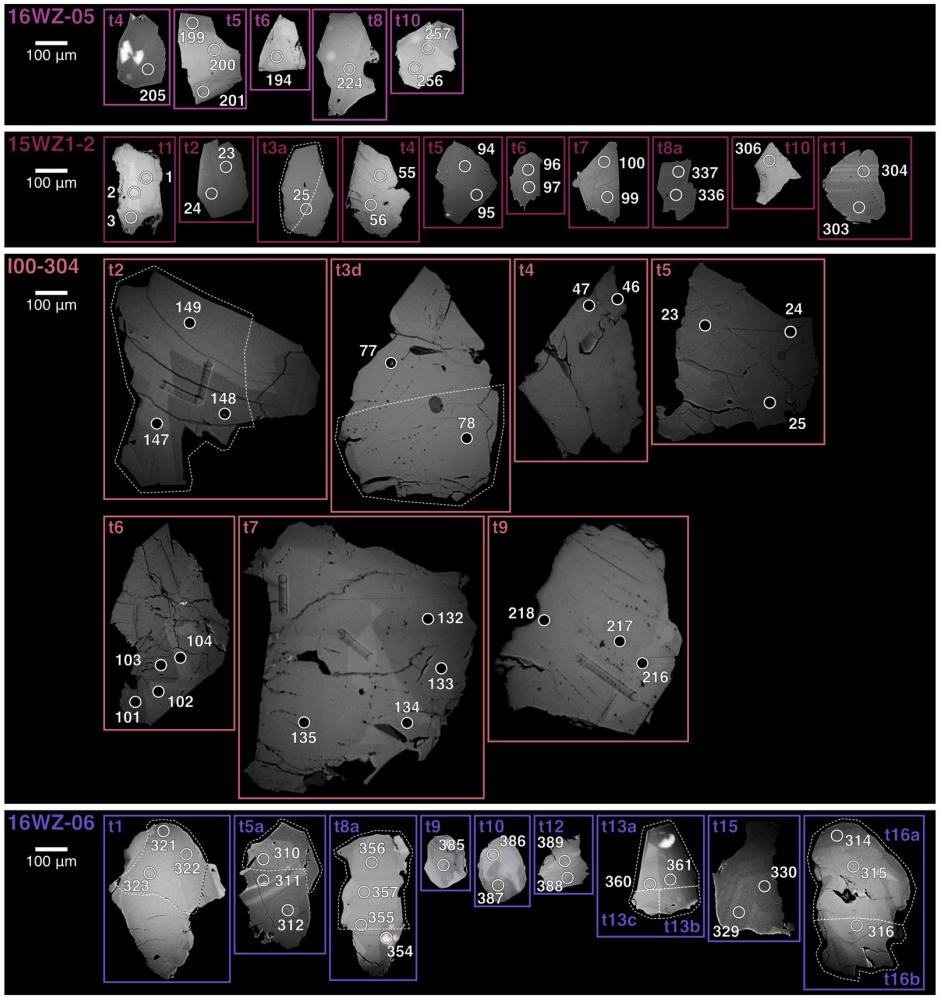

Figure 2.5. BSE images of titanite crystals dated by LA-ICPMS (white circles and white numbers indicate LA-ICPMS spots) and CA-ID-TIMS (dated fragments are outlined with white dashed lines, otherwise entire crystal was dissolved and dated) for samples 16WZ-05, 15WZ1-2, I00-304, and 16WZ-06.

Results

All dates reported below are ID-TIMS $^{206}Pb/^{238}U$ dates with 2σ analytical uncertainties and have been corrected for initial Pb isotopic composition (Figures 2.6. and 2.7.; Tables 2.2., 2.3., 2.4., 2.5, and B2.1.). When appropriate, we calculated a weighted mean age (Table 2.5.). However, for some samples, age dispersion due to temporally distinct periods of zircon growth led us to generally interpret zircon grains or tips with oscillatory and sector zoning in CL as reflecting magmatic crystallization. Inherited cores

and metamorphic rims are a common feature of these granitoid zircons, so we interpreted the dates of the youngest zircon tips without metamorphic rims visible in CL as representing the main phase of pluton crystallization and emplacement. As discussed further below, we generally interpreted titanite dates as a record of (re)crystallization processes during deformation, though one sample yielded relict magmatic titanite.

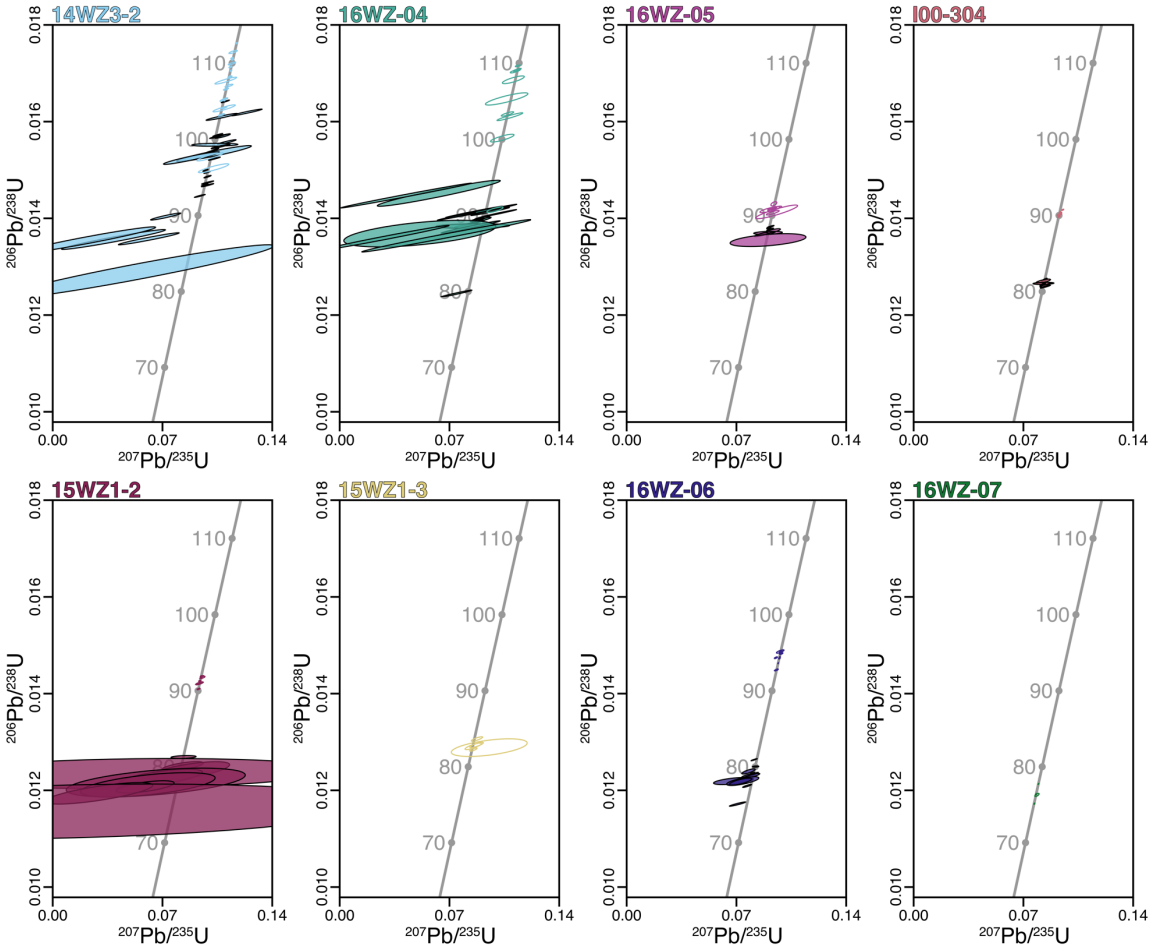

Figure 2.6. Wetherill concordia diagrams of zircon (open ellipses) and titanite (closed ellipses) dated by ID-TIMS.

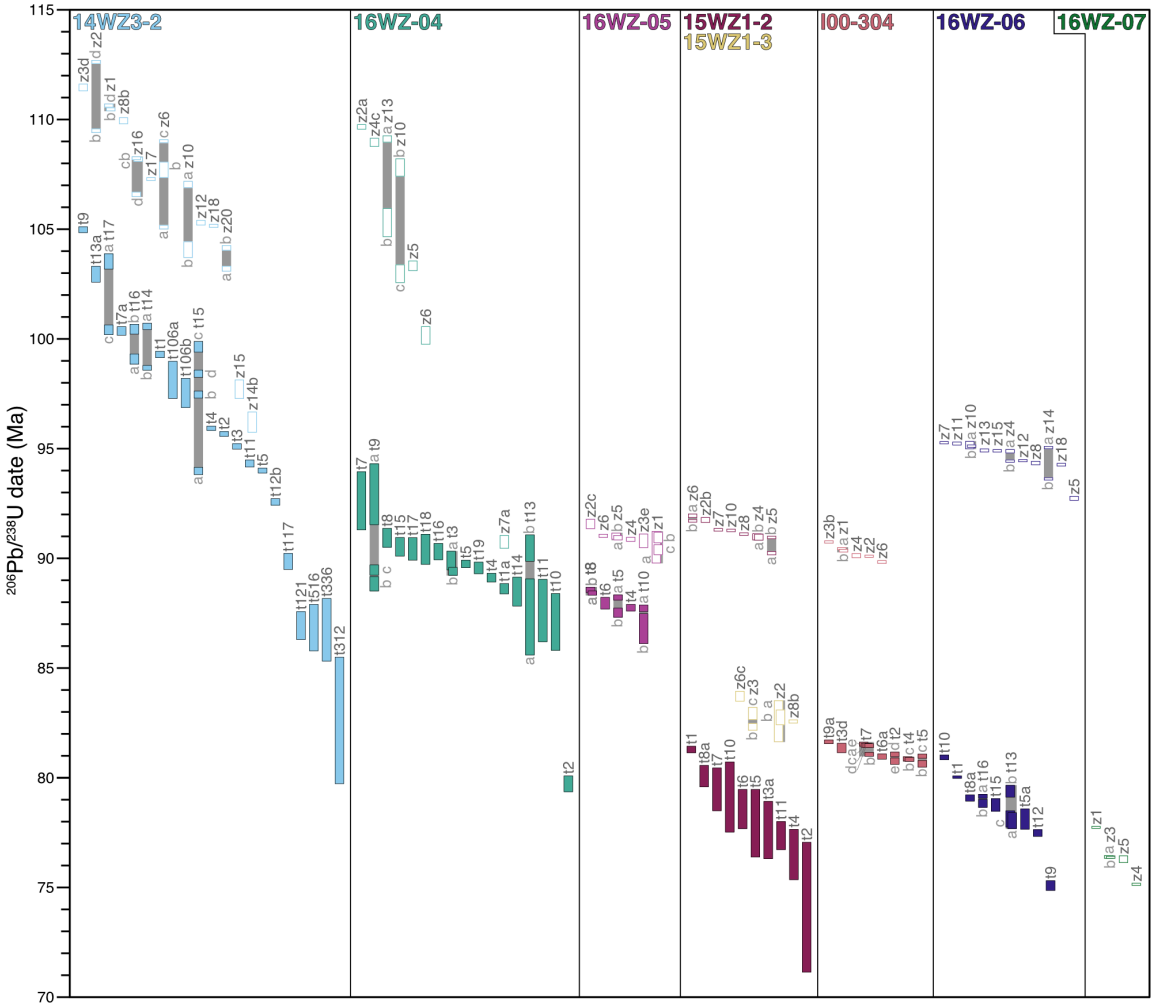

Figure 2.7. Ranked date plot of zircon (open rectangles) and titanite (closed, colored rectangles) crystals and crystal fragments dated by ID-TIMS. Fragments of the same crystal are connected by a vertical gray bar. Samples are arranged from west (left) to east (right).

Table 2.2. Initial Pb isotopic compositions of matrix K-feldspar.

Sample	$^{208}Pb/^{206}Pb$	$^{207}Pb/^{206}Pb$	$^{208}Pb/^{204}Pb$	$^{207}Pb/^{204}Pb$	$^{206}Pb/^{204}Pb$
14WZ3-2	2.045 ± 0.018	0.828 ± 0.011	38.614 ± 0.024	15.636 ± 0.017	18.8809 ± 0.0076
16WZ-04	2.044752 ± 0.000042	0.8282916 ± 0.0000095	38.6024 ± 0.0019	15.63725 ± 0.00065	18.87909 ± 0.00061
16WZ-05	2.03836 ± 0.00073	0.82269 ± 0.00016	38.779 ± 0.026	15.6511 ± 0.0078	19.0244 ± 0.0062
15WZ1-2	2.02826 ± 0.00059	0.81455 ± 0.00012	39.063 ± 0.022	15.6878 ± 0.0067	19.2594 ± 0.0054
15WZ1-3	2.006 ± 0.032	0.806 ± 0.012	39.102 ± 0.022	15.701 ± 0.021	19.49 ± 0.32
I00-304	2.02665 ± 0.00025	0.813191 ± 0.000026	39.118 ± 0.015	15.696 ± 0.0044	19.3017 ± 0.0049
16WZ-06	2.0094 ± 0.00031	0.80165 ± 0.000088	39.432 ± 0.013	15.7316 ± 0.0043	19.624 ± 0.0036
16WZ-07	2.03661 ± 0.000026	0.8131666 ± 0.0000076	39.3562 ± 0.0016	15.7144 ± 0.00062	19.32498 ± 0.00065

Table 2.3. Zircon $^{206}Pb/^{238}U$ dates by ID-TIMS.

Sample	Date ± 2σ uncertainty (Ma)	
14WZ3-2		
z1b	110.464	0.086
z1d	110.635	0.088
z20a	103.20	0.13
z20b	104.15	0.12
z2b	109.49	0.10
z2d	112.624	0.087
z3d	111.46	0.17
z6a	105.10	0.10
z6b	107.71	0.37
z6c	109.011	0.084
z8b	109.94	0.15
z10a	107.04	0.16
z10b	104.07	0.38
z11	134.13	0.11
z12	105.30	0.12
z13a	164.78	0.12
z13b	149.88	0.12
z14b	96.21	0.48
z15	97.71	0.44
z16b	108.233	0.083
z16c	108.18	0.11
z16d	106.59	0.12
z17	107.287	0.081
z18	105.155	0.086
z19a	157.65	0.13
z19b	134.93	0.10

Sample	Date ± 2σ uncertainty (Ma)	
16WZ-04		
z2a	109.66	0.12
z4c	108.96	0.20
z5	103.33	0.24
z6	100.16	0.42
z7a	90.75	0.31
z10b	107.81	0.41
z10c	102.97	0.42
z13a	109.11	0.16
z13b	105.30	0.65
16WZ-05		
z1a	90.51	0.73
z1b	90.95	0.26
z1c	90.39	0.24
z2c	91.57	0.23
z3e	90.80	0.32
z4	90.87	0.11
z5a	90.94	0.12
z5b	91.01	0.15
z6	91.027	0.085
15WZ1-2		
z2b	91.75	0.13
z4a	90.96	0.15
z4b	90.98	0.16
z5a	90.236	0.089
z5b	90.950	0.070
z6a	91.940	0.095
z6b	91.710	0.074
z7	91.301	0.076
z8	91.105	0.075
z10	91.273	0.073

Sample	Date ± 2σ uncertainty (Ma)	
15WZ1-3		
z2a	82.58	0.95
z2b	82.75	0.35
z3b	82.32	0.17
z3c	82.93	0.29
z6c	83.71	0.24
z8b	82.565	0.088
I00-304		
z1a	90.441	0.064
z1b	90.350	0.078
z2	90.096	0.063
z3b	90.746	0.070
z4	90.12	0.11
z6	89.834	0.079

Sample	Date ± 2σ uncertainty (Ma)	
16WZ-06		
z4a	94.881	0.093
z4b	94.431	0.068
z5	92.74	0.11
z7	95.269	0.065
z8	94.343	0.096
z10a	95.16	0.18
z10b	95.114	0.072
z11	95.233	0.085
z12	94.452	0.066
z13	94.918	0.086
z14a	95.046	0.067
z14b	93.621	0.066
z15	94.900	0.070
z18	94.268	0.077
16WZ-07		
z1	77.739	0.058
z3a	76.390	0.082
z3b	76.373	0.060
z4	75.142	0.066
z5	76.29	0.17

Table 2.4. Titanite $^{206}Pb/^{238}U$ dates by ID-TIMS.

Sample	Date ± 2σ uncertainty (Ma)	
14WZ3-2		
t1	99.29	0.16
t2	95.67	0.12
t3	95.10	0.14
t4	95.93	0.11
t5	94.00	0.12
t7a	100.36	0.21
t9	104.98	0.14
t11	94.32	0.17
t12b	92.57	0.16
t13a	102.95	0.37
t14a	100.57	0.16
t14b	98.68	0.12
t15a	93.98	0.17
t15b	97.46	0.17
t15c	99.64	0.25
t15d	98.42	0.17
t16a	99.08	0.24
t16b	100.45	0.23
t17a	103.53	0.36
t17c	100.41	0.23
t106a	98.13	0.86
t106b	97.54	0.68
t117	89.86	0.38
t121	86.93	0.65
t516	86.8	1.1
t312	82.6	2.9
t336	86.7	1.4

Sample	Date ± 2σ uncertainty (Ma)	
16WZ-04		
t1a	88.62	0.24
t2	79.72	0.37
t3a	89.90	0.44
t3b	89.40	0.19
t4	89.12	0.21
t5	89.75	0.18
t7	92.6	1.3
t8	90.93	0.44
t9a	92.9	1.4
t9b	88.84	0.34
t9c	89.47	0.24
t10	87.1	1.3
t11	87.6	1.4
t13a	87.3	1.7
t13b	90.47	0.61
t14	88.48	0.67
t15	90.52	0.43
t16	90.31	0.38
t17	90.43	0.52
t18	90.41	0.70
t19	89.56	0.27
16WZ-05		
t4	87.75	0.16
t5a	88.21	0.13
t5b	87.52	0.22
t6	87.95	0.28
t8a	88.42	0.11
t8b	88.56	0.14
t10a	87.72	0.16
t10b	86.80	0.69

Sample	Date ± 2σ uncertainty (Ma)	
15WZ1-2		
t1	81.29	0.16
t2	74.1	3.0
t3a	77.6	1.3
t4	76.5	1.2
t5	77.9	1.6
t6	78.57	0.90
t7	79.47	0.98
t8a	80.07	0.50
t10	79.1	1.6
t11	77.36	0.65
I00-304		
t2d	81.07	0.11
t2e	80.76	0.16
t3d	81.36	0.22
t4b	80.83	0.10
t4c	80.86	0.11
t5b	80.64	0.16
t5c	80.98	0.11
t6a	80.97	0.13
t7a	81.47	0.10
t7b	81.07	0.10
t7c	81.47	0.11
t7d	81.47	0.10
t7e	81.53	0.10
t9a	81.64	0.10

Sample	Date ± 2σ uncertainty (Ma)	
16WZ-06		
t1	80.029	0.067
t5a	78.12	0.47
t8a	79.08	0.15
t9	75.08	0.23
t10	80.93	0.12
t12	77.48	0.16
t13a	78.04	0.37
t13b	79.38	0.28
t13c	78.12	0.38
t16a	79.16	0.10
t15	78.76	0.30
t16b	78.83	0.19

Table 2.5. Summary of ages.

Sample	Pluton emplacement age (Ma)	Deformation age range (Ma)
Little Goose Creek complex		
14WZ3-2	105.30 ± 0.12 to 103.20 ± 0.13	98.1 ± 0.9 to 82.6 ± 2.9
16WZ-04	105.30 ± 0.65 to 102.97 ± 0.42	92.9 ± 1.4 to 79.7 ± 0.4
16WZ-05	90.88 ± 0.07	88.56 ± 0.14 to 86.80 ± 0.69
Payette River complex		
15WZ1-2	91.94 ± 0.10 to 90.24 ± 0.09	81.3 ± 0.2 to 74.1 ± 3.0
15WZ1-3	82.55 ± 0.07	N.R.
I00-304	90.75 ± 0.07 to 89.83 ± 0.08	81.64 ± 0.10 to 80.64 ± 0.16
Border Zone suite and Idaho batholith		
16WZ-06	95.09 ± 0.03	80.93 ± 0.12 to 75.08 ± 0.23
16WZ-07	77.74 ± 0.06 to 75.14 ± 0.07	N.R.

*Ages are weighted mean ages unless a range is given.
N.R. – not recorded due to lack of titanite in sample.

Little Goose Creek Complex

Sample 14WZ3-2, K-feldspar Porphyritic Granodiorite Orthogneiss

The geochronologic results for sample 14WZ3-2 are presented in detail in Chapter One. In summary, the main phase of pluton emplacement of this porphyritic granodiorite ranged from 105.30 ± 0.12 to 103.20 ± 0.13 Ma (n = 6), and deformation began between 98 and 96 Ma. Deformation continued until at least 82.6 ± 2.9 Ma. There was a lag of >5 Ma between the main phase of pluton emplacement as determined by zircon petrochronology and the onset of deformation as determined by titanite petrochronology. In Chapter One, we used this lag between emplacement and deformation to infer that WISZ is a separate event from Late Jurassic–Early Cretaceous accretionary tectonics, dispelling a previous hypothesis that Salmon River suture zone deformation was continuous through to WISZ fabric development (Gray et al., 2012).

Sample 16WZ-04, K-feldspar Porphyritic Granodiorite Orthogneiss

Zircon from sample 16WZ-04, a K-feldspar porphyritic granodiorite orthogneiss texturally similar to sample 14WZ3-2, recorded dates between 109.66 ± 0.12 and 90.75 ± 0.31 Ma (n = 9). The zircon crystal fragments separated into three populations based on age and CL texture. The dates of the four oldest crystal fragments ranged from 109.66 ± 0.12 to 107.81 ± 0.41 Ma and represent antecrystic cores. We interpreted the three crystal fragments with oscillatory zoning that range from 105.30 ± 0.65 to 102.97 ± 0.42 Ma (z13b, z5, z10c) as reflecting pluton emplacement. The youngest zircon population in this sample has CL-light rims that crosscut the oscillatory zoning. Because of their young ages (z6: 100.16 ± 0.42 Ma; z7a: 90.75 ± 0.31 Ma) and CL zoning patterns, we

interpreted these fragments as reflecting dissolution and reprecipitation of zircon rims during high temperature deformation.

Titanite from sample 16WZ-04 ranged from 92.9 ± 1.4 to 79.7 ± 0.4 Ma (n = 21). The youngest titanite crystal (t2: 79.72 ± 0.37) was >5 Ma younger than the second youngest titanite crystal (t10: 87.1 ± 1.3 Ma). The date of crystal t2 is consistent with the deformation age of 15WZ1-2 (discussed further below), indicating that sample 16WZ-04 recorded two periods of deformation, one associated with LGCC deformation and one associated with later deformation of the PRC.

Sample 16WZ-05, Coarse-Grained Tonalite Orthogneiss

Zircon from sample 16WZ-05 recorded pluton emplacement between 91.57 ± 0.23 and 90.39 ± 0.24 Ma (n = 9). The CL images for these zircon showed oscillatory and sector zoning indicative of a simple magmatic crystallization history, except for crystal fragment z2c which includes an inherited core. Excluding crystal fragment z2c, the eight remaining zircon crystal fragments returned a weighted mean age of 90.88 ± 0.07 Ma (MSWD = 0.65), and we interpreted this age as the age of pluton emplacement for sample 16WZ-05. This emplacement age is consistent with PRC emplacement ages (discussed further below), as well as with the deformation age recorded in sample 16WZ-04, a LGCC porphyritic orthogneiss 1 km northwest from the outcrop from which 16WZ-05 was sampled. The titanite from sample 16WZ-05 ranged from 88.56 ± 0.14 to 86.80 ± 0.69 Ma (n = 8), consistent with the youngest deformation ages from sample 16WZ-04.

Payette River Complex

Sample 15WZ1–2, Tonalite Orthogneiss

Zircon dates from sample 15WZ1-2 ranged from 91.94 ± 0.10 to 90.24 ± 0.09 Ma (n = 10) which we interpreted as reflecting the main phase of tonalite emplacement in this area. This ca. 90 Ma pluton emplacement age is consistent with previous PRC U-Pb zircon geochronology (Manduca et al., 1993; Giorgis et al., 2008; Figure 2.8.). Titanite dates between 81.3 ± 0.2 and 74.1 ± 3.0 Ma (n = 9) record deformation at this site. No magmatic titanite is preserved in this sample. Titanite dates from this sample had larger uncertainties than titanite from other samples in this transect because of low Pb^*/Pb_c values.

Sample 15WZ1–3, Leucocratic Dike

Sample 15WZ1-3 contained zircon but no titanite. Zircon dates ranged from 83.71 ± 0.24 to 82.32 ± 0.17 Ma (n = 6), younger than the emplacement age of 15WZ1-2 (the rock that hosts the 15WZ1-3 dike) but older than the deformation age of 15WZ1-2 titanite. The weighted mean age of the five youngest zircon crystal fragments is 82.55 ± 0.07 Ma (MSWD = 0.98). We interpreted this weighted mean age as the time at which the leucocratic dike intruded into the tonalite orthogneiss.

Sample I00-304, Tonalite

Zircon from sample I00-304 recorded pluton emplacement between 90.75 ± 0.07 and 89.83 ± 0.08 Ma (n = 6). This ca. 90 Ma pluton emplacement age is consistent with previous PRC U-Pb zircon geochronology (Manduca et al., 1993; Giorgis et al., 2008; Figure 2.8.).

Titanite dates from sample I00-304 ranged from 81.64 ± 0.10 to 80.64 ± 0.16 Ma (n = 14), a distinctly younger interval than the zircon emplacement age. This demonstrated that the weak fabric observed in this area of the PRC is not magmatic but, rather, reflects deformation that post-dated emplacement was significant enough to reset the U-Pb systematics of all measured titanite. These titanite results contradict previous interpretations of the emplacement of the PRC and ca. 90 Ma plutons marking the end of WISZ deformation (Giorgis et al., 2008; Braudy et al., 2017; Figures 2.8. and 2.9.) but are consistent with inferences of deformation that post-dates PRC emplacement (Manduca et al., 1993).

Border Zone Suite and Idaho Batholith

Sample 16WZ-06, K-feldspar Porphyritic Granodiorite Orthogneiss

Sample 16WZ-06, a K-feldspar porphyritic granodiorite orthogneiss similar in fabric character to LGCC samples 14WZ3-2 and 16WZ-04, yielded zircon dates between 95.27 ± 0.07 and 92.74 ± 0.11 Ma (n = 14). The youngest zircon fragments displayed CL-bright metamorphic rims. The zircon grains with oscillatory zoning and no metamorphic rims made up a population with a weighted mean age of 95.09 ± 0.03 Ma (n = 7; MSWD = 3.75; z7, z11, z10a, z10b, z14a, z13, z15) that we interpret as the pluton emplacement age. This age indicates that despite being east of the PRC, the main phase of pluton crystallization of the Border Zone orthogneiss is older than the age of PRC tonalite emplacement.

Titanite dates in this sample ranged from 80.93 ± 0.12 to 75.08 ± 0.23 Ma (n = 12), consistent with and younger than the youngest titanite dates from sample I00-304

from the PRC. As in the PRC, the titanite from this sample were all younger than the zircon pluton emplacement age.

Sample 16WZ-07, Monzogranite

Idaho batholith monzogranite sample 16WZ-07 contained zircon but no titanite. Zircon dates ranged from 77.74 ± 0.06 to 75.14 ± 0.07 Ma (n = 5). These ages are consistent with U-Pb zircon emplacement ages of the Atlanta peraluminous suite of the Idaho batholith (Gaschnig et al., 2010), including a sample of biotite granodiorite dated at 78.2 ± 1.8 Ma ~40 km to the east near Yellow Pine, Idaho (Gaschnig et al., 2017; Figure 2.9.).

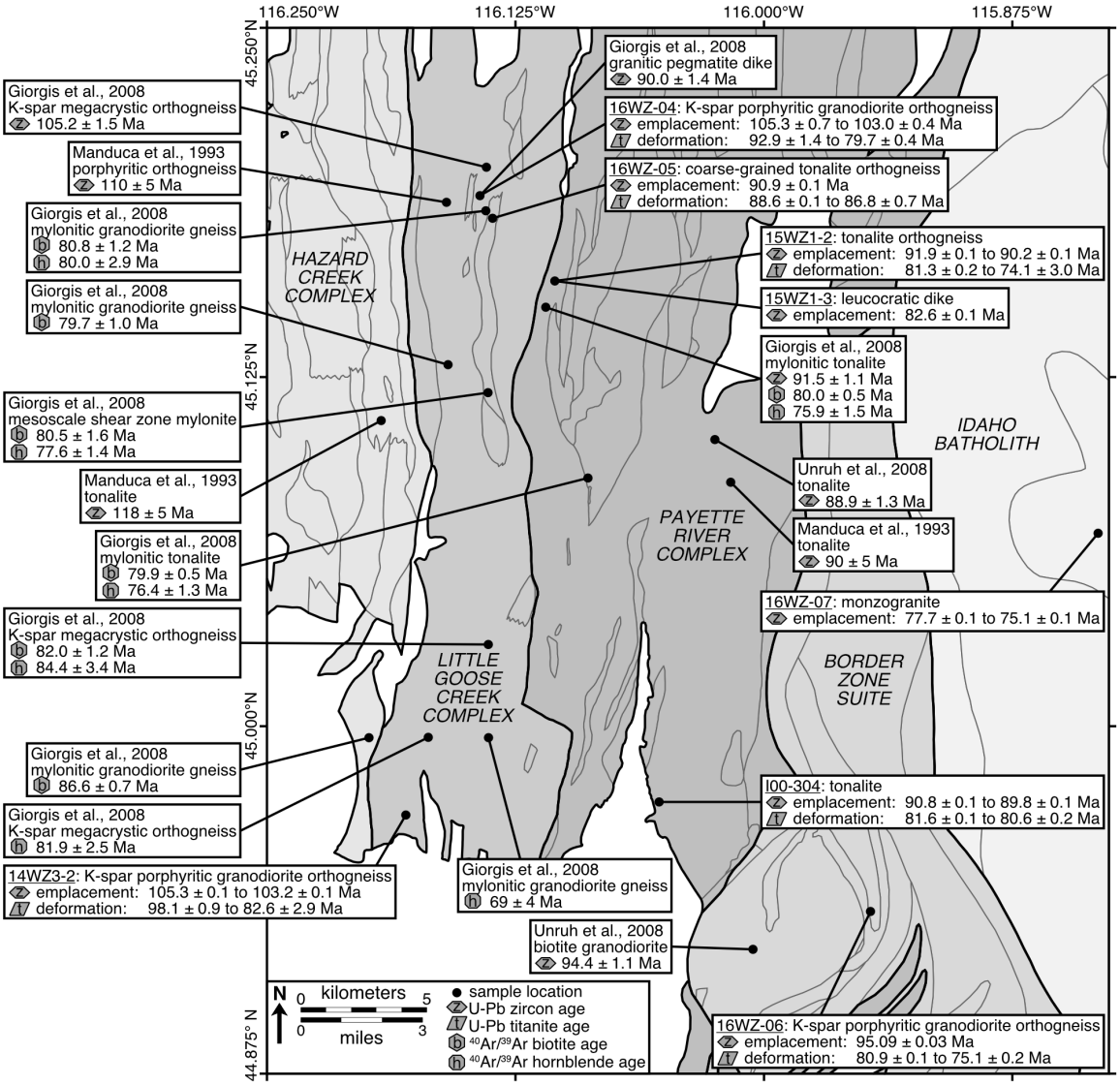

Figure 2.8. Map of the plutonic complexes near McCall, Idaho and associated geochronology from this study and previous work.

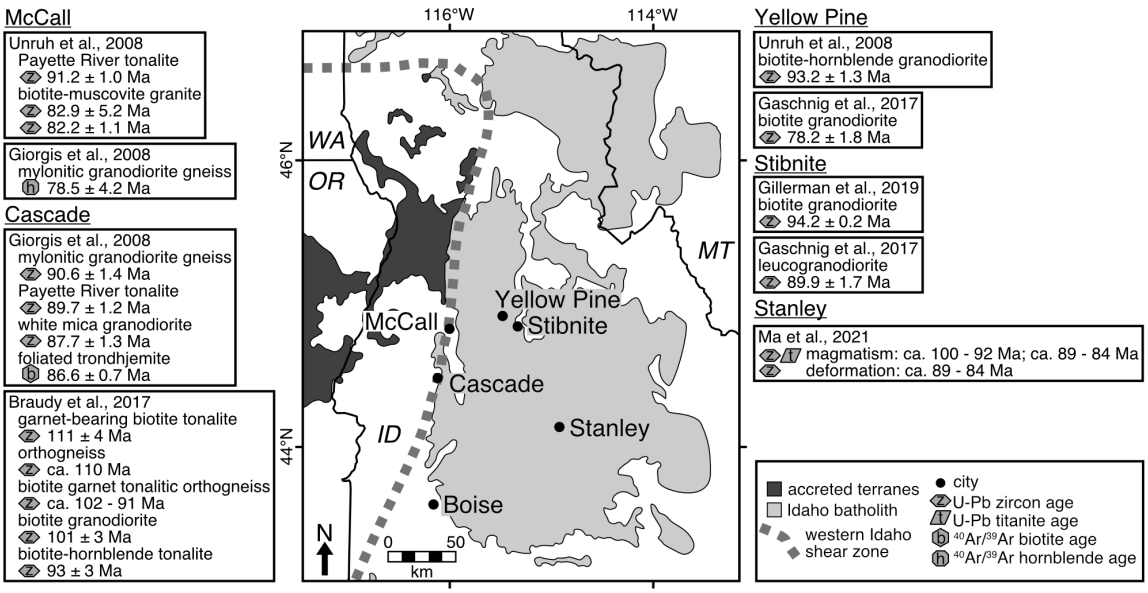

Figure 2.9. Map of Idaho with locations of rocks similar in age to the McCall, Idaho area WISZ rocks.

Discussion

Syntaxial Emplacement of WISZ Plutonic Complexes

Pluton emplacement ages from zircon petrochronology provided an updated model of WISZ intrusive events that is critical for understanding the interplay between magmatism and deformation in the area. The major plutonic bodies near McCall, Idaho, are commonly modeled as a simple west-to-east progression from old to young: HCC, LGCC, PRC, and then the Idaho batholith (Manduca et al., 1993; Tikoff et al., 2001; Kuntz, 2007). This model implies antitaxial sill emplacement, with younger units intruding into the interface between the older plutonic units and the wall rocks (see Stearns and Bartley (2014) for a description of antitaxial and syntaxial dike emplacement models). Antitaxial sill emplacement can create in situ wall rock screens. By contrast, under a regime of syntaxial sill emplacement, new magmatic intrusions are emplaced entirely within, rather than on the margin of, an older phase of magmatism and therefore, theoretically, cannot create wall rock screens. Applying this framework to the WISZ, an

antitaxial model of plutonic complex intrusion apparently satisfies the observed map patterns of west-to-east younging of magmatism and included metasedimentary screens (Manduca, 1988; Kuntz, 2007; Braudy et al., 2017).

However, this new geochronology showed that an antitaxial model of WISZ magmatism is unsatisfactory. Age relationships of units near the LGCC–PRC contact support a model of syntaxial pluton emplacement. The emplacement age of sample 16WZ-05 (90.88 ± 0.07 Ma) is consistent with the emplacement age of the two PRT tonalite samples (15WZ1–2: 91.94 ± 0.10 to 90.24 ± 0.09 Ma; I00-304: 90.75 ± 0.07 to 89.83 ± 0.08 Ma) and previous U-Pb zircon geochronology for the PRC (Manduca et al., 1993; Giorgis et al., 2008; Figure 2.8.), which supports the hypothesis that the coarse-grained tonalite orthogneiss (Gtg) surrounded by LGCC porphyritic orthogneiss (Gpg) is an intrusion of PRC into the LGCC (Manduca, 1988). This result established that the PRC intruded, at least in part, directly into the LGCC rather than entirely to the east of the LGCC.

Furthermore, our new data on the emplacement age of 95.08 ± 0.03 Ma for the Border Zone granodiorite orthogneiss is similar to the emplacement ages of 94.4 ± 1.1 Ma for a biotite granodiorite 5 km east of McCall and 93.2 ± 1.3 Ma for a biotite-hornblende granodiorite near Yellow Pine, Idaho and 94.21 ± 0.22 Ma for a biotite granodiorite in the nearby Stibnite Mining District, ~50 km east of the PRC outcrop belt (Figure 2.9.; Unruh et al., 2008; Stewart et al., 2016; Gillerman et al., 2019; Stewart et al., 2021). Thus, the PRC must have intruded syntaxially into the LGCC–Border Zone suite interface. Another example of syntaxial pluton emplacement is the 82.2 ± 1.1 Ma to 89.9 ± 1.7 Ma biotite and two-mica granodiorites and granites intrusions east of the PRC

that were emplaced into the ca. 95-93 Ma Border Zone suite (Unruh et al., 2008; Gaschnig et al., 2017; Gillerman et al., 2019; Stewart et al., 2016, 2021; Figure 2.9.).

A syntaxial model of WISZ pluton emplacement is significant for correlating the Idaho batholith with other Cretaceous batholiths of the North American Cordillera (Figure 2.1.). Cordilleran intrusive suites are commonly nested or zoned, with intrusions younging towards the center of the complex (e.g., Coleman et al., 2004; Hildebrand and Whalen, 2014). A syntaxial model of early Idaho batholith growth suggests a similar pluton intrusion mechanism to that of other Cordilleran batholiths.

Titanite Ages Reflect Coupled Magmatism and Deformation

We observed a broad pattern across our transect of deformation occurring at the same time as local magmatic intrusions. As expected, there is no systematic lag time in our samples between zircon pluton crystallization ages and titanite ages, confirming that recrystallized titanite ages are not cooling ages (Garber et al., 2017; Holder et al., 2019; Gordon et al., 2021). Instead, titanite is highly reactive to changes in rheological conditions induced by local magmatic intrusions. Only sample 14WZ3-2, a LGCC porphyritic granodiorite orthogneiss, preserved relict magmatic titanite, perhaps owing to the abundance of titanite included in and partially shielded from deformation by K-feldspar porphyroclasts (see Chapter One). In all other samples, the distinctly younger titanite deformation ages compared to the zircon pluton emplacement ages indicated that the record of magmatic titanite, a common accessory mineral in tonalites and granodiorites (Frost et al., 2000), has been erased by deformation-induced recrystallization. We linked titanite recrystallization and neoblastic growth to solid-state fabric development based on the arguments outlined in Chapter One. The localization of

strain due to magmatism has been documented in transpressional shear zones in Idaho and elsewhere (e.g., de Saint Blanquat et al., 1998; Ma et al., 2017), and so we would expect the timing of WISZ deformation and solid-state fabric development to be correlated to the timing of magmatic intrusions.

One example of titanite recrystallization and fabric development in response to a local magmatic intrusion is where the PRC intruded into the LGCC. Sample 16WZ-04, a LGCC porphyritic granodiorite orthogneiss records titanite ages (92.9 ± 1.4 to 79.7 ± 0.4 Ma) consistent with the zircon emplacement age (90.9 ± 0.1 Ma) of nearby sample 16WZ-05, a tonalite orthogneiss associated with the PRC. We infered that the emplacement of the tonalite caused rheological changes in the host porphyritic granodiorite orthogneiss country rock that caused strain to localize around the intrusion, recrystallizing the titanite in the country rock. This indicates that local intrusive events can be significant drivers of titanite recrystallization and that titanite dates represent the timing of the youngest event with sufficiently high pressure and temperature conditions to induce titanite recrystallization.

We saw similar patterns of titanite recrystallization as a response to local pluton emplacement in other places in our transect. Deformation in the PRC (sample I00-304 titanite: 81.64 ± 0.10 to 80.64 ± 0.16 Ma) was the same age as dike emplacement in the complex (sample 15WZ1-3 zircon: 82.55 ± 0.07 Ma). Deformation in the Border Zone suite (sample 16WZ-06 titanite: 80.93 ± 0.12 to 75.08 ± 0.23 Ma) was the same age as emplacement of the local Idaho batholith monzogranite (sample 16WZ-07 zircon: 77.74 ± 0.06 to 75.14 ± 0.07 Ma). These results show that country rocks (i.e., earlier intrusions) record localized strain that results from magmatic intrusions that change the rheology of

the country rock. We also observed different deformation age ranges among the PRC samples, indicating that parts of the PRC, like the tonalite orthogneiss within the LGCC, stopped recrystallizing titanite before other parts of the PRC. This shows that strain localized at a scale less than that of a plutonic complex.

This documented strain localization has implications for reconstructions of WISZ deformation. Previous work has assumed steady, homogenous, monoclinic transpression and used those assumptions to estimate the original width of the magmatic arc and lateral offset during WISZ deformation (e.g., Giorgis and Tikoff, 2004; Davis and Giorgis, 2014). Our work is a step towards more nuanced models of where, when, and for how long strain accumulated in the WISZ.

Extension of WISZ High-Temperature Deformation Eastward and to Younger Ages

Tandem zircon and titanite petrochronology can be used to track the spatial and temporal extent of WISZ deformation. We found evidence of WISZ-related magmatism and deformation further east than previously documented in the McCall area. The weakly foliated tonalite from east of Payette Lake (sample I00-304) yielded titanite dates (81.64 ± 0.10 to 80.64 ± 0.16 Ma) that were significantly younger than the zircon dates from the same sample (90.75 ± 0.07 and 89.83 ± 0.08 Ma), indicating that the weak fabric is not magmatic but, rather, a record of weaker or shorter solid-state deformation than in other parts of the PRC. These young titanite ages indicate that WISZ deformation manifests further east than previously mapped.

WISZ deformation is recorded even further east in the porphyritic granodiorite orthogneiss of the Border Zone suite (sample 16WZ-06). The fabric of the porphyritic granodiorite orthogneiss of the Border Zone suite is consistent with the approximately

north-south, steeply dipping orientation of the foliation in the LGCC and PRC (Figure 2.10., Table B2.2.). Titanite ages in this sample ranged from 80.9 ± 0.1 to 75.1 ± 0.2 Ma, indicating deformation at the same time as deformation in the PRC (sample 15WZ1-2 titanite: 81.3 ± 0.2 to 74.1 ± 3.0 Ma; sample I00-304 titanite: 81.6 ± 0.1 to 80.6 ± 0.2 Ma) and at the same time as local Idaho batholith granitoid emplacement (sample 16WZ-07 zircon: 77.7 ± 0.1 to 75.1 ± 0.1 Ma). In our suite of samples, the Idaho batholith monzogranite was the furthest east significant plutonic body that did not record deformation, and therefore, we propose that the map boundaries of the WISZ near McCall should extend at least to the contact with the Idaho batholith two-mica granites. Dextral transpressional shear zones with similar age relationships, fabric orientations, and kinematics as the WISZ are recorded within the Atlanta Lobe of the Idaho batholith, east of the Border Zone suite. Near Yellow Pine, Idaho, the Johnson Creek shear zone is a high-temperature shear zone with north-northeast striking, very steeply dipping foliation (Lund, 2021; Stewart et al., 2021). Near Stanley, Idaho, U-Pb zircon and titanite ages from the Sawtooth metamorphic complex transpressional zone document magmatism and metamorphism during transpressional deformation between ca. 100 Ma and ca. 84 Ma (Ma et al., 2017, 2021). These shear zones, along with the WISZ, may have been part of a regional, dispersed transpressional system in Idaho during the mid- to Late Cretaceous (Ma et al., 2017).

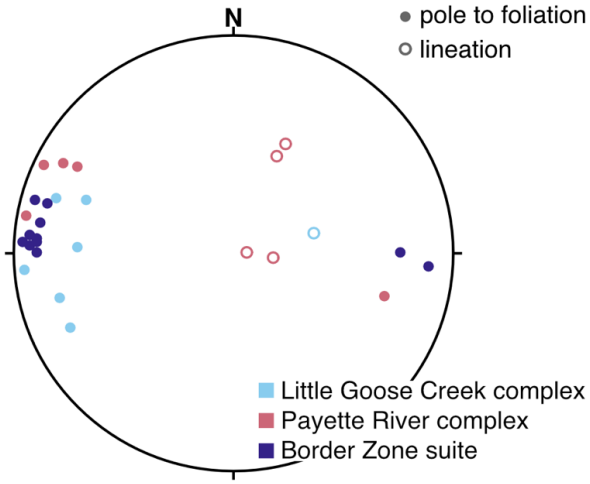

Figure 2.10. Stereonet of poles to foliation (closed circles) and lineation (open circles) of Little Goose Creek complex, Payette River complex, and Border Zone granodiorite.

In addition to reconsidering the spatial extent of the WISZ, our results force a reconsideration of when high temperature deformation ceased. All our titanite-bearing samples recorded deformation ages younger than 90 Ma, the proposed end of deformation near McCall and elsewhere, which is based on the zircon emplacement age of weakly foliated granitoid plutons and dikes (Giorgis et al., 2008; Braudy et al., 2017). Our PRC titanite ages ranged from 81.6 ± 0.1 to 74.1 ± 3.0 Ma, indicating that titanite recrystallization during solid-state fabric development, and thus WISZ deformation, continued after ca. 90 Ma PRC emplacement.

Accepting the PRC as an entirely syndeformational unit resolves our titanite ages but leads to the question of how zircon from leucocratic dikes in the LGCC and PRC indicate that the dikes are older than the titanite-dated fabric development. Giorgis et al. (2008) dated the zircon from a leucocratic granitic pegmatite in the LGCC at 90.0 ± 1.4 Ma using sensitive high-resolution ion microprobe–reverse geometry U-Pb mass spectrometry. The dated dike had a weakly developed foliation defined by quartz ribbons, and Giorgis et al. (2008) used this weak fabric development to infer that the age of this

dike constrains the end of WISZ ductile deformation. With similar motivations, we sampled and dated a leucocratic dike in the PRC (sample 15WZ1-3) that did not have an observable fabric in the field and that crosscut the WISZ foliation in the host rock. The zircon emplacement age for the dike (82.55 ± 0.07 Ma) wass ~1 Ma older than the oldest dated titanite crystal in the surrounding PRC tonalite (sample 15WZ1-2, t1: 81.29 ± 0.16 Ma), demonstrating that this seemingly non-deformed dike is a poor constraint on WISZ deformation because it is older than the recrystallized titanite in the host rock. This dike apparently did not manifest a fabric expression of WISZ deformation, either because its lithology caused it not to accumulate strain or its mineralogy caused it not to develop a field-visible fabric.

Titanite ages as young as ca. 74 Ma indicated that high-temperature deformation in the LGCC, PRC, and Border Zone suite continued not only after PRC emplacement but also up until and during 87 and 70 Ma exhumation as determined by $^{40}Ar/^{39}Ar$ biotite and hornblende cooling ages (Kuntz, 2007; Giorgis et al., 2008). Previous work has interpreted the time difference between PRC intrusion and $^{40}Ar/^{39}Ar$ ages as a lull in activity and that, consequently, transpressional deformation could not have facilitated exhumation (Giorgis et al., 2008). Because our new data show that high-temperature deformation was continuous through the $^{40}Ar/^{39}Ar$ cooling ages, transpressional deformation likely facilitated exhumation of the WISZ.

A Spatial-Temporal Model of WISZ Deformation

Tandem zircon and titanite petrochronology allows us to model the sequence of magmatic and deformation events that produced the observed map patterns of the foliated plutonic complexes of the WISZ near McCall, Idaho (Figures 2.2. and 2.11.). Prior to

WISZ deformation, HCC rocks were emplaced to the west of the $^{87}Sr/^{86}Sr = 0.706$ isopleth, and the rocks of continental North America lay east of the isopleth. Among our transect samples, the first event was the ca. 105 to 103 Ma emplacement of the LGCC porphyritic granodiorite (samples 14WZ3-2 and 16WZ-04) into the HCC and continental North America country rocks. Following the intrusion of the LGCC porphyritic orthogneiss, deformation of the LGCC began between ca. 98 and 96 Ma (see Chapter One). Soon after the LGCC began deforming, the Border Zone granodiorite intruded at ca. 95 Ma, with its intrusion likely facilitated by the rheologically weak, deforming LGCC rocks. Deformation continued in the LGCC and Border Zone suite through to PRC emplacement between ca. 92 to 90 Ma. The PRC, LGCC, and Border Zone suite all continued deforming over another ~15 Ma. High-temperature deformation in the PRC ceased first in the tonalite that intruded into the LGCC (sample 16WZ-05), followed by the tonalite in the interior of the PRC (sample I00-304). The PRC sample on the western margin of the complex (sample 15WZ1-2) continued deforming until ca. 75 Ma, indicating that the margins of the plutonic complexes seemed to localize strain for longer than the plutonic complex interiors. Late-stage dikes also seemed to localize strain, with the youngest titanite analyses from the LGCC porphyritic granodiorite orthogneiss (samples 14WZ3-2 and 16WZ-04) consistent with the ca. 82 Ma dike age from the western margin of the PRC (sample 15WZ1-3). Also, tonalite and granodiorite spatially associated with late-stage dikes either on the outcrop or map scale (samples 15WZ1-2 and 16WZ-06) continued to deform following dike emplacement at ca. 82 Ma and through to ca. 75 Ma emplacement of the easternmost non-foliated Idaho batholith monzogranite.

In the WISZ, there is a clear causal relationship between magmatic intrusions and strain localization, though when taken together across the shear zone, deformation was continuous from when it initiated between ca. 98 and 96 Ma to when magmatism, and therefore strain on the country rocks, migrated far enough east as to no longer deform the WISZ rocks. Although syntaxial pluton emplacement typically cannot preserve country rock screens, our model can accommodate the observed metasedimentary screens in the PRC if initial LGCC emplacement exploited multiple weak zones in the continental North America country rock and emplaced as a series of proximal sills. Following initial magmatism in the area, the rheologically weak newly intruded plutons served as conduits for syntaxial magmatism. Given the similarly aged granitoids in shear zones near Yellow Pine, Stibnite, and Stanley, Idaho (Unruh et al., 2008; Gaschnig et al., 2017; Gillerman et al., 2019; Ma et al., 2017, 2021; Stewart et al., 2016, 2021; Figure 2.9.), it is possible that there was a dispersed, >95 km wide network of mid- to Late Cretaceous plutons and shear zones across Idaho (Gaschnig et al., 2017; Ma et al., 2017), or, alternatively, syntaxial emplacement of the Idaho batholith into the WISZ could have facilitated the lateral transport of WISZ fragments towards eastern Idaho.

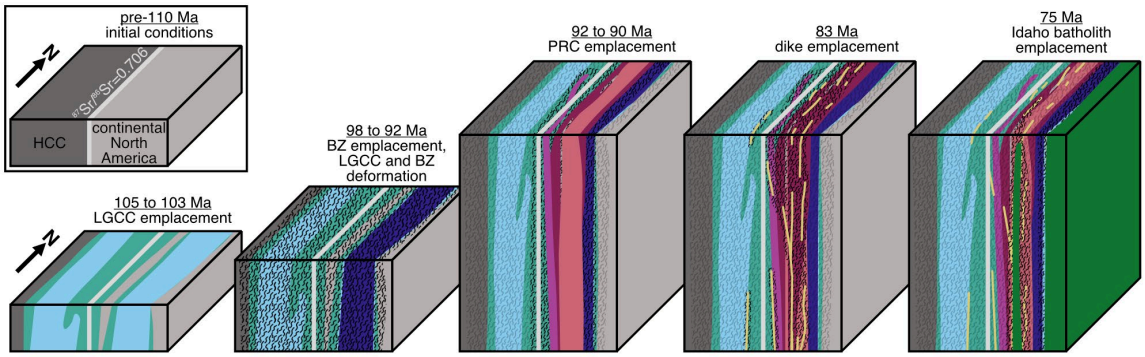

Figure 2.11. Schematic block diagrams showing the development of the WISZ from initial conditions prior to Little Goose Creek complex emplacement (inset) through to Idaho batholith emplacement (lower right). Pluton colors match the colors used in Figures 2.4.-2.7. Black pattern indicates active deformation, and light gray pattern indicates previously deformed areas. The height of the block diagrams schematically relates to the extrusion caused by transpressional deformation. The top of the youngest block broadly matches the observed map patterns of foliated plutonic rocks (Figure 2.2.).

Conclusions

The interplay between magmatism and deformation in contractional arc settings is well-exhibited in the WISZ near McCall, Idaho. Using high precision zircon and titanite petrochronology, we parsed the spatial-temporal patterns of intrusion and strain accumulation in the WISZ and found that solid-state deformation lasted for longer and in a broader area than previously documented. Titanite is highly responsive to changes in pressure and temperature caused by shearing, and thus, titanite recrystallization tracked fabric development and strain accumulation even in rocks with weak foliations. This sensitivity allowed us to identify titanite recrystallization related to deformation further east than previously mapped for the WISZ. We correlated the timing of fabric development with local magmatic intrusions to show how magmatism localized strain in the WISZ, resulting in a pattern of deformation that is more complex than a simple model of west-to-east younging of pluton emplacement and deformation. We documented pluton emplacement in the WISZ and the Idaho batholith between ca. 105 and 75 Ma and

demonstrated that pluton emplacement was syntaxial beginning with PRC intrusion at 92 Ma. Titanite recrystallization and neoblastic growth in response to deformation was protracted between ca. 98 and 74 Ma. The colocation of these processes in space and time indicates that magmatism and deformation are intrinsically linked, with deformation focusing magmatism in the center of the shear zone while magmatism localizes deformation and drives solid-state fabric development near intrusions. In this way, magmatism and deformation create a self-reinforcing feedback cycle.

CHAPTER THREE: RECALIBRATING THE DEVONIAN TIME SCALE: A NEW METHOD FOR INTEGRATING RADIOISOTOPIC AND ASTROCHRONOLOGIC AGES IN A BAYESIAN FRAMEWORK

Harrigan, C.O., Schmitz, M.D., Over, D.J., Trayler, R.B., and Davydov, V.I., 2021, Recalibrating the Devonian time scale: A new method for integrating radioisotopic and astrochronologic ages in a Bayesian framework: Geological Society of America Bulletin, doi:10.1130/b36128.1.

Abstract

The numerous biotic, climatic, and tectonic events of the Devonian cannot be correlated and investigated without a well-calibrated time scale. Here, we updated the calibration of the Devonian time scale using a Bayesian age-depth model that incorporates radioisotopic ages and astrochronology durations. We used existing radioisotopic ages collected and harmonized in the last two geologic time scale compilations, as well as new U-Pb zircon ages from Emsian {Hercules I K-bentonite, Wetteldorf, Germany: 394.290 ± 0.097(0.21)[0.47] Ma} and Eifelian K-bentonites {Tioga B and Tioga F K-bentonites, Fayette, New York, USA: 390.82 ± 0.18(0.26)[0.48] Ma and 390.14 ± 0.14(0.23)[0.47] Ma, respectively}. We anchored floating astrochronology stage durations on radioisotopic ages and chained astrochronologic constraints and uncertainty together to extrapolate conditioning age likelihoods up or down the geologic time scale, which is a new method for integrating astrochronology into age-depth modeling. The modeling results in similar ages and durations for Devonian stages regardless of starting biostratigraphic scaling assumptions. We produced a set of rescaled biostratigraphic zonations, and a new numerical calibration of Devonian stage boundary ages with robust uncertainty estimates, which allow us to evaluate future targets for Devonian time scale research. These methods are broadly applicable for time scale work and provide a template for an integrated stratigraphic approach to time scale modeling.

Introduction

Our ability to contextualize, correlate, and link significant geologic events and processes depends on the accuracy with which numerical time proxies are integrated into

a time scale. Here, we focus on the Devonian Period, wherein numerous studies have investigated the temporal correlation between stratigraphically constrained markers of Devonian biotic crises (House, 2002) and radioisotopically dated causal mechanisms such as meteorite impacts (e.g., Reimold et al., 2005; Gordon et al., 2009) and large igneous provinces (e.g., Ernst et al., 2020). Significant reef expansion and subsequent decline during the Late Devonian is, as of yet, insufficiently explained because of the number of potential causal mechanisms still being explored (Kiessling, 2008; Kiessling and Simpson, 2011, and references therein). Both tectonic factors (e.g., Averbuch et al., 2005) and the expansion and diversification of vascular plants and root systems (e.g., Algeo and Scheckler, 2010), or some combination of the two, have been linked to potential climate effects during the Devonian. Conversely, others have suggested that the evolution of trees was coincident with Devonian climate change, not the cause of climate change (e.g., Retallack and Huang, 2011). In all these cases, to link radioisotopically dated causal mechanisms to events constrained by biostratigraphy, we first need a well-calibrated Devonian time scale. Tectonic, climactic, and biotic factors all interact, and with an improved numerical calibration of the Devonian time scale, we can better understand these interactions. Further, the development of a robust method with which to integrate radioisotopic ages and astrochronology durations can be used to advance chronostratigraphic modeling on any scale.

Numerous efforts (Kaufmann, 2006, and references therein; Becker et al., 2012, 2020; De Vleeschouwer and Parnell, 2014) have sought to refine Devonian stage boundary ages. The fidelity of a chronostratigraphic model for the Devonian depends on three factors: (1) the accuracy and precision of the ages of dated events, (2) the accuracy

and precision of the biostratigraphic constraints on those dated events, which provide the correlations and relative stratigraphic positions used in the model, and (3) the method for modeling the relationship between stratigraphic position and age and the fidelity with which the model extrapolates to the age boundaries of interest.

The Devonian global time scale is constructed from a set of conodont biozones that have undergone continued revision in terms of the marker species that are used to define chronostratigraphic units (e.g., Becker et al., 2020, and references therein). To utilize recent improvements in Devonian biostratigraphy and age-depth modeling techniques and to examine those areas in need of further work, an updated numerical calibration of the Devonian time scale is due. Since the compilation of the *Geologic Time Scale 2012* (GTS2012; Gradstein et al., 2012), there have been efforts to redate events with more modern geochronologic techniques (Husson et al., 2016; Lanik et al., 2016; Bodorkos et al., 2017; McAdams et al., 2017; Percival et al., 2018), as well as efforts to find new biostratigraphically constrained, dateable volcanic layers to increase the density of known radioisotopic ages throughout the Devonian (Myrow et al., 2014; Husson et al., 2016; Lanik et al., 2016; Bodorkos et al., 2017). These newly radioisotopically dated volcanic layers have been incorporated into the *Geologic Time Scale 2020* (GTS2020; Gradstein et al., 2020), but the methodology for modeling the numerical age between dated volcanic layers has not been updated for the GTS2020, as discussed further below.

Time scale modeling is often done by fitting age data and relative stratigraphic position data with a model that passes through the data and maintains monotonicity, commonly a linear, spline, or polynomial fit (Telford et al., 2004). Tucker et al. (1998) modeled the Devonian Period with a linear fit by shifting the stratigraphic position of

dated volcanic layers until a linear age-depth model was achieved. Similarly, Kaufmann (2006) relied on a linear fit to model the Devonian Period, constructing biostratigraphic scales of conodont biozonation from a composite of stratigraphic sections believed to have continuous deposition. The Devonian chapter of the GTS2012 intentionally discarded the assumption of linearity between age and depth and applied a hybrid spline and linear fit (Becker et al., 2012). However, these types of models typically underestimate uncertainty at positions between radioisotopically dated events (Telford et al., 2004; De Vleeschouwer and Parnell, 2014), which is problematic for time scale calibration, particularly when stage boundaries lack proximal radioisotopically dated volcanic layers. De Vleeschouwer and Parnell (2014) addressed the issue of underestimated model error by applying Bchron, a Bayesian age-depth model (Haslett and Parnell, 2008; Parnell et al., 2008), to the GTS2012 ages for the Devonian Period. Additionally, they supplemented the radioisotopic dates in their model with astrochronologic constraints on the duration of the Frasnian and Givetian Stages as a filter on their posterior model results (De Vleeschouwer et al., 2013a, 2013b; De Vleeschouwer and Parnell, 2014). The GTS2020 compiled new Devonian ages and updated the conodont biostratigraphic chart for the Devonian compared to the GTS2012 but returned to a spline fit through the age and stratigraphic position data (Becker et al., 2020).

Recent developments, including an updated version of the Bchron age-depth model optimized for deep-time Bayesian age modeling (Trayler et al., 2020), newly available radioisotopic ages (this work and references in Becker et al., 2020), and astrochronologic constraints for all but one Devonian stage (House, 1995; Ellwood et al.,

2011; De Vleeschouwer et al., 2012, 2015; Ellwood et al., 2015; Da Silva et al., 2016; Whalen et al., 2016; Pas et al., 2018, 2021; Ma et al., 2020), have prompted us to revisit the modeling of the numerical calibration of the Devonian Period. Here, we present new Bayesian age-depth models for the entire Devonian Period and parts of the Silurian and Carboniferous Periods. We applied the methodology to different conodont biozonation schemes to determine the relative scaled stratigraphic positions of our chronological data (radioisotopic ages and astrochronology durations), which we used as model likelihoods. We used the resulting posterior numerical age distributions of the Devonian stage and conodont biozone boundaries to examine how the selection of different biostratigraphic frameworks and their initial scaling assumptions influenced the calibrated time scale ages. We present three Devonian time scales rescaled such that the relative heights of stages and conodont biozones are based on a linear relationship with numerical time.

We also improved the numerical calibration of the Devonian time scale by describing new ages of volcanic layers bracketing the base of the Middle Devonian (Emsian-Eifelian boundary), a section of the Devonian with sparse geochronologic data. We dated three K-bentonites from biostratigraphically well-characterized sedimentary sequences in Wetteldorf, Germany, and Fayette, New York, United States. We leveraged improvements in high-precision U-Pb zircon geochronology by isotope dilution–thermal ionization mass spectrometry (ID-TIMS) over the past couple of decades, namely, the chemical abrasion (CA) technique used to minimize discordance due to Pb loss (Mattinson, 2005), thus improving the accuracy of our ages relative to past attempts to date these K-bentonites.

U-Pb Geochronology

Sample Descriptions

We targeted K-bentonites in Wetteldorf, Germany, and Fayette, New York, with the aim of improving the accuracy and precision the age of the Emsian-Eifelian boundary. The global stratotype section and point (GSSP) for the base of the Middle Devonian (Emsian-Eifelian boundary) is within the uppermost Heisdorf Formation at Wetteldorf Richtschnitt in the Eifel District of western Germany (Ziegler and Klapper, 1985). The Emsian-Eifelian boundary lies in bed 30 of the uppermost Heisdorf Formation (1.9 m below the base of the Lauch Formation) and corresponds to the first occurrence of the conodont *Polygnathus costatus partitus* in this section (Klapper et al., 1978; Ziegler and Klapper, 1985). Other key conodont taxa in the section at Wetteldorf include *Polygnathus costatus patulus* (Klapper, 1971), the first appearance datum (FAD) of which marks the base of the Emsian *P. c. patulus* zone, and *Polygnathus costatus costatus* (Klapper, 1971), the FAD of which marks the base of the Eifelian *P. c. costatus* zone. The Lower and Middle Devonian strata at Wetteldorf contain numerous K-bentonites (named Hercules, Horologium, Libra, etc.) and well-documented, diverse flora and fauna, inclusive of brachiopods, corals, 91racryoconarids, mollusks, ostracodes, trilobites, and spores (Ziegler and Werner, 1982).

Volcanic activity during the Acadian orogeny deposited 80 or more Early to Middle Devonian K-bentonites in the Appalachian Basin (Ver Straeten, 2004). The Emsian-Eifelian boundary in New York State is within the lower Onondaga Formation, which extends from the Hudson Valley to Lake Erie (Ver Straeten, 2007). The Onondaga Formation is primarily limestone with interspersed volcaniclastic layers, including the

Tioga set of K-bentonites (Ver Straeten, 2007). The Tioga K-bentonites outcrop throughout the Appalachian Basin and are labeled from oldest to youngest as Tioga A through H (Way et al., 1986), though some areas only contain beds A through G (Ver Straeten, 2004). Ver Straeten (2004) recognized an additional series of up to 32 tephras in the southern Appalachian Basin that are commonly confused with the Tioga A–H beds; he called these 32 tephras the Tioga Middle Coarse Zone cluster.

Correlation of strata in the Onondaga Formation with the Wetteldorf GSSP and recognition of the Emsian-Eifelian boundary in the Onondaga Formation are equivocal due to the absence of diagnostic conodonts and other fauna that might provide correlation in the lower Onondaga Edgecliff Member. The Emsian-Eifelian boundary is conventionally placed at the base of the Onondaga Nedrow Member based on the occurrence of *P. c. partitus* at the Oriskany Falls quarry in Oneida County, New York (Klapper and Oliver, 1995), but the underlying *P. c. patulus* zone has not been recognized, and the boundary could be lower, in the Onondaga Edgecliff Member. In the upper Onondaga Nedrow Member, the FAD of *P. c. costatus* and the co-occurrence of *P. c. patulus* indicate a position low in the *P. c. costatus* zone (Klapper, 1981). Two black shale beds in the upper Onondaga Nedrow Member, associated with 92racryoconarids and palynomorphs, indicate the global Chotec event and the base of the *P. c. costatus* zone (Brocke et al., 2016). Two potential ties points between the Wetteldorf GSSP and the Onondaga Formation are the base of the Onondaga Nedrow Member, which is equivocally the base of the *P. c. partitus* zone (Emsian-Eifelian boundary), and the uppermost Onondaga Nedrow Member, which is the base of the *P. c. costatus* zone.

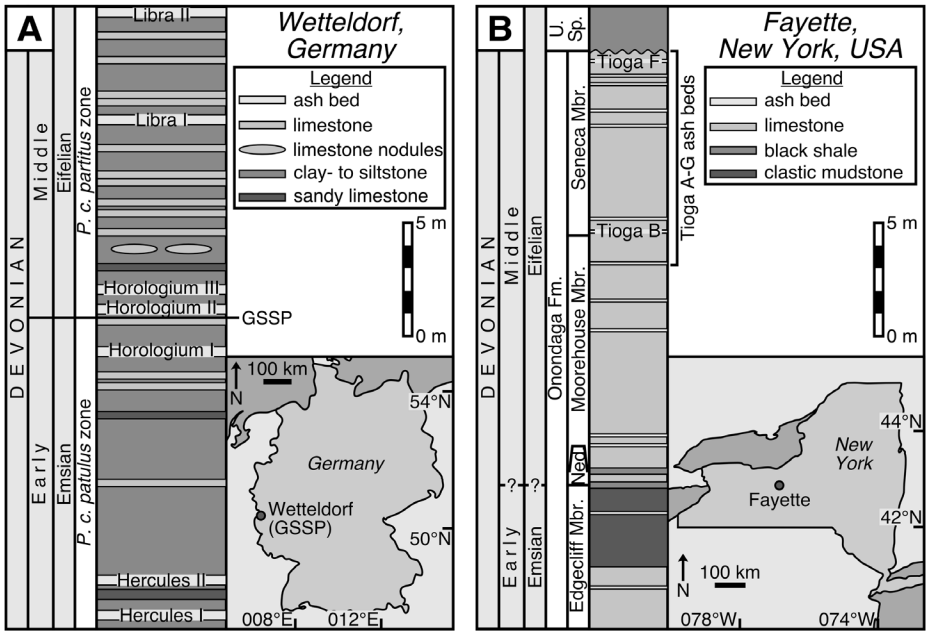

Figure 3.1. (A) Stratigraphic section for Wetteldorf, Germany, showing location of the Hercules I K-bentonite. Stratigraphic column is modified from Kaufmann et al. (2005). (B) Stratigraphic section for Fayette, New York, showing location of the Tioga B and Tioga F K-bentonites. Stratigraphic column is modified from Ver Straeten (2007). P. c.—Polygnathus costatus; GSSP—global stratotype section and point; Fm—Formation; Mbr—Member; Ned—Nedrow Member; U. Sp.—Union Springs Formation.

Hercules I K-Bentonite

We sampled the Hercules I K-bentonite from the GSSP section in Wetteldorf, Germany (50.14983°N, 006.47135°E, World Geodetic System 1984 [WGS84]; Figure 3.1.A.). The sampled K-bentonite is 6–7 cm thick, yellow-gray colored, and located above a resistant limestone layer and below a blue-green–colored siltstone. The Hercules I K-bentonite lies within the upper half of the *P. c. costatus* zone (Werner and Winter, 1975; Weddige, 1977, 1982). For the agedepth model described below, this K-bentonite is designated as D13.

In addition to the Hercules I K-bentonite, we also sampled the Hercules II, Horologium I–III, and Libra I–II K-bentonites from the GSSP section in Wetteldorf, Germany (Figure 3.1.A.). Our attempts to date these K-bentonites were unsuccessful

because of a combination of inheritance and extreme metamictization of U-rich grains. We discuss, as an example, our CA-ID-TIMS U-Pb zircon dates from the Horologium II K-bentonite in Appendix C.

Tioga B K-Bentonite

The Tioga B K-bentonite (Ver Straeten, 2004), also known as the Onondaga Indian Nations bentonite (Brett and Ver Straeten, 1994), outcrops at the Seneca Stone Quarry east of Fayette, New York (42.85462°N, 76.78323°W, WGS84; Figure 3.1.B.). At this location, the Tioga B K-bentonite is ~25 cm thick with a yellow-orange–colored base and a gray-colored, less-altered middle. The upper 5 cm section of the K-bentonite is black and laminated, and we avoided this portion of the bed during sample collection. We interpret the lower 20 cm to represent a single volcanic event despite the internal structure, and we collected a sample that spanned the lower 20 cm of the K-bentonite. The Tioga B K-bentonite defines the upper limit of the Moorehouse Member of the Onondaga Formation (Smith and Way, 1983; Way et al., 1986; Brett and Ver Straeten, 1994; Ver Straeten, 2004) and is placed within the upper half of the *P. c. costatus* zone (Klapper, 1971, 1981). The Tioga B K-bentonite is stratigraphically below the Tioga F K-bentonite. For the age-depth model described below, the Tioga B K-bentonite is designated as D14.

Tioga F K-Bentonite

We also sampled the Tioga F K-bentonite (Ver Straeten, 2004) at the Seneca Stone Quarry (42.85210°N, 76.78977°W, WGS84; Figure 3.1.B.). The Tioga F K-bentonite is ~10 cm thick and gray-black colored, and it appears to be unaltered. The K-bentonite grades from a coarse ash–sized base to a fine ash–sized top. The Tioga F K-

bentonite defines the base of the Marcellus Subgroup of the Union Springs Formation (Brett and Ver Straeten, 1994). The Tioga F K-bentonite is assigned to the *Tortodus kockelianus australis* zone (Brett and Ver Straeten, 1994; Ver Straeten, 2007; Klapper, 1981) but could be part of the *P. c. costatus* zone (Klapper, 1981). For the age-depth model described below, the Tioga F K-bentonite is designated as D15.

Previous Geochronology

Hercules I K-Bentonite

The Hercules I K-bentonite at Wetteldorf, Germany, has been dated by Kaufmann et al. (2005). They air-abraded 19 single zircon grains or grain fragments and dated them by ID-TIMS. Cathodoluminescence (CL) images of some zircon grains from the Hercules I K-bentonite revealed inherited cores, while other zircon grains from the same sample exhibited concentric growth zoning. Of the 19 grains, 13 analyses were concordant and yielded $^{206}Pb/^{238}U$ dates ranging from 407.7 to 392.2 Ma. The tips of long prismatic crystals yielded the youngest $^{206}Pb/^{238}U$ dates, ranging from 396.5 to 392.2 Ma. Assuming varying degrees of inheritance in the analyzed grains, Kaufmann et al. (2005) cautiously interpreted the youngest analysis as the age of eruption of the K-bentonite (392.2 ± 1.5 Ma), noting that this date could be biased to a younger age by unrecognized Pb loss.

Several steps can be taken to determine a more robust age for the Hercules I K-bentonite. Since the Kaufmann et al. (2005) study, chemical abrasion has replaced air abrasion as the primary method for mitigating the effects of Pb loss. Chemical abrasion prior to dissolution dissolves the regions of a zircon grain that have been damaged by U radiation and are most susceptible to Pb loss, resulting in more precise and accurate ages

(Mattinson, 2005). Additionally, Kaufmann et al. (2005) loaded dissolved zircon directly onto filaments for mass spectrometry without chemical purification. Ion-exchange chromatography separates U and Pb from compounds that may create isobaric interferences or hinder ionization during mass spectrometry (Krogh, 1973). Last, reliance on the weighted mean age of multiple concordant analyses will give a more robust age for the K-bentonite than interpreting a single, youngest date.

Tioga B K-Bentonite

There is one age available for the Tioga B K-bentonite. Roden et al. (1990) dated a sample of the Tioga B K-bentonite from Lewisberg, Union County, Pennsylvania, by ID-TIMS using multigrain monazite fractions and determined a weighted mean $^{207}Pb/^{235}U$ age of 390.0 ± 0.5 Ma. They attempted zircon geochronology but rejected the results due to discordance, which they attributed to inherited Pb in inclusion-rich zircon grains. While monazite analyses yielded more concordant results than the zircon analyses, monazite geochronology still has its challenges. Monazite preferentially incorporates Th during crystallization, and thus some of the measured ^{206}Pb must be attributed to the decay of excess ^{230Th}, an intermediate daughter product of ^{238}U, and this consequential excess ^{206}Pb leads to the phenomenon of reverse discordance in monazite. For this reason, Roden et al. (1990) preferred the $^{207}Pb/^{235}U$ age of the monazite, which is not affected by initial ^{230Th} excess. As with the Hercules I K-bentonite, the geochronology of the Tioga B K-bentonite can be improved through chemical abrasion and ion-exchange chromatography of single zircon grains.

Tioga F K-Bentonite

There has been no previous geochronology of the Tioga F K-bentonite. Tucker et al. (1998) erroneously attributed a $^{207}Pb/^{206}Pb$ age of 391.4 ± 1.8 Ma to the Tioga F K-bentonite, but according to Ver Straeten (2004), Tucker et al. (1998) actually dated the Tioga Middle Coarse Zone, which is stratigraphically lower than the Tioga A–G K-bentonites. An age for the Eifelian Tioga F K-bentonite will increase the resolution of age-depth models near the Eifelian-Givetian Stage boundary, which is important because the Givetian Stage currently lacks dated volcanic layers that can be used for time scale modeling.

Geochronology Methods

We did all mineral separation, imaging, chemistry, and mass spectrometry at the Boise State University Isotope Geology Laboratory. We separated zircon from all samples using standard magnetic and density separation techniques, and we annealed all zircon at 900 °C for 60 h. We examined 166 zircon grains from the Hercules I K-bentonite by mounting the grains in epoxy, polishing to grain centers, and imaging by cathodoluminescence (CL) in a JEOL T-300 scanning electron microscope with a Gatan MiniCL detector. We placed 59 spots on 47 grains for preliminary $^{206}Pb/^{238}U$ dating by in situ laser ablation–inductively coupled plasma–mass spectrometry (LA-ICPMS). See Appendix C and Appendix D for LA-ICPMS methods and results. We selected zircon grains for CA-ID-TIMS analysis based on oscillatory zoning in CL with no inherited cores and Devonian $^{206}Pb/^{238}U$ LA-ICPMS ages (for CL images of selected grains, see Figure 3.2.). Zircon grains from the Tioga F and Tioga B K-bentonites were too small for mounting, polishing, and LA-ICPMS analysis, so instead we selected prismatic, needle-

like grains in an effort to exclude detrital grains or grains with inherited cores (for photomicrographs of selected grains, see Figure 3.2.).

We chemically abraded zircon grains selected for high-precision geochronology in a single aggressive step at 190 °C for 12 h, except for grains z1–z8 in the Hercules I K-bentonite sample, which we chemically abraded at 180 °C for 12 h (modified from Mattinson, 2005). We spiked the clean residual grains with the EARTHTIME mixed ^{205}Pb-^{233}U-^{235}U (ET535) tracer solution or the EARTHTIME mixed ^{202}Pb-^{205}Pb-^{233}U-^{235}U (ET2535) tracer solution (Table 3.1.; Condon et al., 2015; McLean et al., 2015). Zircon dissolution and U and Pb separation by ion-exchange chromatography followed the methods described in Davydov et al. (2010).

We took isotopic measurements on an IsotopX GV Isoprobe-T or an IsotopX Phoenix X62 multicollector TIMS with a Daly photomultiplier detector (Pb isotopes as Pb^{+}) and nine Faraday cups fitted with 1012 Ω resistor amplifiers (U isotopes as UO^{2+}). We calculated U-Pb ages and uncertainties using the U decay constants of Jaffey et al. (1971) and the algorithms of Schmitz and Schoene (2007). We report uncertainty (2σ) as ± *X*(*Y*)[*Z*], where *X* is the internal or analytical uncertainty, *Y* is the internal and the tracer calibration uncertainty, and *Z* is the internal, tracer, and decay constant uncertainty.

Table 3.1. U-Pb zircon isotopic data and ages of individual grains.

Compositional parameters[A, B, C, D, E]							
Sample	Spike	Th/U	$^{206}Pb^*$ ($x10^{-13}$ mol)	$^{206}Pb^*$ (mol %)	Pb^*/Pb_c	Pb_c (pg)	$^{206}Pb/^{204}Pb$
Tioga F (2014V27-SSQ-02)							
z6	ET535	0.182	2.6696	99.82%	150	0.41	9811
z5	ET535	0.103	6.2586	99.80%	136	1.03	9155
z1	**ET535**	**0.113**	**6.7774**	**99.89%**	**236**	**0.65**	**15750**
z4	**ET535**	**0.185**	**1.5237**	**99.61%**	**71**	**0.49**	**4674**
z8	**ET2535**	**0.288**	**0.7550**	**99.11%**	**32**	**0.56**	**2027**
z3	**ET535**	**0.066**	**0.3016**	**98.06%**	**14**	**0.49**	**932**
z10	**ET2535**	**0.159**	**0.6892**	**98.87%**	**24**	**0.65**	**1602**
z7	**ET535**	**0.221**	**1.1056**	**98.64%**	**20**	**1.26**	**1334**
z12	**ET2535**	**0.272**	**0.7876**	**99.32%**	**41**	**0.45**	**2641**
z11	**ET2535**	**0.283**	**0.7579**	**99.31%**	**41**	**0.44**	**2613**
Tioga B (2014V27-SSQ-01)							
z2	**ET535**	**0.196**	**0.9581**	**99.26%**	**37**	**0.59**	**2437**
z5	**ET535**	**0.230**	**0.5704**	**98.37%**	**17**	**0.79**	**1106**
z3	**ET535**	**0.255**	**1.1943**	**99.45%**	**51**	**0.55**	**3259**
z6	**ET535**	**0.172**	**0.6975**	**98.67%**	**20**	**0.78**	**1362**
z8	**ET535**	**0.355**	**0.7171**	**99.14%**	**33**	**0.52**	**2103**
z13	**ET2535**	**0.291**	**0.5114**	**99.02%**	**29**	**0.42**	**1838**
z4	**ET535**	**0.305**	**0.6323**	**98.89%**	**25**	**0.59**	**1625**
z18	ET2535	0.411	0.3893	97.72%	13	0.75	791
z11	ET2535	0.377	1.0173	99.39%	48	0.52	2971
z9	ET2535	0.221	0.4290	98.60%	20	0.50	1290
z20	ET2535	0.420	0.6458	98.74%	23	0.68	1435
Hercules I (12VD-80)							
z5	**ET535**	**1.070**	**1.8731**	**99.69%**	**113**	**0.48**	**5909**
z6	**ET535**	**1.066**	**1.1925**	**99.70%**	**117**	**0.29**	**6108**
z1	**ET535**	**0.834**	**0.8937**	**99.55%**	**73**	**0.33**	**4054**
z8	**ET535**	**1.044**	**1.3286**	**99.61%**	**88**	**0.43**	**4653**
z12	**ET2535**	**1.276**	**1.7298**	**99.68%**	**111**	**0.47**	**5565**
z11	**ET2535**	**0.698**	**0.8935**	**98.95%**	**30**	**0.79**	**1725**
z3	**ET535**	**0.631**	**0.7858**	**99.49%**	**61**	**0.33**	**3532**
z4	**ET535**	**0.841**	**0.4685**	**98.88%**	**29**	**0.44**	**1608**
z7	**ET535**	**1.349**	**1.3601**	**99.27%**	**50**	**0.83**	**2462**

Radiogenic Isotope Ratios[F, G, H]								
Sample	$^{208}Pb/^{206}Pb$	$^{207}Pb/^{206}Pb$	% err	$^{207}Pb/^{235}U$	% err	$^{206}Pb/^{238}U$	% err	corr. Coef.
Tioga F (2014V27-SSQ-02)								
z6	0.0574	0.054500	0.078	0.47223	0.135	0.062842	0.064	0.943
z5	0.0325	0.054596	0.066	0.47115	0.129	0.062589	0.065	0.986
z1	**0.0357**	**0.054515**	**0.066**	**0.46928**	**0.127**	**0.062433**	**0.063**	**0.977**
z4	**0.0583**	**0.054615**	**0.109**	**0.47012**	**0.166**	**0.062431**	**0.080**	**0.838**
z8	**0.0906**	**0.054615**	**0.180**	**0.46995**	**0.199**	**0.062409**	**0.036**	**0.569**
z3	**0.0209**	**0.054615**	**0.498**	**0.46993**	**0.558**	**0.062405**	**0.119**	**0.584**
z10	**0.0500**	**0.054339**	**0.235**	**0.46748**	**0.253**	**0.062395**	**0.044**	**0.494**
z7	**0.0697**	**0.054409**	**0.171**	**0.46799**	**0.221**	**0.062383**	**0.071**	**0.787**
z12	**0.0859**	**0.054421**	**0.183**	**0.46799**	**0.205**	**0.062369**	**0.059**	**0.495**
z11	**0.0890**	**0.054557**	**0.161**	**0.46909**	**0.180**	**0.062359**	**0.031**	**0.676**
Tioga B (2014V27-SSQ-01)								
z2	**0.0618**	**0.054610**	**0.151**	**0.47091**	**0.199**	**0.062541**	**0.068**	**0.794**
z5	**0.0724**	**0.054529**	**0.253**	**0.47008**	**0.302**	**0.062524**	**0.079**	**0.693**
z3	**0.0802**	**0.054511**	**0.127**	**0.46992**	**0.177**	**0.062523**	**0.065**	**0.836**
z6	**0.0541**	**0.054697**	**0.227**	**0.47150**	**0.273**	**0.062519**	**0.069**	**0.739**
z8	**0.1117**	**0.054532**	**0.190**	**0.46993**	**0.236**	**0.062499**	**0.069**	**0.740**
z13	**0.0917**	**0.054597**	**0.275**	**0.47029**	**0.299**	**0.062474**	**0.049**	**0.566**
z4	**0.0959**	**0.054579**	**0.230**	**0.46994**	**0.277**	**0.062448**	**0.081**	**0.679**
z18	0.1293	0.054420	0.329	0.46835	0.357	0.062418	0.059	0.532
z11	0.1185	0.054545	0.138	0.46913	0.153	0.062380	0.035	0.518
z9	0.0696	0.054568	0.349	0.46926	0.376	0.062370	0.053	0.567
z20	0.1323	0.054519	0.206	0.46841	0.225	0.062313	0.045	0.507
Hercules I (12VD-80)								
z5	**0.3368**	**0.054638**	**0.098**	**0.47551**	**0.151**	**0.063119**	**0.064**	**0.890**
z6	**0.3353**	**0.054531**	**0.095**	**0.47445**	**0.149**	**0.063102**	**0.065**	**0.903**
z1	**0.2625**	**0.054615**	**0.129**	**0.47505**	**0.178**	**0.063085**	**0.066**	**0.832**
z8	**0.3286**	**0.054483**	**0.096**	**0.47385**	**0.154**	**0.063078**	**0.064**	**0.939**
z12	**0.4015**	**0.054671**	**0.066**	**0.47544**	**0.085**	**0.063072**	**0.032**	**0.721**
z11	**0.2195**	**0.054589**	**0.186**	**0.47470**	**0.206**	**0.063069**	**0.038**	**0.570**
z3	**0.1985**	**0.054622**	**0.146**	**0.47488**	**0.193**	**0.063055**	**0.068**	**0.793**
z4	**0.2647**	**0.054503**	**0.255**	**0.47376**	**0.301**	**0.063043**	**0.075**	**0.688**
z7	**0.4246**	**0.054575**	**0.126**	**0.47437**	**0.177**	**0.063040**	**0.065**	**0.859**

Isotopic Ages (Ma)[F, I]						
Sample	$^{207}Pb/^{206}Pb$	±	$^{207}Pb/^{235}U$	±	$^{206}Pb/^{238}U$	±
Tioga F (2014V27-SSQ-02)						
z6	391.77	1.75	392.73	0.44	392.89	0.2
z5	395.71	1.48	391.98	0.42	391.35	0.2
z1	**392.38**	**1.48**	**390.69**	**0.41**	**390.40**	**0.2**
z4	**396.48**	**2.43**	**391.27**	**0.54**	**390.39**	**0.3**
z8	**396.48**	**4.04**	**391.16**	**0.64**	**390.26**	**0.1**
z3	**396.50**	**11.17**	**391.14**	**1.81**	**390.23**	**0.4**
z10	**385.14**	**5.27**	**389.45**	**0.82**	**390.17**	**0.1**
z7	**388.00**	**3.83**	**389.80**	**0.72**	**390.10**	**0.2**
z12	**388.53**	**4.11**	**389.80**	**0.66**	**390.01**	**0.2**
z11	**394.12**	**3.61**	**390.56**	**0.58**	**389.96**	**0.1**
Tioga B (2014V27-SSQ-01)						
z2	**396.31**	**3.39**	**391.82**	**0.65**	**391.06**	**0.2**
z5	**392.96**	**5.68**	**391.25**	**0.98**	**390.96**	**0.3**
z3	**392.21**	**2.86**	**391.13**	**0.57**	**390.95**	**0.2**
z6	**399.87**	**5.09**	**392.22**	**0.89**	**390.93**	**0.2**
z8	**393.11**	**4.27**	**391.14**	**0.77**	**390.81**	**0.2**
z13	**395.75**	**6.16**	**391.39**	**0.97**	**390.65**	**0.1**
z4	**395.03**	**5.16**	**391.15**	**0.90**	**390.49**	**0.3**
z18	388.47	7.39	390.05	1.15	390.32	0.2
z11	393.61	3.10	390.59	0.50	390.08	0.1
z9	394.58	7.82	390.68	1.22	390.02	0.2
z20	392.54	4.63	390.09	0.73	389.68	0.1
Hercules I (12VD-80)						
z5	**397.44**	**2.20**	**394.99**	**0.49**	**394.57**	**0.2**
z6	**393.03**	**2.12**	**394.26**	**0.49**	**394.47**	**0.2**
z1	**396.49**	**2.88**	**394.67**	**0.58**	**394.36**	**0.2**
z8	**391.07**	**2.16**	**393.85**	**0.50**	**394.32**	**0.2**
z12	**398.78**	**1.47**	**394.94**	**0.28**	**394.28**	**0.1**
z11	**395.41**	**4.18**	**394.43**	**0.67**	**394.26**	**0.1**
z3	**396.77**	**3.27**	**394.55**	**0.63**	**394.18**	**0.2**
z4	**391.88**	**5.73**	**393.78**	**0.98**	**394.10**	**0.2**
z7	**394.86**	**2.82**	**394.20**	**0.58**	**394.09**	**0.2**

Table 3.1. Notes

A. z1, z2 etc. are labels for single zircon grains or fragments annealed and chemically abraded after Mattinson (2005). Samples and their corresponding values in bold were used in the weighted mean age calculation.

B. Samples were spiked with the EARTHTIME mixed ^{205}Pb-^{233}U-^{235}U (ET535) tracer solution or the EARTHTIME mixed ^{202}Pb-^{205}Pb-^{233}U-^{235}U (ET2535) tracer solution (Condon et al., 2015; McLean et al., 2015).

C. Model Th/U ratio iteratively calculated from the radiogenic $^{208}Pb/^{206}Pb$ ratio and $^{206}Pb/^{238}U$ age.

D. Pb* and Pbc represent radiogenic and common Pb, respectively; mol % ^{206}Pb* with respect to radiogenic, blank and initial common Pb.

E. Measured ratio corrected for spike and fractionation only. Fractionation estimated at 0.18 ± 0.03%/a.m.u. for Daly analyses, based on analysis of NBS-981 and NBS-982.

F. Corrected for fractionation, spike, and common Pb; up to 1 pg of common Pb was assumed to be procedural blank: $^{206}Pb/2^{04}Pb$ = 18.042 ± 0.61%; $^{207}Pb/^{204}Pb$ = 15.537 ± 0.52%; $^{208}Pb/^{204}Pb$ = 37.686 ± 0.63% (all uncertainties 1σ). Excess over blank was assigned to initial common Pb, using the Stacey and Kramers (1975) two-stage Pb isotope evolution model at the nominal sample age.

G. Errors are 2σ, propagated using the algorithms of Schmitz and Schoene (2007).

H. corr. Coef. – correlation coefficient

I. Calculations are based on the decay constants of Jaffey et al. (1971). $^{206}Pb/^{238}U$ and $^{207}Pb/^{206}Pb$ ages corrected for initial disequilibrium in $^{230Th}/^{238}U$ using Th/U(magma) = 3.

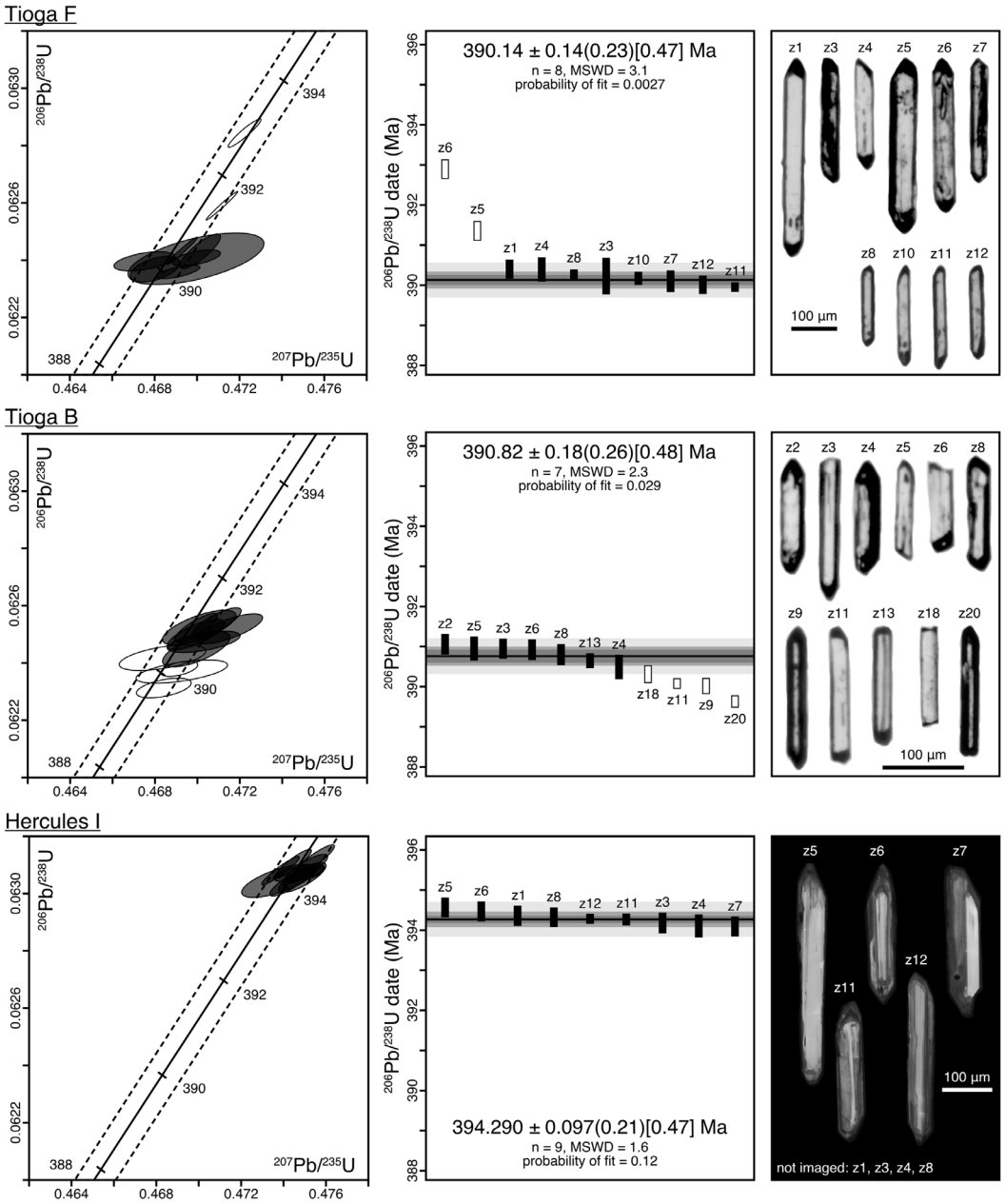

Figure 3.2. Concordia diagrams (left column) and ranked date plots (center column) of U-Pb zircon chemical abrasion–isotope dilution–thermal ionization mass spectrometry (CA-ID-TIMS) results. Error ellipses and error bars are 2σ. Closed symbols are analyses used in weighted mean calculations, and open symbols are analyses excluded from weighted mean calculations. The error on the weighted mean date is reported as a 95% confidence interval on the ranked date plots. The horizontal black band indicates the weighted mean date, the darkest gray horizontal band indicates the internal analytical uncertainty, the medium-gray band incorporates the tracer uncertainty, and the lightest gray band incorporates the decay constant uncertainty. (Right column) Photomicrographs of Tioga F and Tioga B zircon grains and cathodoluminescence images of Hercules I zircon grains. MSWD—mean square of weighted deviates.

Geochronology Results

U-Pb zircon CA-ID-TIMS results are shown in Figure 3.2 (concordia diagrams and ranked date plots with weighted mean ages) and Table 3.1. (isotopic data and dates for individual grains), described below for each sample, and summarized in Table 3.2. (weighted mean ages for each sample).

Table 3.2. Summary of U-Pb zircon sample ages.

Location K-bentonite (Sample number)	$^{206}Pb/^{238}U$ weighted mean age (Ma)	MSWD	prob. Of fit	n
Fayette, New York, USA				
Tioga F (2014V27-SSQ-02)	390.14 ± 0.14(0.23)[0.47]	3.1	0.0027	8
Tioga B (2014V27-SSQ-01)	390.82 ± 0.18(0.26)[0.48]	2.3	0.029	7
Wetteldorf, Germany				
Hercules I (12VD-80)	394.290 ± 0.097(0.21)[0.47]	1.6	0.12	9

Weighted mean ages are at the 95% confidence interval, as calculated from the internal 2σ errors. Uncertainties are quoted as ± *X*(*Y*)[*Z*] where *X* is the internal or analytical uncertainty, *Y* is the uncertainty including the tracer calibration, and *Z* includes the decay constant uncertainty.

MSWD – mean square weighted deviation; prob. Of fit – probability of fit; n – number of analyses included in weighted mean.

Hercules I K-Bentonite

We dated nine zircon grains from the Hercules I K-bentonite (sample name: 12VD-80) by CA-ID-TIMS. We selected grains based on Devonian LA-ICPMS age, oscillatory zoning in CL, and elongate, prismatic shape. The nine grains yielded a weighted mean $^{206}Pb/^{238}U$ age of 394.290 ± 0.097(0.21)[0.47] Ma with a mean square of weighted deviates (MSWD) of 1.6 and a probability of fit of 0.12 (Figure 3.2.). We interpret this age as the age of eruption and deposition of the Hercules I K-bentonite. Two of the eight grains (z11, z12) were dated using the ET2535 tracer solution, and the ages

of these grains are consistent with the ages of the other grains, which were analyzed using the ET535 tracer solution. There is no discernible difference in dates between crystals chemically abraded at 180 °C and those chemically abraded at 190 °C.

Tioga B K-Bentonite

We dated 11 elongate, prismatic zircon grains from the Tioga B K-bentonite (sample name: 2014V27-SSQ-01) by CA-ID-TIMS. Seven of the 11 grains (z2, z5, z3, z6, z8, z13, z4) yielded a weighted mean $^{206}Pb/^{238}U$ age of 390.82 ± 0.18(0.26)[0.48] Ma with an MSWD of 2.3 and a probability of fit of 0.029, which we interpret as the age of eruption and deposition of the Tioga B K-bentonite (Figure 3.2.). The four other grains (z18, z11, z9, z20) yielded younger dates, likely because of varying amounts of Pb loss. We dated five of the 11 grains (z9, z11, z13, z18, z20) using the ET2535 tracer solution, and the ages of these grains are consistent with the ages of the other grains, which we analyzed using the ET535 tracer solution.

Tioga F K-Bentonite

We dated 10 elongate, prismatic zircon grains from the Tioga F K-bentonite (sample name: 2014V27-SSQ-02) by CA-ID-TIMS. Of those 10 grains, eight single-grain zircon analyses (z1, z4, z8, z3, z10, z7, z12, z11) yielded a weighted mean $^{206}Pb/^{238}U$ age of 390.14 ± 0.14(0.23)[0.47] Ma with an MSWD of 3.1 and a probability of fit of 0.0027 (Figure 3.2.). We rejected the other grains (z5, z6) based on varying amounts of inheritance. We interpret the weighted mean age as the age of eruption and deposition of the Tioga F K-bentonite. We dated four of the 10 grains (z8, z10, z11, z12) using the ET2535 tracer solution, and the ages of these grains are consistent with the ages of the other grains, which we analyzed using the ET535 tracer solution.

Age-Depth Modeling

Modeling Methods

We used the modifiedBChron R package (Trayler et al., 2020) to create Bayesian age-depth models of the Devonian using likelihood functions based upon the radioisotopic ages of biostratigraphically constrained events and astrochronologic constraints on Devonian stage durations. Although we were not explicitly modeling in the accumulative stratal depth domain, the biostratigraphic position in a time scale is the product of an accumulative (evolutionary) process with stochastic variability in the number of events and accumulation rates, and thus we posit that the underling mathematical models of Bayesian age-depth modeling are applicable. While we retain the term "age-depth" modeling for its simplicity, the reader is asked to intuit the identity of depth as the relative distance measure of the rock bodies that comprise a chronostratigraphic scale. The "age-depth" models we produced allowed us to determine the age and uncertainty of stratigraphic positions between dated events, specifically stage and conodont biozone boundaries.

Our model inputs were based on radioisotopic ages, biostratigraphic constraints on dated events, and astrochronology stage durations. We investigated how varying relative stratigraphic position of radioisotopic ages influenced the resulting age-depth model by creating a model for three different published conodont biozonation schemes. We incorporated 28 radioisotopic ages into our models (Table 3.3.). We incorporated astrochronologic constraints (Table 3.4.) on the duration of Devonian stages by anchoring an astrochronology duration constraint on a radioisotopic age.

Table 3.3. Model likelihoods: Radioisotopic ages.

Identifier	Age (Ma)[A]	Reference	Tracer	Model likelihood, age (Ma)[B]
Cb2	358.43 ± 0.06(0.19)[0.42]	Davydov et al., 2011	ET535 or ET2535	358.43 ± 0.06
Cb1	358.71 ± 0.06(0.19)[0.42]	Davydov et al., 2011	ET2535	358.71 ± 0.06
D27	358.89 ± 0.20(0.29)[0.48]	Myrow et al., 2014	ET535	358.89 ± 0.20
D26	358.97 ± 0.11(0.19)[0.43]	Myrow et al., 2014	ET535	358.97 ± 0.11
D25	359.25 ± 0.06(0.18)[0.42]	Davydov et al., 2011	ET535 or ET2535	359.25 ± 0.06
D23	363.4 ± 1.8	Tucker et al., 1998	in-house	362.87 ± 0.53
D22	363.8 ± 2.2	Tucker et al., 1998	in-house	364.08 ± 2.05
D19	372.360 ± 0.053(0.11)[0.41]	Percival et al., 2018	ET2535	372.360 ± 0.053
D18	375.14 ± 0.12(0.22)[0.45]	Lanik et al., 2016	ET535 or ET2535	375.14 ± 0.12
D17	375.25 ± 0.13(0.22)[0.45]	Lanik et al., 2016	ET535 or ET2535	375.25 ± 0.13
D16	375.55 ± 0.10(0.21)[0.44]	Lanik et al., 2016	ET535 or ET2535	375.55 ± 0.10
D15	390.14 ± 0.14(0.23)[0.47]	this work	ET535 or ET2535	390.14 ± 0.14
D14	390.82 ± 0.18(0.26)[0.48]	this work	ET535 or ET2535	390.82 ± 0.18
D13	394.290 ± 0.097(0.21)[0.47]	this work	ET535 or ET2535	394.290 ± 0.097
D12	407.7 ± 0.7	Kaufmann et al., 2005	in-house	407.75 ± 1.08
D11	411.7 ± 0.9	Bodorkos et al., 2017	not described	411.7 ± 0.9
D10	411.5 ± 1.1(1.2)[1.3]	Parry et al., 2011	not described	411.5 ± 1.2
D9	415.6 ± 0.8	Bodorkos et al., 2017	not described	415.6 ± 0.8
D8	417.7 ± 0.5	Bodorkos et al., 2017	not described	417.7 ± 0.5
D7	417.22 ± 0.21(0.23)[0.50]	Husson et al., 2016	ET535 or ET2535	417.22 ± 0.21
D6	417.61 ± 0.12(0.23)[0.50]	McAdams et al., 2017	ET535	417.61 ± 0.12

Identifier	Age (Ma)[A]	Reference	Tracer	Model likelihood, age (Ma)[B]
D5	417.68 ± 0.21(0.27)[0.52]	Husson et al., 2016	ET535 or ET2535	417.68 ± 0.21
D4	417.56 ± 0.20(0.26)[0.51]	Husson et al., 2016	ET535 or ET2535	417.56 ± 0.20
D3	417.73 ± 0.22(0.28)[0.53]	Husson et al., 2016	ET535 or ET2535	417.73 ± 0.22
D2	417.85 ± 0.23(0.29)[0.54]	Husson et al., 2016	ET535 or ET2535	417.85 ± 0.23
D1	418.42 ± 0.21(0.27)[0.53]	Husson et al., 2016	ET535 or ET2535	418.42 ± 0.21
S8	422.91 ± 0.07(0.21)[0.49]	Cramer et al., 2014	ET535	422.91 ± 0.07
S7	424.08 ± 0.20(0.29)[0.53]	Cramer et al., 2014	ET535	424.08 ± 0.20

Identifier	Scaled stratigraphic position[C]		
	Kaufmann Scale	Becker 2012 Scale	Becker 2020 Scale
Cb2	101.32 ± 0.78	102.93 ± 0.83	101.76 ± 0.44
Cb1	100.27 ± 0.27	101.05 ± 1.05	100.66 ± 0.66
D27	98.97 ± 1.02	99.19 ± 0.81	98.96 ± 0.35
D26	98.97 ± 1.02	99.19 ± 0.81	98.21 ± 0.39
D25	98.97 ± 1.02	99.19 ± 0.81	97.82 ± 0.79
D23	95.73 ± 0.68	97.37 ± 1.01	95.25 ± 0.59
D22	95.73 ± 0.68	97.37 ± 1.01	95.25 ± 0.59
D19	71.40 ± 1.03	75.05 ± 1.45	78.76 ± 0.48
D18	63.81 ± 0.37	67.76 ± 0.98	73.90 ± 0.46
D17	64.62 ± 0.43	67.76 ± 0.98	74.75 ± 0.39
D16	63.72 ± 1.32	67.76 ± 0.98	74.75 ± 0.39
D15	49.89 ± 0.97	48.66 ± 0.99	48.37 ± 2.77

Identifier	Scaled stratigraphic position[C]		
	Kaufmann Scale	Becker 2012 Scale	Becker 2020 Scale
D14	49.63 ± 0.72	48.66 ± 0.99	47.41 ± 1.81
D13	44.73 ± 1.01	42.47 ± 0.52	40.83 ± 0.55
D12	21.62 ± 1.21	23.77 ± 2.10	24.34 ± 0.70
D11	12.94 ± 2.78	16.63 ± 2.66	12.64 ± 1.58
D10	17.23 ± 5.05	19.24 ± 4.34	12.64 ± 1.58
D9	4.04 ± 2.63	6.95 ± 3.79	3.00 ± 3.00
D8	1.74 ± 2.47	3.84 ± 3.84	3.00 ± 3.00
D7	4.38 ± 1.52	8.28 ± 2.46	3.39 ± 1.13
D6	4.38 ± 1.52	8.28 ± 2.46	3.39 ± 1.13
D5	4.38 ± 1.52	8.28 ± 2.46	3.39 ± 1.13
D4	4.38 ± 1.52	8.28 ± 2.46	3.39 ± 1.13
D3	4.38 ± 1.52	8.28 ± 2.46	3.39 ± 1.13
D2	4.38 ± 1.52	8.28 ± 2.46	3.39 ± 1.13
D1	4.38 ± 1.52	8.28 ± 2.46	3.39 ± 1.13
S8	-4.62 ± 0.40	-6.31 ± 0.65	-6.11 ± 0.72
S7	-6.49 ± 0.49	-9.33 ± 0.80	-8.76 ± 0.68

A. Ages are from the listed references, except for D12, D22, D23 which have been recalculated by Schmitz (2012). When available, we show 2σ uncertainty as ± *X*(*Y*)[*Z*] where *X* is the analytical uncertainty, *Y* is the uncertainty including the tracer calibration, and *Z* includes the decay constant uncertainty.

B. For samples dated using an EARTHTIME tracer (Condon et al., 2015; McLean et al., 2015), we used the analytical uncertainty in our modeling. If the tracer was in-house or unknown, we used the uncertainty including the tracer calibration. Age uncertainty is 2σ.

C. The units of scaled stratigraphic position are relative to the Siluian-Devonian boundary set equal to 0 and the Devonian-Carboniferous boundary set equal to 100. The uncertainty on scaled stratigraphic position is expressed as ± the half width.

Table 3.4. Astrochronology constraints.

Duration (Myr)	Reported uncertainty sources	Reference	Revised uncertainty (Myr)[A]	Reasons for revised uncertainty[A]	Combined duration (Myr)[A]
<u>Famennian</u>					
13.5 ± 0.5	Stratigraphic uncertainty on Stage boundaries + 1 cycle counting error	Pas et al., 2018	N.A.	N.A.	13.82 ± 0.16
14.40 ± 0.28	Stratigraphic uncertainty on Stage boundaries	Ma et al., 2020	± 0.68	added one 405 kyr counting error	
<u>Frasnian</u>					
6.7 ± 0.4	1 cycle counting error	De Vleeschouwer et al., 2012; Whalen et al., 2016	± 0.50	added one 100 kyr uncertainty to account for stratigraphic uncertainty on Stage boundaries	6.7 ± 0.5
<u>Givetian</u>					
6.5	Not reported	House, 1995	± 1.95	arbitrary 30% uncertainty on duration estimate to account for counting error and uncertainty on precession period	4.91 ± 0.35
5.6	Not reported	Ellwood et al., 2011	± 1.10	two 405 kyr cycles counting error + three 100 kyr stratigraphic uncertainty on composite construction	
4.35 ± 0.45	Stratigraphic uncertainty on Stage boundaries + 1 cycle counting error	De Vleeschouwer et al., 2014	± 0.75	added three 100 kyr stratigraphic uncertainty on composite construction	

Duration (Myr)	Reported uncertainty sources	Reference	Revised uncertainty (Myr)[A]	Reasons for revised uncertainty[A]	Combined duration (Myr)[A]
<u>Eifelian</u>					
6.28	Not reported	Ellwood et al., 2015	± 1.00	two 405 kyr cycles counting error + two 100 kyr stratigraphic uncertainty on composite construction	5.50 ± 0.39
5	Not reported	Pas et al., 2021	± 0.80	one 405 kyr cycle counting error + two 200 kyr uncertainty to account for stratigraphic uncertainty on Stage boundaries	
<u>Pragian</u>					
1.7 ± 0.7	Stratigraphic uncertainty on Stage boundaries + 1 cycle counting error	Da Silva et al., 2016	N.A.	N.A.	1.7 ± 0.7
<u>Lochkovian</u>					
7.7 ± 2.8	Stratigraphic uncertainty on Stage boundaries + 6 cycle counting error	Da Silva et al., 2016	N.A.	N.A.	7.7 ± 2.8

A. this study

N.A. – not applicable

We ran models in R (R Core Team, 2021) using the input parameters listed in Tables 3.3. and 3.5., using 10,000 iterations (following burn-in) of a Markov chain Monte Carlo simulation to produce the highest density interval that modeled the relationship between age and depth. Age-depth model inputs and results are available in Appendix D, and code for executing the model is available as Appendix E.

From the model output, we determined stage and conodont biozone boundary ages and uncertainties. To create time-linear biostratigraphic time scales where the relative intervals of the biostratigraphic scale are directly correlative to numerical time, we adjusted the stratigraphic positions of stage and conodont biozones boundaries such that the Bayesian posterior median was linearized between the Silurian-Devonian and Devonian-Carboniferous boundaries. This essentially stretched portions of the time scale for which the scaled stratigraphic position (*y* axis) increased at a lesser rate than the passage of numerical time (*x* axis) and compressed portions of the time scale for which numerical time increased less rapidly than the relative time represented by the scaled stratigraphic position. This created linearized time scales with stage and conodont biozone scaling informed by numerical time and allowed us to assess how strongly different initial conodont biozonation schemes influenced the results of the modeling.

Table 3.5. Model likelihoods: Astrochronology constraints.

Model input identifier	Anchor		
	Identifier	Radiometric age (Ma)	Reference
A-baseFamennian-D27	D27	358.89 ± 0.20	Myrow et al., 2014
A-baseFrasnian-D27	D27	358.89 ± 0.20	Myrow et al., 2014
A-baseGivetian-D27	D27	358.89 ± 0.20	Myrow et al., 2014
A-baseEifelian-D27	D27	358.89 ± 0.20	Myrow et al., 2014
A-baseCarboniferous-D15	D15	390.14 ± 0.14	this paper
A-baseFamennian-D15	D15	390.14 ± 0.14	this paper
A-baseFrasnian-D15	D15	390.14 ± 0.14	this paper
A-baseGivetian-D15	D15	390.14 ± 0.14	this paper
A-D15	D15	390.14 ± 0.14	this paper
A-baseEifelian-D15	D15	390.14 ± 0.14	this paper
A-baseCarboniferous-D14	D14	390.82 ± 0.18	this paper
A-baseFamennian-D14	D14	390.82 ± 0.18	this paper
A-baseFrasnian-D14	D14	390.82 ± 0.18	this paper
A-baseGivetian-D14	D14	390.82 ± 0.18	this paper
A-D14	D14	390.82 ± 0.18	this paper
A-baseEifelian-D14	D14	390.82 ± 0.18	this paper
A-baseCarboniferous-D13	D13	394.290 ± 0.097	this paper
A-baseFamennian-D13	D13	394.290 ± 0.097	this paper
A-baseFrasnian-D13	D13	394.290 ± 0.097	this paper
A-baseGivetian-D13	D13	394.290 ± 0.097	this paper
A-baseEmsian-D6	D6	417.61 ± 0.12	McAdams et al., 2017
A-basePragian-D6	D6	417.61 ± 0.12	McAdams et al., 2017
A-baseLochkovian-D6	D6	417.61 ± 0.12	McAdams et al., 2017
A-baseEmsian-D5	D5	417.68 ± 0.21	Husson et al., 2016
A-basePragian-D5	D5	417.68 ± 0.21	Husson et al., 2016
A-baseLochkovian-D5	D5	417.68 ± 0.21	Husson et al., 2016

Model input identifier	Model likelihood, age (Ma)[A]		
	Kaufmann Scale	Becker 2012 Scale	Becker 2020 Scale
A-baseFamennian-D27	372.71 ± 0.27	372.71 ± 0.27	372.71 ± 0.27
A-baseFrasnian-D27	379.41 ± 0.64	379.41 ± 0.64	379.41 ± 0.64
A-baseGivetian-D27	384.32 ± 0.76	384.32 ± 0.76	384.32 ± 0.76
A-baseEifelian-D27	389.82 ± 0.88	389.82 ± 0.88	389.82 ± 0.88
A-baseCarboniferous-D15	363.36 ± 0.78	363.36 ± 0.78	363.36 ± 0.78
A-baseFamennian-D15	377.18 ± 0.76	377.18 ± 0.76	377.18 ± 0.76
A-baseFrasnian-D15	383.88 ± 0.50	383.88 ± 0.50	383.88 ± 0.50
A-baseGivetian-D15	388.79 ± 0.29	388.79 ± 0.29	388.79 ± 0.29
A-D15	390.14 ± 0.14	390.14 ± 0.14	390.14 ± 0.14
A-baseEifelian-D15	393.79 ± 0.69	393.79 ± 0.69	393.79 ± 0.69
A-baseCarboniferous-D14	362.43 ± 0.92	362.43 ± 0.92	362.43 ± 0.92
A-baseFamennian-D14	376.25 ± 0.91	376.25 ± 0.91	376.25 ± 0.91
A-baseFrasnian-D14	382.95 ± 0.70	382.95 ± 0.70	382.95 ± 0.70
A-baseGivetian-D14	387.86 ± 0.57	387.86 ± 0.57	387.86 ± 0.57
A-D14	390.82 ± 0.18	390.82 ± 0.18	390.82 ± 0.18
A-baseEifelian-D14	392.86 ± 0.42	392.86 ± 0.42	392.86 ± 0.42
A-baseCarboniferous-D13	363.36 ± 0.86	363.36 ± 0.86	363.36 ± 0.86
A-baseFamennian-D13	377.18 ± 0.84	377.18 ± 0.84	377.18 ± 0.84
A-baseFrasnian-D13	383.88 ± 0.61	383.88 ± 0.61	383.88 ± 0.61
A-baseGivetian-D13	388.79 ± 0.46	388.79 ± 0.46	388.79 ± 0.46
A-baseEmsian-D6	411.53 ± 2.02	412.78 ± 1.54	410.57 ± 2.39
A-basePragian-D6	413.23 ± 1.84	414.48 ± 1.32	412.27 ± 2.25
A-baseLochkovian-D6	420.94 ± 1.40	422.18 ± 1.92	419.97 ± 1.00
A-baseEmsian-D5	411.60 ± 2.02	412.85 ± 1.56	410.64 ± 2.39
A-basePragian-D5	413.30 ± 1.85	414.55 ± 1.33	412.34 ± 2.25
A-baseLochkovian-D5	421.01 ± 1.41	422.24 ± 1.93	420.04 ± 1.02

Model input identifier	Scaled stratigraphic position[B]		
	Kaufmann Scale	Becker 2012 Scale	Becker 2020 Scale
A-baseFamennian-D27	73.19 ± 1.02	77.88 ± 0.81	80.23 ± 0.69
A-baseFrasnian-D27	59.78 ± 1.02	60.54 ± 0.81	67.17 ± 0.69
A-baseGivetian-D27	52.42 ± 1.02	52.19 ± 0.81	56.45 ± 0.69
A-baseEifelian-D27	45.74 ± 1.02	43.03 ± 0.81	41.37 ± 0.69
A-baseCarboniferous-D15	100.00 ± 0.50	100.00 ± 0.50	100.00 ± 0.50
A-baseFamennian-D15	73.19 ± 0.50	77.88 ± 0.50	80.23 ± 0.50
A-baseFrasnian-D15	59.78 ± 0.50	60.54 ± 0.50	67.17 ± 0.50
A-baseGivetian-D15	52.42 ± 0.50	52.19 ± 0.50	56.45 ± 0.50
A-D15	50.61 ± 0.50	49.71 ± 0.50	52.36 ± 0.50
A-baseEifelian-D15	45.74 ± 0.50	43.03 ± 0.50	41.37 ± 0.50
A-baseCarboniferous-D14	100.00 ± 0.50	100.00 ± 0.50	100.00 ± 0.50
A-baseFamennian-D14	73.19 ± 0.50	77.88 ± 0.50	80.23 ± 0.50
A-baseFrasnian-D14	59.78 ± 0.50	60.54 ± 0.50	67.17 ± 0.50
A-baseGivetian-D14	52.42 ± 0.50	52.19 ± 0.50	56.45 ± 0.50
A-D14	48.47 ± 0.50	46.77 ± 0.50	47.53 ± 0.50
A-baseEifelian-D14	45.74 ± 0.50	43.03 ± 0.50	41.37 ± 0.50
A-baseCarboniferous-D13	100.00 ± 1.01	100.00 ± 0.52	100.00 ± 0.55
A-baseFamennian-D13	73.19 ± 1.01	77.88 ± 0.52	80.23 ± 0.55
A-baseFrasnian-D13	59.78 ± 1.01	60.54 ± 0.52	67.17 ± 0.55
A-baseGivetian-D13	52.42 ± 1.01	52.19 ± 0.52	56.45 ± 0.55
A-baseEmsian-D6	15.73 ± 1.52	19.28 ± 2.46	14.22 ± 1.13
A-basePragian-D6	10.16 ± 1.52	13.96 ± 2.46	11.06 ± 1.13
A-baseLochkovian-D6	0.00 ± 1.52	0.00 ± 2.46	0.00 ± 1.13
A-baseEmsian-D5	15.73 ± 1.52	19.28 ± 2.46	14.22 ± 1.13
A-basePragian-D5	10.16 ± 1.52	13.96 ± 2.46	11.06 ± 1.13
A-baseLochkovian-D5	0.00 ± 1.52	0.00 ± 2.46	0.00 ± 1.13

A. Ages are based on anchored 115racryoconarids durations extrapolated to each position of interest. Age uncertainty is 2σ.

B. The units of scaled stratigraphic position are relative to the Siluian-Devonian boundary set equal to 0 and the Devonian-Carboniferous boundary set equal to 100. The uncertainty on scaled stratigraphic position is expressed as ± the half width.

Starting Conodont Biozonation Schemes

We created three age-depth models based on three different conodont biozonation schemes to understand how the initial construction of the biostratigraphic scale influenced the final model results. Hereafter, "Kaufmann scale" refers to the alternative and standard conodont biostratigraphic scales of Kaufmann (2006). The term "Becker 2012 scale" refers to the conodont biozones of the GTS2012 (Becker et al., 2012). The term "Becker 2020 scale" refers to the conodont biozones from the GTS2020 (Becker et al., 2020). The three conodont biozonation schemes and relative scales are documented in Figure 3.3.

Importantly, the Kaufmann and Becker biostratigraphic scales were constructed with contrasting fundamental assumptions in zonal scaling. The Kaufmann scale is a composite scale of nine well-characterized sections from around the world, and the scale was constructed under the assumption that those sections had constant stratal accumulation rates. The relative durations of biozones are thus linked to lithostratigraphic thickness. Conversely, the Becker scales were initially built upon the implicit assumption of equal biozone durations, although subsequent calibration exercises in successive Geologic Time Scale volumes (House and Gradstein, 2004; Becker et al., 2012, 2020) have modulated this starting assumption. Neither starting assumption is fully realistic, and these assumptions can be examined, and their resultant scales modified, through the use of age modeling that can stretch and compress the duration of stages and biozones pulled from these existing scales. The emphasis on scaffolding and modifying the Devonian time scale based on radioisotopic ages is present in the work by Kaufmann (2006) and Becker et al. (2012, 2020) and continues here.

We projected the three starting scales to the same normalized interval such that position 0 indicates the Silurian-Devonian boundary and position 100 indicates the Devonian-Carboniferous boundary. This allowed us to directly compare the scales, particularly in terms of the numerical ages of stage boundaries that resulted from the modeling.

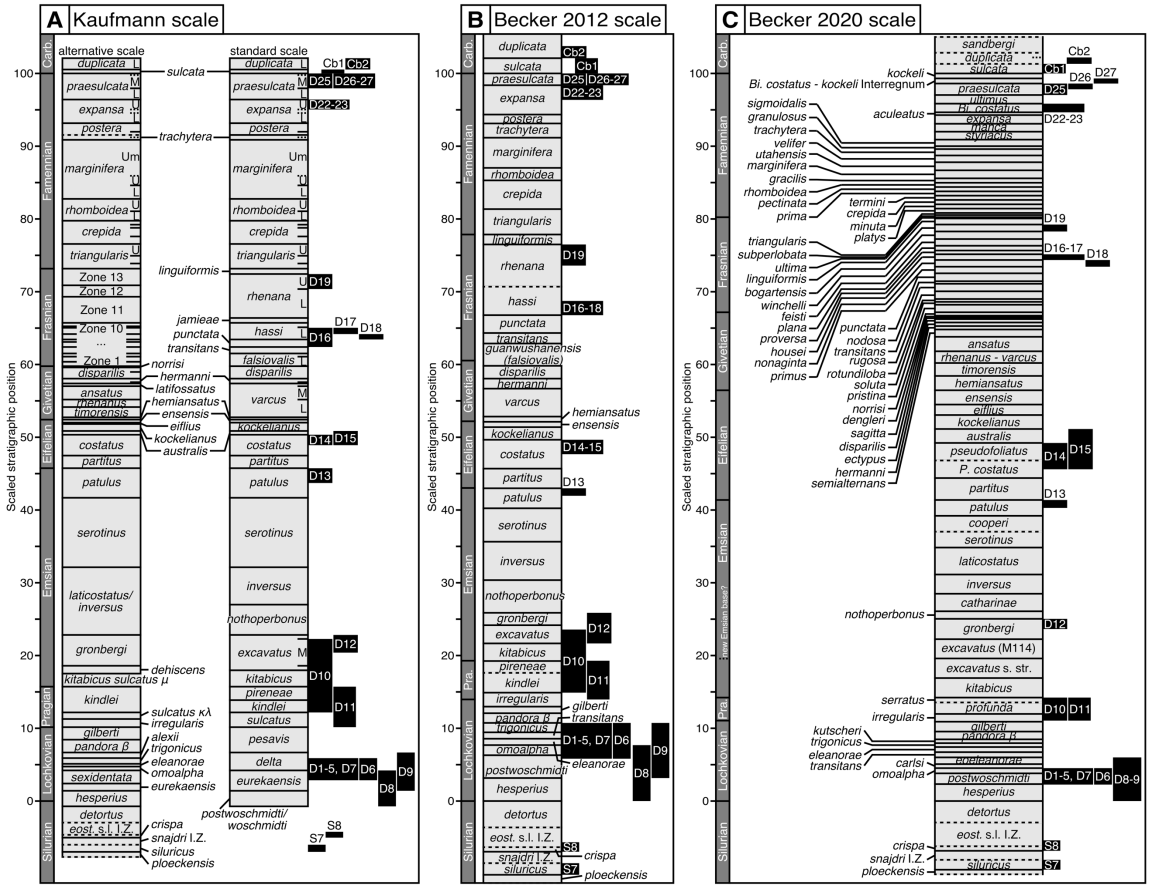

Figure 3.3. The three different starting biostratigraphic scales and the assigned position of the radioisotopic ages on those scales: (A) Kaufmann scale based on Kaufmann (2006), (B) Becker 2012 scale based on the Devonian chapter of the Geologic Time Scale 2012 (Becker et al., 2012), and (C) Becker 2020 scale based on the Devonian chapter of the Geologic Time Scale 2020 (Becker et al., 2020). The time scale (dark-gray rectangles) and the conodont biozone positions and scaling (light-gray rectangles) are reproduced from those references and scaled along the y axis (scaled stratigraphic position) such that each time scale ranges from 0 at the Silurian-Devonian boundary and 100 at the Devonian-Carboniferous boundary. The relative stratigraphic position of each dated volcanic layer is represented by the horizontal midpoint of the black rectangles, and the stratigraphic uncertainty is equal to ± the half-height of the black rectangles. The abbreviations we use for each age (i.e., "D1") matches that of the Geologic Time Scale 2020. Conodont genera as in references used to construct the different scales (Kaufmann 2006 and references therein; Becker et al., 2012, 2020; Aretz et al., 2020; Melchin et al., 2020). L—lower; M—middle; U—upper; Um—uppermost; Carb—Carboniferous; Pra—Pragian; M114—Morphotype 114; s. str.—sensu stricto; eost—eosteinhornensis; s.l.—sensu lato; I.Z.—interval zone; Bi— Bispathodus; P—Polygnathus.

Radioisotopic Age Constraints for Model

We used 24 $^{206}Pb/^{238}U$ zircon ages from this work and the Devonian chapter of the GTS2020 (Becker et al., 2020, and references therein), two U-Pb zircon ages from the Silurian chapter of the GTS2020 (Melchin et al., 2020, and references therein), and two U-Pb zircon ages from the Carboniferous chapter of the GTS2020 (Aretz et al., 2020, and references therein), and we assigned those ages to a scaled stratigraphic position for our modeling (Figure 3.3.; Table 3.3.). We included Silurian and Carboniferous ages in our models to minimize uncertainty caused by the model extrapolating across the SilurianDevonian and Devonian-Carboniferous boundaries. Generally, we accepted the conodont biozone assignment from the references that published each age, and we assigned a scaled stratigraphic position to each age for each scale based on that conodont biozone assignment. See the Appendix C for a detailed description of the way in which we assigned each age to a relative stratigraphic position. The abbreviations we use for each age (e.g., "D1") match those of the GTS2020. When available, we report age uncertainty as ± $X(Y)[Z]$, where X is the internal or analytical uncertainty, Y is the uncertainty including the tracer calibration, and Z includes the decay constant uncertainty. For modeling, we used the X uncertainty for zircon dated using an EARTHTIME-calibrated isotope-dilution tracer (Condon et al., 2015; McLean et al., 2015), as the shared use of this SI-traceable reference material in time scale calibration eliminates this significant source of interlaboratory systematic errors. We used the Y uncertainty for legacy ages dated with an unknown or in-house tracer. For all legacy ages from GTS2020, any excess geologic scatter in the data was also accommodated into the age uncertainty. As all radioisotopic age constraints for our Devonian time scale utilized

the same ^{238}U-^{206}Pb radioactive decay scheme, we can eliminate decay constant *Z* uncertainties while maintaining a self-consistent geochronological framework—a strategy that is more generally true for the entire Paleozoic.

Astrochronologic Constraints for Modeling

We incorporated astrochronologic constraints into our model by anchoring floating stage durations and uncertainties to radioisotopic ages (Figure 3.4.). Table 3.4. aggregates available astrochronologic constraints for Devonian stages and documents how we revised uncertainties in the stage durations (see Appendix C for more detail on the astrochronologic studies and associated uncertainties). Astrochronology studies vary in terms of the sources of error that they incorporate into the duration uncertainty (Sinnesael et al., 2019), so our revised uncertainties incorporated at least one cycle-counting error as well as stratigraphic uncertainty in an attempt to standardize the uncertainties used in our modeling. When a stage had multiple published durations, we combined the durations into a weighted average (μ_{Stage}) using individual stage durations (μ_1, μ_2,...μ_n, where *n* is the number of individual cyclostratigraphy studies for a stage) weighted by our revised uncertainties (σ_1, σ_2,...σ_n, where *n* is the number of individual cyclostratigraphy studies for a stage) according to:

$$\mu_{Stage} = \frac{\frac{\mu_1}{(\sigma_1)^2}+\frac{\mu_2}{(\sigma_2)^2}+\cdots+\frac{\mu_n}{(\sigma_n)^2}}{\frac{1}{(\sigma_1)^2}+\frac{1}{(\sigma_2)^2}+\cdots+\frac{1}{(\sigma_n)^2}}.$$

We determined a combined uncertainty (σ_{Stage}) using the harmonic sum of the revised uncertainties for each duration as:

$$\sigma_{Stage} = \frac{1}{\frac{1}{(\sigma_1)^2}+\frac{1}{(\sigma_2)^2}+\cdots+\frac{1}{(\sigma_n)^2}}.$$

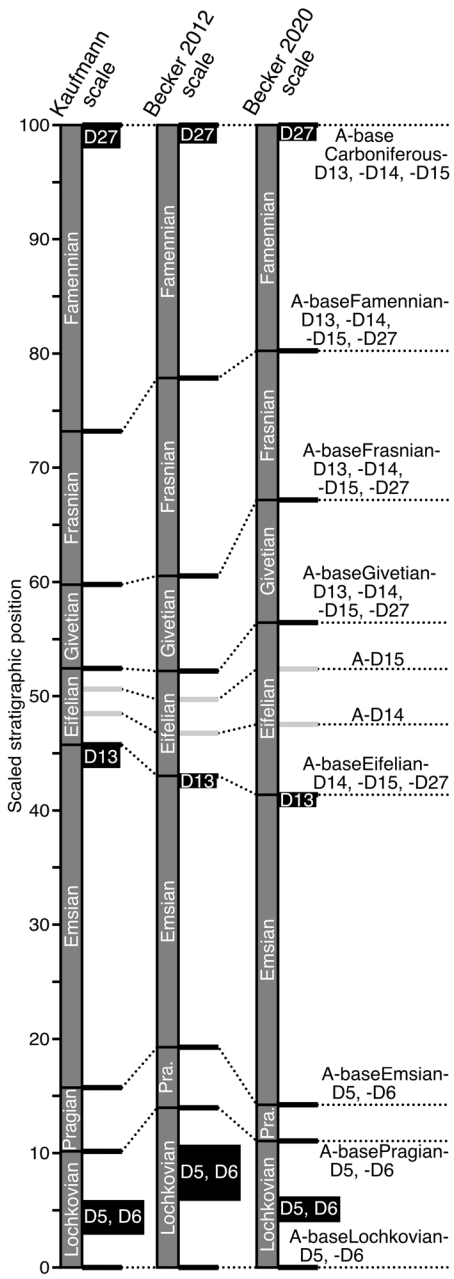

Figure 3.4. Scaled stratigraphic positions of the anchored astrochronologic constraints on each of the three starting time scales (Kaufmann, 2006; Becker et al., 2012, 2020) are shown as thick black lines and labeled to the right side of the figure. Floating stage durations and uncertainties are anchored on D5, D6, D13, or D27 (black rectangles with white labels) or A-D14 or A-D15 (thick gray lines). Dashed lines connect the position of each model input to its label on the right side of the figure. A-D14 and A-D15 function as both anchors and age constraints input into the model; see text for details. The uncertainty on D27 of the Becker et al. (2020) scale has been extended up to the Devonian-Carboniferous boundary for the purposes of anchoring astrochronology stage durations. Pra—Pragian.

We used the combined duration and uncertainty for each stage, except for the Eifelian, where we used both the combined duration and uncertainty (Ellwood et al., 2015; combined with Pas et al., 2021) and the duration and revised uncertainty of Pas et al. (2021) as two separate astrochronologic constraints. Because we dated the Tioga B and Tioga F K-bentonites from within the same section studied by Pas et al. (2021), the Seneca Stone Quarry in New York, we could anchor the Pas et al. (2021) duration directly on radioisotopic dates for which the stratigraphic position within the section is known. This allowed us to compare how our anchoring and chaining process, described further below, varied between durations anchored on radioisotopic ages from the same section and combined durations anchored on radioisotopic ages from other sections. We used the astrochronologic constraints listed in Table 3.4. in our model for all three scales (Kaufmann, 2006; Becker et al., 2012, 2020), although uncertainty from the anchoring process caused each model to have unique astrochronologic inputs. To our knowledge, there is no astrochronology study on the duration of the Emsian Stage. The code used to do the astrochronology extrapolations is available in Appendix E. We indicate model inputs based on astrochronologic constraints with a prefix “A-”, and the suffix on the astrochronologic constraints (e.g., “-D5”) indicates the anchoring radioisotopic age. Table 3.5. shows the results of extrapolating the floating astrochronology durations to create inputs for the age-depth model.

To propagate the uncertainty in anchoring floating stage durations to radioisotopic ages, we used a Monte Carlo approach to sum the Gaussian error distributions of radioisotopic ages and uniform error distributions of astrochronology durations to extrapolate to the stage boundary of interest. We used the mean and standard deviation of

the resulting summed distribution as the stage boundary age. We anchored the floating stage durations on ages D5, D6, D13, and D27 and used the combined astrochronology durations for each stage to chain up or down the time scale. Since ages D14 and D15 (Tioga B and Tioga F K-bentonites) are from the same section (Seneca Stone Quarry east of Fayette, New York) as some Eifelian cyclostratigraphy work (Pas et al., 2021), we built an additional astrochronology constraint into our model by using D14 and D15 as midstage anchors paired with the astrochronology duration determined on the same section. Because the scaled stratigraphic position of the Tioga B and Tioga F K-bentonites differed between the conodont biozone assignment and the position within the measured Eifelian section (Pas et al., 2021), we used A-D14 and A-D15 to indicate the radioisotopic ages of those K-bentonites at the measured stratigraphic positions, and we used D14 and D15 to indicate those radioisotopic ages at a scaled stratigraphic position corresponding to the conodont biozone assignment. For midstage anchors, we proportionally divided the astrochronology duration and uncertainty according to the relative stratigraphic position within the stage. See Appendix C for a graphical explanation of this process.

We tied these extrapolated stage boundary ages to scaled stratigraphic positions based on the positions of the stage boundaries on each of the three conodont scales. We assigned a scaled stratigraphic uncertainty on the astrochronologic constraints according to the uncertainty on the anchoring position: a half width of 0.5 composite units for marker beds in a measured section and a half width equal to the conodont biozone half width for ages anchored to conodont biozones. For the Becker 2020 scale, we extended the stratigraphic position of D27 up to the Devonian-Carboniferous boundary, assuming

that the Devonian-Carboniferous boundary lies within the uncertainty of the D27 age (Myrow et al., 2014).

Age-Depth Model Results

Entering the radioisotopic ages and astrochronologic constraints and their scaled stratigraphic positions into a Bayesian age-depth model using the modifiedBChron R package (Trayler et al., 2020) resulted in a modeled age and uncertainty for all stratigraphic positions on each of the three scales (Figure 3.5.). We report model ages as the median and the 95% highest density interval of the 10,000 iterations of the Markov chain Monte Carlo simulations. This creates a "beaded bracelet" pattern, where the uncertainty of the age model is smallest near well-constrained ages and increases where there are few or only poorly constrained ages, where the degree of constraint is determined by *both* the precision of the age and the precision of the placement of the age on the conodont biostratigraphic scale. The three conodont zonation schemes produced broadly similar age-depth models, particularly in the Early Devonian and near the Devonian-Carboniferous boundary. The model medians and 95% highest density intervals are least similar from ca. 390 to 368 Ma, suggesting the greatest discrepancy among the conodont biozonation schemes during this interval.

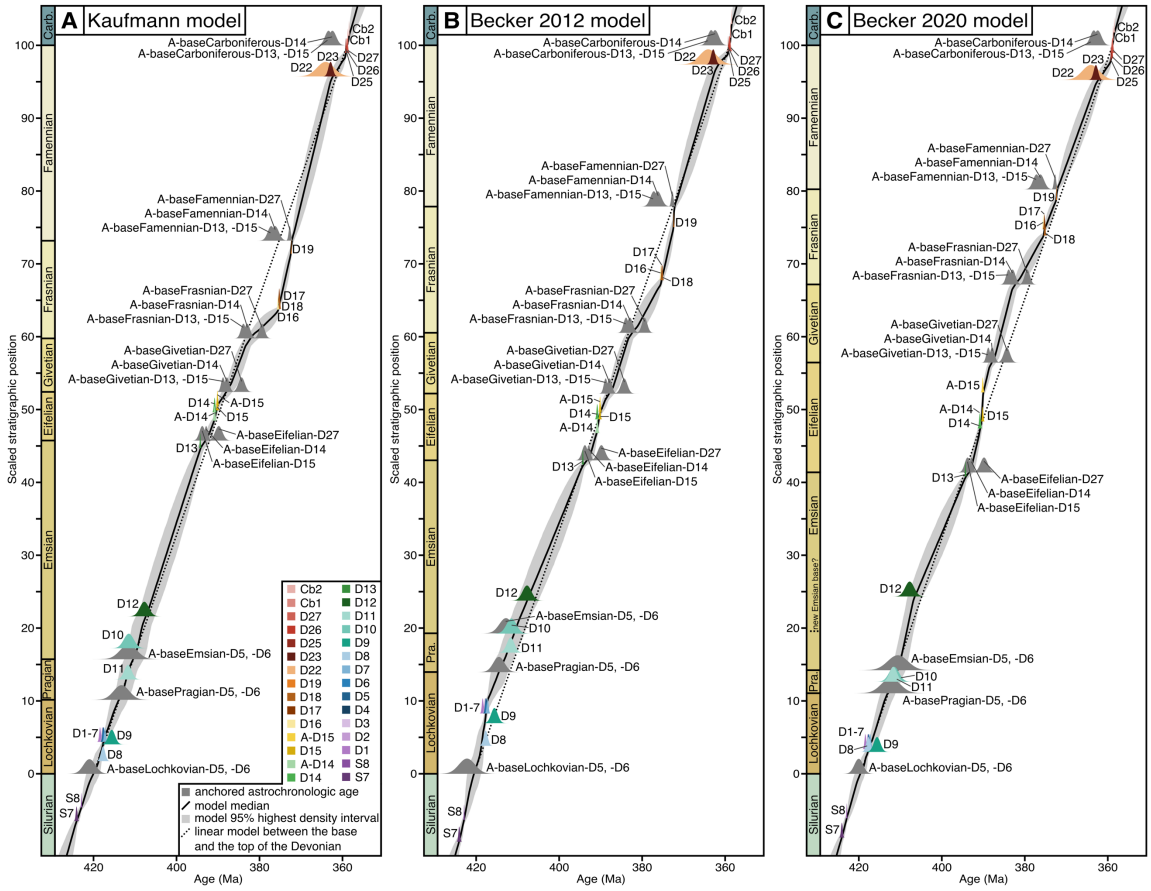

Figure 3.5. Age-depth model results for the (A) Kaufmann (2006) model, (B) Becker et al. (2012) model, and (C) Becker et al. (2020) model. The radioisotopic ages are shown as colored probability density functions, and the anchored astrochronologic constraints are shown as gray probability density functions. The model median is indicated by a solid black line, and the model 95% highest density interval is shown as a light-gray shaded region. A linear model from the base of the Devonian to the base of the Carboniferous is shown as a dotted line. Carb—Carboniferous; Pra—Pragian.

We rescaled each of the three age models, including the stages and the conodont biozones, according to the amount of offset between the median of the age-depth model and a linear projection (dotted line, Figure 3.5.) from the base of the Devonian to the base of the Carboniferous (Figure 3.6.). We compared the three revised scales after compressing and stretching the stages and conodont biozones from each scale (Figure 3.6.D.) and found broad agreement between the three revised scales, particularly for the Middle to Late Devonian. Despite differences in the likelihoods input into the models, the

age-depth modeling and linearization process produced remarkably similar stages, both in terms of duration and absolute age. The ages and scaled stratigraphic positions of stage boundaries after modeling and linearization are given in Table 3.6.

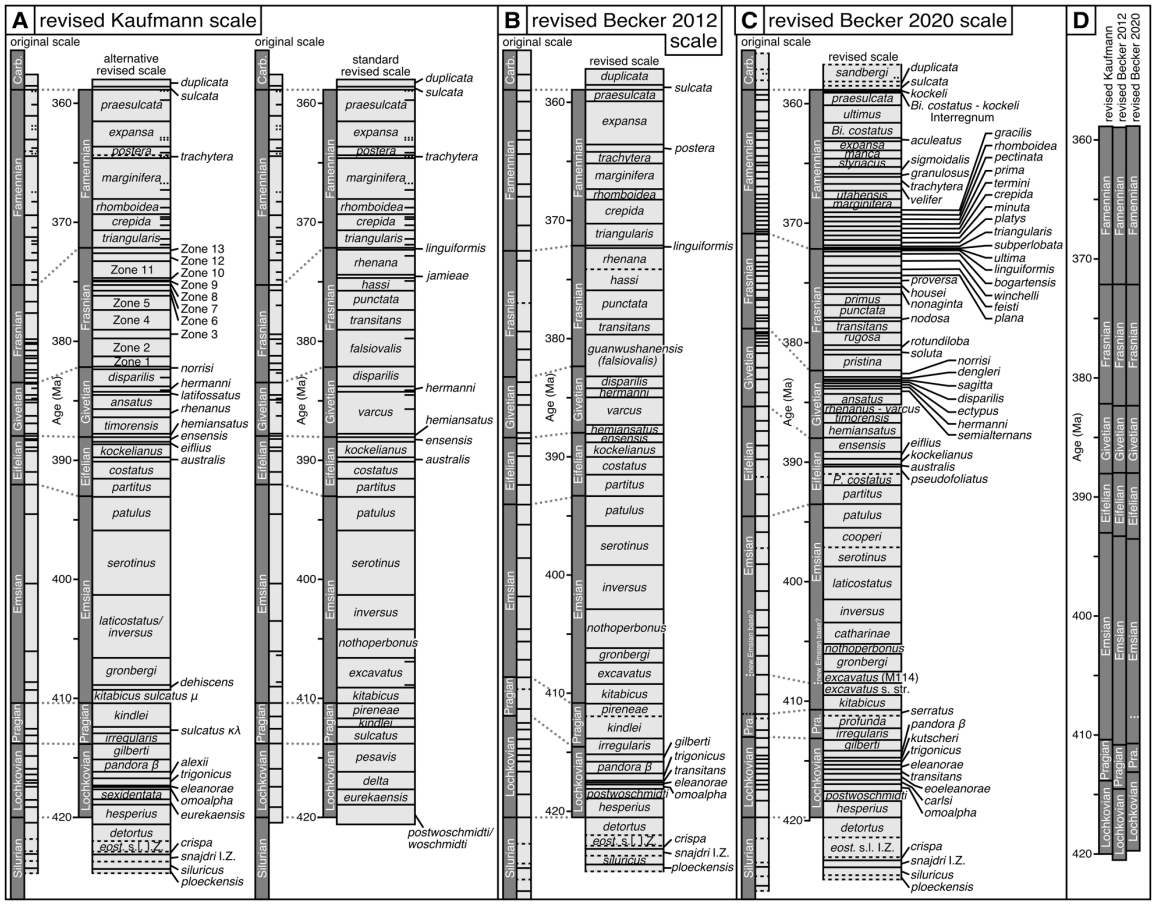

Figure 3.6. Revised conodont biozonation schemes as a result of linearizing the age-depth model to match relative stratigraphic position to numerical time: (A) Kaufmann (2006) alternative and standard scales; (B) Becker et al. (2012) scale; (C) Becker et al. (2020) scale. For each of the three biostratigraphic scales, the original time scale is shown on the left, and the revised stage (dark-gray rectangles) and conodont biozone (light-gray rectangles) heights are shown to the right of the original time scale. (D) Comparison of the revised stage heights for the three biostratigraphic scales. Conodont genera as in references used to construct the different scales (Kaufmann 2006 and references therein; Becker et al., 2012, 2020; Aretz et al., 2020; Melchin et al., 2020). Carb—Carboniferous; Pra—Pragian; M114—Morphotype 114; s. str.—sensu stricto; eost—eosteinhornensis; s.l.—sensu lato; I.Z.—interval zone; Bi—Bispathodus; P—Polygnathus.

Table 3.6. Model results: Stage boundary ages.

Stage (or Period) base	Posterior age (Ma)	Scaled stratigraphic position[B]
Kaufmann Scale		
base of the Carboniferous	358.88 +0.23 / -0.23	100.00
base of the Famennian	372.17 +0.30 / -0.48	73.17
base of the Frasnian	382.19 +1.52 / -2.00	59.76
base of the Givetian	388.06 +1.04 / -1.44	52.42
base of the Eifelian	393.04 +1.03 / -1.31	45.75
proposed base of the Emsian[A]	N.A.	N.A.
base of the Emsian	410.41 +2.14 / -2.44	15.73
base of the Pragian	413.86 +1.87 / -2.18	10.16
base of the Lochkovian	420.02 +1.72 / -1.51	0.00
Becker 2012 Scale		
base of the Carboniferous	358.96 +0.20 / -0.22	100.00
base of the Famennian	372.15 +0.23 / -0.44	77.86
base of the Frasnian	382.36 +1.33 / -1.59	60.54
base of the Givetian	387.98 +0.93 / -1.27	52.19
base of the Eifelian	393.31 +0.84 / -1.19	43.03
proposed base of the Emsian[A]	N.A.	N.A.
base of the Emsian	410.84 +2.17 / -2.49	19.29
base of the Pragian	414.55 +1.92 / -2.17	13.96
base of the Lochkovian	420.52 +1.64 / -1.67	0.00
Becker 2020 Scale		
base of the Carboniferous	358.86 +0.19 / -0.19	100.00
base of the Famennian	372.15 +0.46 / -0.46	80.24
base of the Frasnian	382.31 +1.08 / -1.36	67.18
base of the Givetian	387.95 +0.82 / -1.04	56.45
base of the Eifelian	393.47 +0.72 / -0.99	41.38
proposed base of the Emsian[A]	408.41 +1.55 / -1.67	19.58
base of the Emsian	410.62 +1.66 / -1.95	14.22
base of the Pragian	413.02 +1.75 / -1.91	11.06
base of the Lochkovian	419.62 +1.36 / -1.14	0.00

A. Proposed new Emisian base discussed in Becker et al. (2020).

B. The units of scaled stratigraphic position are relative to the Siluian-Devonian boundary set equal to 0 and the Devonian-Carboniferous boundary set equal to 100.

N.A. – not applicable.

Discussion

New U-Pb Zircon Ages Aid in Improving the Devonian Time Scale

Our new ages for the Hercules I, Tioga B, and Tioga F K-bentonites improve the Devonian time scale by more precisely and accurately radioisotopically dating K-bentonites constrained within existing biostratigraphic frameworks. Our age for the Hercules I K-bentonite is more precise and older than the age of Kaufmann et al. (2005) (Figure 3.7.). They dated the tips of prismatic zircon grains and found a scattering of ages along the U-Pb concordia curve from 396.5 to 392.2 Ma, and they interpreted the youngest age of that cluster, 392.2 ± 1.5 Ma, as the eruption age of the K-bentonite (Kaufmann et al., 2005). Our weighted mean age on elongate, prismatic zircon grains from the Hercules I K-bentonite is 394.290 ± 0.097(0.21)[0.47] Ma, which falls within the range of oldest grains from Kaufmann et al. (2005). We believe our weighted mean age is a more robust eruption age for the K-bentonite because we chemically abraded the dated grains at 180 °C or 190 °C for 12 h in concentrated HF to eliminate Pb loss (modified from Mattinson, 2005), while Kaufmann et al. (2005) did a low-temperature (80 °C) leach in concentrated HF and HNO_3 for 2 h, which is likely insufficient to eliminate all Pb loss and therefore would bias their results to a younger age.

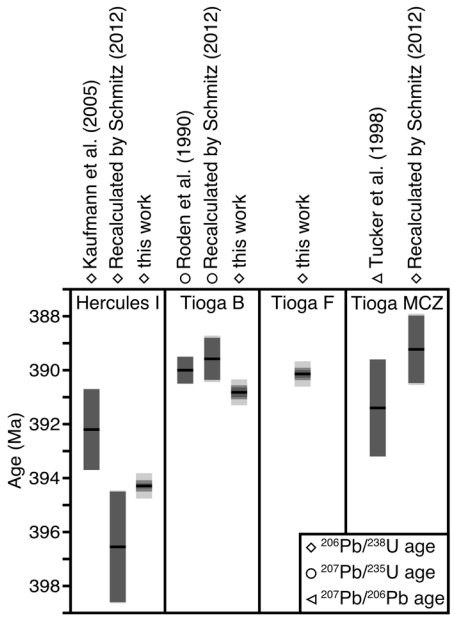

Figure 3.7. Comparison between new high-precision U-Pb zircon ages from this work and existing literature ages for the Hercules I, Tioga B, and Tioga F K-bentonites. Each age is indicated with a horizontal black line and surrounded by dark-, medium-, and light-gray rectangles that represent the 2σ analytical, analytical + tracer calibration, and analytical + tracer calibration + decay constant uncertainty, respectively. MCZ— Middle Coarse Zone cluster.

Similarly, we improved the age of the Tioga B K-bentonite by dating chemically abraded single zircon grains. Roden et al. (1990) dated multigrain monazite fractions from the Tioga B K-bentonite to avoid inheritance in zircon and determined a $^{207}Pb/^{235}U$ age of 390.0 ± 0.5 Ma. This age was recalculated to an equivalent $^{206}Pb/^{238}U$ age of 389.58 ± 0.86 Ma (including decay constant uncertainty) for the GTS2012 (Schmitz, 2012). We mitigated the issue of inheritance by selecting needle-shaped zircon unlikely to have an inherited core, and we found the age of the Tioga B K-bentonite to be 390.82 ± 0.18(0.26)[0.48] Ma, which is not only more precise but also without the systematic error amplification associated with using the ^{235}U-^{207}Pb chronometer.

To our knowledge, our work provides the first age for the Tioga F K-bentonite because Tucker et al. (1998) erroneously reported an age for the Tioga Middle Coarse

Zone as the age of the Tioga F K-bentonite (Ver Straeten, 2004). Our weighted mean age of zircon from the Tioga F K-bentonite is 390.14 ± 0.14(0.23) [0.47] Ma. The two Tioga K-bentonites have distinguishable ages that are consistent with their stratigraphic superposition. The resolution of these radioisotopic ages and the ability to temporally distinguish between them currently exceed our ability to biostratigraphically constrain the K-bentonites; however, the age-depth modeling, in its ability to leverage stratigraphic superposition, helps us to overcome the current limitations of biostratigraphic resolution. Accurate and precise ages and positions for the Tioga K-bentonites are critical for achieving a useful age-depth model through the Givetian, a stage without radioisotopic ages, because these K-bentonites are the dated events nearest to the Eifelian-Givetian boundary.

Anchoring Astrochronology Durations

We integrated astrochronologic constraints as likelihood functions in our Bayesian age-depth models by anchoring floating astrochronology durations on radioisotopic ages. In general, it is not uncommon for studies to anchor astrochronology durations on a radioisotopic age from the same section (e.g., Da Silva et al., 2020; Pas et al., 2021) or on a time scale stage boundary age (e.g., Ma et al., 2020), but, to our knowledge, this is the first effort to chain multiple stage durations together for Bayesian modeling. Given the global distribution of Devonian ages and the scarcity of sections with both cyclostratigraphic and radioisotopic constraints, it can be difficult to pair astrochronologic constraints with radioisotopic age anchors. We managed this difficulty by providing the model with multiple astrochronology likelihoods and allowing the algorithm to determine the most probable age at a given scaled stratigraphic position. We

anchored and chained together sequences of combined stage durations both forward and backward in time and repeated this process for multiple radioisotopic age anchors. This created multiple likelihood functions based on astrochronology at each stage boundary, providing our age-depth models with additional inputs beyond just radioisotopic ages. Adding astrochronology data improved our models because Bayesian age-depth models have improved precision as additional likelihood functions are added to the model (Blaauw et al., 2018).

Additionally, we found that the anchoring and chaining process yielded similar likelihoods for combined durations anchored on radioisotopic ages near stage boundaries and for an individual duration (Eifelian Seneca Stone Quarry section; Pas et al., 2021) anchored on radioisotopic ages from K-bentonites within that section. For example, the likelihood probability density functions (PDFs) produced through anchoring on D13 (anchor near the stage boundary) and D15 (anchor within a section) overlapped with very similar mean ages and similar uncertainties (Figure 3.5., see PDFs labeled "A-...-D13" and "A-...-D15"). This demonstrates the flexibility and reproducibility of our method of incorporating astrochronology durations into Bayesian modeling.

Integration of astrochronologic constraints as model likelihood data is a significant aspect of this work and differs from work done previously for time scale modeling. Rather than using astrochronology as likelihood functions, the Bayesian age-depth model of the Devonian by De Vleeschouwer and Parnell (2014) used astrochronology stage durations as rejection criteria to filter the posterior model results, subsampling the model runs that were in agreement with the Frasnian and Givetian durations available at the time. The resultant thinning of model runs leads to some

concerns as to the recovery of the target stationary posterior distribution. Rather than integrating astrochronology and radioisotope geochronology, Baresel et al. (2017) discussed the results of their radioisotopic Bayesian age-depth models for the Permian-Triassic boundary in the context of existing astrochronological time scales to find both agreement and disagreement in terms of the duration of the extinction event, depending on which astrochronology data set was compared. Our approach conserves all well-mixed Markov chains and treats astrochronologic constraints as information the algorithm uses to generate the model, not just a way to evaluate a model generated by radioisotopic ages alone. Because Bayesian modeling can convolve disparate data sources, we can integrate and reconcile conflicting astrochronologic and radioisotopic data to produce a more robust age-depth model, rather than being left with potentially opposing astrochronology and radioisotopic time scale results.

Influence of Primary Conodont Biozone Scaling on the Time Scale

The Kaufmann (2006) and Becker et al. (2012, 2020) scales differ in the fundamental prior assumptions upon which the conodont biostratigraphic scales were constructed, with an assumption of either constant sedimentation rates in measured sections (Kaufmann, 2006) or equal biozone durations (Becker et al., 2012, 2020). Despite this difference, our Bayesian age-depth modeling process produced remarkably similar posterior scaled time scales. The age-depth models prior to linearization had overlapping 95% highest density intervals for most of the Devonian except for the late Eifelian through early Famennian (Figure 3.5.). During those times, the Kaufmann (2006) and Becker et al. (2012) age-depth models showed better agreement with each other than did either with the Becker et al. (2020) age-depth model, suggesting that it is not the

method of constructing the biostratigraphic scale (assumption of constant sedimentation rates or assumption of roughly equal biozone durations) that controls the age-depth modeling result, but rather the interpolation method for each scale that creates the relationship between zonal durations and numerical time.

The choice of the number of biozones to include in a conodont biozonation scheme has implications for the resulting age-depth model and how that conodont biozonation scheme is used by other workers. For the GTS2020, the number of conodont biozones in the Devonian grew to 85, up from 40 conodont biozones in the GTS2012 (Becker et al., 2012, 2020). Many of these additions occurred in the Late Devonian section. The addition of conodont biozones automatically shrank the average duration of conodont biozones. A consequence of shorter duration conodont biozones is that a biostratigraphic constraint on an age within a particular biozone appears to be relatively more precise. For example, the duration of the *Caudicriodus postwoschmidti* zone was halved from the GTS2012 to the GTS2020, which means the precision of the relative stratigraphic height of an age assigned to this biozone similarly improved for the GTS2020 relative to the GTS2012. However, previous workers who paired a biostratigraphic constraint with an age may not have known the position of that age with such precision nor considered the biostratigraphic assignment with the newly added conodont biozones in mind, and thus the Becker et al. (2020) scale might have overestimated how well constrained those ages are in the biostratigraphic framework. Further, as additional biozones were added to the biozonation scheme, the absolute position of that age may also have changed, not just the precision, depending on how many biozones were added and where they were added. Most conodont biozones have

been shifted to lower (older) relative stratigraphic positions on the Becker et al. (2020) scale relative to the Becker et al. (2012) scale, in some cases shifting to a position entirely below, with no overlap with the position on the Becker et al. (2012) scale (e.g., *Gondwania irregularis*, *Palmatolepis marginifera*). The modification of a conodont biozonation scheme is a natural result of more regional and global biostratigraphic studies, and improvements to conodont biozonation schemes should be embraced, but the discrepancies between the three biostratigraphic scales analyzed here emphasize the need for careful contextualization of dated volcanic layers so that radioisotopic ages can be applied accurately to future biostratigraphic scales.

The age-depth modeling process can be leveraged to examine and improve the consistency between the three biostratigraphic scales. When rescaled via their median Bayesian age-depth relationship, the agreement among the three models in terms of stage duration and numerical age is noteworthy (Figure 3.6.D.). This convergence demonstrates that Bayesian age-depth modeling, particularly with the added step of time-linear rescaling, can produce robust time scales even with significant uncertainty in the relative stratigraphic positions of radioisotopic ages. The convergence on similar stage boundary ages for our three time scales, especially when compared to previous Devonian time scales (Figure 3.8.), suggests that model inputs that varied between the scales, namely, the starting conodont biozonation schemes and consequently the scaled stratigraphic positions of ages, are not an overly sensitive influence on the resulting time scales, perhaps because of the size of the scaled stratigraphic position uncertainty on each age (Appendix C). Thus, this modeling process allows us to manage our current limitations in

biostratigraphic resolution and dampens the effects of variation between different conodont biozonation schemes.

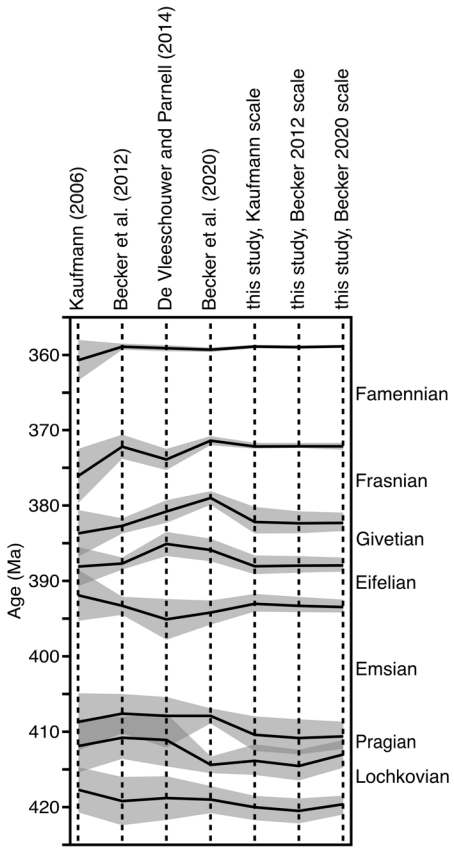

Figure 3.8. Comparison between stage boundary ages and uncertainties from this work and the previous literature. The vertical dashed lines represent a time scale, and the thick black lines represent the stage boundary age for each reference. The gray shaded region represents the stage boundary age uncertainty.

Age-Depth Modeling and Future Time Scale Work

The ultimate goal of time scale modeling should be to produce an objective and reproducible time scale given the available data, not one that underestimates uncertainty for the sake of "improving" stage boundary ages by making them more precise without accompanying improvements in accuracy. Our age-depth models produced calibrated stage boundary ages with uncertainties ranging from 0.19 to 2.49 m.y. (Table 3.6.), which quantitatively convolved both geochronologic and stratigraphic uncertainty. The

calibrated stage boundary ages with the highest uncertainty and the portions of the age-depth model with the widest 95% highest density interval signal areas of the time scale to target for future work. For example, the ages of the bases of the Lochkovian, Pragian, and Emsian Stages have relatively high uncertainty that has not changed significantly with these new models (Figure 3.8.), largely because of the poor biostratigraphic control on radioisotopic ages. Nonetheless, the time scales derived from this study generally show more similarity to each other than they do to previous time scales or than previous time scales do to each other (Figure 3.8.).

Apart from creating newly calibrated time scales, this modeling process also prompted us to reflect on the quality of our model inputs. For example, radioisotopic ages D10–D12 have large stratigraphic and age uncertainties, and thus the model 95% highest density interval only slightly constricts at those events, since there is a large spread in positions that the algorithm can select to represent those events (Figure 3.9.). Better age precision may be achieved by redating some of these volcanic layers, but our ability to decrease relative stratigraphic uncertainty in our modeling may be limited by the actual lack of biotic variability during certain stages, particularly the Emsian (Brett et al., 2020). By contrast, the radioisotopic ages and conodont biozone assignments for D16–D18 are tightly constrained, so much so that the conodont zonal boundaries are within the resolution of the uncertainty on the radioisotopic ages, and the model 95% highest density interval in the Frasnian near D16–D18 is much more restricted than that in the Pragian and early Emsian near D10–D12 (Figure 3.9.). Further, the median of the age-depth model near D16–D18 requires a significant shift during the linearization process for the Kaufmann (2006) and Becker et al. (2012) models, showing that for those models,

tightly constrained radioisotopic ages can indicate where the time scale most strongly diverges from scaling with numerical time (Figure 3.5.).

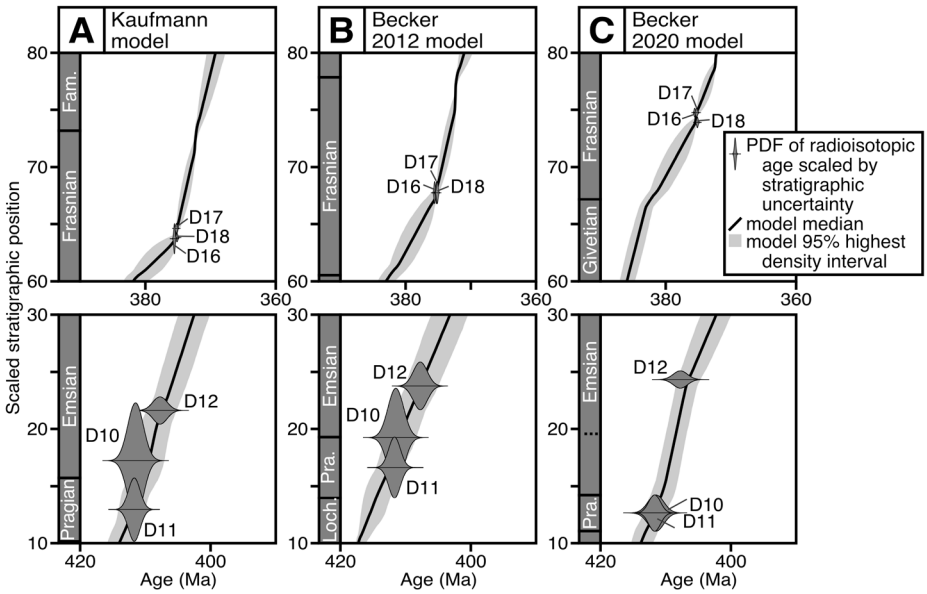

Figure 3.9. Age-depth model results for the (A) Kaufmann model, (B) Becker et al. (2012) model, and (C) Becker et al. (2020) model highlighting radioisotopic ages D16–D18 (top panels) and D10–D12 (bottom panels). Radioisotopic ages are shown as horizontally mirrored probability density functions (PDFs), where the height of the PDF is scaled to the uncertainty in stratigraphic position for that age. Fam—Famennian; Loch—Lochkovian; Pra—Pragian.

The age-depth models also reveal shortcomings in the astrochronology ages input into the model. For the anchored astrochronology ages of the Middle and Late Devonian, the further they are extrapolated from their anchor point, generally the greater is the offset between the astrochronology age input and the linearized model position of that astrochronology age. For example, the astrochronology durations anchored on A-D14 and A-D15, the Tioga K-bentonites, have increasing horizontal offset from the linearized model with increasing scaled stratigraphic position (Figure 3.5.). This suggests that the astrochronology durations that are chained together to create extrapolated anchored astrochronology ages are systematically too short. This appears to indicate the potential

for hiatuses and a bias for undercounting cycles, although there could be further issues of extrapolation and correlation to biotic events. Future work should target sections that contain global stage markers and/or completely span stages and include interspersed dateable volcanic layers.

Conclusions

(1) The Devonian time scale was improved in this work by dating key K-bentonites with greater precision and accuracy. The U-Pb zircon age of the Emsian Hercules I K-bentonite is 394.290 ± 0.097(0.21)[0.47] Ma. The ages of the Eifelian Tioga B and Tioga F K-bentonites are 390.82 ± 0.18(0.26)[0.48] Ma and 390.14 ± 0.14(0.23)[0.47] Ma, respectively.

(2) A Bayesian age-depth modeling process managed the dissimilarities of different starting conodont biozonation schemes, incorporated radioisotopic ages, and integrated floating astrochronology durations to produce a robust calibration of the Devonian time scale. The age-depth models can be linearized to create a time scale scaled by numeric time, creating a time scale that is a useful template on which to contextualize and understand climatic, biotic, and stratigraphic proxies. These methods can be applied to improve the time scale for other periods, as well.

(3) The three linearized time scales (one for each starting conodont biozonation scheme) are remarkably similar, demonstrating that a probabilistic model can account for the differences in starting biostratigraphic scales, and lending confidence to the stage boundary ages produced by this modeling.

(4) The Bayesian age-depth models for the Kaufmann (2006) and Becker et al. (2012) scales show the most divergence from linearity during the Frasnian, suggesting that

the prior biostratigraphic scales were most disassociated from the numerical time scale during that stage. By comparison, the Becker et al. (2020) model more closely matches linearity during the Frasnian, indicating that Frasnian modifications to the Becker et al. (2020) conodont biozonation scheme created a better match to numerical time. This shows how the process of Bayesian age-depth modeling is helpful in evaluating modifications to conodont biozonation schemes, and it demonstrates an approach for linking and comparing previously disconnected data sets.

(5) Bayesian age-depth modeling can inform targets for future time scale work. Our models demonstrate that the Devonian time scale would benefit from additional work refining the ages of the bases of the Lochkovian, Pragian, and Emsian Stages by acquiring radioisotopic ages with better stratigraphic position control. Currently dated volcanic layers from the Pragian and early Emsian generally have significant uncertainty and therefore exert minimal influence on the model, so future work could redate these volcanic layers with increased precision or seek out similarly positioned volcanic layers to add to the time scale.

REFERENCES

Aleinikoff, J.N., Wintsch, R.P., Tollo, R.P., Unruh, D.M., Fanning, C.M., and Schmitz, M.D., 2007, Ages and origins of rocks of the Killingworth dome, south-central Connecticut: Implications for the tectonic evolution of southern New England: American Journal of Science, v. 307, p. 63–118, https://doi.org/10.2475/01.2007.04.

Algeo, T.J., and Scheckler, S.E., 2010, Land plant evolution and weathering rate changes in the Devonian: Journal of Earth Science, v. 21, p. 75–78, https://doi.org/10.1007/ s12583-010-0173-2.

Aretz, M., Herbig, H.G., Wang, X.D., Gradstein, F.M., Agterberg, F.P., and Ogg, J.G., 2020, Chapter 23 – The Carboniferous Period, in Gradstein, F.M., Ogg, J.G., Schmitz, M.D., and Ogg, G.M., eds., Geologic Time Scale 2020: Amsterdam, Netherlands, Elsevier, p. 811–874, https://doi.org/10.1016/B978-0-12-824360-2.00023-1.

Armstrong, R.L., Taubeneck, W.H., and Hales, P.O., 1977, Rb-Sr and K-Ar geochronometry of Mesozoic granitic rocks and their Sr isotopic composition, Oregon, Washington, and Idaho: GSA Bulletin, v. 88, p. 397–411, https://doi.org/10.1130/0016-7606(1977)88<397:rakgom>2.0.co;2.

Averbuch, O., Tribovillard, N., De Vleeschouwer, X., Riquier, L.,Mistiaen,B.,andVliet-Lanoe,B.V.,2005,Mountain building–enhanced continental weathering and organic carbon burial as major causes for climatic cooling at the Frasnian-Famennian boundary (c. 376 Ma)?: Terra Nova, v. 17, p. 25–34, https://doi.org/10.1111/j.13653121.2004.00580.x.

Axen, G.J., Wijk, J.W. van, and Currie, C.A., 2018, Basal continental mantle lithosphere displaced by flat-slab subduction: Nature Geoscience, v. 11, p. 961–964, https://doi.org/10.1038/s41561-018-0263-9.

Bachmann, F., Hielscher, R., and Schaeben, H., 2010, Texture Analysis with MTEX – Free and Open Source Software Toolbox: Solid State Phenomena, v. 160, p. 63–68.

Baresel, B., Bucher, H., Brosse, M., Cordey, F., Guodun, K., and Schaltegger, U., 2017, Precise age for the PermianTriassic boundary in South China from high-precision U-Pb geochronology and Bayesian age-depth modeling: Solid Earth, v. 8, p. 361–378, https://doi.org/10.5194/ se-8-361-2017.

Bartley, J.M., Glazner, A.F., and Coleman, D.S., 2018, Dike intrusion and deformation during growth of the Half Dome pluton, Yosemite National Park, California: Geosphere, v. 14, p. 1283 1297, https://doi.org/10.1130/ges01458.1.

Becker, R.T., Gradstein, F.M., and Hammer, O., 2012, Chapter 22 – The Devonian Period, in Gradstein, F.M., Ogg, J.G., Schmitz, M.D., and Ogg, G.M., eds., The Geologic Time Scale 2012: Amsterdam, Netherlands, Elsevier BV, p. 559–601, https://doi.org/10.1016/B978-0- 444-59425-9.00022-6.

Becker, R.T., Marshall, J.E.A., Da Silva, A.-C., Agterberg, F.P., Gradstein, F.M., and Ogg, J.G., 2020, Chapter 22 – The Devonian Period, in Gradstein, F.M., Ogg, J.G., Schmitz, M.D., and Ogg, G.M., eds., Geologic Time Scale 2020: Amsterdam, Netherlands, Elsevier, p. 733–810, https://doi.org/10.1016/B978-0-12-824360-2.00022-X.

Benford, B., Crowley, J., Schmitz, M.D., Northrup, C.J., and Tikoff, B., 2010, Mesozoic magmatism and deformation in the northern Owyhee Mountains, Idaho: Implications for along-zone variations for the western Idaho shear zone: Lithosphere, v. 2, p. 93–118, https://doi.org/10.1130/l76.1.

Blaauw, M., Christen, J.A., Bennett, K.D., and Reimer, P.J., 2018, Double the dates and go for Bayes—Impacts of model choice, dating density and quality on chronologies: Quaternary Science Reviews, v. 188, p. 58–66, https://doi.org/10.1016/j.quascirev.2018.03.032.

Black, L.P., et al., 2004, Improved $^{206}Pb/^{238}U$ microprobe geochronology by the monitoring of a trace-element-related matrix effect; SHRIMP, ID–TIMS, ELA–ICP–MS and oxygen isotope documentation for a series of zircon standards: Chemical Geology, v. 205, p. 115–140, https://doi.org/10.1016/j.chemgeo.2004.01.003.

Bodorkos, S., Pogson, D., and Friedman, R., 2017, Zircon U-Pb dating of biostratigraphically constrained felsic volcanism in the Lachlan orogen via SHRIMP and CAIDTIMS: Implications for the division of Early Devonian time [abs.], *in* Vearncombe, J., ed., Bulletin No. 65: Granites2017@Benalla: Australia, Australian Institute of Geoscientists, p. 11–14.

Bonamici, C.E., and Blum, T.B., 2020, Reconsidering initial Pb in titanite in the context of in situ dating: American Mineralogist, v. 105, p. 1672–1685, https://doi.org/10.2138/am-2020-7274.

Bonamici, C.E., Fanning, C.M., Kozdon, R., Fournelle, J.H., and Valley, J.W., 2015, Combined oxygen-isotope and U-Pb zoning studies of titanite: New criteria for age preservation: Chemical Geology, v. 398, p. 70 84, https://doi.org/10.1016/j.chemgeo.2015.02.002.

Braudy, N., Gaschnig, R.M., Wilford, D.E., Vervoort, J.D., Nelson, C.L., Davidson, C., Kahn, M.J., and Tikoff, B., 2017, Timing and deformation conditions of the western Idaho shear zone, West Mountain, west-central Idaho: Lithosphere, v. 9, p. 157–183, https://doi.org/10.1130/l519.1.

Brett, C.E., and Ver Straeten, C.A., 1994, Stratigraphy and facies relationships of the Eifelian Onondaga Limestone (Middle Devonian) in western and west central New York State, *in* Brett, C.E., and Scatterday, J., eds., 66th Annual Meeting Guidebook: Rochester, New York, New York State Geological Association, p. 221–269.

Brett, C.E., Zambito, J.J., McLaughlin, P.I., and Emsbo, P., 2020, Revised perspectives on Devonian biozonation and environmental volatility in the wake of recent timescale revisions: Palaeogeography, Palaeoclimatology, Palaeoecology, v. 549, 108843, https://doi.org/10.1016/ j.palaeo.2018.06.037.

Brocke, R., Fatka, O., Lindemann, R.H., Schindler, E., and Ver Straeten, C.A., 2016, Palynology, 143racryoconarids and the lower Eifelian (Middle Devonian) basal Chotec event: Case studies from the Prague and Appalachian Basins, *in* Becker, R.T., Königshof, P., and Brett, C.E., eds., Devonian Climate, Sea Level and Evolutionary Events: Geological Society [London] Special Publication 423, p. 123–169, https://doi.org/10.1144/SP423.8.

Carls, P., Slavík, L., and Valenzuela-Ríos, J.I., 2007, Revisions of conodont biostratigraphy across the Silurian-Devonian boundary: Bulletin of Geosciences, v. 82, p. 145–164, https://doi.org/10.3140/bull.geosci.2007.02.145.

Coleman, D.S., Gray, W., and Glazner, A.F., 2004, Rethinking the emplacement and evolution of zoned plutons: Geochronologic evidence for incremental assembly of the Tuolumne Intrusive Suite, California: Geology, v. 32, p. 433-435, https://doi.org/10.1130/g20220.1.

Condon, D.J., Schoene, B., McLean, N.M., Bowring, S.A., and Parrish, R.R., 2015, Metrology and traceability of U-Pb isotope dilution geochronology (EARTHTIME tracer calibration Part I): Geochimica et Cosmochimica Acta, v. 164, p. 464–480, https://doi.org/10.1016/ j.gca.2015.05.026.

Corfu, F., Hanchar, J.M., Hoskin, P.W.O., and Kinny, P., 2003, Atlas of Zircon Textures: Reviews in Mineralogy and Geochemistry, v. 53, p. 469–500, https://doi.org/10.2113/0530469.

Corradini, C., and Corriga, M.G., 2012, A Přídolí–Lochkovian conodont zonation in Sardinia and the Carnic Alps: implications for a global zonation scheme: Bulletin of Geosciences, v. 87, p. 635–650, https://doi.org/10.3140/bull.geosci.1304.

Cramer, B.D., Schmitz, M.D., Huff, W.D., and Bergström, S.M., 2014, High-precision U-Pb zircon age constraints on the duration of rapid biogeochemical events during the Ludlow Epoch (Silurian Period): Journal of the Geological Society [London], v. 172, p. 157–160, https://doi.org/10.1144/jgs2014-094.

Criss, R.E., and Fleck, R.J., 1987, Petrogenesis, geochronology, and hydrothermal systems of the northern Idaho batholith and adjacent areas based on 18O/16O, D/H, $^{87}Sr/^{86}Sr$, K-Ar, and $^{40}Ar/^{39}Ar$ studies, *in* Vallier, T.L. and Brooks, H.C. eds., Geology of the Blue Mountains region of Oregon, Idaho, and Washington: The Idaho batholith and its border zone, U.S. Geological Survey Professional Paper 1436, p. 95–138.

Da Silva, A.-C., Hladil, J., Chadimová, L., Slavík, L., Hilgen, F.J., Bábek, O., and Dekkers, M.J., 2016, Refining the Early Devonian time scale using Milankovitch cyclicity in Lochkovian–Pragian sediments (Prague Synform, Czech Republic): Earth and Planetary Science Letters, v. 455, p. 125–139, https://doi.org/10.1016/j.epsl.2016.09.009.

Da Silva, A.-C., Sinnesael, M., Claeys, P., Davies, J.H.F.L., de Winter, N.J., Percival, L.M.E., Schaltegger, U., and Vleeschouwer, D.D., 2020, Anchoring the Late Devonian mass extinction in absolute time by integrating climatic controls and radio-isotopic dating: Scientific Reports, v. 10, 12940, https://doi.org/10.1038/s41598020-69097-6.

Davenport, K.K., Hole, J.A., Tikoff, B., Russo, R.M., and Harder, S.H., 2017, A strong contrast in crustal architecture from accreted terranes to craton, constrained by controlled-source seismic data in Idaho and eastern Oregon: Lithosphere, v. 9, p. 325–340, https://doi.org/10.1130/l553.1.

Davis, D.W., Williams, I.S., and Krogh, T.E., 2003, Historical Development of Zircon Geochronology: Reviews in Mineralogy and Geochemistry, v. 53, p. 145–181, https://doi.org/10.2113/0530145.

Davis, J.R., and Giorgis, S., 2014, An inverse approach to constraining strain and vorticity using rigid clast shape preferred orientation data: Journal of Structural Geology, v. 68, p. 337–346, https://doi.org/10.1016/j.jsg.2014.05.027.

Davydov, V., Schmitz, M.D., and Korn, D., 2011, The Hangenberg Event was abrupt and short at the global scale; the quantitative intergration and intercalibration of biotic and geochronologic data within the Devonian-Carboniferous transition: Geological Society of America Abstracts with Programs, v. 43, no. 5, p. 128, https://gsa.confex.com/gsa/2011AM/webprogram/Paper195211.html.

Davydov, V.I., Crowley, J.L., Schmitz, M.D., and Poletaev, V.I., 2010, High-precision U-Pb zircon age calibration of the global Carboniferous time scale and Milankovitch band cyclicity in the Donets Basin, eastern Ukraine: Geochemistry Geophysics Geosystems, v. 11, Q0AA04, https://doi.org/10.1029/2009GC002736.

Davydov, V.I., Korn, D., and Schmitz, M.D., 2012, Chapter 23 – The Carboniferous Period, in Gradstein, F.M., Ogg, J.G., Schmitz, M.D., and Ogg, G.M., eds., The Geologic Time Scale 2012, Elsevier BV, p. 603–651, https://doi.org/10.1016/B978-0-444-59425-9.00023-8.

De Saint Blanquat, M., and Tikoff, B., 1997, Development of Magmatic to Solid-State Fabrics during Syntectonic Emplacement of the Mono Creek Granite, Sierra Nevada Batholith, *in* Bouchez, J.L. et al., eds., Granite: From Segregation of Melt to Emplacement Fabrics, Netherlands, Kluwer Academic Publishers, p. 231–252, https://doi.org/10.1007/978-94-017-1717-5_15.

De Saint Blanquat, M., Tikoff, B., Teyssier, C., and Vigneresse, J.L., 1998, Transpressional kinematics and magmatic arcs: Geological Society, London, Special Publications, v. 135, p. 327–340, https://doi.org/10.1144/gsl.sp.1998.135.01.21.

De Vleeschouwer, D., and Parnell, A.C., 2014, Reducing time-scale uncertainty for the Devonian by integrating astrochronology and Bayesian statistics: Geology, v. 42, p. 491–494, https://doi.org/10.1130/ G35618.1.

De Vleeschouwer, D., Boulvain, F., Da Silva, A.-C., Pas, D., Labaye, C., and Claeys, P.F., 2013a, The astronomical calibration of the Givetian (Middle Devonian) time scale (Dinant synclinorium, Belgium): San Francisco, California, American Geophysical Union, Fall Meeting supplement, abstract GP43A–1184.

De Vleeschouwer, D., Boulvain, F., Da Silva, A.-C., Pas, D., Labaye, C., and Claeys, P., 2015, The astronomical calibration of the Givetian (Middle Devonian) time scale (Dinant synclinorium, Belgium): Geological Society [London] Special Publication 414, p. 245–256, https:// doi.org/10.1144/SP414.3.

De Vleeschouwer, D., Boulvain, F., Da Silva, A.-C., Pas, D., Labaye, C., and Claeys, P., 2014, The astronomical calibration of the Givetian (Middle Devonian) time scale (Dinant Synclinorium, Belgium): Geological Society of London, Special Publications, v. 414,
p. 245–256, https://doi.org/10.1144/SP414.3.

De Vleeschouwer, D., Königshof, P., and Claeys, P., 2018, Reading time and paleoenvironmental change in the Emsian–Eifelian boundary GSSP section (Wetteldorf, Germany): A combination of cyclostratigraphy and facies analysis: Newsletters on Stratigraphy, v. 51, p. 209–226,
https://doi.org/10.1127/nos/2017/0397.

De Vleeschouwer, D., Rakociński, M., Racki, G., Bond, D.P.G., Sobień, K., and Claeys, P., 2013b, The astronomical rhythm of Late Devonian climate change (Kowala section, Holy Cross Mountains, Poland): Earth and Planetary Science Letters, v. 365, p. 25–37, https:// doi.org/10.1016/j.epsl.2013.01.016.

De Vleeschouwer, D., Whalen, M.T., Day, J.E., and Claeys, P., 2012, Cyclostratigraphic calibration of the Frasnian (Late Devonian) time scale (western Alberta, Canada): Geological Society of America Bulletin, v. 124, p. 928– 942,
https://doi.org/10.1130/B30547.1.

El Korh, A., Schmidt, S.T., Ulianov, A., and Potel, S., 2009, Trace Element Partitioning in HP–LT Metamorphic Assemblages during Subduction-related Metamorphism, Ile de Groix, France: a Detailed LA-ICPMS Study: Journal of Petrology, v. 50, p. 1107–1148, https://doi.org/10.1093/petrology/egp034.

Ellwood, B.B., El Hassani, A., Tomkin, J.H., and Bultynck, P., 2015, A climate-driven model using time-series analysis of magnetic susceptibility (χ) datasets to represent a floating-point high-resolution geological timescale for the Middle Devonian Eifelian Stage: Geological Society [London] Special Publication 414, p. 209–223, https://doi.org/10.1144/SP414.4.

Ellwood, B.B., Tomkin, J.H., Hassani, A.E., Bultynck, P., Brett, C.E., Schindler, E., Feist, R., and Bartholomew, A.J., 2011, A climate-driven model and development of a floating point time scale for the entire Middle Devonian Givetian Stage: A test using magnetostratigraphy susceptibility as a climate proxy: Palaeogeography, Palaeoclimatology, Palaeoecology, v. 304, p. 85–95, https://doi.org/10.1016/j.palaeo.2010.10.014.

Ernst, R.E., Rodygin, S.A., and Grinev, O.M., 2020, Age correlation of large igneous provinces with Devonian biotic crises: Global and Planetary Change, v. 185, 103097, https://doi.org/10.1016/j.gloplacha.2019.103097.

Fitch, T.J., 1972, Plate convergence, transcurrent faults, and internal deformation adjacent to Southeast Asia and the western Pacific: Journal of Geophysical Research, v. 77, p. 4432–4460.

Fleck, R.J., and Criss, R.E., 1985, Strontium and oxygen isotope variations in Mesozoic and Tertiary plutons of central Idaho: Contributions to Mineralogy and Petrology, v. 90, p. 291–308, https://doi.org/10.1007/bf00378269.

Fleck, R.J., and Criss, R.E., 1988, Location, Age, and Tectonic Significance of the Western Idaho Suture Zone (WISZ) and its Relation to the Idaho Batholith: Abstracts with Programs – Geological Society of America, v. 20, p. 414.

Frost, R.B., Chamberlain, K.R., and Schumacher, J.C., 2000, Sphene (titanite): phase relations and role as a geochronometer: Chemical Geology, v. 172, p. 131–148, https://doi.org/10.1016/s0009-2541(00)00240-0.

Garber, J.M., Hacker, B.R., Kylander-Clark, A.R.C., Stearns, M.A., and Seward, G., 2017, Controls on Trace Element Uptake in Metamorphic Titanite: Implications for Petrochronology: Journal of Petrology, v. 58, p. 1031–1058, https://doi.org/10.1093/petrology/egx046.

Gaschnig, R.M., Vervoort, J.D., Lewis, R.S., and McClelland, W.C., 2010, Migrating magmatism in the northern US Cordillera: in situ U–Pb geochronology of the Idaho batholith: Contributions to Mineralogy and Petrology, v. 159, p. 863–883, https://doi.org/10.1007/s00410-009-0459-5.

Gaschnig, R.M., Vervoort, J.D., Lewis, R.S., and Tikoff, B., 2011, Isotopic Evolution of the Idaho Batholith and Challis Intrusive Province, Northern US Cordillera: Journal of Petrology, v. 52, p. 2397 2429, https://doi.org/10.1093/petrology/egr050.

Gaschnig, R.M., Vervoort, J.D., Tikoff, B., and Lewis, R.S., 2017, Construction and preservation of batholiths in the northern U.S. Cordillera: Lithosphere, v. 9, p. 315–324, https://doi.org/10.1130/l497.1.

Getty, S.R., and Gromet, L.P., 1992, Geochronological constraints on ductile deformation, crustal extension, and doming about a basement-cover boundary, New England Appalachians: American Journal of Science, v. 292, p. 359–397, https://doi.org/10.2475/ajs.292.6.359.

Getty, S.R., Selverstone, J., Wernicke, B.P., Jacobson, S.B., Aliberti, E., and Lux, D.R., 1993, Sm-Nd dating of multiple garnet growth events in an arc-continent collision zone, northwestern U.S. Cordillera: Contributions to Mineralogy and Petrology, v. 115, p. 45–57.

Gillerman, V.S., Schmitz, M.D., Benowitz, J.A., and Layer, P.W., 2019, Geology and Temporal Evolution of Alteration and Au-Sb-W Mineralization, Stibnite Mining District, Idaho: Idaho Geological Survey Bulletin 31, 163 p.

Giorgis, S., and Tikoff, B., 2004, Constraints on kinematics and strain from feldspar porphyroclast populations: Geological Society, London, Special Publications, v. 224, p. 265 285, https://doi.org/10.1144/gsl.sp.2004.224.01.17.

Giorgis, S., McClelland, W., Fayon, A., Singer, B.S., and Tikoff, B., 2008, Timing of deformation and exhumation in the western Idaho shear zone, McCall, Idaho: Geological Society of America Bulletin, v. 120, p. 1119–1133, https://doi.org/10.1130/b26291.1.

Giorgis, S., Tikoff, B., and McClelland, W.C., 2005, Missing Idaho arc: Transpressional modification of the $^{87}Sr/^{86}Sr$ transition on the western edge of the Idaho batholith: Geology, v. 33, p. 469 4, https://doi.org/10.1130/g20911.1.

Gordon, G.W., Rockman, M., Turekian, K.K., and Over, J., 2009, Osmium isotopic evidence against an impact at the Frasnian-Famennian boundary: American Journal of Science, v. 309, p. 420–430, https://doi .org/10.2475/05.2009.03.

Gordon, S.M., Kirkland, C.L., Reddy, S.M., Blatchford, H.J., Whitney, D.L., Teyssier, C., Evans, N.J., and McDonald, B.J., 2021, Deformation-enhanced recrystallization of titanite drives decoupling between U-Pb and trace elements: Earth and Planetary Science Letters, v. 560, p. 116810, https://doi.org/10.1016/j.epsl.2021.116810.

Gradstein, F.M., Ogg, J.G., Schmitz, M.D., and Ogg, G.M., eds., 2012, Geologic Time Scale 2012: Amsterdam, Netherlands, Elsevier, 1176 p., https://doi.org/10.1016/c2011-1-08249-8.

Gradstein, F.M., Ogg, J.G., Schmitz, M.D., and Ogg, G.M., eds., 2020, Geologic Time Scale 2020: Amsterdam, Netherlands, Elsevier, 1390 p., https://doi.org/10.1016/c2020-1-02369-3.

Gray, K.D., Watkinson, A.J., Gaschnig, R.M., and Isakson, V.H., 2012, Age and structure of the Crevice pluton: overlapping orogens in west-central Idaho? Canadian Journal of Earth Sciences, v. 49, p. 709–731, https://doi.org/10.1139/e2012-016.

Hamilton, W., 1963, Overlapping of Late Mesozoic Orogens in Western Idaho: GSA Bulletin, v. 74, p. 779–787, https://doi.org/10.1130/0016-7606(1963)74[779:oolmoi]2.0.co;2.

Hartnady, M.I.H., Kirkland, C.L., Clark, C., Spaggiari, C.V., Smithies, R.H., Evans, N.J., and McDonald, B.J., 2019, Titanite dates crystallization: Slow Pb diffusion during super-solidus re-equilibration: Journal of Metamorphic Geology, v. 37, p. 823–838, https://doi.org/10.1111/jmg.12489.

Haslett, J., and Parnell, A.C., 2008, A simple monotone process with application to radiocarbon-dated depth chronologies: Applied Statistics, v. 57, p. 399–418, https://doi.org/10.1111/j.1467-9876.2008.00623.x.

Hayden, L.A., Watson, E.B., and Wark, D.A., 2008, A thermobarometer for sphene (titanite): Contributions to Mineralogy and Petrology, v. 155, p. 529–540, https://doi.org/10.1007/s00410-007-0256-y.

Hildebrand, R.S., and Whalen, J.B., 2014, Arc and Slab-Failure Magmatism in Cordilleran Batholiths II – The Cretaceous Peninsular Ranges Batholith of Southern and Baja California: Geoscience Canada, v. 41, p. 399–458, http://doi.org/10.12789/geocanj.2014.41.059.

Holder, R.M., Hacker, B.R., Seward, G.G.E., and Kylander-Clark, A.R.C., 2019, Interpreting titanite U–Pb dates and Zr thermobarometry in high-grade rocks: empirical constraints on elemental diffusivities of Pb, Al, Fe, Zr, Nb, and Ce: Contributions to Mineralogy and Petrology, v. 174, p. 1–19, https://doi.org/10.1007/s00410-019-1578-2.

House, M.R., 1995, Devonian precessional and other signatures for establishing a Givetian timescale, *in* House, M.R., and Gale, A.S., eds., Orbital Forcing Timescales and Cyclostratigraphy: Geological Society [London] Special Publication 85, p. 37–49, https://doi .org/10.1144/GSL.SP.1995.085.01.03.

House, M.R., 2002, Strength, timing, setting and cause of mid-Palaeozoic extinctions: Palaeogeography, Palaeoclimatology, Palaeoecology, v. 181, p. 5–25, https://doi .org/10.1016/S0031-0182(01)00471-0.

House, M.R., and Gradstein, F.M., 2004, The Devonian Period, *in* Ogg, J.G., Gradstein, F.M., and Smith, A.G., eds., A Geologic Time Scale 2004: Cambridge, UK, Cambridge University Press, p. 202–221, https://doi.org/10.1017/CBO9780511536045.015.

Housh, T., and Bowring, S.A., 1991, Lead isotopic heterogeneities within alkali feldspars: Implications for the determination of initial lead isotopic compositions: Geochimica et Cosmochimica Acta, v. 55, p. 2309–2316, https://doi.org/10.1016/0016-7037(91)90106-f.

Husson, J.M., Schoene, B., Bluher, S., and Maloof, A.C., 2016, Chemostratigraphic and U-Pb geochronologic constraints on carbon cycling across the Silurian-Devonian boundary: Earth and Planetary Science Letters, v. 436, p. 108–120, https://doi.org/10.1016/ j.epsl.2015.11.044.

Hutton, D.H.W., Dempster, T.J., Brown, P.E., and Becker, S.D., 1990, A new mechanism of granite emplacement: Intrusion in active extensional shear zones: Nature, v. 343, p. 452–455.

Jaffey, A.H., Flynn, K.F., Glendenin, L.E., Bentley, W.T., and Essling, A.M., 1971, Precision measurement of half-lives and specific activities of ^{235}U and ^{238}U: Physical Review C, v. 4, p. 1889–1906.

Kaufmann, B., 2006, Calibrating the Devonian Time Scale: A synthesis of U–Pb ID–TIMS ages and conodont stratigraphy: Earth-Science Reviews, v. 76, p. 175 190, http://doi.org/10.1016/j.earscirev.2006.01.001.

Kaufmann, B., Trapp, E., Mezger, K., and Weddige, K., 2005, Two new Emsian (Early Devonian) U-Pb zircon ages from volcanic rocks of the Rhenish Massif (Germany): Implications for the Devonian time scale: Journal of the Geological Society [London], v. 162, p. 363–371, https://doi.org/10.1144/0016-764904-012.

Kennedy, A.K., Wotzlaw, J.-F., Schaltegger, U., Crowley, J.L., and Schmitz, M., 2014, Eocene zircon reference material for microanalysis of U-Th-Pb isotopes and trace elements: The Canadian Mineralogist, v. 52, p. 409–421, https://doi.org/10.3749/canmin.52.3.409.

Kiessling, W., 2008, Sampling-standardized expansion and collapse of reef building in the Phanerozoic: Fossil Record (Weinheim), v. 11, p. 7–18, https://doi .org/10.5194/fr-11-7-2008.

Kiessling, W., and Simpson, C., 2011, On the potential for ocean acidification to be a general cause of ancient reef crises: Global Change Biology, v. 17, p. 56–67, https:// doi.org/10.1111/j.1365-2486.2010.02204.x.

Klapper, G., 1971, Sequence within the conodont genus *Polygnathus* in the New York lower Middle Devonian: Geologica et Palaeontologica, v. 5, p. 59–79.

Klapper, G., 1981, Review of New York Devonian conodont biostratigraphy, *in* Oliver, W.A., Jr., and Klapper, G., eds., Devonian Biostratigraphy of New York: Binghampton, New York, International Union of Geological Sciences Subcommission on Devonian Stratigraphy, p. 57–66.

Klapper, G., and Oliver, W.A., Jr., 1995, The Detroit River Group is Middle Devonian: Discussion on "Early Devonian age of the Detroit River Group, inferred from Arctic stromatoporoids": Canadian Journal of Earth Sciences, v. 32, p. 1070–1073, https://doi.org/10.1139/ e95-088.

Klapper, G., Ziegler, W., and Mashkova, T.V., 1978, Conodonts and correlation of Lower-Middle Devonian boundary beds in the Barrandian area of Czechoslovakia: Geologica et Palaeontologica, v. 12, p. 103–116.

Kohn, M.J., 2017, Titanite Petrochronology: Reviews in Mineralogy and Geochemistry, v. 83, p. 419–441, https://doi.org/10.2138/rmg.2017.83.13.

Krogh, T.E., 1973, A low-contamination method for hydrothermal decomposition of zircon and extraction of U and Pb for isotopic age determinations: Geochimica et Cosmochimica Acta, v. 37, p. 485–494, https://doi .org/10.1016/0016-7037(73)90213-5.

Kuntz, M.A., 2007, The Idaho Batholith near McCall, Idaho—Field Relations, Petrology, Major-Element Chemistry, Emplacement History, and Magma Genesis, *in* Kuntz, M.A. and Snee, L.W. eds., Geological Studies of the Salmon River Suture Zone and Adjoining Areas, West-Central Idaho and Eastern Oregon, p. 123–161.

Lanik, A., Over, D.J., Schmitz, M., and Kirchgasser, W.T., 2016, Testing the limits of chronostratigraphic resolution in the Appalachian Basin, Late Devonian (middle Frasnian), eastern North America: New U-Pb zircon dates for the Belpre Tephra suite: Geological Society of America Bulletin, v. 128, p. 1813–1821, https://doi.org/10.1130/B31408.1.

Lewis, R.S., Kiilsgaard, T.H., Bennett, E.H., and Hall, W.E., 1987, Lithologic and chemical characteristics of the central and southeastern part of the southern lobe of the Idaho Batholith, *in* Vallier, T.L. and Brooks, H.C. eds., Geology of the Blue Mountains region of Oregon, Idaho, and Washington; the Idaho batholith and its border zone, U.S. Geological Survey Professional Paper 1436, p. 171–196.

Ludwig, K.R., 1998, On the treatment of concordant uranium-lead ages: Geochimica et Cosmochimica Acta, v. 62, p. 665–676.

Lund, K., 1995, Metamorphic and structural development of island-arc rocks in the Slate Creek-John Day Creek area, west-central Idaho, *in* Vallier, T.L. and Brooks, H.C. eds., Geology of the Blue Mountains Region of Oregon, Idaho, and Washington: Petrology and Tectonic Evolution of Pre-Tertiary Rocks of the Blue Mountains Region, v. U.S. Geological Survey Professional Paper 1438, p. 517–540.

Lund, K., 2021, Geology of the Payette National Forest and Vicinity, West-Central Idaho: U.S. Geological Survey Professional Paper 1666, 89 p., https://doi.org/10.3133/i2765.

Lund, K., and Snee, L.W., 1988, Metamorphism, structural development, and age of the continent-island arc juncture in west-central Idaho, *in* Ernst, W.G. ed., Metamorphism and Crustal Evolution of the Western United States, Englewood Cliffs, NJ, Prentice-Hall, Rubey, v. 7, p. 296–331.

Ma, C., Foster, D.A., Mueller, P.A., and Dutrow, B.L., 2017, Magma-facilitated transpressional strain partitioning within the Sawtooth metamorphic complex, Idaho: A zone accommodating Cretaceous orogen-parallel translation in the Idaho batholith: Tectonics, v. 36, p. 444–465, https://doi.org/10.1002/2016tc004264.

Ma, C., Foster, D.A., Mueller, P.A., Dutrow, B.L., and Marsh, J., 2021, Mesozoic crustal melting and metamorphism in the U.S. Cordilleran hinterland: Insights from the Sawtooth metamorphic complex, central Idaho: GSA Bulletin, https://doi.org/10.1130/b35837.1.

Ma, K., Hinnov, L.A., Zhang, X., and Gong, Y., 2020, Astronomical time calibration of the Upper Devonian Lali section, South China: Global and Planetary Change, v. 193, p. 103267, https://doi.org/10.1016/j.gloplacha.2020.103267.

Macdonald, F.A., Schmitz, M.D., Strauss, J.V., Halverson, G.P., Gibson, T.M., Eyster, A., Cox, G., Mamrol, P., and Crowley, J.L., 2018, Cryogenian of Yukon: Precambrian Research, v. 319, p. 114–143, https://doi.org/10.1016/j.precamres.2017.08.015.

Manduca, C.A., Kuntz, M.A., and Silver, L.T., 1993, Emplacement and deformation history of the western margin of the Idaho batholith near McCall, Idaho: Influence of a major terrane boundary: Geological Society of America Bulletin, v. 105, p. 749–765, https://doi.org/10.1130/0016-7606(1993)105<0749:eadhot>2.3.co;2.

Manduca, C.A., Silver, L.T., and Taylor, H.P., 1992, $^{87}Sr/^{86}Sr$ and $^{18}O/^{16}O$ isotopic systematics and geochemistry of granitoid plutons across a steeply-dipping boundary between contrasting lithospheric blocks in western Idaho: Contributions to Mineralogy and Petrology, v. 109, p. 355–372, https://doi.org/10.1007/bf00283324.

Manduca, C.C.A., 1988, Geology and geochemistry of the oceanic arc-continent boundary in the western Idaho Batholith near McCall [Ph.D. thesis]: California Institute of Technology, 272 p.

Mattinson, J.M., 2005, Zircon U-Pb chemical abrasion (“CA-TIMS”) method: Combined annealing and multi-step partial dissolution analysis for improved precision and accuracy of zircon ages: Chemical Geology, v. 220, p. 47–66, https://doi.org/10.1016/ j.chemgeo.2005.03.011.

McAdams, N.E.B., Schmitz, M.D., Kleffner, M.A., Verniers, J., Vandenbroucke, T.R.A., Ebert, J.R., and Cramer, B.D., 2017, A new, high-precision CA-ID-TIMS date for the 'Kalkberg' K-bentonite (Judds Falls Bentonite): Lethaia, v. 51, p. 344–356, https://doi.org/10.1111/ let.12241.

McClelland, W.C., Tikoff, B., and Manduca, C.A., 2000, Two-phase evolution of accretionary margins: examples from the North American Cordillera: Tectonophysics, v. 326, p. 37–55, https://doi.org/10.1016/s0040-1951(00)00145-1.

McLean, N.M., Condon, D.J., Schoene, B., and Bowring, S.A., 2015, Evaluating uncertainties in the calibration of isotopic reference materials and multi-element isotopic tracers (EARTHTIME tracer calibration part II): Geochimica et Cosmochimica Acta, v. 164, p. 481– 501, https://doi.org/10.1016/j.gca.2015.02.040.

Melchin, M.J., Sadler, P.M., and Cramer, B.D., 2020, Chapter 21 – The Silurian Period, in Gradstein, F.M., Ogg, J.G., Schmitz, M.D., and Ogg, G.M., eds., Geologic Time Scale 2020: Amsterdam, Netherlands, Elsevier, p. 695–732, https://doi.org/10.1016/B978-0-12-824360- 2.00021-8.

Michels, Z.D., Kruckenberg, S.C., Davis, J.R., and Tikoff, B., 2015, Determining vorticity axes from grain-scale dispersion of crystallographic orientations: Geology, v. 43, p. 803–806, https://doi.org/10.1130/g36868.1.

Montz, W.J., and Kruckenberg, S.C., 2017, Cretaceous partial melting, deformation, and exhumation of the Potters Pond migmatite domain, west-central Idaho: Lithosphere, v. 9, p. 205–222, https://doi.org/10.1130/l555.1.

Myrow, P.M., Ramezani, J., Hanson, A.E., Bowring, S.A., Racki, G., and Rakociński, M., 2014, High-precision U-Pb age and duration of the latest Devonian (Famennian) Hangenberg event, and its implications: Terra Nova, v. 26, p. 222–229, https://doi.org/10.1111/ ter.12090.

Papapavlou, K., Darling, J.R., Storey, C.D., Lightfoot, P.C., Moser, D.E., and Lasalle, S., 2017, Dating shear zones with plastically deformed titanite: New insights into the orogenic evolution of the Sudbury impact structure (Ontario, Canada): Precambrian Research, v. 291, p. 220–235, https://doi.org/10.1016/j.precamres.2017.01.007.

Parnell, A.C., Haslett, J., Allen, J.R., Buck, C.E., and Huntley, B., 2008, A flexible approach to assessing synchroneity of past events using Bayesian reconstructions of sedimentation history: Quaternary Science Reviews, v. 27, p. 1872–1885, https://doi.org/10.1016/ j.quascirev.2008.07.009.

Parry, S.F., Noble, S.R., Crowley, Q.G., and Wellman, C.H., 2011, A high-precision U-Pb age constraint on the Rhynie Chert Konservat-Lagerstätte: Time scale and other implications: Journal of the Geological Society [London], v. 168, p. 863–872, https://doi .org/10.1144/0016-76492010-043.

Pas, D., Da Silva, A.-C., Over, D.J., Brett, C.E., Brandt, L., Over, J.-S., Hilgen, F.J., and Dekkers, M.J., 2021, Cyclostratigraphic calibration of the Eifelian Stage (Middle Devonian, Appalachian Basin, western New York, USA): Geological Society of America Bulletin, v. 133, p. 277–286, https://doi.org/10.1130/ B35589.1.

Pas, D., Hinnov, L., Day, J.E., Kodama, K., Sinnesael, M., and Liu, W., 2018, Cyclostratigraphic calibration of the Famennian Stage (Late Devonian, Illinois Basin, USA): Earth and Planetary Science Letters, v. 488, p. 102– 114, https://doi.org/10.1016/j.epsl.2018.02.010.

Pennacchioni, G., and Zucchi, E., 2013, High temperature fracturing and ductile deformation during cooling of a pluton: The Lake Edison granodiorite (Sierra Nevada batholith, California): Journal of Structural Geology, v. 50, p. 54 81, https://doi.org/10.1016/j.jsg.2012.06.001.

Percival, L.M.E., Davies, J.H.F.L., Schaltegger, U., De Vleeschouwer, D., Da Silva, A.-C., and Föllmi, K.B., 2018, Precisely dating the Frasnian–Famennian boundary: implications for the cause of the Late Devonian mass extinction: Scientific Reports, v. 8, p. 9578, https://doi.org/10.1038/s41598-018-27847-7.

Prior, D.J. et al., 1999, The application of electron backscatter diffraction and orientation contrast imaging in the SEM to textural problems in rocks: American Mineralogist, v. 84, p. 1741–1759, https://doi.org/10.2138/am-1999-11-1204.

Prior, D.J., Wheeler, J., Peruzzi, L., Spiess, R., and Storey, C., 2002, Some garnet microstructures: An illustration of the potential of orientation maps and misorientation analysis in microstructural studies: Journal of Structural Geology, v. 24, p. 999–1011.

R Core Team, 2021, R: A language and environment for statistical computing: Vienna, Austria, R Foundation for Statistical Computing, https://www.R-project.org/ (accessed July 2021).

R Core Team, 2022, R: A language and environment for statistical computing. R Foundation for Statistical Computing, Vienna, Austria. https://www.R-project.org/ (accessed May 2022).

Reimold, W.U., Kelley, S.P., Sherlock, S.C., Henkel, H., and Koeberl, C., 2005, Laser argon dating of melt breccias from the Siljan impact structure, Sweden: Implications for a possible relationship to Late Devonian extinction events: Meteoritics & Planetary Science, v. 40, p. 591– 607, https://doi.org/10.1111/j.1945-5100.2005. Tb00965.x.

Resor, P.G., Chamberlain, K.R., Frost, C.D., Snoke, A.W., and Frost, B.R., 1996, Direct dating of deformation: U-Pb age of syndeformational sphene growth in the Proterozoic Laramie Peak shear zone: Geology, v. 24, p. 623–626, https://doi.org/10.1130/0091-7613(1996)024<0623:ddodup>2.3.co;2.

Retallack, G.J., and Huang, C., 2011, Ecology and evolution of Devonian trees in New York, USA: Palaeogeography, Palaeoclimatology, Palaeoecology, v. 299, p. 110–128, https://doi.org/10.1016/j.palaeo.2010.10.040.

Roden, M.K., Parrish, R.R., and Miller, D.S., 1990, The absolute age of the Eifelian Tioga Ash Bed, Pennsylvania: The Journal of Geology, v. 98, p. 282–285, https://doi.org/10.1086/629399.

Rossetti, F., Asti, R., Faccenna, C., Gerdes, A., Lucci, F., and Theye, T., 2017, Magmatism and crustal extension: Constraining activation of the ductile shearing along the Gediz detachment, Menderes Massif (western Turkey): Lithos, v. 282, p. 145–162, https://doi.org/10.1016/j.lithos.2017.03.003.

Schaltegger, U., Schmitt, A.K., and Horstwood, M.S.A., 2015, U–Th–Pb zircon geochronology by ID-TIMS, SIMS, and laser ablation ICP-MS: Recipes, interpretations, and opportunities: Chemical Geology, v. 402, p. 89–110, https://doi.org/10.1016/j.chemgeo.2015.02.028.

Schmitz, M.D., 2012, Appendix 2—Radiometric ages used in GTS2012, *in* Gradstein, F.M., Ogg, J.G., Schmitz, M.D., and Ogg, G.M., eds., The Geologic Time Scale 2012: Amsterdam, Netherlands, Elsevier BV, p. 1045– 1082, https://doi.org/10.1016/B978-0-444-594259.15002-4.

Schmitz, M.D., and Bowring, S.A., 2001, U-Pb zircon and titanite systematics of the Fish Canyon Tuff: an assessment of high-precision U-Pb geochronology and its application to young volcanic rocks: Geochimica et Cosmochimica Acta, v. 65, p. 2571–2587, https://doi.org/10.1016/s0016-7037(01)00616-0.

Schmitz, M.D., and Schoene, B., 2007, Derivation of isotope ratios, errors, and error correlations for U-Pb geochronology using ^{205}Pb-^{235}U-(^{233}U)-spiked isotope dilution thermal ionization mass spectrometric data: Geochemistry, Geophysics, Geosystems, v. 8, Q08006, https://doi.org/10.1029/2006gc001492.

Schmitz, M.D., Southwick, D.L., Bickford, M.E., Mueller, P.A., and Samson, S.D., 2018, Neoarchean and Paleoproterozoic events in the Minnesota River Valley subprovince, with implications for southern Superior craton evolution and correlation: Precambrian Research, v. 316, p. 206–226, doi:10.1016/j.precamres.2018.08.010.

Selby, D., and Creaser, R.A., 2005, Direct radiometric dating of the Devonian-Mississippian time-scale boundary using the Re-Os black shale geochronometer: Geology, v. 33, p. 545– 548, https://doi.org/10.1130/G21324.1.

Sinnesael, M., et al., 2019, The Cyclostratigraphy Intercomparison Project (CIP): Consistency, merits and pitfalls: Earth-Science Reviews, v. 199, 102965, https://doi .org/10.1016/j.earscirev.2019.102965.

Sláma, J., et al., 2008, Plešovice zircon — A new natural reference material for U–Pb and Hf isotopic microanalysis: Chemical Geology, v. 249, p. 1–35, https://doi.org/10.1016/j.chemgeo.2007.11.005.

Smith, R.C., and Way, J.H., 1983, The Tioga Ash Beds at Selinsgrove Junction, *in* Nickelsen, R.P., and Cotter, E., eds., Silurian Depositional History and Alleghenian Deformation in the Pennsylvania Valley and Ridge: 48th Annual Field Conference of Pennsylvania Geologists: Danville, Pennsylvania, Field Conference of Pennsylvania Geologists, p. 74–88.

Spandler, C., Hammerli, J., Sha, P., Hilbert-Wolf, H., Hu, Y., Roberts, E., and Schmitz, M.D., 2016, MKED1: A new titanite standard for in situ analysis of Sm-Nd isotopes and U-Pb geochronology: Chemical Geology, v. 425, p. 110–126, https://doi.org/10.1016/j.chemgeo.2016.01.002.

Stacey, J.S., and Kramers, J.D., 1975, Approximation of terrestrial lead isotope evolution by a two-stage model: Earth and Planetary Science Letters, v. 26, p. 207–221, https://doi.org/10.1016/0012-821X(75)90088-6.

Stearns, M.A., and Bartley, J.M., 2014, Multistage emplacement of the McDoogle pluton, an early phase of the John Muir intrusive suite, Sierra Nevada, California, by magmatic crack-seal growth: Geological Society of America Bulletin, v. 126, p. 1569 1579, https://doi.org/10.1130/b31062.1.

Stern, R.A., 1997, The GSC Sensitive High Resolution Ion Microprobe (SHRIMP): analytical techniques of zircon U-Th-Pb age determinations and performance evaluation: Geological Society of Canada, Current Research, v. 1997-F, p. 1–31, https://doi.org/10.4095/209089.

Stewart, D.E., Lewis, R.S., Stewart, E.D., and Lifton, Z.M., 2021, Geologic Map of the Yellow Pine Quadrangle, Valley County, Idaho: Idaho Geological Survey.

Stewart, D.E., Stewart, E.D., Lewis, R.S., Weppner, K.N., and Isakson, V.H., 2016, Geologic Map of the Stibnite Quadrangle, Valley County, Idaho: Idaho Geological Survey.

Storey, C.D., Jeffries, T.E., and Smith, M., 2006, Common lead-corrected laser ablation ICP–MS U–Pb systematics and geochronology of titanite: Chemical Geology, v. 227, p. 37–52, https://doi.org/10.1016/j.chemgeo.2005.09.003.

Strelow, F.W.E., and Toerien, F.V.S., 1966, Separation of Lead(ll) from Bismuth(lll), Thallium(lll), Cadmium(ll), Mercury(ll), Gold(lll), Platinum(IV), Palladium(ll), and Other Elements by Anion Exchange Chromatography: Analytical Chemistry, v. 38, p. 545–548.

Taubeneck, W.H., 1971, Idaho Batholith and Its Southern Extension: Geological Society of America Bulletin, v. 82, p. 1899–1928, https://doi.org/10.1130/0016-7606(1971)82[1899:ibaise]2.0.co;2.

Telford, R.J., Heegaard, E., and Birks, H.J.B., 2004, All age-depth models are wrong: But how badly?: Quaternary Science Reviews, v. 23, p. 1–5, https://doi.org/10.1016/j.quascirev.2003.11.003.

Tikoff, B., Housen, B.A., Maxson, J.A., Nelson, E.M., Trevino, S., Shipley, T.F., 2022, Hit- and-run model for Cretaceous–Paleogene tectonism along the western margin of Laurentia, *in* Whitmeyer, S.J., Williams, M.L., Kellett, D.A., Tikoff, B., eds., Laurentia: Turning Points in the Evolution of a Continent: Geological Society of America Memoir 220. https://doi.org/10.1130/2022.1220(32).

Tikoff, B., Kelso, P., Manduca, C., Markley, M.J., and Gillaspy, J., 2001, Lithospheric and crustal reactivation of an ancient plate boundary: the assembly and disassembly of the Salmon River suture zone, Idaho, USA: Geological Society, London, Special Publications, v. 186, p. 213–231, https://doi.org/10.1144/gsl.sp.2001.186.01.13.

Titus, S.J., Clark, R., and Tikoff, B., 2005, Geologic and geophysical investigation of two fine-grained granites, Sierra Nevada Batholith, California: Evidence for structural controls on emplacement and volcanism: Geological Society of America Bulletin, v. 117, p. 1256 16, https://doi.org/10.1130/b25689.1.

Torvela, T., Mänttäri, I., and Hermansson, T., 2008, Timing of deformation phases within the South Finland shear zone, SW Finland: Precambrian Research, v. 160, p. 277–298, https://doi.org/10.1016/j.precamres.2007.08.002.

Trayler, R.B., Schmitz, M.D., Cuitiño, J.I., Kohn, M.J., Bargo, M.S., Kay, R.F., Strömberg, C.A.E., and Vizcaíno, S.F., 2020, An improved approach to age-modeling in deep time: Implications for the Santa Cruz Formation, Argentina: Geological Society of America Bulletin, v. 132, p. 233–244, https://doi.org/10.1130/B35203.1.

Tucker, R.D., Bradley, D.C., Ver Straeten, C.A., Harris, A.G., Ebert, J.R., and McCutcheon, S.R., 1998, New U-Pb zircon ages and the duration and division of Devonian time: Earth and Planetary Science Letters, v. 158, p. 175–186, https://doi.org/10.1016/ S0012-821X(98)00050-8.

Turgeon, S.C., Creaser, R.A., and Algeo, T.J., 2007, Re–Os depositional ages and seawater Os estimates for the Frasnian–Famennian boundary: Implications for weathering rates, land plant evolution, and extinction mechanisms: Earth and Planetary Science Letters, v. 261, p. 649–661, https://doi.org/10.1016/j.epsl.2007.07.031.

Unruh, D.M., Lund, K., Kuntz, M.A., and Snee, L.W., 2008, Uranium-Lead Zircon Ages and Sr, Nd, and Pb Isotope Geochemistry of Selected Plutonic Rocks from Western Idaho: U.S. Geological Survey Open-File Report 2008-1142, 37 p.

Ver Straeten, C.A., 2004, K-bentonites, volcanic ash preservation, and implications for Early to Middle Devonian volcanism in the Acadian orogen, eastern North America: Geological Society of America Bulletin, v. 116, p. 474–489, https://doi.org/10.1130/B25244.1.

Ver Straeten, C.A., 2007, Basinwide stratigraphic synthesis and sequence stratigraphy, upper Pragian, Emsian and Eifelian Stages (Lower to Middle Devonian), Appalachian Basin, *in* Becker, R.T., and Kirchgasser, W.T., eds., Devonian Events and Correlations: Geological Society [London] Special Publication 278, p. 39–81, https://doi.org/10.1144/SP278.3.

Way, J.H., Smith, R.C., and Roden, M.K., 1986, Detailed correlations across 175 miles of the Valley and Ridge of Pennsylvania using 7 ash beds in the Tioga zone, *in* Sevon, W.D., ed., Selected Geology of Bedford and Huntington Counties: 51st Annual Field Conference of Pennsylvania Geologists: Huntington, Pennsylvania, Field Conference of Pennsylvania Geologists, p. 55–72.

Weddige, K., 1977, Die Conodonten der Eifel-Stufe im Typusgebiet und inbenachbarten Faziesgebieten: Senckenbergiana Lethaea, v. 58, p. 271–419.

Weddige, K., 1982, The Wetteldorf Richtschnitt as boundary stratotype from the view point of conodont stratigraphy, *in* Ziegler, W., and Werner, R., eds., On Devonian Stratigraphy and Palaeontology of the Ardenno-Rhenish Mountains and Related Devonian Matters: Courier Forschungsinstitut Senckenberg, v. 55, p. 26–37.

Wellman, C.H., 2004, Palaeoecology and palaeophytogeography of the Rhynie chert plants: evidence from integrated analysis of in situ and dispersed spores: Proceedings of the Royal Society of London. Series B, Biological Sciences, v. 271, p. 985–992, https://doi.org/10.1098/rspb.2004.2686.

Werner, R., and Winter, J., 1975, Bentonit-Horizonte im Grenzbereich Unterdevon/Mitteldevon in den Eifeler Richtschnitten: Senckenbergiana Lethaea, v. 56, p. 335–364.

Whalen, M.T., De Vleeschouwer, D., Payne, J.H., Day, J.E., Over, D.J., and Claeys, P., 2016, Pattern and timing of the Late Devonian biotic crisis in western Canada: Insights from carbon isotopes and astronomical calibration of magnetic susceptibility data, *in* Playton, T.E., Kerans, C., and Weissenberger, J.A.W., eds., New Advances in Devonian Carbonates: Outcrop Analogs, Reservoirs, and Chronostratigraphy: Society for Sedimentary Geology (SEPM) Special Publication 107, p. 185–201, https://doi.org/10.2110/ sepmsp.107.02.

Whalen, M.T., De Vleeschouwer, D., Payne, J.H., Day, J.E., Over, D.J., and Claeys, P., 2016, Pattern and timing of the Late Devonian biotic crisis in western Canada: Insights from carbon isotopes and astronomical calibration of magnetic susceptibility data, in Playton, T.E., Kerans, C., and Weissenberger, J.A.W., eds., New Advances in Devonian Carbonates: Outcrop Analogs, Reservoirs, and Chronostratigraphy, SEPM Special Publication No. 107, p. 185–201, https://doi.org/10.2110/sepmsp.107.02.

Zen, E., and Hammarstrom, J.M., 1984, Magmatic epidote and its petrologic significance: Geology, v. 12, p. 515–518.

Ziegler, W., and Klapper, G., 1985, Stages of the Devonian System: Episodes, v. 8, p. 104–109, https://doi.org/10.18814/epiiugs/1985/v8i2/006.

Ziegler, W., and Werner, R., eds., 1982, On Devonian Stratigraphy and Palaeontology of the Ardenno-Rhenish Mountains and Related Devonian Matters: Courier Forschungsinstitut Senckenberg, v. 55, p. 498.

APPENDIX A

Supplementary Material for Chapter One

Available as a separate file:

Table A1.1. Metadata for zircon LA-ICPMS U-Pb analyses.

Table A1.2. Zircon U-Pb isotope ratios and trace element concentrations by LA-ICPMS: sample data.

Table A1.3. Zircon U-Pb isotope ratios and trace element concentrations by LA-ICPMS: standard data.

Table A1.4. Metadata for titanite LA-ICPMS U-Pb analyses.

Table A1.5. Titanite U-Pb isotope ratios and trace element concentrations by LA-ICPMS: sample data.

Table A1.6. Titanite U-Pb isotope ratios and trace element concentrations by LA-ICPMS: standard data.

Table A1.7. Zircon and titanite U-Th-Pb isotopic data by ID-TIMS.

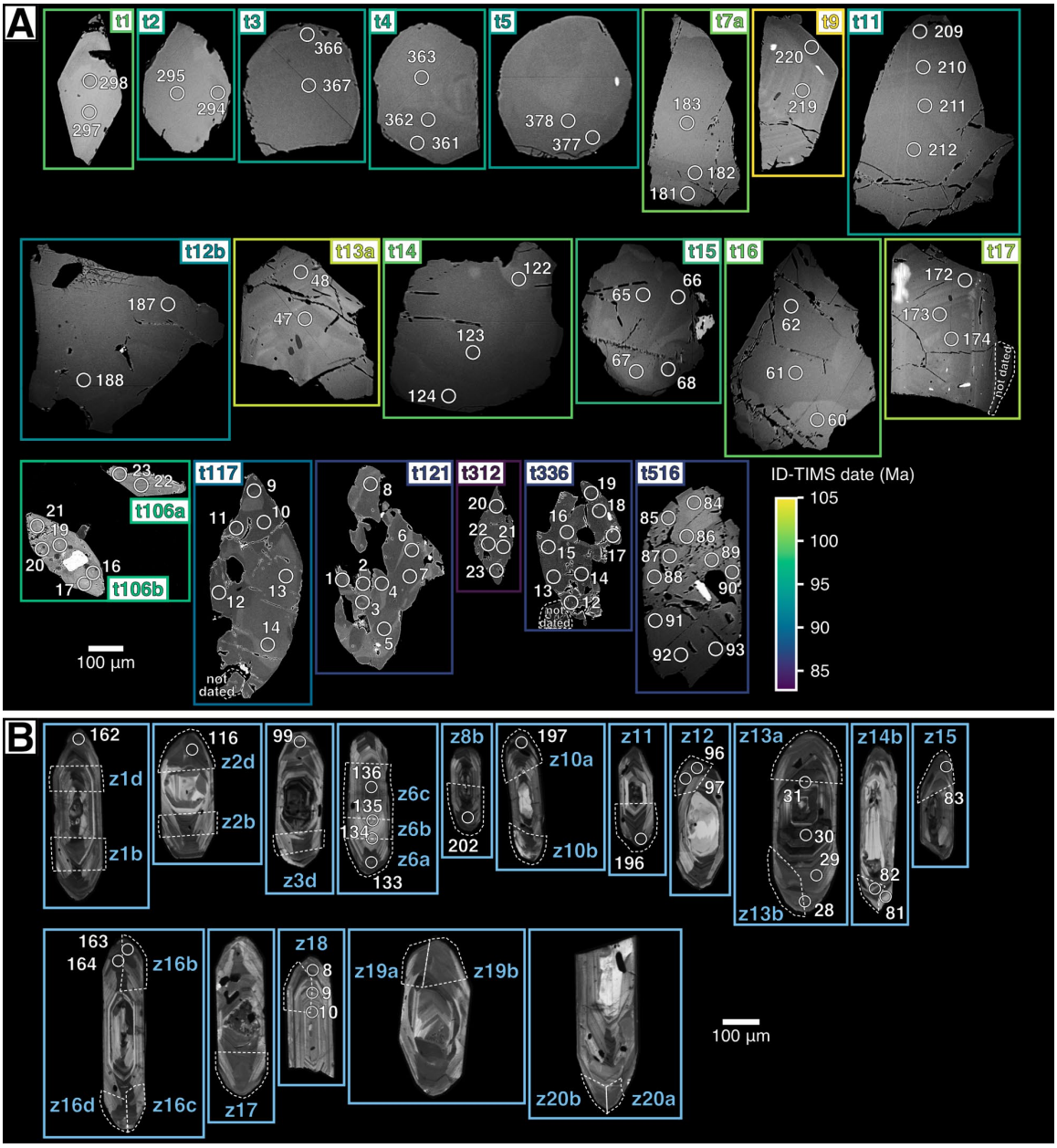

Figure A1.1. (A) Backscattered electron (BSE) images of isotope dilution–thermal ionization mass spectrometry (ID-TIMS)–dated titanite crystals with borders colored by ID-TIMS date. White open circles and white numbers on the BSE images indicate laser ablation–inductively coupled plasma mass spectrometry (LA-ICPMS) spot placement and reference number. Locations of subsampled titanite crystal fragments not indicated because some fragments were taken from entirely below the plane of the BSE image. (B) Cathodoluminescence images of zircon dated by ID-TIMS with dated fragments indicated (white dashed polygons). White open circles and white numbers indicate LA-ICPMS spot placement and reference number.

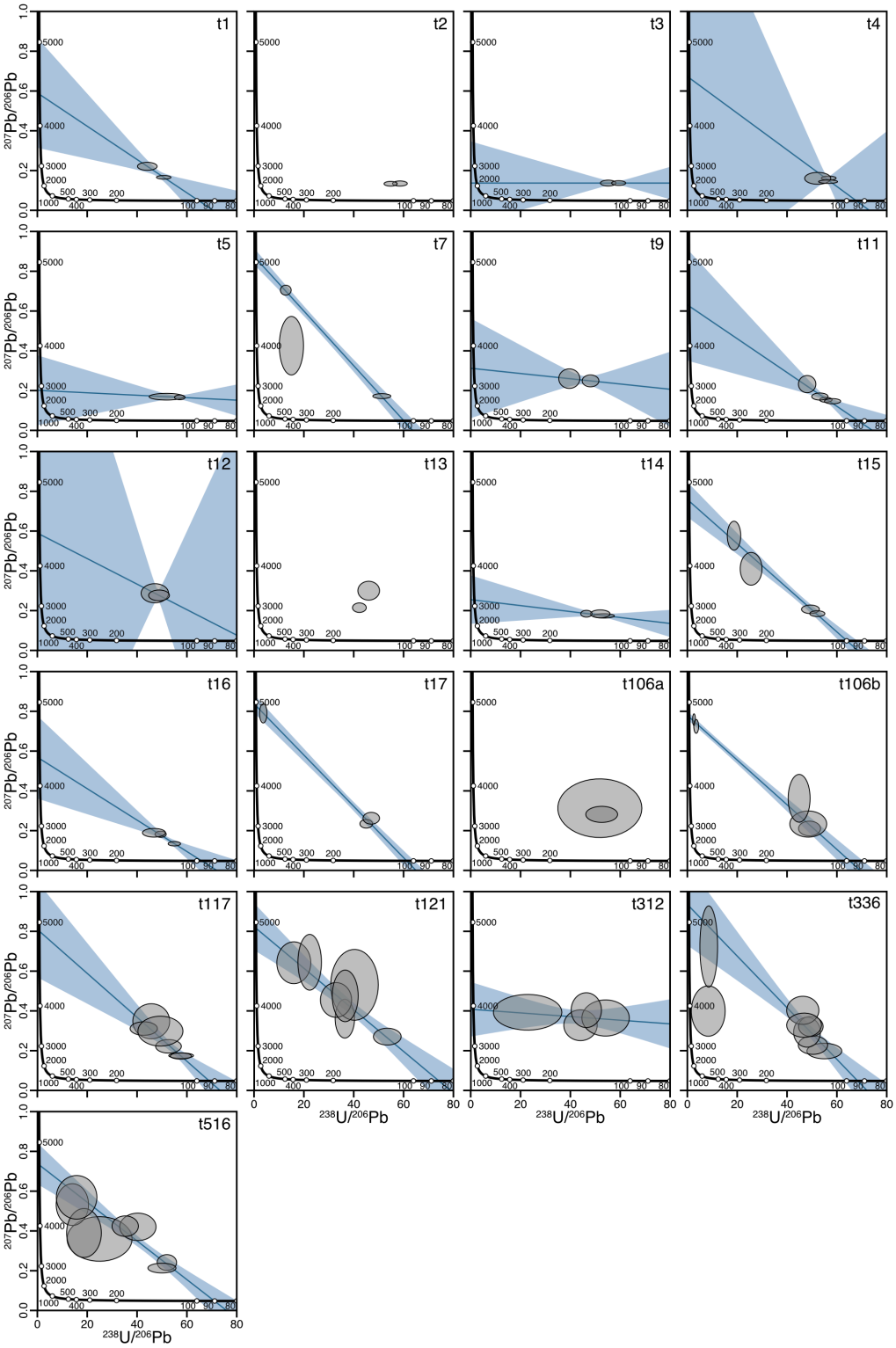

Figure A1.2. Regressions for initial $^{207}Pb/^{206}Pb$ value and intercept age for LA-ICPMS isotopic data of ID-TIMS–dated titanite grains in Tera-Wasserburg concordia space, calculated using the maximum likelihood algorithm of Ludwig (1998). Uncertainty in the LA-ICPMS isotopic measurements is shown as 95% confidence ellipses.

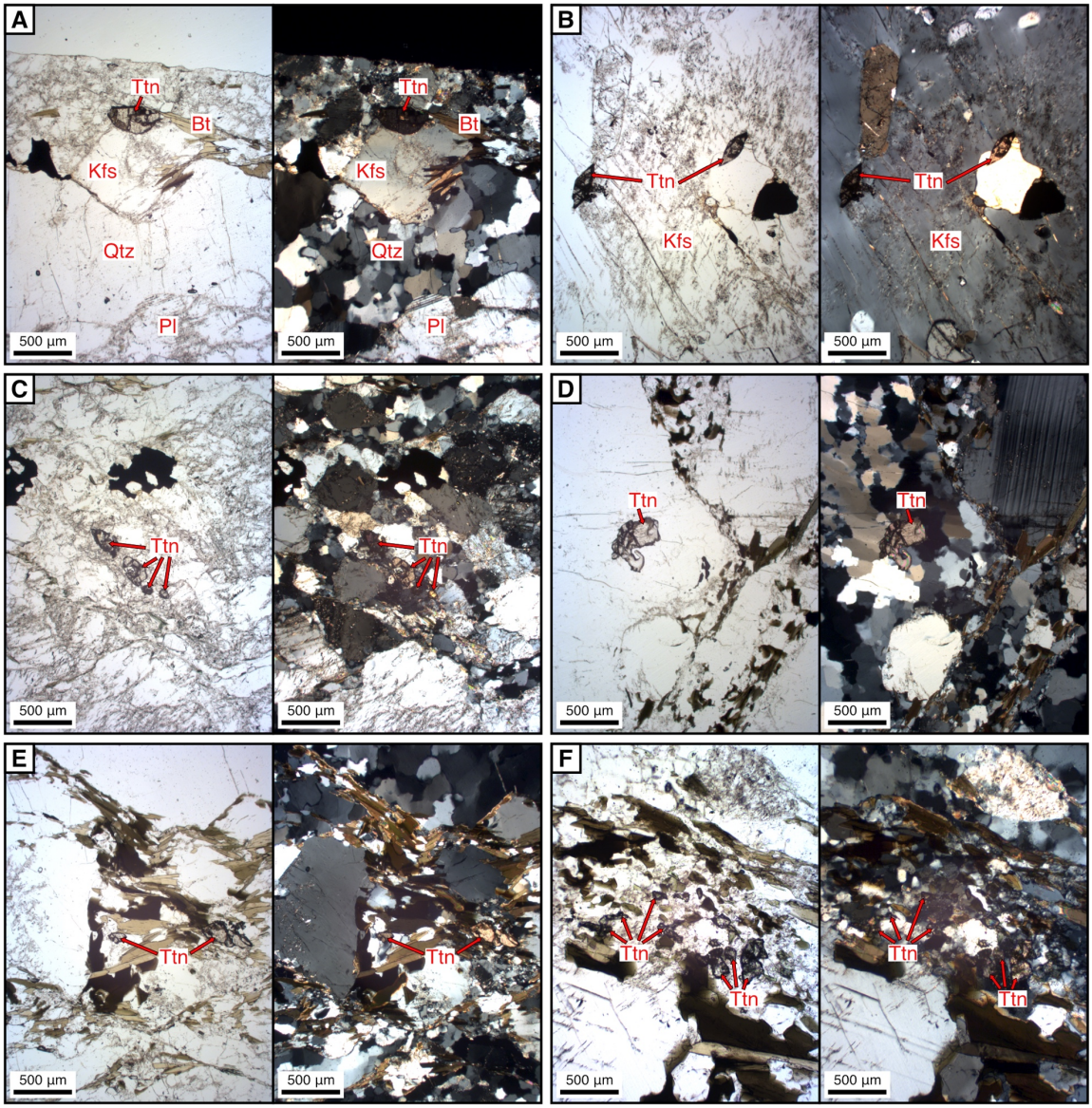

Figure A1.3. Plane polarized light (left) and cross polarized light (right) photomicrographs of sample 14WZ3-2, a K-feldspar porphyritic granodiorite orthogneiss composed of K-feldspar (Kfs), plagioclase (Pl), quartz (Qtz), biotite (Bt) ± hornblende, titanite (Ttn), allanite, apatite, zircon, and oxides. Quartz subgrains have cuspate and lobate boundaries (e.g., A). Titanite is present as inclusions in potassium feldspar megacrysts and in the matrix. Titanite grains included in the megacrysts are euhedral and dark brown (e.g., B). In the matrix, titanite ranges from suhedral (e.g., C) to anhedral (e.g., D) and tends to be lighter in color than the euhedral grains included in the megacrysts. Titanite in the matrix is primarily found in areas with a higher concentration of biotite, like the folia surrounding a K-feldspar porphyroclast (e.g., A, E). Where a titanite grain in the matrix has a subhedral wedge shape, the longest axis of the wedge tends to align with nearby biotite folia (e.g., E). Titanite is also found in clusters of anhedral grains (e.g., F), and these grains are typically smaller than solitary matrix titanite (e.g., D).

APPENDIX B

Supplementary Material for Chapter Two

Available as separate files:

Zircon grain images: Cathodoluminescent images of zircon grains with laser ablation–inductively coupled plasma mass spectrometry spot locations for all samples

Titanite grain images: Backscattered electron images of titanite grains with laser ablation–inductively coupled plasma mass spectrometry spot locations for all samples

Table B2.3. Titanite U-Th-Pb isotopic data by ID-TIMS

Table B2.4. Titanite U-Th-Pb isotopic data by ID-TIMS

Table B2.5. Metadata for zircon LA-ICPMS U-Pb analyses.

Table B2.6. Zircon U-Pb isotope ratios and trace element concentrations by LA-ICPMS: sample data.

Table B2.7. Zircon U-Pb isotope ratios and trace element concentrations by LA-ICPMS: standard data.

Table B2.8. Metadata for titanite LA-ICPMS U-Pb analyses.

Table B2.9. Titanite U-Pb isotope ratios and trace element concentrations by LA-ICPMS: sample data.

Table B2.10. Titanite U-Pb isotope ratios and trace element concentrations by LA-ICPMS: standard data.

Table B2.1. Initial Pb measurements.

Analysis	$^{208}Pb/^{206}Pb$	$^{207}Pb/^{206}Pb$	$^{208}Pb/^{204}Pb$	$^{207}Pb/^{204}Pb$	$^{206}Pb/^{204}Pb$	Method*
14WZ3-2 matrix K-feldspar						
Leachate 3	2.045	0.828	38.608	15.634	18.8808	IC
Leachate 4	2.045	0.828	38.610	15.634	18.8795	IC
Leachate 5	2.046	0.828	38.625	15.639	18.8824	IC
average	*2.045*	*0.828*	***38.614***	***15.636***	***18.8809***	
± 1σ %	*0.018*	*0.011*	***0.024***	***0.017***	***0.0076***	
14WZ3-2 porphyroclast K-feldspar						
Leachate 3	2.045	0.828	38.605	15.634	18.880	IC
Leachate 4	2.044	0.828	38.585	15.629	18.877	IC
Leachate 5	2.043	0.828	38.586	15.628	18.885	IC
average	*2.044*	*0.828*	*38.592*	*15.630*	*18.880*	
± 1σ %	*0.036*	*0.032*	*0.029*	*0.021*	*0.021*	
16WZ-04 matrix K-feldspar						
Leachate 3 ± 1σ %	2.044863 ± 0.000032	0.8283266 ± 0.000009	38.6086 ± 0.0015	15.63967 ± 0.00056	18.88105 ±	DS74
Leachate 4 ± 1σ %	2.044752 ± 0.000042	0.8282916 ± 0.0000095	**38.6024 ± 0.0019**	**15.63725 ± 0.00065**	**18.87909 ±**	DS74
Leachate 5 ± 1σ %	2.045031 ± 0.000087	0.82833 ± 0.000018	38.6116 ± 0.0035	15.6395 ± 0.0011	18.88065 ±	DS74
16WZ-05 matrix K-feldspar						
Leachate 3	2.03774	0.82252	38.761	15.6458	19.0217	IC
Leachate 4	2.03917	0.82285	38.808	15.6601	19.0315	IC
Leachate 5	2.03817	0.82268	38.766	15.6474	19.0200	IC
average	*2.03836*	*0.82269*	***38.779***	***15.6511***	***19.0244***	
± 1σ %	*0.00073*	*0.00016*	***0.026***	***0.0078***	***0.0062***	
15WZ1-2 matrix K-feldspar						
Leachate 3	2.02835	0.81458	39.070	15.6903	19.2619	IC
Leachate 4	2.02879	0.81466	39.081	15.6928	19.2630	IC
Leachate 5	2.02763	0.81443	39.038	15.6803	19.2531	IC
average	*2.02826*	*0.81455*	***39.063***	***15.6878***	***19.2594***	
± 1σ %	*0.00059*	*0.00012*	***0.022***	***0.0067***	***0.0054***	

Analysis	$^{208}Pb/^{206}Pb$	$^{207}Pb/^{206}Pb$	$^{208}Pb/^{204}Pb$	$^{207}Pb/^{204}Pb$	$^{206}Pb/^{204}Pb$	Method*
15WZ1-3 matrix K-feldspar						
Leachate 3	1.969	0.792	39.107	15.724	19.86	IC
Leachate 4	2.025	0.813	39.078	15.684	19.30	IC
Leachate 5	2.025	0.813	39.121	15.696	19.32	IC
average	*2.006*	*0.806*	***39.102***	***15.701***	***19.49***	
± 1σ %	*0.032*	*0.012*	***0.022***	***0.021***	***0.32***	
I00-304 matrix K-feldspar						
Leachate 3	2.02683	0.813201	39.129	15.6994	19.3057	IC
Leachate 4	2.02676	0.813211	39.123	15.6975	19.3031	IC
Leachate 5	2.02636	0.813161	39.101	15.6910	19.2962	IC
average	*2.02665*	*0.813191*	***39.118***	***15.6960***	***19.3017***	
± 1σ %	*0.00025*	*0.000026*	***0.015***	***0.0044***	***0.0049***	
16WZ-06 matrix K-feldspar						
Leachate 3	2.00943	0.801608	39.436	15.7321	19.6257	IC
Leachate 4	2.00908	0.801590	39.418	15.7271	19.6198	IC
Leachate 5	2.00969	0.801751	39.443	15.7356	19.6265	IC
average	*2.00940*	*0.801650*	***39.432***	***15.7316***	***19.6240***	
± 1σ %	*0.00031*	*0.000088*	***0.013***	***0.0043***	***0.0036***	
16WZ-07 matrix K-feldspar						
Leachate 3 ± 1σ %	2.036744 ± 0.000044	0.81295 ± 0.00001	39.397 ± 0.0024	15.72482 ± 0.00087	19.34309 ±	DS74
Leachate 4 ± 1σ %	2.03661 ± 0.000026	0.8131666 ± 0.0000076	**39.3562 ± 0.0016**	**15.7144 ± 0.00062**	**19.32498 ±**	DS74
Leachate 5 ± 1σ %	2.036537 ± 0.00004	0.81288 ± 0.0000087	39.3792 ± 0.0018	15.71802 ± 0.00062	19.33628 ± 0.0006	DS74

Bold text indicates values used as an initial Pb isotopic composition for zircon and titanite isotope dilution thermal ionization mass spectrometry ages.

Isotope ratios include an external fractionation correction of 0.10 ± 0.02% (1σ) per atomic mass unit, based upon NBS981 measurements on similar sized ion beams at the same run temperatures. Fractionation uncertainty imposes the following minimum absolute uncertainties (1σ): $^{208}Pb/^{204}Pb$, 0.019; $^{207}Pb/^{204}Pb$, 0.007; $^{206}Pb/^{204}Pb$, 0.008; $^{208}Pb/^{206}Pb$, 0.0009; $^{207}Pb/^{206}Pb$, 0.0004.

*IC–isotope concentration; DS74 – ^{207}Pb-^{204}Pb double spike

Table B2.2. Structural measurements of fabric of plutonic rocks near McCall, Idaho.

Sample	Sample Description	Latitude, Longitude[A]	Foliation	Lineation
Little Goose Creek complex				
14WZ3-2	K-feldspar porphyritic granodiorite orthogneiss	44.9669°N, 116.1809°W	N002°, 60°E	59/076
16-IGC-01	hornblende-biotite tonalite orthogneiss	45.1782°N, 116.1774°W	N017°, 73°E	N.R.
Payette River complex				
16WZ-05	coarse-grained tonalite orthogneiss	45.1822°N, 116.1380°W	N010°, 85°E	85/089
15WZ1-2	tonalite orthogneiss	45.1596°N, 116.1072°W	N029°, 70°E	44/026
I00-304	tonalite	44.9720°N, 116.0548°W	N196°, 61°W	N.R.
14WZ2	tonalite	44.9731°N, 116.0547°W	N028°, 76°E	75/098
15WZ1	hornblende-rich band in foliated tonalite gneiss	45.1584°N, 116.1058°W	N025°, 84°E	50/025
Border Zone suite				
20WZ-02	tonalite orthogneiss	44.9333°N, 115.9469°W	N003°, 78°E	N.R.
20WZ-02	tonalite orthogneiss	44.9333°N, 115.9469°W	N015°, 82°E	N.R.
20WZ-02	tonalite orthogneiss	44.9333°N, 115.9469°W	N009°, 78°E	N.R.
20WZ-03	K-feldspar porphyritic granodiorite orthogneiss	44.9340°N, 115.9481°W	N020°, 60°E	N.R.
20WZ-01	K-feldspar porphyritic granodiorite orthogneiss	44.9336°N, 115.9455°W	N015°, 76°W	N.R.
20WZ-01	K-feldspar porphyritic granodiorite orthogneiss	44.9336°N, 115.9455°W	N002°, 82°W	N.R.
20WZ-01	K-feldspar porphyritic granodiorite orthogneiss	44.9336°N, 115.9455°W	N003°, 85°W	N.R.
20WZ-01	K-feldspar porphyritic granodiorite orthogneiss	44.9336°N, 115.9455°W	N005°, 82°W	N.R.
20WZ-01	K-feldspar porphyritic granodiorite orthogneiss	44.9336°N, 115.9455°W	N000°, 78°W	N.R.
20WZ-01	K-feldspar porphyritic granodiorite orthogneiss	44.9336°N, 115.9455°W	N355°, 85°W	N.R.
20WZ-01	K-feldspar porphyritic granodiorite orthogneiss	44.9336°N, 115.9455°W	N004°, 78°W	N.R.
20WZ-04	K-feldspar porphyritic biotite granodiorite	45.0017°N, 115.9762°W	N335°, 70°E	N.R.
20WZ-04	K-feldspar porphyritic biotite granodiorite	45.0017°N, 115.9762°W	N345°, 70°E	N.R.
20WZ-06	leucogranodiorite	44.9192°N, 115.9943°W	N180°, 65°N	N.R.
16WZ-06	K-feldspar porphyritic granodiorite orthogneiss	44.9336°N, 115.9455°W	N184°, 78°S	N.R.

A. World Geodetic System 1984 (WGS84).
N.A.–not applicable; N.R.–not recorded.

APPENDIX C

Supplementary Material for Chapter Three: LA-ICPMS and age-depth modeling methods and results

Geochronology of the Horologium II K-Bentonite

We sampled the Horologium II K-bentonite from the *Polygnathus costatus partitus* Zone from the GSSP section in Wetteldorf, Germany (N50.14983°, E006.47135° (WGS84); sample 12VD-83; Figure 3.1.A. of Chapter Three). We targeted this K-bentonite because of its proximity to the GSSP, but we were unable to determine an age for the associated volcanic event because of significant inheritance and extreme metamictization of U-rich zircon grains. Similarly, Kaufmann et al. (2005) and De Vleeschouwer et al. (2018) document issues with dating the Horologium II K-bentonite.

We mounted, polished to grain centers, and imaged 76 Horologium II zircon grains by cathodoluminescence (CL; Figure C3.1.). The zircon grains in this sample were generally equant and small. Zircon grains were commonly very dark in CL, indicating U-rich grains that were likely to have too much lattice damage to be successfully dated. Also, many grains were too small for laser ablation inductively coupled plasma mass spectrometry (LA-ICPMS) followed by chemical abrasion isotope dilution thermal ionization mass spectrometry (CA-ID-TIMS).

We dated 19 spots on 18 Horologium II zircon grains by LA-ICPMS (methods described below, results given in Table D3.2.). Based on zoning patterns visible in CL images and LA-ICPMS $^{206}Pb/^{238}U$ dates, we selected seven zircon grains for dating by CA-ID-TIMS. Our CA-ID-TIMS methods for zircon followed those described in the Geochronology methods section of Chapter Three. We were only able to successfully date four zircon grains because some zircon grains dissolved during chemical abrasion.

CA-ID-TIMS dates for the Horologium II K-bentonite ranged from 394.07 ± 0.31 Ma to 391.85 ± 0.31 Ma (Table D3.4.).

We decided not to include the Horologium II K-bentonite in our Devonian time scale compilation because we were not confident in our ability to accurately date the associated volcanic event. About half of the LA-ICPMS-dated grains yielded dates older than the Devonian Period. Of the zircon grains selected for CA-ID-TIMS that did not dissolve during chemical abrasion, we were unable generate a weighted mean age that we were confident represented the age of the volcanic event and not inheritance or Pb loss. For this work we chose to focus instead on the Hercules I ash bed because of the greater availability of Devonian age, elongate, prismatic grains.

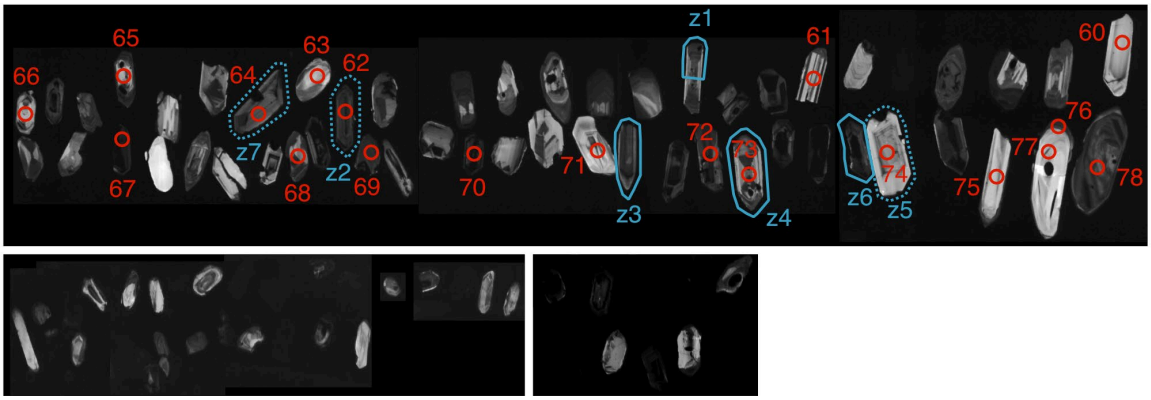

Figure C3.1. CL grain images and LA-ICPMS spot locations for zircon from the Horologium II K-bentonite. Red open circles are 25 µm in diameter LA-ICPMS spots, and the red numbers indicate the LA-ICPMS spot number. The zircon grains plucked for CA-ID-TIMS work are indicated by blue outlines and a label starting with "z." The solid blue outlines indicate grains successfully dated by CA-ID-TIMS and the dashed blue outlines indicate grains that we attempted to but were unable to date by CA-ID-TIMS.

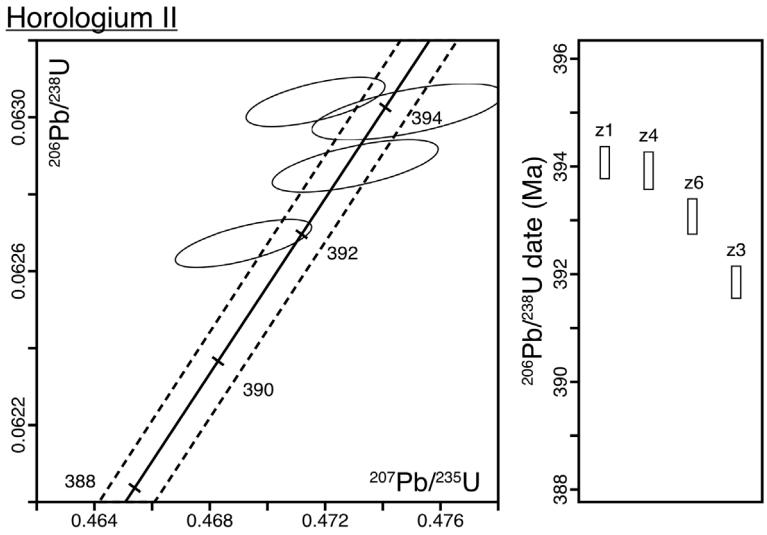

Figure C3.2. Concordia diagram (left) and ranked date plot (right) of U-Pb zircon CA-ID-TIMS results for the Horologium II K-bentonite. Error ellipses and error bars are 2σ.

LA-ICPMS Analysis

One hundred and sixty-six zircon crystals from the Hercules I K-bentonite (sample 12VD-80) were mounted in epoxy, polished to grain centers, and imaged by cathodoluminescence (CL). Fifty-nine laser ablation inductively coupled plasma mass spectrometry (LA-ICPMS) spots were placed on 47 zircon crystals following the methods described in Macdonald et al. (2018) and with analytical parameters described in Table D3.1. to produce preliminary age determinations and trace element concentrations (Tables D3.2. and D3.3.). Of the 59 LA-ICPMS spots, only 15 spots had Devonian dates. This is consistent with the inherited cores visible in the CL. The youngest LA-ICPMS dates and their associated errors are equivalent to the CA-ID-TIMS weighted mean ages for this sample.

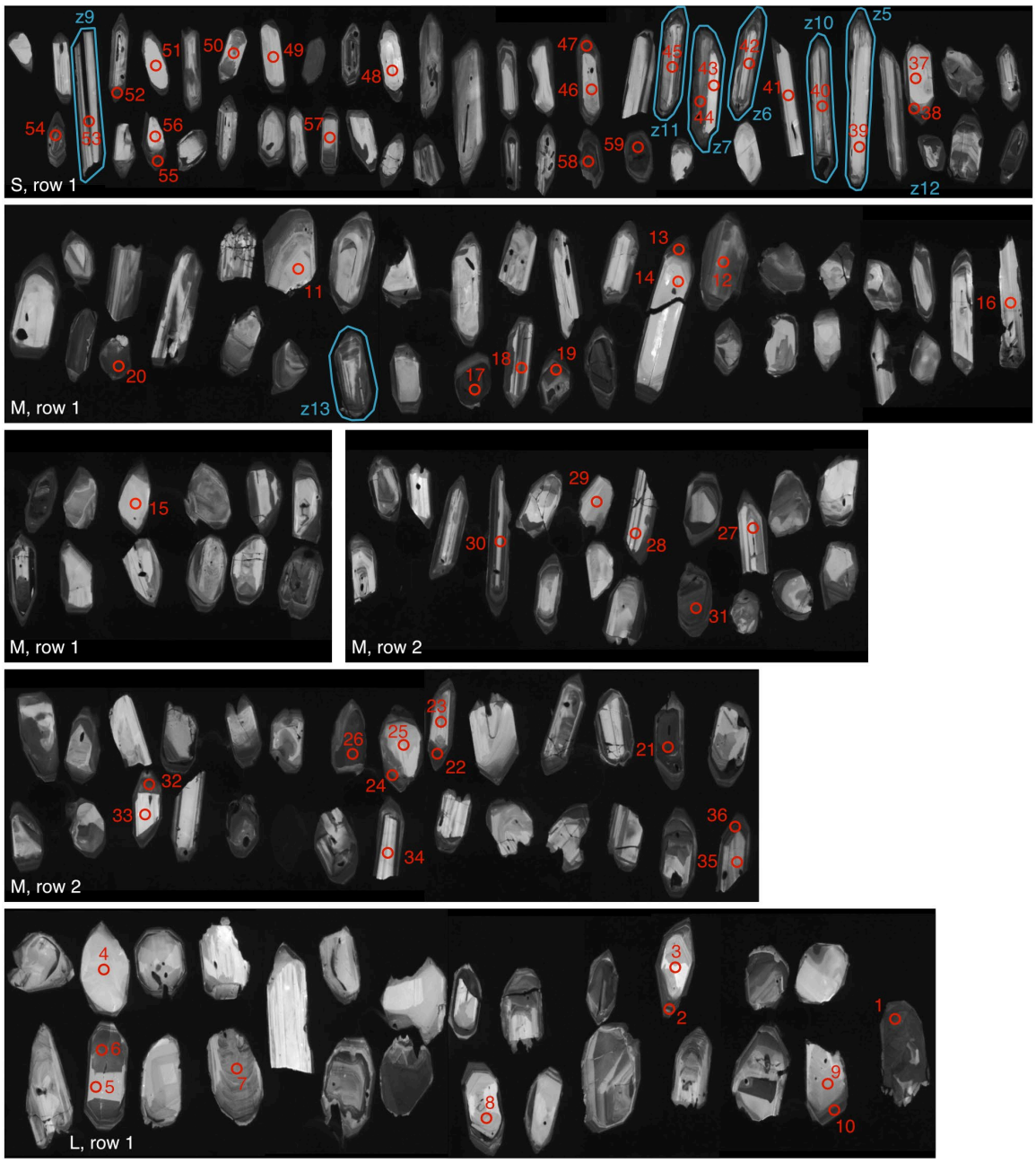

Figure C3.3. CL grain images and LA-ICPMS spot locations for zircon from the Hercules I K-bentonite. Red open circles are 25 μm in diameter LA-ICPMS spots, and the red numbers indicate the LA-ICPMS spot number. The zircon grains plucked for ID-TIMS work are indicated by a light blue outline and a TIMS label starting with "z."

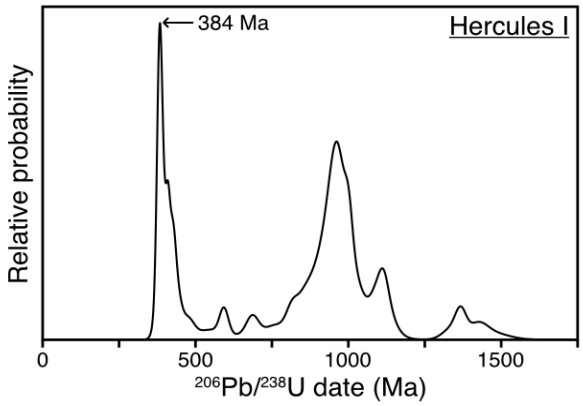

Figure C3.4. Probability density plot of LA-ICPMS U-Pb zircon dates for the Hercules I K-bentonite.

Additional Age-Depth Modeling Methods

Sourcing Conodont Biozonation Schemes for Age-Depth Modeling

Our three conodont biozonation schemes used in the age-depth modeling, the Kaufmann, Becker 2012, and Becker 2020 scales, are derived from Kaufmann (2006), Becker et al. (2012), and Becker et al. (2020), respectively. We needed to append additional conodont biozones to the biostratigraphic scales to include Silurian and Carboniferous ages in our modeling. The inclusion of ages outside of the Devonian Period minimizes model uncertainty at the Silurian-Devonian and Devonian-Carboniferous boundaries caused by extrapolating across those boundaries. The Kaufmann scale includes some Carboniferous conodont biozones, making the addition of Carboniferous radioisotopic ages into the model straightforward. We added Carboniferous conodont biozones to the Becker 2012 scale by matching the thickness of the *Siphonodella sulcata* Zone in the Carboniferous chapter of the GTS2012 (Figure 23.5, Davydov et al., 2012) to the thickness of the *S. sulcata* Zone on the Becker 2012 scale. We followed the same procedure to append the Carboniferous conodont biozones from the GTS2020 (Figure 23.7, Aretz et al., 2020) to the Becker 2020 scale, matching the

thickness of the *S. sulcata* Zone. We added the Pridoli and Ludlow conodont biozones of the Silurian using Figure 9 of McAdams et al. (2017), matching the thickness of the *Ancyrodelloides trigonicus* through the *Caudicriodus postwoschmidti/Caudicriodus hesperius* Zones on the Kaufmann scale and the thickness of the *A. trigonicus* through the *C. hesperius* Zones between on the Becker 2012 and Becker 2020 scales.

We normalized the y axis across the three biostratigraphic scales, assigning a position of 0 to the Silurian-Devonian boundary and a position of 100 to the Devonian-Carboniferous boundary.

Assignment of Relative Stratigraphic Position to Radioisotopic Ages

Following the logic described below for each age, we assigned relative stratigraphic positions to the radioisotopic ages and used these ages and positions as input into our age-depth models. Based on which conodont biozone, biozones, or portions of a biozone correspond to each radioisotopic age, we assigned each age a scaled stratigraphic position and uncertainty on each scale, represented by the black rectangles on Figure 3.3. of Chapter 3. The y axis value of the midpoints of the black rectangles in Figure 3.3. is used as the scaled stratigraphic position, and the box height, representing uncertainty in the biozone assignment, is used as the uncertainty on those positions. Figure C3.3. illustrates the radioisotopic ages and uncertainties as probability density functions whose bases are positioned at the assigned scaled stratigraphic position for each age. The uncertainty on the scaled stratigraphic position of each age is represented by a vertical error bar.

We generally favored the conodont biozone assignment of the references that published each radioisotopic age. The text below describes how we translated a conodont

biozone assignment from the literature to the Kaufman and Becker 2012 scales. Becker et al. (2020) does the work of assessing the validity of the biozone assignments of the referenced papers. We drew the biostratigraphic assignments for the Becker 2020 scale from the text of Becker et al. (2020); see that text for more detailed explanations of the biostratigraphic assignments. In cases where Becker et al. (2020) assigned an age to a specific but difficult to accurately replicate interval (e.g., age D19 assigned to the "middle part of the *Pa. bogartensis* Zone"), we generally preferred to use a more generous relative stratigraphic assignment, typically spanning the entire conodont zone or zones. Those instances and other clarifications on how we associated radioisotopic ages with the conodont biozones of Becker 2020 scale are noted below.

All biozones listed below are implied to be conodonts unless otherwise specified.

S7: Cramer et al. (2014) dated an ash bed from the Hrynchuk Formation, Podolia, Ukraine at 424.08 ± 0.20(0.29)[0.53] Ma and associated this age to the *Polygnathoides siluricus* Zone. We use the *P. siluricus* Zone on the Kaufmann, Becker 2012, and Becker 2020 scales as the relative stratigraphic position for the S7 age.

S8: Cramer et al. (2014) dated an ash bed from the Pryhorodok Formation, Podolia, Ukraine at 422.91 ± 0.07(0.21)[0.49] Ma and assigned this age to the *Ozarkodina crispa* Zone. Following reassignment of this age described in the Silurian chapter of the GTS2020 (Melchin et al., 2020), we assigned this age to the *O. crispa* Zone and the lowermost quarter of the *Ozarkodina eosteinhornensis* sensu lado Interval Zone on the Kaufmann, Becker 2012, and Becker 2020 scales.

D1-D5, D7: Ages D1 through D5 and D7 from Husson et al. (2016) are a series of bentonites from the Helderberg Group, Cobleskill and Cherry Valley, New York, USA

and Smoke Hole, West Virgina, USA with relative position to each other known but with poor biostratigraphic context provided in the paper. The ages range from 418.42 ± 0.21(0.27)[0.53] Ma (D1) to 417.22 ± 0.21(0.23)[0.50] Ma (D7). D5 (sample H1-1 of Husson et al. (2016)) is the same ash bed as D6 (sample CV-2 of McAdams et al. (2017)) described below, therefore we use the biostratigraphic constraints described by McAdams et al. (2017) for samples D1-D5 and D7 on the Kaufmann and Becker 2012 scales, assigning these ages to part of the *Caudicriodus postwoschmidti* Zone through the end of the *Ancyrodelloides trigonicus* Zone. See below. For the Becker 2020 scale, we assigned these ages to the upper half of the Lower Lochkovian.

D6: McAdams et al. (2017) assigned their age of 417.61 ± 0.12(0.23)[0.50] Ma of the Judd Falls metabentonite, Cherry Valley, New York, USA to parts of the *Caudicriodus postwoschmidti* Zone, and all of the *Lanea omoalpha*, *Lanea transitans*, *Lanea eleanorae*, and *Ancyrodelloides trigonicus* Zones. The Kaufmann alternative scale includes the *L. omoalpha*, *L. eleanorae*, and *A. trigonicus* Zones, but lacks the *L. transitans* Zone between *L. omoalpha* and *L. eleanorae*. The Kaufmann alternative scale also lacks *C. postwoschmidti* and assigns *Caudicriodus hesperius* to the location occupied by *C. postwoschmidti* on the Kaufmann standard scale. When assigning a position to D6 on the Kaufmann scale, we scaled the McAdams et al. (2017) scale such that the upper boundary of the *A. trigonicus* Zone and the lower boundary of the *C. postwoschmidti/C. hesperius* Zones aligned between the McAdams et al. (2017) and Kaufmann alternative scales. The thickness, or uncertainty on the stratigraphic position, of D6 scaled accordingly. For assignment of D6 to the Becker 2012 scale, we similarly aligned the upper boundary of the *A. trigonicus* Zone and the lower boundary of the *C. hesperius*

Zone between the McAdams et al. (2017) and Becker 2012 scales, and the thickness of D6 scaled accordingly. McAdams et al. (2017) notes that the *L. transitans* and *L. eleanorae* Zones are reversed on the Becker 2012 scale, and the order in the McAdams et al. (2017) scale is consistent with the order of conodont zones described by Corradini and Corriga (2012). As mentioned above, D6 is the same ash bed as D5, and we use the biostratigraphic constraints on D6 for D1-D5 and D7. For the Becker 2020 scale, we assigned these ages to the upper half of the Lower Lochkovian.

D8: Bodorkos et al. (2017) assigned their age of 417.7 ± 0.5 Ma of the Bulls Camp Volcanics, eastern Australia to the *Caudicriodus woschmidti* through *Eurekadonta eurekaensis* Zones. For the Kaufmann scale, assignment of stratigraphic position for modelling was straightforward, and we assigned D8 to span the *C. postwoschmidti/C. woschmidti* and *E. eurekaensis* Zones. For the Becker scale, however, the *C. woschmidti* to *E. eurekaensis* Zones are not present. The *Caudicriodus hesperius* Zone is equivalent to the *C. woschmidti* Zone (Carls et al., 2007; Corradini and Corriga, 2012) and the *E. eurekaensis* Zone is equivalent to the *C. postwoschmidti*, *Ancyrodelloides carlsi*, and the lower part of the *Ozarkodina delta* (*Lanea omoalpha*) Zones (Corradini and Corriga, 2012), so we assigned D8 to span the *C. hesperius* and *L. omoalpha* Zones on the Becker 2012 scale. Becker et al. (2020) noted the difficulty in assessing the biostratigraphic age of this volcanic ash bed, associated this age with "much of the lower Lochkovian," and noted that this age is older than the *Ancyrodelloides transitans* Zone. Therefore, we assigned D8 to span from the base of the Lochkovian to the base of the *A. transitans* Zone on the Becker 2020 scale.

D9: Bodorkos et al. (2017) assigned their age of 415.6 ± 0.8 of the volcanic Turondale Formation, eastern Australia to the *Eurekadonta eurekaensis* to *Ozarkodina delta* Zones. We assigned D9 to span the *E. eurekaensis* and *O. delta* Zones on the Kaufmann scale. We assigned D9 to span from the *C. postwoschmidti* (see explanation for D8 above) to the *A. trigonicus* Zones on the Becker 2012 scale because the *O. delta* Zone includes *L. omoalpha*, *L. transitans*, *L. eleanorae*, and *A. trigonicus* Zones (Corradini and Corriga, 2012). Following the same reasoning as D8, we assigned the D9 age to the base of the Lochkovian through to the base of the *A. transitans* Zone on the Becker 2020 scale.

D10: Parry et al. (2011) associated their Milton of Noth andesite lava flow, Rhynie, Scotland age of 411.5 ± 1.1(1.2)[1.3] Ma to the early (but not earliest) Pragian to earliest Emsian based on *polygonalis-emsiensis* spore assemblages (Wellman, 2004). Becker et al. (2012) charted spore biozones which can be linked to their conodont biozones using the scaling of the Devonian Stages. We assigned D10 to the *Gondwania kindlei* Zone through most of *Eocostapolygnathus excavatus* Zone on the Becker 2012 scale. For the Kaufmann scale, we assigned D10 to *G. kindlei* through middle *E. excavatus*. For the Becker 2020 scale, the text of Becker et al. (2020) notes that the *polygonalis-emsiensis* spore Zone "occupies most of the Pragian" so we have assigned this age to span the entire Pragian.

D11: Bodorkos et al. (2017) dated three felsic volcanic samples from the Merrions Formation, eastern Australia, at 411.7 ± 0.9 Ma, 413.8 ± 0.8 Ma, and 412.7 ± 1.0 Ma for the Lower, Middle, and Upper Merrions Formation, respectively. The Merrions Formation lacks conodonts but overlying brachiopod and dacryoconarid fossils

constrain the formation to likely be Pragian and likely lower to middle Pragian. The GTS2020 only used the Lower Merrions Formation age from Bodorkos et al. (2017) for D11, 411.7 Ma, and uses an uncertainty of ± 0.9 Ma, consistent with the uncertainty listed in Table 1 of Bodorkos et al. (2017), while the text of Bodorkos et al. (2017) lists an uncertainty of ± 0.8 Ma. We have opted to use the larger uncertainty in our modeling. We followed the GTS2020 in using the Lower Merrions Formation age (411.7 ± 0.9 Ma) and assigned D11 to span the entire Pragian for the Kaufmann, Becker 2012, and Becker 2020 scales.

D12: Kaufmann et al. (2005) dated a volcaniclastic layer from Bundenbach, Germany at 407.7 ± 0.7 Ma and assigned this age to the upper part of the *Polygnathus excavatus* Zone. The GTS2012 (Appendix 2, Schmitz, 2012) recalculated the age of concordant analyses as 407.75 ± 1.08(1.33)[1.40] Ma, and we use this age for our modeling. In this case, the recalculated uncertainty of 1.08 Ma includes analytical uncertainty and the uncertainty associated with spike calibration relative to the EARTHTIME tracers. We assigned this age to the upper half of the *P. excavatus* Zone on the Kaufmann scale. Kaufmann et al. (2005) also assigned this age to the upper half of the *Polygnathus gronbergi* Zone which they explain as equivalent to the *P. excavatus* Zone. However, the Becker 2012 scale lists both *Eocostapolygnathus excavatus* and *Eocostapolygnathus gronbergi* Zones. Thus, the assignment on the Becker scale is not straightforward, so we have assigned D12 to span the *E. excavatus* and *E. gronbergi* Zones on the Becker 2012 scale. Becker et al. (2020) assigned this age to the overlap of the *Nowakia (Dimitriella) praecuror* dracryoconarids Zone and the *E. gronbergi*

conodont Zone, equivalent to approximately the upper half of the *E. gronbergi* conodont Zone which is where we assigned this age on the Becker 2020 scale.

D13: Our new age for the Hercules I K-bentonite, Wetteldorf, Germany is 394.290 ± 0.097(0.21)[0.47] Ma. As discussed in Chapter Three, we assigned this age to the upper half of the *Polygnathus costatus patulus* Zone on the Kaufmann, Becker 2012, and Becker 2020 scales.

D14: Our new age for the Tioga B K-bentonite, Fayette, New York, USA is 390.82 ± 0.18(0.26)[0.48] Ma. As discussed in Chapter Three, we assigned this age to the upper half of the *Polygnathus costatus costatus* Zone on the Kaufmann, Becker 2012, and Becker 2020 scales. The Becker 2020 scale, however, has a dashed boundary at the base of the *Polygnathus pseudofoliatus* Zone above the *P.c. costatus* Zone. We have extended D14 on the Becker 2020 scale through the *P. pseudofoliatus* Zone to account for this uncertainty on the upper bounds of the *P.c. costatus* Zone.

D15: Our new age for the Tioga F K-bentonite, Fayette, New York, USA is 390.14 ± 0.14(0.23)[0.47] Ma. As discussed in Chapter Three, we assigned this age to the *Tortodus kockelianus australis* Zone and the upper half of the *Polygnathus costatus costatus* Zone on the Kaufmann scale. The Becker 2012 scale lacks a *T.k. australis* Zone so we assigned this age to the upper half of the *P. c. costatus* Zone. We have assigned D15 on the Becker 2020 scale from the base of the *P.c. costatus* Zone through the *T.k. australis* Zone.

D16: Lanik et al. (2016) dated a tephra layer from the Belpre Tephra Suite, Tennessee, USA at 375.55 ± 0.10(0.21)[0.44] Ma. They associated this age with Frasnian Zones 5-8, which they say is approximately equivalent to the upper part of the lower

Palmatolepis hassi Zone. We assigned this age to Frasnian Zones 5-8 on the Kaufmann alternative scale and the lower half of the *P. hassi* Zone on the Becker 2012 scale. For the Becker 2020 scale, we assigned D16 to the *Palmatolepis housei* Zone as suggested by Becker et al. (2020).

D17: Lanik et al. (2016) dated a second tephra layer from the Belpre Tephra Suite, Tennessee, USA at 375.25 ± 0.13(0.22)[0.45] Ma. D17 was collected in the same site as D16 and yields a younger age D16, consistent with D17 being found stratigraphically higher than D16. They assigned age D17 to Frasnian Zone 8, and we use this same assignment on the Kaufmann scale. For the Becker 2012 scale, we assigned this age to the lower half of the *Palmatolepis hassi* Zone, the same assignment as D16. For the Becker 2020 scale, we assigned this age to the *Palmatolepis housei* Zone, the same assignment as D16.

D18: Lanik et al. (2016) dated a tephra layer from the Rhinestreet Formation, New York, USA at 375.14 ± 0.12(0.22)[0.45] Ma. This age is younger than D17 which is contrary to what Lanik et al. (2016) expected given the biostratigraphic constraints that place this tephra layer in Frasnian Zone 7, a constraint which would make this layer older than D17. They discuss this conflict between the radioisotopic ages and the biostratigraphic constraints and conclude that the zonal boundaries are within the resolution of the uncertainty on the radioisotopic ages. We assigned this age to Frasnian Zone 7 on the Kaufmann scale and the lower half of the *Palmatolepis hassi* Zone on the Becker 2012 scale. For the Becker 2020 scale, we assigned D18 to the *"Ozarkodina" nonaginta* Zone as suggested by Becker et al. (2020).

D19: Pervical et al. (2018) dated a bentonite from Kellerwald, Germany at 372.360 ± 0.053(0.11)[0.41] Ma and assigned this age to the late *Palmatolepis rhenana* Zone. We assigned this age to the upper *P. rhenana* Zone of the Kaufmann scale and the upper half of the *P. rhenana* Zone of the Becker 2012 scale. Becker et al. (2020) correlated this age with the middle part of the *Palmatolepis bogartensis* Zone, and we assigned this age to all of the *P. bogartensis* Zone.

D20-21: We omitted the Re-Os ages of black shales by Turgeon et al. (2007) and restricted this modeling to U-Pb ages to eliminate decay constant uncertainty.

D22: Tucker et al. (1998) dated a pumiceous tuff from the Carrow Formation, New Brunswick, Canada at 363.8 ± 2.2 Ma (weighted mean $^{207}Pb/^{206}Pb$ age) and assigned the Carrow Formation to the upper *Palmatolepis gracilis expansa* Zone. The GTS2012 (Appendix 2, Schmitz, 2012) recalculated the $^{206}Pb/^{238}U$ age as 364.08 ± 2.05(2.17)[2.20] Ma, and we used this age for our modeling. In this case, the recalculated uncertainty of 2.05 Ma includes analytical uncertainty and the uncertainty associated with spike calibration relative to the EARTHTIME tracers. We assigned this age to the upper *Pa. g. expansa* Zone on the Kaufmann scale and the upper half of the *Pa. g. expansa* Zone on the Becker 2012 scale. Becker et al. (2020) assigned this age to the "middle to upper parts of the *Bi. costatus* Subzone" and we assigned this age to the entire *Bispathodus costatus* Zone on the Becker 2020 scale to mitigate uncertainty in where the middle part of the *Bi. costatus* Zone begins on the Becker 2020 scale.

D23: Tucker et al. (1998) dated the Bailey Rock Rhyolite, which intrudes and/or overlies the Carrow Formation, New Brunswick, Canada, at 363.4 ± 1.8 Ma. They associated the Carrow Formation and this age with the upper *Palmatolepis gracilis*

expansa Zone. The GTS2012 (Appendix 2, Schmitz, 2012) recalculated the $^{206}Pb/^{238}U$ age as 362.87 ± 0.53(0.88)[0.96] Ma, and we use this age for our modeling. In this case, the recalculated uncertainty of 0.53 Ma includes analytical uncertainty and the uncertainty associated with spike calibration relative to the EARTHTIME tracers. We assigned this age to the upper *Pa. g. expansa* Zone on the Kaufmann scale and the upper half of the *Pa. g. expansa* Zone on the Becker 2012 scale. Following the same reasoning as the assignment for D22, we assigned D23 to all of the *Bispathodus costatus* Zone on the Becker 2020 scale.

D24: We omitted the Re-Os ages of a black shale by Selby and Creaser (2005) and restricted this modeling to U-Pb ages to eliminate decay constant uncertainty.

D25: Davydov et al. (2011) dated an ash bed from the Wocklum Limestone, Rhenish Mountains, Germany at 359.25 ± 0.06(0.18)[0.42] Ma. They assigned this age to the Upper *Siphonodella praesulcata* Zone. We assigned this age to the Middle to Upper *S. praesulcata* Zone on the Kaufmann scale and the entire *S. praesulcata* Zone of the Becker 2012 scale. The biostratigraphic assignment for D25 is not discussed in the text of Becker et al. (2020), so we assigned this age to the entire *S. praesulcata* Zone of the Becker 2020 scale for consistency with how we assign this age on the Becker 2012 scale.

D26: Myrow et al. (2014) dated an ash bed from the Woclumeria Limestone, Kielce, Poland at 358.97 ± 0.11(0.19)[0.43] Ma and assigned this age to the middle *Palmatolepis gracilis expansa* to late *Siphonodella praesulcata* Zones. The location of the ash bed in the stratigraphic section (Figures 1-2, Myrow et al., 2014) relative to the conodont biozones in Figure 1 of Myrow et al. (2014) suggests a position in the middle to upper *S. praesulcata* Zone, so we assigned this age to the middle to upper *S. praesulcata*

Zone on the Kaufmann scale and the entire *S. praesulcata* Zone on the Becker 2012 scale. Becker et al. (2020) assigned this age to the upper part of the *Siphonodella (Eosiphonodella) praesulcata* conodont Zone and the *Wocklumeria sphaeroides* ammonoid Zone, so we assigned this age to the upper half of the *S. praesulcata* Zone of the Becker 2020 scale.

D27: Myrow et al. (2014) dated an ash bed from the Hangenberg Limestone, Kielce, Poland at 358.89 ± 0.20(0.29)[0.48] Ma and assigned this age to the middle *Palmatolepis gracilis expansa* to late *Siphonodella praesulcata* Zones. Following the same reasoning as with age D26, we assigned this age to the middle to upper *S. praesulcata* Zone on the Kaufmann scale and the entire *S. praesulcata* Zone of the Becker 2012 scale. Becker et al. (2020) assigned this age to the middle/upper *Bispathodus costatus – Protognathodus kockeli* Interregnum, and we assigned this age to all of the *Bi. costatus – P. kockeli* Interregnum on the Becker 2020 scale.

Cb1: Davydov et al. (2011) dated an ash bed, Bed 79 from the Hangenberg Limestone, Rhenish Mountains, Germany, at 358.71 ± 0.06(0.19)[0.42] Ma and assigned this age to the Upper *Siphonodella sulcata* Zone. We assigned this age to the *S. sulcata* Zone on the Kaufmann, Becker 2012, and Becker 2020 scales.

Cb2: Davydov et al. (2011) dated an ash bed, Bed 15 from the Hangenberg Limestone, Rhenish Mountains, Germany, at 358.43 ± 0.06(0.19)[0.42] Ma and assigned this age to the Lower *Siphonodella duplicata* Zone. We assigned this age to the Lower *S. duplicata* Zone on the Kaufmann and Becker 2020 scales and the lower half of the *S. duplicata* Zone on the Becker 2012 scale.

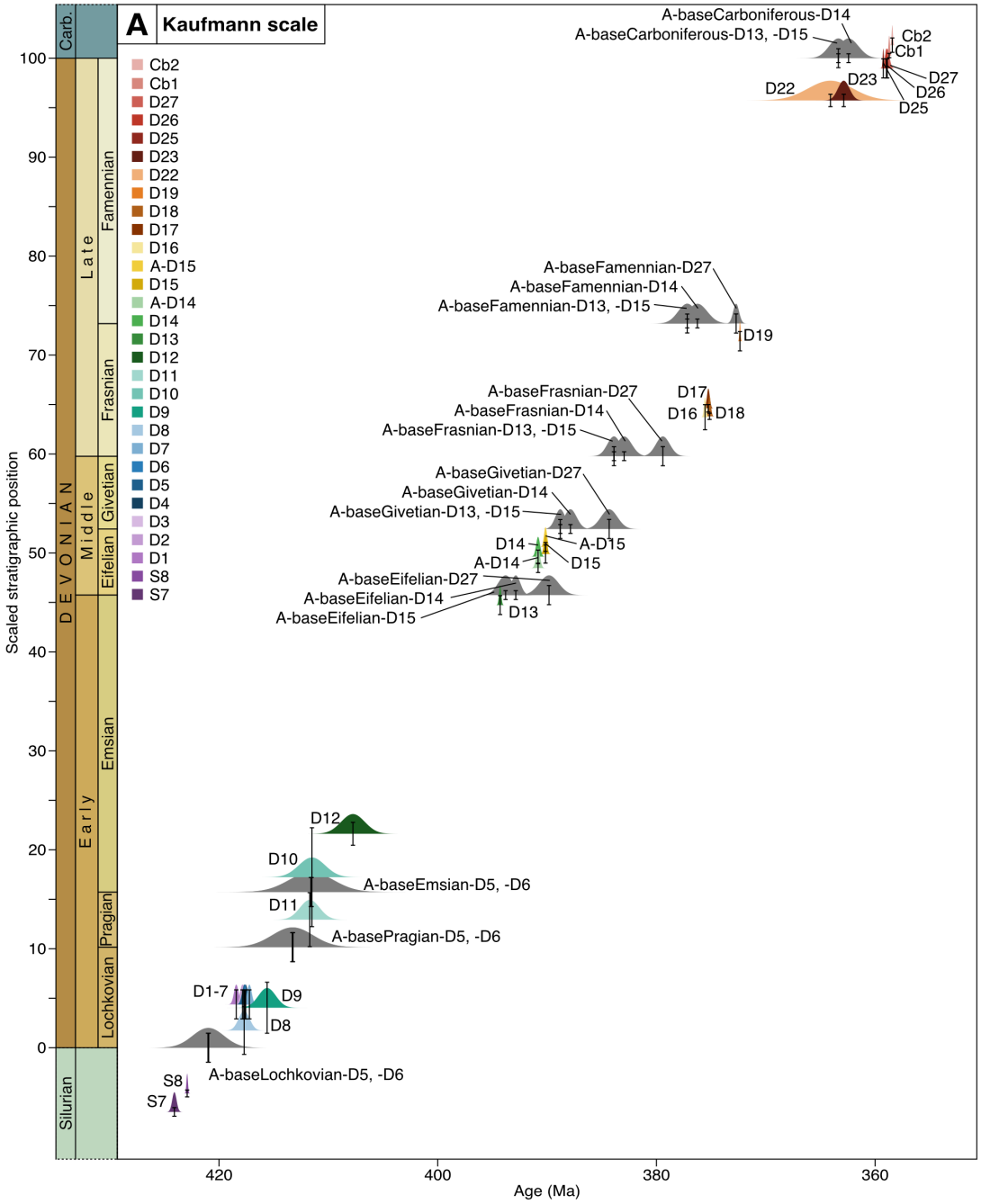

Figure C3.5.A. Radioisotopic ages and relative stratigraphic positions of age-depth model inputs based on the Kaufmann scale. The colored probability density functions illustrate the radioisotopic age constraints. The dark gray probability density functions illustrate the anchored and extrapolated astrochronologic constraints for the model, described below. The vertical error bars show the scaled stratigraphic uncertainty associated with each age constraint.

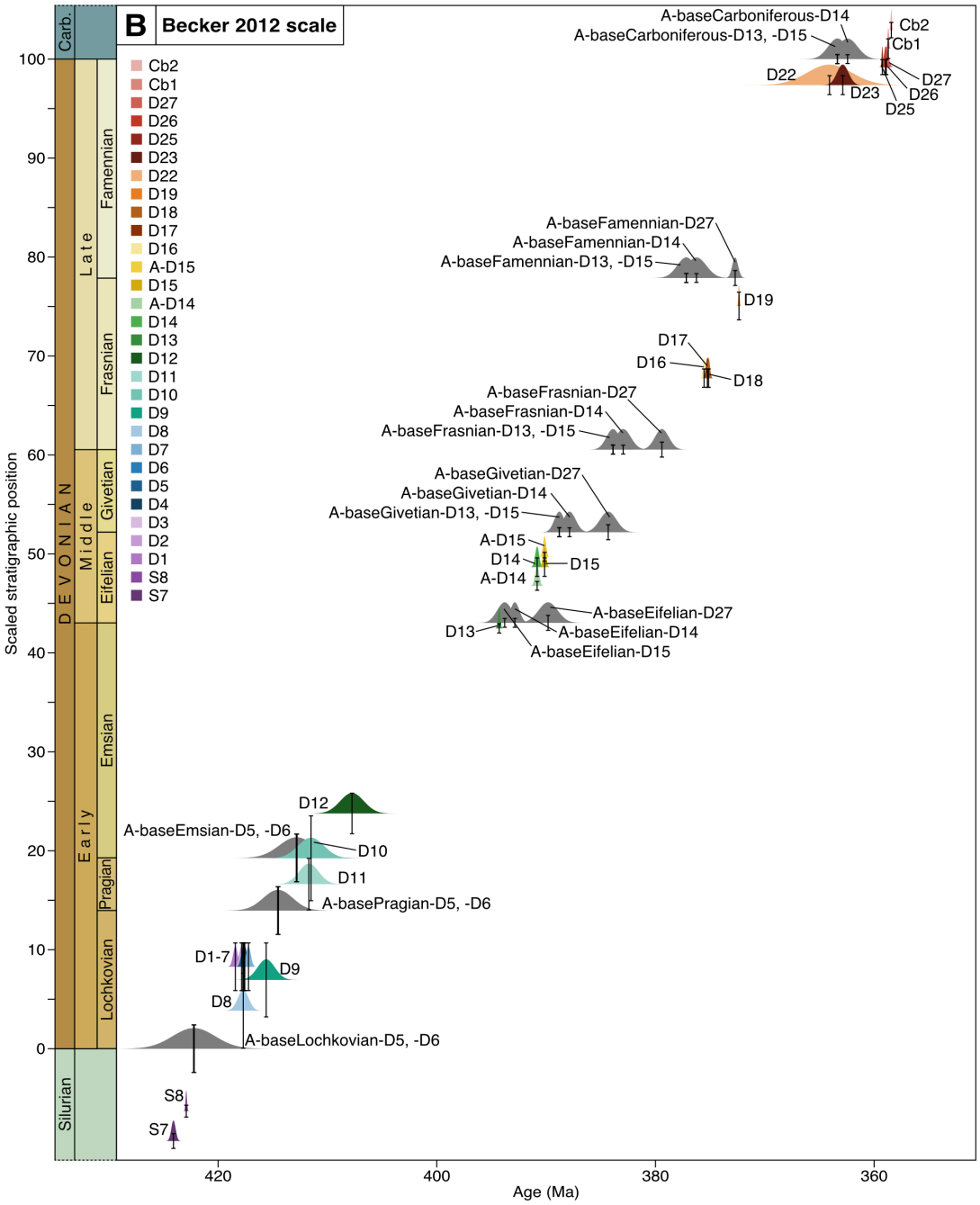

Figure C3.5.B. Radioisotopic ages and relative stratigraphic positions of age-depth model inputs based on the Becker 2012 scale. See caption to Figure C3.5.A. for more detail.

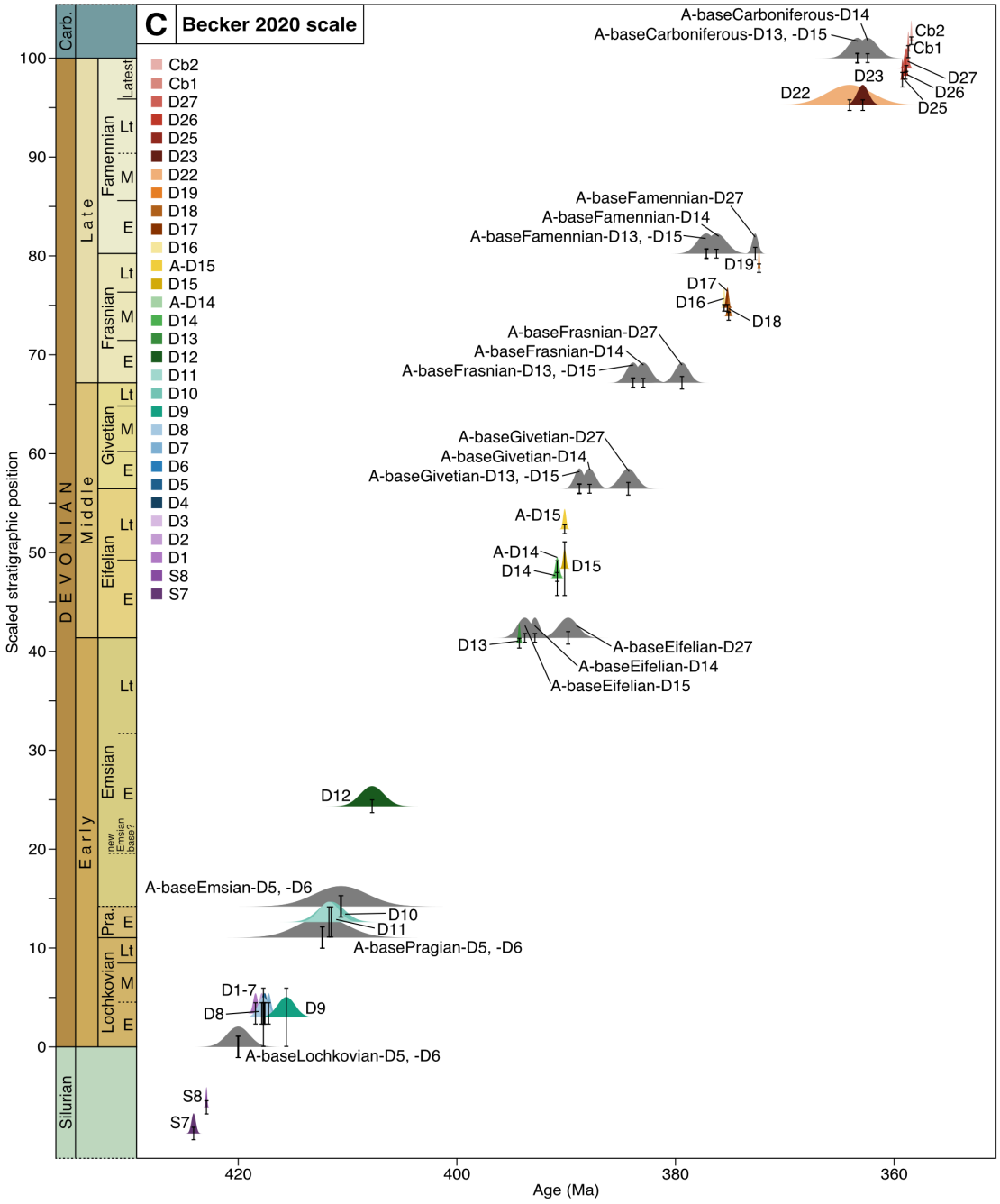

Figure C3.5.C. Radioisotopic ages and relative stratigraphic positions of age-depth model inputs based on the Becker 2020 scale. See caption to Figure C3.5.A. for more detail.

Astrochronology Constraints for Model

The process of incorporating floating astrochronology Stage durations into the age-depth models involves anchoring the floating durations on radioisotopic ages. We used astrochronology duration estimates for entire Stages (studies described below), revised the uncertainties as necessary to include cycle counting error and stratigraphic uncertainty, and combined durations and uncertainties together when multiple durations were available for a single Stage (Famennian, Givetian, and Eifelian Stages; see the Chapter Three for equations used to combine durations and uncertainties). It would be possible to create astrochronology model inputs based on individual Stage durations, rather than combined durations, or model inputs based on astrochronology durations less than the length of a Stage, but we opted to use one combined duration for each Stage to allow us to focus on the effect of how the durations are anchored and chained together rather than the variations in different astrochronology studies. In one case, however, we used a duration from an individual study (Eifelian Stage; Pas et al., 2021) because we had radioisotopic ages (D14, D15) from the same section as the cyclostratigraphy work and could thus anchor the astrochronology directly on K-bentonites from the same section. We linked combined Stage durations (Table 3.4.) to some of the radioisotopic ages described in the previous section (D5, D6, D13, D27). These anchors allowed us to extrapolate up or down through the Devonian to create 26 astrochronology inputs for the age-depth model (Figure C3.5.).

In the anchoring process, we summed Gaussian distributions of radioisotopic ages and uniform distributions of astrochronology durations to extrapolate to the Stage boundary of interest. We used the mean and standard deviation of the resulting summed

distribution as the Stage boundary age. When the anchoring age fell within a Stage, we proportionally divided the astrochronology duration and uncertainty according to the relative stratigraphic position within the Stage. For example, if an anchoring age was located one-third of the way up from the base of a Stage, one-third of the duration and uncertainty would be allocated to the Stage below the midpoint of the anchoring age and two-thirds of the duration and uncertainty would be allocated to the Stage above the midpoint of the anchoring age. To extrapolate up or down the time scale, we took the summed distribution for a Stage boundary and added the uniform distribution of the next astrochronology duration up or down the time scale. Again, we used the mean and standard deviation of the new summed distribution as the age of the next Stage boundary. Using the mean and standard deviation of the summed distribution assumes a normal distribution which was generally a good approximation for the summed distributions, particularly as the extrapolation processes added more distributions together. See Figure C3.4. for a graphical explanation of this process on anchor D14 and Figures C3.5. and C3.6. for documentation of how this process was done for anchors D15, D5, and D6.

Lochkovian: Da Silva et al. (2016) determined the duration of the Lochkovian Stage to be 7.7 ± 2.8 Myr using records from the Czech Republic of magnetic susceptibility and gamma ray spectrometry analyzed by multiple spectral analysis and statistical techniques. They relied on the 405 kyr eccentricity metronome to determine the duration of the Stage. Their uncertainty of 2.8 Myr describes the uncertainty in cycle counting in the section and the uncertainty in the location of the Lochkovian boundaries in the formation studied. We did not revise this uncertainty estimate because it included at least one cycle counting error as well as stratigraphic uncertainty.

Pragian: Da Silva et al. (2016) determined the duration of the Pragian Stage to be 1.7 ± 0.7 Myr using records from the Czech Republic of magnetic susceptibility and gamma ray spectrometry analyzed by multiple spectral analysis and statistical techniques. As with their Lochkovian work, they used the 405 kyr eccentricity metronome to determine the duration of the Pragian, and their uncertainty describes uncertainty in cycle counting and in the location of the boundaries of the formation studied. We did not revise this uncertainty estimate because it included at least one cycle counting error as well as stratigraphic uncertainty.

Emsian: To our knowledge, there is no cyclostratigraphic study on the duration of the Emsian.

Eifelian: Ellwood et al. (2015) determined the Eifelian Stage to be 6.28 Myr long and did not report an uncertainty. Their study used magnetic susceptibility records from Morocco to identity signals of the 405 kyr eccentricity cycle. We estimate uncertainty to be ± 1.00 Myr, composed of two 405 kyr cycle counting errors and two 200 kyr uncertainties to account for stratigraphic uncertainty on Stage boundaries.

Pas et al. (2021) determined the duration of the Eifelian Stage to be 5 Myr using the 100 kyr eccentricity cycle. They did not report a numerical value that represents all of the uncertainty on their reported Eifelian duration, noting that uncertainty in the duration can be due to stratigraphic uncertainty on the position of the Eifelian boundaries, cycle counting uncertainty, the use of an artificial signal representing areas where ash bed data has been omitted, and uncertainty due to differences in the results from tuning versus the average spectral misfit technique. To account for these uncertainties in the age-depth model, we assigned a numerical value for the uncertainty of the Eifelian duration of ±

0.80 Myr. We arrived at this uncertainty by adding one 405 kyr cycle counting error and two 200 kyr uncertainties to account for stratigraphic uncertainty on Stage boundaries.

The section that Pas et al. (2021) sampled at the Seneca Stone Quarry east of Fayette, New York is the same section from which we sampled the Tioga F (D15) and Tioga B (D14; referred to as the Onondaga Indian Nation bentonite by Pas et al. (2021)) ash beds. We used D14 and D15 as points on which to anchor the floating duration of Pas et al. (2021). We used our radioisotopic ages for D14 and D15 and the position within the stage according to Pas et al. (2021) to create A-D14 and A-D15 as model inputs.

Our combined duration and uncertainty for the Eifelian is 5.50 ± 0.39 Myr, computed using the equations in Chapter Three.

Givetian: With no radioisotopic ages available for the Givetian, astrochronology provides a useful constraint on the duration of the Givetian Stage.

House (1995) estimated the duration of the Givetian at 6.5 Myr based on a section in France with microcyclicity caused by precession. With no uncertainty provided, we use an arbitrary 30% uncertainty (± 1.95 Myr) on the duration to account for counting errors and uncertainty on the precession period.

Ellwood et al. (2011) used a model of the 405 kyr eccentricity cycle in the Givetian, tested against and refined by magnetic susceptibility records from sections in France, Morocco, and the eastern United States, to determine a 5.6 Myr duration for the Givetian. They did not report a numerical uncertainty value, so we estimate uncertainty to be ± 1.10 Myr, composed of two 405 kyr cycle counting errors and three 200 kyr uncertainties to account for the stratigraphic uncertainty in the composite construction.

De Vleeschouwer et al. (2014) used the 405 kyr eccentricity cycle in magnetic susceptibility records of Belgium sections to determine a duration of the Givetian Stage of 4.35 ± 0.45 Myr. The 0.45 Myr uncertainty is due to stratigraphic uncertainty in the Stage boundaries and cycle counting uncertainty, and we revised this uncertainty to ± 0.75 Myr based on an additional three 100 kyr uncertainties to account for the stratigraphic uncertainty in the composite construction.

Our combined duration and uncertainty for the Givetian is 4.91 ± 0.35 Myr, computed using the equations in Chapter Three.

Frasnian: De Vleeschouwer et al. (2012) determined the duration of the Frasnian to be 6.5 ± 0.4 Myr based on 405 kyr eccentricity cycles in magnetic susceptibility data from Alberta, Canada. The uncertainty on this duration is based on one cycle counting error, and the stratigraphic uncertainty of the Stage boundaries is assumed to be small and encompassed by the cycling counting uncertainty of 0.405 Myr. Whalen et al. (2016) revised the duration of the Frasnian to 6.7 Myr after reassessing the De Vleeschouwer et al. (2012) magnetic susceptibility data from Alberta, Canada, adding a half cycle of the 405 kyr eccentricity cycle. We revised the uncertainty to be ± 0.50 Myr by adding one 100 kyr uncertainty to account for stratigraphic uncertainty on Stage boundaries, resulting in a revised duration and uncertainty for the Frasnian of 6.7 ± 0.50 Myr.

Famennian: Pas et al. (2018) determined the duration of the Famennian to be 13.5 ± 0.5 Myr based on magnetic susceptibility records from three cores from the Illinois Basin, United States, analyzed with multiple spectral techniques and tuned to the 405 kyr eccentricity cycle or the 34.4 kyr obliquity cycle, depending on the core analyzed. We did

not revise this uncertainty estimate because it included at least one cycle counting error as well as stratigraphic uncertainty.

Ma et al. (2020) determined the duration of the Famennian to be 14.4 ± 0.28 Myr based on the spectral analysis of the 405 kyr eccentricity cycle in the calcium concentration of rocks from a continuous section in Lali, China. The uncertainty on their duration is based on stratigraphic uncertainty on Stage boundaries. We revised this uncertainty to ± 0.68 Myr by adding one 405 kyr counting error.

We combined the durations from Pas et al. (2018) and Ma et al. (2020) using a weighted average and a harmonic sum of revised uncertainties (see the equations in Chapter Three) and used a combined duration for the Famennian of 13.82 ± 0.16 Myr in our models.

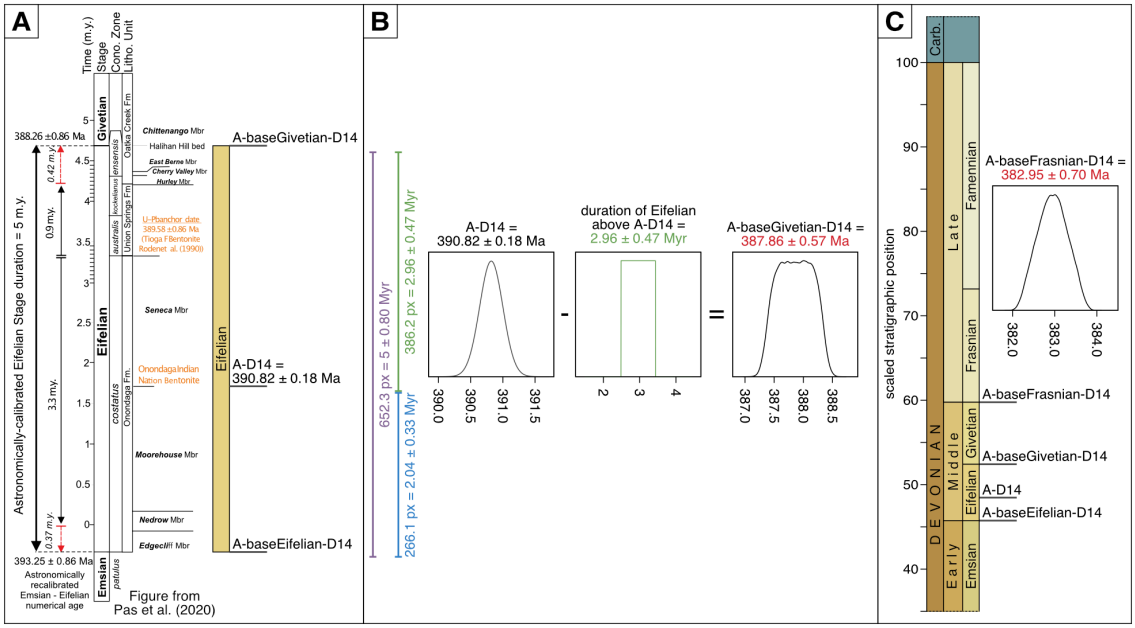

Figure C3.6. Graphical example of method for anchoring and extrapolating astrochronology constraints. (A) We noted the location of the marker bed (Onondaga Indian Nation Bentonite = D14) and the base and top of the section relative to the stratigraphic thickness of the Eifelian section from Pas et al. (2021). We paired the D14 radioisotopic age with the relative stratigraphic position of the D14 ash bed within the Eifelian section as measured by Pas et al. (2021) to create model input A-D14. (B) We sampled the normally distributed A-D14 radioisotopic age and the uniformly distributed astrochronology duration to extrapolate to the next position of interest. For example, to determine the age and uncertainty of A-baseGivetian-D14, we first determined the proportion of the stratigraphic thickness between ash bed A-D14 and the base of the Givetian relative to the thickness of the Eifelian section. We used this proportion as a proxy to estimate how much time in the astrochronology-determined Eifelian duration is likely associated with the time between the A-D14 ash bed and the base of the Givetian. In this example, A-D14 and A-baseGivetian-D14 are separated by 386.2 pixels in our graphics software, and that equates to 2.96 Myr if the Stage is 5 Myr long and 652.3 pixels tall. We proportionally distributed the astrochronology uncertainty in the same way. We sampled a normal distribution of the radioisotopic age of A-D14 and subtracted from it the uniform distribution representing the astronomical duration of the proportion of the Eifelian between A-D14 and A-baseGivetian-D14. This gave us a distribution for A-baseGivetian-D14 from which we extracted mean and two standard deviation values which can be used to approximate a normal distribution in the age-depth model. (C) We continued adding (or subtracting) distributions to determine the age of other Stage boundaries. For example, our combined duration for the Givetian is 4.91 ± 0.35 Myr (Table 3.4.), so we subtracted this from the age distribution of A-baseGivetian-D14 to determine an age and uncertainty for A-baseFrasnian-D14.

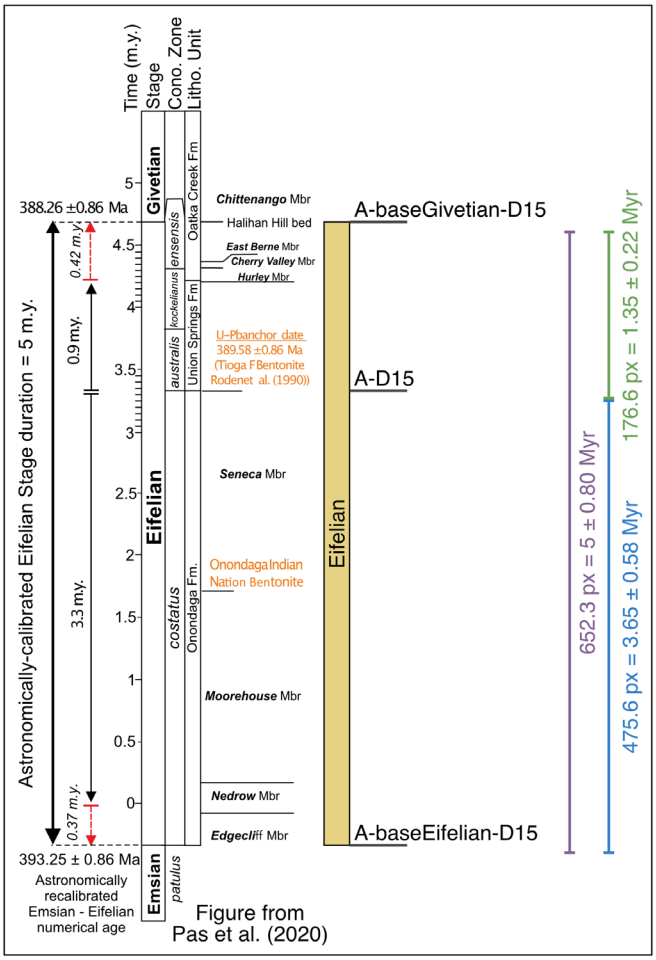

Figure C3.7. Following the same method described in Figure C3.4., we proportioned the astrochronology duration and uncertainty for the Eifelian based on the location of A-D15, the model input corresponding to the age of D15 and the stratigraphic position within the section measured by Pas et al. (2021).

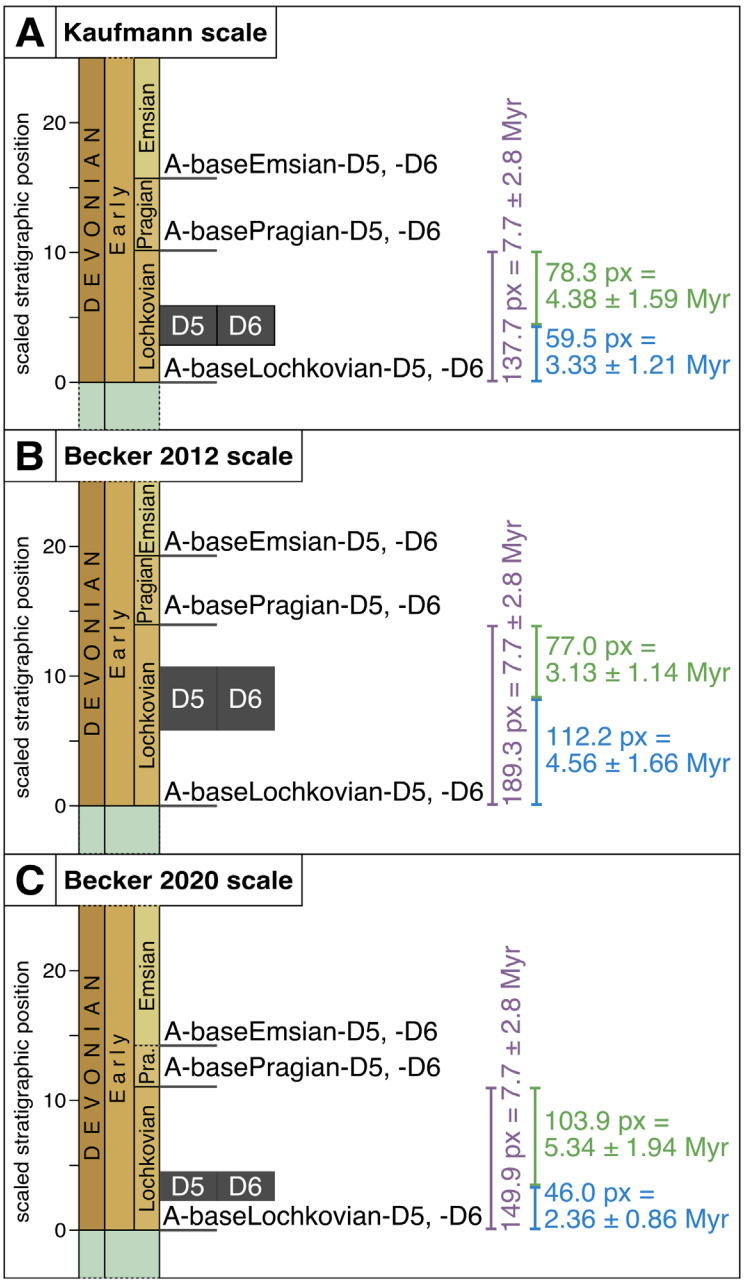

Figure C3.8. Following the same method described in Figure C3.4., we proportioned the astrochronology duration and uncertainty for the Lochkovian based on the stratigraphic positions of D5 and D6 on each of the three scales.

APPENDIX D

Supplementary Material for Chapter Three: LA-ICPMS Data for Hercules I K-Bentonite and Age-Depth Model Inputs and Results

Available as a separate file:

Table D3.1. Metadata for LA-ICPMS U-Pb analyses.

Table D3.2. U-Pb isotope ratios and trace element concentrations by LA-ICPMS: sample data.

Table D3.3. U-Pb isotope ratios and trace element concentrations by LA-ICPMS: standard data.

Table D3.4. R input data for astrochronology anchoring.

Table D3.5. Results from astrochronology anchoring.

Table D3.6. R input data for age-depth modeling of Kaufmann scale.

Table D3.7. R input data for age-depth modeling of Becker 2012 scale.

Table D3.8. R input data for age-depth modeling of Becker 2020 scale.

Table D3.9. Age-depth model results: Recalibrated conodont biozones of the Kaufmann scale.

Table D3.10. Age-depth model results: Recalibrated conodont biozones of the Becker 2012 scale.

Table D3.11. Age-depth model results: Recalibrated conodont biozones of the Becker 2020 scale.

APPENDIX E

Supplementary Material for Chapter Three: Modeling Code

The astrochronology extrapolations and age-depth modeling was done in R (R Core Team, 2021), and the scripts below and on GitHub (https://github.com/cohgeo/DevonianAgeDepthModel).

One R script is used to anchor astrochronology durations to determine the astrochronology age of Stage boundaries used in the age-depth modeling. The .csv files used as input in that script are available on GitHub and summarized in Table D3.4. The results of anchoring the floating astrochronology durations are provided in Table D3.5.

The other R script is used to run an age-depth model on Devonian radioisotopic and anchored astrochronology ages and their associated relative stratigraphic positions to predict the age of Devonian Stage boundaries and the ages of conodont biozones boundaries. The .csv files used as input in that script are available on GitHub and summarized in Tables D3.6., D3.7., and D3.8.

Running the age-depth model script results in recalibrated Stage and conodont biozone boundary ages and scaled stratigraphic positions for each scale. Because this procedure relies on a probabilistic model, the model results will vary slightly each time the model is run, even with the same starting parameters and data. Since the model highest density interval and 95% confidence interval will vary slightly between model runs, the linearization process will result in slightly different final Stage and conodont biozone boundary scaled stratigraphic positions. We have provided the conodont biozone model results in Tables D3.9., D3.10., and D3.11. with the caveat that these are one possible model outcome and running the code again could produce slight differences in the predicted ages and scaled stratigraphic positions. In sensitivity tests, we found that

Stage and conodont biozone boundary positions typically varied by an average of about 0.07 scaled stratigraphic position units (where 0 = the position of the base of the Devonian and 100 = the position of the base of the Carboniferous), and ages varied by an average of about 0.03 Ma.

R Script for Executing Age-Depth Modeling Procedure

```
# This script runs an age-depth model on Devonian ages and their associated
# relative stratigraphic position to predict the age of Devonian Stage
# boundaries and the age of conodont biozones boundaries.  This code is
# designed to be run in R.

# Updated 2020.09.10 CH

## SETUP ---------------------------------------------------------------------
--

# Clear all from your environment.
  # rm(list = ls())  # Uncomment if needed

# Install and load modifiedBChron from Robin Trayler's GitHub repository.
  # install.packages("devtools")  # Uncomment if needed
  # devtools::install_github("robintrayler/modifiedBChron")  # Uncomment if
needed
  library(modifiedBChron)

# Set working directory
  # Change the text in quotes to match your directory on your computer.
  setwd("/Users/claireharrigan/Dropbox/IGL +
research/Devonian/DevonianAgeDepthModel")


# IMPORT MODEL INPUTS -------------------------------------------------------
--

# The code required to run each model is the same, so to change which scale
you
# use for the starting point, uncomment and run the code below that
corresponds
# to your starting scale. To run the next model, clear everything from your
# environment and uncomment and run the code below that corresponds to the
next
# scale for which you want to run a model.

# Import model inputs.
  # KAUFMANN SCALE
    # # Import radioisotpic ages, anchored astrochronology durations, and
relative
    # # stratigraphic positions.
    # DevonianData <- read.csv("DevonianData_Kaufmann.csv",
```

```
    #                           header = TRUE)
    # # Import relative stratigraphic position of Stages.
    # DevonianPositions <- read.csv("DevonianPositions_Kaufmann.csv",
    #                               header = TRUE)
    # # Import relative stratigraphic position of conodont biozone positions.
    # # Because the Kaufmann scale is comprised of an alternative and a
standard
    # # scale, you will need to run agePredict for each of the lines below.
    # DevonianPositions.c <- read.csv("DevonianPositions_Kaufmann_alt
conodont.csv",
    #                                 header = TRUE)
    # DevonianPositions.c <- read.csv("DevonianPositions_Kaufmann_std
conodont.csv",
    #                                 header = TRUE)
    # # Save a title for the plots.
    # title <- "Kaufmann scale"

  # BECKER 2012 SCALE
    # # Import radioisotpic ages, anchored astrochronology durations, and
relative
    # # stratigraphic positions.
    # DevonianData <- read.csv("DevonianData_Becker2012.csv",
    #                          header = TRUE)
    # # Import relative stratigraphic position of Stages.
    # DevonianPositions <- read.csv("DevonianPositions_Becker2012.csv",
    #                               header = TRUE)
    # # Import relative stratigraphic position of conodont biozone positions.
    # DevonianPositions.c <- read.csv("DevonianPositions_Becker
2012_conodont.csv",
    #                                 header = TRUE)
    # # Save a title for the plots.
    # title <- "Becker 2012 scale"

  # BECKER 2020 SCALE
    # # Import radioisotpic ages, anchored astrochronology durations, and
relative
    # # stratigraphic positions.
    # DevonianData <- read.csv("DevonianData_Becker2020.csv",
    #                          header = TRUE)
    # # Import relative stratigraphic position of Stages.
    # DevonianPositions <- read.csv("DevonianPositions_Becker2020.csv",
    #                               header = TRUE)
    # # Import relative stratigraphic position of conodont biozone positions.
    # DevonianPositions.c <- read.csv("DevonianPositions_Becker
2020_conodont.csv",
    #                                 header = TRUE)
    # # Save a title for the plots.
    # title <- "Becker 2020 scale"


## VISUALIZE MODEL INPUTS ------------------------------------------------
--

# Visualize the age distributions and relative stratigraphic positions prior
to
```

```
# running the model.
  ageDepthPlot(ages = DevonianData$age,
               ageSds = DevonianData$uncertainty_2sig,
               positions = DevonianData$midpoint,
               positionThicknesses = DevonianData$halfwidth,
               distTypes = DevonianData$distTypes,
               ids = DevonianData$ids,
               xlim = c(435, 345),
               ylim = c(-10, 110),
               main = title)


## RUN MODEL ------------------------------------------------------------
--

# Run ageModel function to create an age-depth model.
  DevonianModel <- ageModel(ages = DevonianData$age,
                            ageSds = DevonianData$uncertainty_2sig,
                            positions = DevonianData$midpoint,
                            positionThicknesses = DevonianData$halfwidth,
                            distTypes = DevonianData$distTypes,
                            ids = DevonianData$ids,
                            predictPositions = seq(from = -20,
                                                   to = 120,
                                                   by = 0.25))

# Or,
# Load in previous model results.
  # Uncomment and run the following code to load a previously saved model.
  # # KAUFMANN SCALE
  #   DevonianModel <- readRDS("DevonianModel_Kaufmann.rds")
  # # BECKER 2012 SCALE
  #   DevonianModel <- readRDS("DevonianModel_Becker2012.rds")
  # # BECKER 2020 SCALE
  #   DevonianModel <- readRDS("DevonianModel_Becker2020.rds")

## SAVE MODEL ------------------------------------------------------------
--

# Save model.
  # Uncomment and run the following code to save the ouput of the ageModel
  # function (write DevonianModel to a file) so that it can be loaded into R
and
  # used again later.
  # # KAUFMANN SCALE
  #   saveRDS(DevonianModel, file = "DevonianModel_Kaufmann.rds",
  #           ascii = FALSE, version = NULL, compress = TRUE, refhook = NULL)
  # # BECKER 2012 SCALE
  #   saveRDS(DevonianModel, file = "DevonianModel_Becker2012.rds",
  #           ascii = FALSE, version = NULL, compress = TRUE, refhook = NULL)
  # # BECKER 2020 SCALE
  #   saveRDS(DevonianModel, file = "DevonianModel_Becker2020.rds",
  #           ascii = FALSE, version = NULL, compress = TRUE, refhook = NULL)
```

```
## PREDICT STAGE OR CONODONT BIOZONE BOUNDARY AGES ---------------------------
--

# Predict the age of the Stage boundaries using the agePredict function.
  DevonianPredict <- agePredict(model = DevonianModel,
                                newPositions =
DevonianPositions$predictPositions,
                                ids = DevonianPositions$ids)
  # Save the median and 95% HDI bounds from the model results.
  HDI <- DevonianPredict$HDI

# Predict the age of the conodont biozone boundaries using the agePredict
# function.
  DevonianPredict.c <- agePredict(model = DevonianModel,
                                newPositions =
DevonianPositions.c$predictPositions,
                                ids = DevonianPositions.c$ids)
  # Save the median and 95% HDI bounds from the model results.
  HDI.c <- DevonianPredict.c$HDI


## SAVE STAGE OR CONODONT BIOZONE BOUNDARY AGES -----------------------------
--

# Save model results (predicted Stage or conodont biozone boundary ages).
  # Uncomment and run the following code to write the median and highest
  # denisty interval results for predicted positions to to a csv file.
  # # KAUFMANN SCALE
  #   write.csv(HDI,
  #             file = "Results_Kaufmann_stage ages.csv")
  #   write.csv(HDI.c,
  #             file = "Results_Kaufmann_alternative conodont biozone
ages.csv")
  #   write.csv(HDI.c,
  #             file = "Results_Kaufmann_standard conodont biozone ages.csv")
  # # BECKER 2012 SCALE
  #   write.csv(HDI,
  #             file = "Results_Becker2012_stages ages.csv")
  #   write.csv(HDI.c,
  #             file = "Results_Becker2012_conodont biozone ages.csv")
  # # BECKER 2020 SCALE
  #   write.csv(HDI,
  #             file = "Results_Becker2020_stage ages.csv")
  #   write.csv(HDI.c,
  #             file = "Results_Becker2020_conodont biozone ages.csv")


## VISUALIZE MODEL RESULTS --------------------------------------------------
--

# Visualize the parameter plots.
  # posteriorPlot(model = DevonianModel, prob = 0.95)

# Visualize the age-depth model with a plot of the likelihoods illustrated as
# PDFs.
```

```
  modelPlot(model = DevonianModel,
            scale = 0.5, predictLabels = c("both"), legend = c("adjacent"),
            main = title,
            xlim = c(435, 345),
            ylim = c(-10, 110))
  # Add a dashed line that goes from the model median position at the base of
  # the Devonian to the model median position at the top of the Devonian. This
  # line shows the position of the model median if the model is linearized.
  lines(x = c(HDI[which(HDI$ids == "baseLochkovian"), "0.5"],
              HDI[which(HDI$ids == "baseCarboniferous"), "0.5"]),
        y = c(0, 100),
        col = "black",
        lty = "dashed",
        lwd = 2)

# Visualize the age model plot with the likelihoods illustrated as PDFs and
# the predicted Stage boundary positions shown as red error bars.
  # modelPlot(model = DevonianModel,
  #           agePredictOutput = DevonianPredict,
  #           scale = 0.5, predictLabels = c("both"), legend = c("adjacent"),
  #           main = title)

# Visualize the age model plot with the likelihoods illustrated as PDFs and
# the predicted conodont biozone boundary positions shown as red error bars.
  # modelPlot(model = DevonianModel,
  #           agePredictOutput = DevonianPredict.c,
  #           scale = 0.5, predictLabels = c("both"), legend = c("adjacent"),
  #           main = title)


## LINERIZE MODEL, EXTRACT STAGE POSITIONS ON REVISED SCALE ------------------
--

# Calculate an equation for a line that passes through the base of the
Devonian
# and the base of the Carboniferous.
  # Store the values for this line in a list.
  linearModel <- list(
    m = (100 - 0) / (HDI[which(HDI$ids == "baseCarboniferous"), "0.5"] -
                       HDI[which(HDI$ids == "baseLochkovian"), "0.5"]),
    b = (((100 - 0) / (HDI[which(HDI$ids == "baseCarboniferous"), "0.5"] -
                         HDI[which(HDI$ids == "baseLochkovian"), "0.5"])) *
           HDI[which(HDI$ids == "baseLochkovian"), "0.5"]) * -1)

# Make a data frame of x and y values before and after rescaling.
  # Make data frame, save names of positions.
  rescaledScale <- data.frame(ids = DevonianPositions$ids,
                    # Save original y values (input into model).
                    y0 = DevonianPositions$predictPositions,
                    # Save the x value of the linearized model at horizons of
                    # interest (same as x values produced by the model).
                    x0 = HDI$`0.5`,
                    # Save y value of the linearized model at x0.
                    y.rescale = (linearModel$m * HDI$`0.5`) + linearModel$b)
```

```
# Plot difference between positions on model before and after rescaling.
  # Plot crosses representing Stage positions of ages from the age-depth
model.
  plot(x = rescaledScale$x0,
       y = rescaledScale$y0,
       type = "p",
       main = title,
       xlim = c(435, 345),
       ylim = c(-10, 110),
       xlab = "age (Ma)",
       ylab = "scaled stratigraphic position",
       col = "blue",
       pch = 3)
  # Plot crosses representing shifting Stage positions along the y axis to
  # linearize the model results.
  points(x = rescaledScale$x0,
         y = rescaledScale$y.rescale,
         col = "red",
         pch = 3)
  # Add a legend.
  legend(425, 100,
         title = "Stage positions",
         legend = c("age-depth model", "linearized model"),
         col = c("blue", "red"),
         pch = 3)


##  LINERIZE MODEL, EXTRACT CONODONT BIOZONE POSITIONS ON REVISED SCALE ------
--

# Calculate an equation for a line that passes through the base of the
Devonian
# and the base of the Carboniferous.
  # Store the values for this line in a list.
  linearModel.c <- list(
    m = (100 - 0) / (HDI.c[which(HDI.c$ids == "baseCb"), "0.5"] -
                       HDI.c[which(HDI.c$ids == "baseD"), "0.5"]),
    b = (((100 - 0) / (HDI.c[which(HDI.c$ids == "baseCb"), "0.5"] -
                         HDI.c[which(HDI.c$ids == "baseD"), "0.5"])) *
           HDI.c[which(HDI.c$ids == "baseD"), "0.5"]) * -1)

# Make a data frame of x and y values before and after rescaling.
  # Make data frame, save names of positions.
  rescaledScale.c <- data.frame(ids = DevonianPositions.c$ids,
                  # Save original y values (input into model).
                  y0 = DevonianPositions.c$predictPositions,
                  # Save the x value of the linearized model at horizons of
                  # interest (same as x values produced by the model).
                  x0 = HDI.c$`0.5`,
                  # Save y value of the linearized model at x0.
                  y.rescale = (linearModel.c$m * HDI.c$`0.5`) +
linearModel.c$b)

# Plot difference between positions on model before and after rescaling.
```

```
  # Plot crosses representing Stage positions of ages from the age-depth
model.
  plot(x = rescaledScale.c$x0,
       y = rescaledScale.c$y0,
       type = "p",
       main = title,
       xlim = c(435, 345),
       ylim = c(-10, 110),
       xlab = "age (Ma)",
       ylab = "scaled stratigraphic position",
       col = "blue",
       pch = 3)
  # Plot crosses representing shifting Stage positions along the y axis to
  # linearize the model results.
  points(x = rescaledScale.c$x0,
         y = rescaledScale.c$y.rescale,
         col = "red",
         pch = 3)
  # Add a legend.
  legend(425, 100,
         title = "conodont biozone positions",
         legend = c("age-depth model", "linearized model"),
         col = c("blue", "red"),
         pch = 3)


## SAVE STAGE OR CONODONT BIOZONE BOUNDARY RESCALED STRATIGRAPHIC POSITIONS --
--

# Save model results (predicted Stage or conodont biozone boundary ages).
  # Uncomment and run the following code to write the median and highest
  # denisty interval results for predicted positions to to a csv file.
  # # KAUFMANN SCALE
  #   write.csv(rescaledScale,
  #     file = "Results_Kaufmann_rescaled stage positions.csv")
  #   write.csv(rescaledScale.c,
  #     file = "Results_Kaufmann_rescaled alternative conodont biozone
positions.csv")
  #   write.csv(rescaledScale.c,
  #     file = "Results_Kaufmann_rescaled standard conodont biozone
positions.csv")
  # # BECKER 2012 SCALE
  #   write.csv(rescaledScale,
  #     file = "Results_Becker2012_rescaled stage positions.csv")
  #   write.csv(rescaledScale.c,
  #     file = "Results_Becker2012_rescaled conodont biozone positions.csv")
  # # BECKER 2020 SCALE
  #   write.csv(rescaledScale,
  #     file = "Results_Becker2020_rescaled stage positions.csv")
  #   write.csv(rescaledScale.c,
  #     file = "Results_Becker2020_rescaled conodont biozone positions.csv")
```

R Script for Anchoring Floating Astrochronology Durations.

```
# This script calculates ages and propagates uncertainty for floating
# astrochronology Stage durations.

# Updated 2021.06.18 CH

## SETUP ---------------------------------------------------------------
------

# Clear all from workspace/environment.
# rm(list = ls())  # Uncomment if needed

# Import data frames.
  # Import data frame of ages and uncertainties of anchor points.
  DF.ast.anchors <- read.csv("DF.ast.anchors.csv",
                             header = TRUE)
  # Import data frame of durations and uncertainties of Stages and parts
of
  # Stages.
  DF.ast.dur <- read.csv("DF.ast.dur.csv",
                         header = TRUE)
  # Import data frame to hold results of the astrochronology propagation
done in
  # this script.
  DF.ast <- read.csv("DF.ast.csv",
                     header = TRUE)

# # Indicate which of the conodont scales (Kaufmann, Becker 2012, Becker
2020) to
# # use for this iteration of running the script below.
#   # KAUFMANN SCALE
#     scale <- "Kaufmann"
#     # Set where to store extrapolation results in DF.ast.
#     age.col <- 2
#     age.uncert.col <- 3
#   # BECKER 2012 SCALE
#     # scale <- "Becker 2012"
#     # # Set where to store extrapolation results in DF.ast.
#     # age.col <- 4
#     # age.uncert.col <- 5
#   # BECKER 2020 SCALE
#     # scale <- "Becker 2020"
#     # # Set where to store extrapolation results in DF.ast.
#     # age.col <- 6
#     # age.uncert.col <- 7


## PLOTTING TEMPLATES --------------------------------------------------
------

# Plot anchoring age distribution (Gaussian).
```

```
  # Set the anchoring age to plot.
  anchor <- "D6"
  # Create a sequence of x values.
  x.G <- seq(DF.ast.anchors[which(DF.ast.anchors$anchor == anchor),
                            colnames(DF.ast.anchors) == "age"] -
               (5 * DF.ast.anchors[which(DF.ast.anchors$anchor == anchor),
                                   colnames(DF.ast.anchors) ==
"age.uncertainty"]),
             DF.ast.anchors[which(DF.ast.anchors$anchor == anchor),
                            colnames(DF.ast.anchors) == "age"] +
               (5 * DF.ast.anchors[which(DF.ast.anchors$anchor == anchor),
                                   colnames(DF.ast.anchors) ==
"age.uncertainty"]),
             length = 1000)
  # Calculate y values based on age and uncertainty.
  y.G <- dnorm(x.G,
               DF.ast.anchors[which(DF.ast.anchors$anchor == anchor),
                              colnames(DF.ast.anchors) == "age"],
               DF.ast.anchors[which(DF.ast.anchors$anchor == anchor),
                              colnames(DF.ast.anchors) ==
"age.uncertainty"])
  # Make plot of age distribution.
  plot(x.G, y.G / max(y.G),
       type = "l", main = anchor, xlab = "Age (Ma)", ylab = "Probability")

# Plot an astrochronology duration distribution (uniform).
  # Set the Stage duration to plot.
  stage <- "EifelianPas.above.A-D14"
  # Create a squence of x values.
  x.U <- seq((DF.ast.dur[which(DF.ast.dur$stage == stage),
                         colnames(DF.ast.dur) == "duration"] -
                DF.ast.dur[which(DF.ast.dur$stage == stage),
                           colnames(DF.ast.dur) == "dur.uncertainty"] -
1),
             (DF.ast.dur[which(DF.ast.dur$stage == stage),
                         colnames(DF.ast.dur) == "duration"] +
                DF.ast.dur[which(DF.ast.dur$stage == stage),
                           colnames(DF.ast.dur) == "dur.uncertainty"] +
1),
             length = 1000)
  y.U <- dunif(x.U,
               DF.ast.dur[which(DF.ast.dur$stage == stage),
                          colnames(DF.ast.dur) == "duration"] -
                 DF.ast.dur[which(DF.ast.dur$stage == stage),
                            colnames(DF.ast.dur) == "dur.uncertainty"],
               DF.ast.dur[which(DF.ast.dur$stage == stage),
                          colnames(DF.ast.dur) == "duration"] +
                 DF.ast.dur[which(DF.ast.dur$stage == stage),
                            colnames(DF.ast.dur) == "dur.uncertainty"])
  # Make plot of age distribution.
  plot(x.U, y.U / max(y.U),
       type = "l", main = stage, xlab = "Age (Ma)", ylab = "Probability")
```

```
## ANCHOR: D27 ------------------------------------------------------------
------
# NOTE: The ages for the Stage boundaries based on anchors D27, D15, D14,
and
# D13 are the same for the three scales (Kaufmann, Becker 2012, Becker
2020).

# Using D27 as an anchor, determine the age and uncertainty of the next
Stage
# boundary down in depth. Sample a Gaussian distribution for the anchoring
age
# and a uniform distribution for the astrochronology duration n times to
get a
# new distribution representing the age of the Stage boundary of interest.
# Use the mean and two standard deviation value to represent the age of
that
# distribution (assumes a Gaussian distribution).

# Set the number of times to randomly sample each distribution.
  n <- 100000

# Set the anchor point and Stage.
  anchor <- "D27"
  stage <- "Famennian"

# Create a new distribution for the base of the Famennian.
  # Sample the distribution for D27. Divide age.uncertainty by 2 to get 1
sigma.
  dist.A_baseFamennian_D27 <- rnorm(n,
    DF.ast.anchors[which(DF.ast.anchors$anchor == anchor),
                   colnames(DF.ast.anchors) == "age"],
    DF.ast.anchors[which(DF.ast.anchors$anchor == anchor),
                   colnames(DF.ast.anchors) == "age.uncertainty"] / 2) +
    # Sample the distribution of the Famennian duration.
    runif(n,
          DF.ast.dur[which(DF.ast.dur$stage == stage),
                     colnames(DF.ast.dur) == "duration"] -
            DF.ast.dur[which(DF.ast.dur$stage == stage),
                       colnames(DF.ast.dur) == "dur.uncertainty"],
          DF.ast.dur[which(DF.ast.dur$stage == stage),
                     colnames(DF.ast.dur) == "duration"] +
            DF.ast.dur[which(DF.ast.dur$stage == stage),
                       colnames(DF.ast.dur) == "dur.uncertainty"])
# Make a density plot of the new distribution.
  plot(density(dist.A_baseFamennian_D27))
# Make a histogram of the new distribution.
  hist(dist.A_baseFamennian_D27)
# Save results.
  # Calculate the mean of the new distribution to use as the new age for
  # the base of the Famennian.
```

```
  DF.ast[which(DF.ast$ID == "A-baseFamennian-D27"), c(2, 4, 6)] <-
    mean(dist.A_baseFamennian_D27)
  # Calculate the standard deviation of the new distribution and multiply
it by
  # 2 to use as the 2-sigma uncertainty for this distribution.
  DF.ast[which(DF.ast$ID == "A-baseFamennian-D27"), c(3, 5, 7)] <-
    sd(dist.A_baseFamennian_D27) * 2

# Create a new distribution for the base of the Frasnian.
  stage <- "Frasnian"
  # Sample dist.A_baseFamennian_D27 and the duration of the Frasnian.
  dist.A_baseFrasnian_D27 <- sample(dist.A_baseFamennian_D27,
                                    size = n,
                                    replace = TRUE,
                                    prob = dist.A_baseFamennian_D27) +
    runif(n,
          DF.ast.dur[which(DF.ast.dur$stage == stage),
                     colnames(DF.ast.dur) == "duration"] -
            DF.ast.dur[which(DF.ast.dur$stage == stage),
                       colnames(DF.ast.dur) == "dur.uncertainty"],
          DF.ast.dur[which(DF.ast.dur$stage == stage),
                     colnames(DF.ast.dur) == "duration"] +
            DF.ast.dur[which(DF.ast.dur$stage == stage),
                       colnames(DF.ast.dur) == "dur.uncertainty"])
  # Plot results.
  plot(density(dist.A_baseFrasnian_D27))
  # Save results.
  DF.ast[which(DF.ast$ID == "A-baseFrasnian-D27"), c(2, 4, 6)] <-
    mean(dist.A_baseFrasnian_D27)  # mean
  DF.ast[which(DF.ast$ID == "A-baseFrasnian-D27"), c(3, 5, 7)] <-
    sd(dist.A_baseFrasnian_D27) * 2  # 2 sigma

# Create a new distribution for the base of the Givetian.
  stage <- "Givetian"
  # Sample dist.A_baseFrasnian_D27 and the duration of the Givetian.
  dist.A_baseGivetian_D27 <- sample(dist.A_baseFrasnian_D27,
                                    size = n,
                                    replace = TRUE,
                                    prob = dist.A_baseFrasnian_D27) +
    runif(n,
          DF.ast.dur[which(DF.ast.dur$stage == stage),
                     colnames(DF.ast.dur) == "duration"] -
            DF.ast.dur[which(DF.ast.dur$stage == stage),
                       colnames(DF.ast.dur) == "dur.uncertainty"],
          DF.ast.dur[which(DF.ast.dur$stage == stage),
                     colnames(DF.ast.dur) == "duration"] +
            DF.ast.dur[which(DF.ast.dur$stage == stage),
                       colnames(DF.ast.dur) == "dur.uncertainty"])
  # Plot results.
  plot(density(dist.A_baseGivetian_D27))
  # Save results.
  DF.ast[which(DF.ast$ID == "A-baseGivetian-D27"), c(2, 4, 6)] <-
```

```
    mean(dist.A_baseGivetian_D27)  # mean
  DF.ast[which(DF.ast$ID == "A-baseGivetian-D27"), c(3, 5, 7)] <-
    sd(dist.A_baseGivetian_D27) * 2  # 2 sigma

# Create a new distribution for the base of the Eifelian.
  stage <- "EifelianCombined"
  # Sample dist.A_baseGivetian_D27 and the duration of the Eifelian.
  dist.A_baseEifelian_D27 <- sample(dist.A_baseGivetian_D27,
                                    size = n,
                                    replace = TRUE,
                                    prob = dist.A_baseGivetian_D27) +
    runif(n,
          DF.ast.dur[which(DF.ast.dur$stage == stage),
                     colnames(DF.ast.dur) == "duration"] -
            DF.ast.dur[which(DF.ast.dur$stage == stage),
                       colnames(DF.ast.dur) == "dur.uncertainty"],
          DF.ast.dur[which(DF.ast.dur$stage == stage),
                     colnames(DF.ast.dur) == "duration"] +
            DF.ast.dur[which(DF.ast.dur$stage == stage),
                       colnames(DF.ast.dur) == "dur.uncertainty"])
  # Plot results.
  plot(density(dist.A_baseEifelian_D27))
  # Save results.
  DF.ast[which(DF.ast$ID == "A-baseEifelian-D27"), c(2, 4, 6)] <-
    mean(dist.A_baseEifelian_D27)  # mean
  DF.ast[which(DF.ast$ID == "A-baseEifelian-D27"), c(3, 5, 7)] <-
    sd(dist.A_baseEifelian_D27) * 2  # 2 sigma


## ANCHOR: D15 -----------------------------------------------------------
------
# NOTE: The ages for the Stage boundaries based on anchors D27, D15, D14
and
# D13 are the same for the three scales (Kaufmann, Becker 2012, Becker
2020).

# Using D15 as an anchor, determine the age and uncertainty of the Stage
# boundaries.

# Set the anchor point.
  anchor <- "D15"

# Set the age and uncertainty of A-D15 to be the same as D15.
  DF.ast[which(DF.ast$ID == "A-D15"), c(2, 4, 6)] <-
    DF.ast.anchors[which(DF.ast.anchors$anchor == "D15"), 2]
  DF.ast[which(DF.ast$ID == "A-D15"), c(3, 5, 7)] <-
    DF.ast.anchors[which(DF.ast.anchors$anchor == "D15"), 3]

# Create a new distribution for the base of the Eifelian.
  # Set the Stage.
  stage <- "EifelianPas.below.A-D15"
```

```
  # Sample the distribution for A-D15. Divide age.uncertainty by 2 to get
1
  # sigma.
  dist.A_baseEifelian_D15 <- rnorm(n,
    DF.ast.anchors[which(DF.ast.anchors$anchor == anchor),
                   colnames(DF.ast.anchors) == "age"],
    DF.ast.anchors[which(DF.ast.anchors$anchor == anchor),
                   colnames(DF.ast.anchors) == "age.uncertainty"] / 2) +
    # Sample the distribution of the Eifelian duration below A-D15.
    runif(n,
          DF.ast.dur[which(DF.ast.dur$stage == stage),
                     colnames(DF.ast.dur) == "duration"] -
            DF.ast.dur[which(DF.ast.dur$stage == stage),
                       colnames(DF.ast.dur) == "dur.uncertainty"],
          DF.ast.dur[which(DF.ast.dur$stage == stage),
                     colnames(DF.ast.dur) == "duration"] +
            DF.ast.dur[which(DF.ast.dur$stage == stage),
                       colnames(DF.ast.dur) == "dur.uncertainty"])
  # Make a density plot of the new distribution.
  plot(density(dist.A_baseEifelian_D15))
  # Save results.
  DF.ast[which(DF.ast$ID == "A-baseEifelian-D15"), c(2, 4, 6)] <-
    mean(dist.A_baseEifelian_D15)
  DF.ast[which(DF.ast$ID == "A-baseEifelian-D15"), c(3, 5, 7)] <-
    sd(dist.A_baseEifelian_D15) * 2

# Create a new distribution for the base of the Givetian.
  stage <- "EifelianPas.above.A-D15"
  # Sample the distribution for A-D15. Divide age.uncertainty by 2 to get
1
  # sigma.
  dist.A_baseGivetian_D15 <- rnorm(n,
    DF.ast.anchors[which(DF.ast.anchors$anchor == anchor),
                   colnames(DF.ast.anchors) == "age"],
    DF.ast.anchors[which(DF.ast.anchors$anchor == anchor),
                   colnames(DF.ast.anchors) == "age.uncertainty"] / 2) -
    # Sample the distribution of the Eifelian duration below A-D15.
    runif(n,
          DF.ast.dur[which(DF.ast.dur$stage == stage),
                     colnames(DF.ast.dur) == "duration"] -
            DF.ast.dur[which(DF.ast.dur$stage == stage),
                       colnames(DF.ast.dur) == "dur.uncertainty"],
          DF.ast.dur[which(DF.ast.dur$stage == stage),
                     colnames(DF.ast.dur) == "duration"] +
            DF.ast.dur[which(DF.ast.dur$stage == stage),
                       colnames(DF.ast.dur) == "dur.uncertainty"])
  # Make a density plot of the new distribution.
  plot(density(dist.A_baseGivetian_D15))
  # Save results.
  DF.ast[which(DF.ast$ID == "A-baseGivetian-D15"), c(2, 4, 6)] <-
    mean(dist.A_baseGivetian_D15)
  DF.ast[which(DF.ast$ID == "A-baseGivetian-D15"), c(3, 5, 7)] <-
```

```
    sd(dist.A_baseGivetian_D15) * 2

# Sample dist.A_baseGivetian_D15 and the duration of the Givetian to get
an age
# for the base of the Frasnian.
  stage <- "Givetian"
  dist.A_baseFrasnian_D15 <- sample(dist.A_baseGivetian_D15,
                                    size = n,
                                    replace = TRUE,
                                    prob = dist.A_baseGivetian_D15) -
    runif(n,
          DF.ast.dur[which(DF.ast.dur$stage == stage),
                     colnames(DF.ast.dur) == "duration"] -
            DF.ast.dur[which(DF.ast.dur$stage == stage),
                       colnames(DF.ast.dur) == "dur.uncertainty"],
          DF.ast.dur[which(DF.ast.dur$stage == stage),
                     colnames(DF.ast.dur) == "duration"] +
            DF.ast.dur[which(DF.ast.dur$stage == stage),
                       colnames(DF.ast.dur) == "dur.uncertainty"])
  # Plot results.
  plot(density(dist.A_baseFrasnian_D15))
  # Save results.
  DF.ast[which(DF.ast$ID == "A-baseFrasnian-D15"), c(2, 4, 6)] <-
    mean(dist.A_baseFrasnian_D15)  # mean
  DF.ast[which(DF.ast$ID == "A-baseFrasnian-D15"), c(3, 5, 7)] <-
    sd(dist.A_baseFrasnian_D15) * 2  # 2 sigma

# Sample dist.A_baseFrasnian_D15 and the duration of the Frasnian to get
an age
  # for the base of the Frasnian.
  stage <- "Frasnian"
  dist.A_baseFamennian_D15 <- sample(dist.A_baseFrasnian_D15,
                                    size = n,
                                    replace = TRUE,
                                    prob = dist.A_baseFrasnian_D15) -
    runif(n,
          DF.ast.dur[which(DF.ast.dur$stage == stage),
                     colnames(DF.ast.dur) == "duration"] -
            DF.ast.dur[which(DF.ast.dur$stage == stage),
                       colnames(DF.ast.dur) == "dur.uncertainty"],
          DF.ast.dur[which(DF.ast.dur$stage == stage),
                     colnames(DF.ast.dur) == "duration"] +
            DF.ast.dur[which(DF.ast.dur$stage == stage),
                       colnames(DF.ast.dur) == "dur.uncertainty"])
  # Plot results.
  plot(density(dist.A_baseFamennian_D15))
  # Save results.
  DF.ast[which(DF.ast$ID == "A-baseFamennian-D15"), c(2, 4, 6)] <-
    mean(dist.A_baseFamennian_D15)  # mean
  DF.ast[which(DF.ast$ID == "A-baseFamennian-D15"), c(3, 5, 7)] <-
    sd(dist.A_baseFamennian_D15) * 2  # 2 sigma
```

```
# Sample dist.A_baseFamennian_D15 and the duration of the Famennian to get
an
# age for the base of the Carboniferous.
  stage <- "Famennian"
  dist.A_baseCarboniferous_D15 <- sample(dist.A_baseFamennian_D15,
                                         size = n,
                                         replace = TRUE,
                                         prob = dist.A_baseFamennian_D15) -
    runif(n,
          DF.ast.dur[which(DF.ast.dur$stage == stage),
                     colnames(DF.ast.dur) == "duration"] -
            DF.ast.dur[which(DF.ast.dur$stage == stage),
                       colnames(DF.ast.dur) == "dur.uncertainty"],
          DF.ast.dur[which(DF.ast.dur$stage == stage),
                     colnames(DF.ast.dur) == "duration"] +
            DF.ast.dur[which(DF.ast.dur$stage == stage),
                       colnames(DF.ast.dur) == "dur.uncertainty"])
  # Plot results.
  plot(density(dist.A_baseCarboniferous_D15))
  # Save results.
  DF.ast[which(DF.ast$ID == "A-baseCarboniferous-D15"), c(2, 4, 6)] <-
    mean(dist.A_baseCarboniferous_D15)  # mean
  DF.ast[which(DF.ast$ID == "A-baseCarboniferous-D15"), c(3, 5, 7)] <-
    sd(dist.A_baseCarboniferous_D15) * 2  # 2 sigma


## ANCHOR: D14 -----------------------------------------------------------
------
# NOTE: The ages for the Stage boundaries based on anchors D27, D15, D14,
and
# D13 are the same for the three scales (Kaufmann, Becker 2012, Becker
2020).

# Using D14 as an anchor, determine the age and uncertainty of the Stage
# boundaries.

# Set the anchor point.
  anchor <- "D14"

# Set the age and uncertainty of A-D14 to be the same as D14.
  DF.ast[which(DF.ast$ID == "A-D14"), c(2, 4, 6)] <-
    DF.ast.anchors[which(DF.ast.anchors$anchor == "D14"), 2]
  DF.ast[which(DF.ast$ID == "A-D14"), c(3, 5, 7)] <-
    DF.ast.anchors[which(DF.ast.anchors$anchor == "D14"), 3]

# Create a new distribution for the base of the Eifelian.
  # Set the Stage.
  stage <- "EifelianPas.below.A-D14"
  # Sample the distribution for A-D14. Divide age.uncertainty by 2 to get
1
  # sigma.
  dist.A_baseEifelian_D14 <- rnorm(n,
```

```
    DF.ast.anchors[which(DF.ast.anchors$anchor == anchor),
                   colnames(DF.ast.anchors) == "age"],
    DF.ast.anchors[which(DF.ast.anchors$anchor == anchor),
                   colnames(DF.ast.anchors) == "age.uncertainty"] / 2) +
    # Sample the distribution of the Eifelian duration below A-D14.
    runif(n,
          DF.ast.dur[which(DF.ast.dur$stage == stage),
                     colnames(DF.ast.dur) == "duration"] -
            DF.ast.dur[which(DF.ast.dur$stage == stage),
                       colnames(DF.ast.dur) == "dur.uncertainty"],
          DF.ast.dur[which(DF.ast.dur$stage == stage),
                     colnames(DF.ast.dur) == "duration"] +
            DF.ast.dur[which(DF.ast.dur$stage == stage),
                       colnames(DF.ast.dur) == "dur.uncertainty"])
  # Make a density plot of the new distribution.
  plot(density(dist.A_baseEifelian_D14))
  # Save results.
  DF.ast[which(DF.ast$ID == "A-baseEifelian-D14"), c(2, 4, 6)] <-
    mean(dist.A_baseEifelian_D14)
  DF.ast[which(DF.ast$ID == "A-baseEifelian-D14"), c(3, 5, 7)] <-
    sd(dist.A_baseEifelian_D14) * 2

# Create a new distribution for the base of the Givetian.
  stage <- "EifelianPas.above.A-D14"
  # Sample the distribution for A-D14. Divide age.uncertainty by 2 to get
1
  # sigma.
  dist.A_baseGivetian_D14 <- rnorm(n,
    DF.ast.anchors[which(DF.ast.anchors$anchor == anchor),
                   colnames(DF.ast.anchors) == "age"],
    DF.ast.anchors[which(DF.ast.anchors$anchor == anchor),
                   colnames(DF.ast.anchors) == "age.uncertainty"] / 2) -
    # Sample the distribution of the Eifelian duration below A-D14.
    runif(n,
          DF.ast.dur[which(DF.ast.dur$stage == stage),
                     colnames(DF.ast.dur) == "duration"] -
            DF.ast.dur[which(DF.ast.dur$stage == stage),
                       colnames(DF.ast.dur) == "dur.uncertainty"],
          DF.ast.dur[which(DF.ast.dur$stage == stage),
                     colnames(DF.ast.dur) == "duration"] +
            DF.ast.dur[which(DF.ast.dur$stage == stage),
                       colnames(DF.ast.dur) == "dur.uncertainty"])
  # Make a density plot of the new distribution.
  plot(density(dist.A_baseGivetian_D14))
  # Save results.
  DF.ast[which(DF.ast$ID == "A-baseGivetian-D14"), c(2, 4, 6)] <-
    mean(dist.A_baseGivetian_D14)
  DF.ast[which(DF.ast$ID == "A-baseGivetian-D14"), c(3, 5, 7)] <-
    sd(dist.A_baseGivetian_D14) * 2

# Sample dist.A_baseGivetian_D14 and the duration of the Givetian to get
an age
```

```
# for the base of the Frasnian.
  stage <- "Givetian"
  dist.A_baseFrasnian_D14 <- sample(dist.A_baseGivetian_D14,
                                    size = n,
                                    replace = TRUE,
                                    prob = dist.A_baseGivetian_D14) -
    runif(n,
          DF.ast.dur[which(DF.ast.dur$stage == stage),
                     colnames(DF.ast.dur) == "duration"] -
            DF.ast.dur[which(DF.ast.dur$stage == stage),
                       colnames(DF.ast.dur) == "dur.uncertainty"],
          DF.ast.dur[which(DF.ast.dur$stage == stage),
                     colnames(DF.ast.dur) == "duration"] +
            DF.ast.dur[which(DF.ast.dur$stage == stage),
                       colnames(DF.ast.dur) == "dur.uncertainty"])
  # Plot results.
  plot(density(dist.A_baseFrasnian_D14))
  # Save results.
  DF.ast[which(DF.ast$ID == "A-baseFrasnian-D14"), c(2, 4, 6)] <-
    mean(dist.A_baseFrasnian_D14)  # mean
  DF.ast[which(DF.ast$ID == "A-baseFrasnian-D14"), c(3, 5, 7)] <-
    sd(dist.A_baseFrasnian_D14) * 2  # 2 sigma

# Sample dist.A_baseFrasnian_D14 and the duration of the Frasnian to get
an age
# for the base of the Frasnian.
  stage <- "Frasnian"
  dist.A_baseFamennian_D14 <- sample(dist.A_baseFrasnian_D14,
                                     size = n,
                                     replace = TRUE,
                                     prob = dist.A_baseFrasnian_D14) -
    runif(n,
          DF.ast.dur[which(DF.ast.dur$stage == stage),
                     colnames(DF.ast.dur) == "duration"] -
            DF.ast.dur[which(DF.ast.dur$stage == stage),
                       colnames(DF.ast.dur) == "dur.uncertainty"],
          DF.ast.dur[which(DF.ast.dur$stage == stage),
                     colnames(DF.ast.dur) == "duration"] +
            DF.ast.dur[which(DF.ast.dur$stage == stage),
                       colnames(DF.ast.dur) == "dur.uncertainty"])
  # Plot results.
  plot(density(dist.A_baseFamennian_D14))
  # Save results.
  DF.ast[which(DF.ast$ID == "A-baseFamennian-D14"), c(2, 4, 6)] <-
    mean(dist.A_baseFamennian_D14)  # mean
  DF.ast[which(DF.ast$ID == "A-baseFamennian-D14"), c(3, 5, 7)] <-
    sd(dist.A_baseFamennian_D14) * 2  # 2 sigma

# Sample dist.A_baseFamennian_D14 and the duration of the Famennian to get
an
# age for the base of the Carboniferous.
  stage <- "Famennian"
```

```
  dist.A_baseCarboniferous_D14 <- sample(dist.A_baseFamennian_D14,
                                         size = n,
                                         replace = TRUE,
                                         prob = dist.A_baseFamennian_D14)
-
    runif(n,
          DF.ast.dur[which(DF.ast.dur$stage == stage),
                     colnames(DF.ast.dur) == "duration"] -
            DF.ast.dur[which(DF.ast.dur$stage == stage),
                       colnames(DF.ast.dur) == "dur.uncertainty"],
          DF.ast.dur[which(DF.ast.dur$stage == stage),
                     colnames(DF.ast.dur) == "duration"] +
            DF.ast.dur[which(DF.ast.dur$stage == stage),
                       colnames(DF.ast.dur) == "dur.uncertainty"])
  # Plot results.
  plot(density(dist.A_baseCarboniferous_D14))
  # Save results.
  DF.ast[which(DF.ast$ID == "A-baseCarboniferous-D14"), c(2, 4, 6)] <-
    mean(dist.A_baseCarboniferous_D14)  # mean
  DF.ast[which(DF.ast$ID == "A-baseCarboniferous-D14"), c(3, 5, 7)] <-
    sd(dist.A_baseCarboniferous_D14) * 2  # 2 sigma


## ANCHOR: D13 -----------------------------------------------------------
------
# NOTE: The ages for the Stage boundaries based on anchors D27, D15, D14,
and
# D13 are the same for the three scales (Kaufmann, Becker 2012, Becker
2020).

  # Using D13 as an anchor, determine the age and uncertainty of the next
Stage
  # boundary up in depth. Sample a Gaussian distribution for the anchoring
age
  # and a uniform distribution for the astrochronology duration n times to
get a
  # new distribution representing the age of the Stage boundary of
interest.
  # Use the mean and two standard deviation value to represent the age of
that
  # distribution (assumes a Gaussian distribution).

# Set the anchor point and Stage.
  anchor <- "D13"

# Create a new distribution for the base of the Givetian.
  stage <- "EifelianCombined"
# Sample the distribution for D13. Divide age.uncertainty by 2 to get 1
# sigma.
  dist.A_baseGivetian_D13 <- rnorm(n,
    DF.ast.anchors[which(DF.ast.anchors$anchor == anchor),
                   colnames(DF.ast.anchors) == "age"],
```

```
    DF.ast.anchors[which(DF.ast.anchors$anchor == anchor),
                   colnames(DF.ast.anchors) == "age.uncertainty"] / 2) -
    # Sample the distribution of the EifelianCombined duration above D13.
    runif(n,
          DF.ast.dur[which(DF.ast.dur$stage == stage),
                     colnames(DF.ast.dur) == "duration"] -
            DF.ast.dur[which(DF.ast.dur$stage == stage),
                       colnames(DF.ast.dur) == "dur.uncertainty"],
          DF.ast.dur[which(DF.ast.dur$stage == stage),
                     colnames(DF.ast.dur) == "duration"] +
            DF.ast.dur[which(DF.ast.dur$stage == stage),
                       colnames(DF.ast.dur) == "dur.uncertainty"])
  # Make a density plot of the new distribution.
  plot(density(dist.A_baseGivetian_D13))
  # Save results.
  # Calculate the mean of the new distribution to use as the new age for
  # the base of the Givetian.
  DF.ast[which(DF.ast$ID == "A-baseGivetian-D13"), c(2, 4, 6)] <-
    mean(dist.A_baseGivetian_D13)
  # Calculate the standard deviation of the new distribution and multiply
it by
  # 2 to use as the 2-sigma uncertainty for this distribution.
  DF.ast[which(DF.ast$ID == "A-baseGivetian-D13"), c(3, 5, 7)] <-
    sd(dist.A_baseGivetian_D13) * 2

# Sample dist.A_baseGivetian_D13 and the duration of the Givetian to get
an
# age for the base of the Frasnian.
  stage <- "Givetian"
  dist.A_baseFrasnian_D13 <- sample(dist.A_baseGivetian_D13,
                                    size = n,
                                    replace = TRUE,
                                    prob = dist.A_baseGivetian_D13) -
    runif(n,
          DF.ast.dur[which(DF.ast.dur$stage == stage),
                     colnames(DF.ast.dur) == "duration"] -
            DF.ast.dur[which(DF.ast.dur$stage == stage),
                       colnames(DF.ast.dur) == "dur.uncertainty"],
          DF.ast.dur[which(DF.ast.dur$stage == stage),
                     colnames(DF.ast.dur) == "duration"] +
            DF.ast.dur[which(DF.ast.dur$stage == stage),
                       colnames(DF.ast.dur) == "dur.uncertainty"])
  # Plot results.
  plot(density(dist.A_baseFrasnian_D13))
  # Save results.
  DF.ast[which(DF.ast$ID == "A-baseFrasnian-D13"), c(2, 4, 6)] <-
    mean(dist.A_baseFrasnian_D13)
  DF.ast[which(DF.ast$ID == "A-baseFrasnian-D13"), c(3, 5, 7)] <-
    sd(dist.A_baseFrasnian_D13) * 2

# Sample dist.A_baseFrasnian_D13 and the duration of the Frasnian to get
an
```

```
# age for the base of the Famennian
  stage <- "Frasnian"
  dist.A_baseFamennian_D13 <- sample(dist.A_baseFrasnian_D13,
                                     size = n,
                                     replace = TRUE,
                                     prob = dist.A_baseFrasnian_D13) -
    runif(n,
          DF.ast.dur[which(DF.ast.dur$stage == stage),
                     colnames(DF.ast.dur) == "duration"] -
            DF.ast.dur[which(DF.ast.dur$stage == stage),
                       colnames(DF.ast.dur) == "dur.uncertainty"],
          DF.ast.dur[which(DF.ast.dur$stage == stage),
                     colnames(DF.ast.dur) == "duration"] +
            DF.ast.dur[which(DF.ast.dur$stage == stage),
                       colnames(DF.ast.dur) == "dur.uncertainty"])
  # Plot results.
  plot(density(dist.A_baseFamennian_D13))
  # Save results.
  DF.ast[which(DF.ast$ID == "A-baseFamennian-D13"), c(2, 4, 6)] <-
    mean(dist.A_baseFamennian_D13)
  DF.ast[which(DF.ast$ID == "A-baseFamennian-D13"), c(3, 5, 7)] <-
    sd(dist.A_baseFamennian_D13) * 2

# Sample dist.A_baseFamennian_D13 and the duration of the Famennian to get
an
# age for the base of the Carboniferous
  stage <- "Famennian"
  dist.A_baseCarboniferous_D13 <- sample(dist.A_baseFamennian_D13,
                                       size = n,
                                       replace = TRUE,
                                       prob = dist.A_baseFamennian_D13) -
    runif(n,
          DF.ast.dur[which(DF.ast.dur$stage == stage),
                     colnames(DF.ast.dur) == "duration"] -
            DF.ast.dur[which(DF.ast.dur$stage == stage),
                       colnames(DF.ast.dur) == "dur.uncertainty"],
          DF.ast.dur[which(DF.ast.dur$stage == stage),
                     colnames(DF.ast.dur) == "duration"] +
            DF.ast.dur[which(DF.ast.dur$stage == stage),
                       colnames(DF.ast.dur) == "dur.uncertainty"])
  # Plot results.
  plot(density(dist.A_baseCarboniferous_D13))
  # Save results.
  DF.ast[which(DF.ast$ID == "A-baseCarboniferous-D13"), c(2, 4, 6)] <-
    mean(dist.A_baseCarboniferous_D13)
  DF.ast[which(DF.ast$ID == "A-baseCarboniferous-D13"), c(3, 5, 7)] <-
    sd(dist.A_baseCarboniferous_D13) * 2


## ANCHOR: D6, KAUFMANN ------------------------------------------------
-------
```

```
# Using D6 as an anchor, determine the age and uncertainty of the Kaufmann
# Stage boundaries.

# Set the anchor point.
  anchor <- "D6"

# Create a new distribution for the base of the Lochkovian.
  # Set the Stage.
  stage <- "Lochkovian.below.D5D6.K"
  # Sample the distribution for D6. Divide age.uncertainty by 2 to get 1
  # sigma.
  dist.A_baseLochkovian_D6_K <- rnorm(n,
    DF.ast.anchors[which(DF.ast.anchors$anchor == anchor),
                   colnames(DF.ast.anchors) == "age"],
    DF.ast.anchors[which(DF.ast.anchors$anchor == anchor),
                   colnames(DF.ast.anchors) == "age.uncertainty"] / 2) +
    # Sample the distribution of the Lochkovian duration below D6.
    runif(n,
          DF.ast.dur[which(DF.ast.dur$stage == stage),
                     colnames(DF.ast.dur) == "duration"] -
            DF.ast.dur[which(DF.ast.dur$stage == stage),
                       colnames(DF.ast.dur) == "dur.uncertainty"],
          DF.ast.dur[which(DF.ast.dur$stage == stage),
                     colnames(DF.ast.dur) == "duration"] +
            DF.ast.dur[which(DF.ast.dur$stage == stage),
                       colnames(DF.ast.dur) == "dur.uncertainty"])
  # Make a density plot of the new distribution.
  plot(density(dist.A_baseLochkovian_D6_K))
  # Save results.
  DF.ast[which(DF.ast$ID == "A-baseLochkovian-D6"), 2] <-
    mean(dist.A_baseLochkovian_D6_K)
  DF.ast[which(DF.ast$ID == "A-baseLochkovian-D6"), 3] <-
    sd(dist.A_baseLochkovian_D6_K) * 2

# Create a new distribution for the base of the Pragian.
  stage <- "Lochkovian.above.D5D6.K"
  # Sample the distribution for D6. Divide age.uncertainty by 2 to get 1
  # sigma.
  dist.A_basePragian_D6_K <- rnorm(n,
    DF.ast.anchors[which(DF.ast.anchors$anchor == anchor),
                   colnames(DF.ast.anchors) == "age"],
    DF.ast.anchors[which(DF.ast.anchors$anchor == anchor),
                   colnames(DF.ast.anchors) == "age.uncertainty"] / 2) -
    # Sample the distribution of the Pragian duration above D6.
    runif(n,
          DF.ast.dur[which(DF.ast.dur$stage == stage),
                     colnames(DF.ast.dur) == "duration"] -
            DF.ast.dur[which(DF.ast.dur$stage == stage),
                       colnames(DF.ast.dur) == "dur.uncertainty"],
          DF.ast.dur[which(DF.ast.dur$stage == stage),
                     colnames(DF.ast.dur) == "duration"] +
            DF.ast.dur[which(DF.ast.dur$stage == stage),
```

```
                      colnames(DF.ast.dur) == "dur.uncertainty"])
  # Make a density plot of the new distribution.
  plot(density(dist.A_basePragian_D6_K))
  # Save results.
  DF.ast[which(DF.ast$ID == "A-basePragian-D6"), 2] <-
    mean(dist.A_basePragian_D6_K)
  DF.ast[which(DF.ast$ID == "A-basePragian-D6"), 3] <-
    sd(dist.A_basePragian_D6_K) * 2

# Sample dist.A_basePragian_D6_K and the duration of the Pragian to get an
age
  # for the base of the Emsian
  stage <- "Pragian"
  dist.A_baseEmsian_D6_K <- sample(dist.A_basePragian_D6_K,
                                   size = n,
                                   replace = TRUE,
                                   prob = dist.A_basePragian_D6_K) -
    runif(n,
          DF.ast.dur[which(DF.ast.dur$stage == stage),
                     colnames(DF.ast.dur) == "duration"] -
            DF.ast.dur[which(DF.ast.dur$stage == stage),
                       colnames(DF.ast.dur) == "dur.uncertainty"],
          DF.ast.dur[which(DF.ast.dur$stage == stage),
                     colnames(DF.ast.dur) == "duration"] +
            DF.ast.dur[which(DF.ast.dur$stage == stage),
                       colnames(DF.ast.dur) == "dur.uncertainty"])
  # Plot results.
  plot(density(dist.A_baseEmsian_D6_K))
  # Save results.
  DF.ast[which(DF.ast$ID == "A-baseEmsian-D6"), 2] <-
    mean(dist.A_baseEmsian_D6_K)  # mean
  DF.ast[which(DF.ast$ID == "A-baseEmsian-D6"), 3] <-
    sd(dist.A_baseEmsian_D6_K) * 2  # 2 sigma


## ANCHOR: D5, KAUFMANN ------------------------------------------------
-------

# Using D5 as an anchor, determine the age and uncertainty of the Kaufmann
# Stage boundaries.

# Set the anchor point.
  anchor <- "D5"

# Create a new distribution for the base of the Lochkovian.
  # Set the Stage.
  stage <- "Lochkovian.below.D5D6.K"
  # Sample the distribution for D5. Divide age.uncertainty by 2 to get 1
  # sigma.
  dist.A_baseLochkovian_D5_K <- rnorm(n,
    DF.ast.anchors[which(DF.ast.anchors$anchor == anchor),
                   colnames(DF.ast.anchors) == "age"],
```

```
    DF.ast.anchors[which(DF.ast.anchors$anchor == anchor),
                   colnames(DF.ast.anchors) == "age.uncertainty"] / 2) +
    # Sample the distribution of the Lochkovian duration below D5.
    runif(n,
          DF.ast.dur[which(DF.ast.dur$stage == stage),
                     colnames(DF.ast.dur) == "duration"] -
            DF.ast.dur[which(DF.ast.dur$stage == stage),
                       colnames(DF.ast.dur) == "dur.uncertainty"],
          DF.ast.dur[which(DF.ast.dur$stage == stage),
                     colnames(DF.ast.dur) == "duration"] +
            DF.ast.dur[which(DF.ast.dur$stage == stage),
                       colnames(DF.ast.dur) == "dur.uncertainty"])
  # Make a density plot of the new distribution.
  plot(density(dist.A_baseLochkovian_D5_K))
  # Save results.
  DF.ast[which(DF.ast$ID == "A-baseLochkovian-D5"), 2] <-
    mean(dist.A_baseLochkovian_D5_K)
  DF.ast[which(DF.ast$ID == "A-baseLochkovian-D5"), 3] <-
    sd(dist.A_baseLochkovian_D5_K) * 2

  # Create a new distribution for the base of the Pragian.
  stage <- "Lochkovian.above.D5D6.K"
  # Sample the distribution for D5. Divide age.uncertainty by 2 to get 1
  # sigma.
  dist.A_basePragian_D5_K <- rnorm(n,
    DF.ast.anchors[which(DF.ast.anchors$anchor == anchor),
                   colnames(DF.ast.anchors) == "age"],
    DF.ast.anchors[which(DF.ast.anchors$anchor == anchor),
                   colnames(DF.ast.anchors) == "age.uncertainty"] / 2) -
    # Sample the distribution of the Pragian duration above D5.
    runif(n,
          DF.ast.dur[which(DF.ast.dur$stage == stage),
                     colnames(DF.ast.dur) == "duration"] -
            DF.ast.dur[which(DF.ast.dur$stage == stage),
                       colnames(DF.ast.dur) == "dur.uncertainty"],
          DF.ast.dur[which(DF.ast.dur$stage == stage),
                     colnames(DF.ast.dur) == "duration"] +
            DF.ast.dur[which(DF.ast.dur$stage == stage),
                       colnames(DF.ast.dur) == "dur.uncertainty"])
  # Make a density plot of the new distribution.
  plot(density(dist.A_basePragian_D5_K))
  # Save results.
  DF.ast[which(DF.ast$ID == "A-basePragian-D5"), 2] <-
    mean(dist.A_basePragian_D5_K)
  DF.ast[which(DF.ast$ID == "A-basePragian-D5"), 3] <-
    sd(dist.A_basePragian_D5_K) * 2

  # Sample dist.A_basePragian_D5_K and the duration of the Pragian to get
an age
  # for the base of the Emsian
  stage <- "Pragian"
  dist.A_baseEmsian_D5_K <- sample(dist.A_basePragian_D5_K,
```

```
                                size = n,
                                replace = TRUE,
                                prob = dist.A_basePragian_D5_K) -
    runif(n,
          DF.ast.dur[which(DF.ast.dur$stage == stage),
                     colnames(DF.ast.dur) == "duration"] -
            DF.ast.dur[which(DF.ast.dur$stage == stage),
                       colnames(DF.ast.dur) == "dur.uncertainty"],
          DF.ast.dur[which(DF.ast.dur$stage == stage),
                     colnames(DF.ast.dur) == "duration"] +
            DF.ast.dur[which(DF.ast.dur$stage == stage),
                       colnames(DF.ast.dur) == "dur.uncertainty"])
  # Plot results.
  plot(density(dist.A_baseEmsian_D5_K))
  # Save results.
  DF.ast[which(DF.ast$ID == "A-baseEmsian-D5"), 2] <-
    mean(dist.A_baseEmsian_D5_K)  # mean
  DF.ast[which(DF.ast$ID == "A-baseEmsian-D5"), 3] <-
    sd(dist.A_baseEmsian_D5_K) * 2  # 2 sigma

## ANCHOR: D6, BECKER 2012 ---------------------------------------------
-------

# Using D6 as an anchor, determine the age and uncertainty of the Becker
2012
# Stage boundaries.

# Set the anchor point.
  anchor <- "D6"

# Create a new distribution for the base of the Lochkovian.
  # Set the Stage.
  stage <- "Lochkovian.below.D5D6.B12"
  # Sample the distribution for D6. Divide age.uncertainty by 2 to get 1
  # sigma.
  dist.A_baseLochkovian_D6_B12 <- rnorm(n,
    DF.ast.anchors[which(DF.ast.anchors$anchor == anchor),
                   colnames(DF.ast.anchors) == "age"],
    DF.ast.anchors[which(DF.ast.anchors$anchor == anchor),
                   colnames(DF.ast.anchors) == "age.uncertainty"] / 2) +
    # Sample the distribution of the Lochkovian duration below D6.
    runif(n,
          DF.ast.dur[which(DF.ast.dur$stage == stage),
                     colnames(DF.ast.dur) == "duration"] -
            DF.ast.dur[which(DF.ast.dur$stage == stage),
                       colnames(DF.ast.dur) == "dur.uncertainty"],
          DF.ast.dur[which(DF.ast.dur$stage == stage),
                     colnames(DF.ast.dur) == "duration"] +
            DF.ast.dur[which(DF.ast.dur$stage == stage),
                       colnames(DF.ast.dur) == "dur.uncertainty"])
  # Make a density plot of the new distribution.
  plot(density(dist.A_baseLochkovian_D6_B12))
```

```
  # Save results.
  DF.ast[which(DF.ast$ID == "A-baseLochkovian-D6"), 4] <-
    mean(dist.A_baseLochkovian_D6_B12)
  DF.ast[which(DF.ast$ID == "A-baseLochkovian-D6"), 5] <-
    sd(dist.A_baseLochkovian_D6_B12) * 2

# Create a new distribution for the base of the Pragian.
  stage <- "Lochkovian.above.D5D6.B12"
  # Sample the distribution for D6. Divide age.uncertainty by 2 to get 1
  # sigma.
  dist.A_basePragian_D6_B12 <- rnorm(n,
    DF.ast.anchors[which(DF.ast.anchors$anchor == anchor),
                   colnames(DF.ast.anchors) == "age"],
    DF.ast.anchors[which(DF.ast.anchors$anchor == anchor),
                   colnames(DF.ast.anchors) == "age.uncertainty"] / 2) -
    # Sample the distribution of the Pragian duration above D6.
    runif(n,
          DF.ast.dur[which(DF.ast.dur$stage == stage),
                     colnames(DF.ast.dur) == "duration"] -
            DF.ast.dur[which(DF.ast.dur$stage == stage),
                       colnames(DF.ast.dur) == "dur.uncertainty"],
          DF.ast.dur[which(DF.ast.dur$stage == stage),
                     colnames(DF.ast.dur) == "duration"] +
            DF.ast.dur[which(DF.ast.dur$stage == stage),
                       colnames(DF.ast.dur) == "dur.uncertainty"])
  # Make a density plot of the new distribution.
  plot(density(dist.A_basePragian_D6_B12))
  # Save results.
  DF.ast[which(DF.ast$ID == "A-basePragian-D6"), 4] <-
    mean(dist.A_basePragian_D6_B12)
  DF.ast[which(DF.ast$ID == "A-basePragian-D6"), 5] <-
    sd(dist.A_basePragian_D6_B12) * 2

# Sample dist.A_basePragian_D6_B12 and the duration of the Pragian to get
an age
# for the base of the Emsian.
  stage <- "Pragian"
  dist.A_baseEmsian_D6_B12 <- sample(dist.A_basePragian_D6_B12,
                                     size = n,
                                     replace = TRUE,
                                     prob = dist.A_basePragian_D6_B12) -
    runif(n,
          DF.ast.dur[which(DF.ast.dur$stage == stage),
                     colnames(DF.ast.dur) == "duration"] -
            DF.ast.dur[which(DF.ast.dur$stage == stage),
                       colnames(DF.ast.dur) == "dur.uncertainty"],
          DF.ast.dur[which(DF.ast.dur$stage == stage),
                     colnames(DF.ast.dur) == "duration"] +
            DF.ast.dur[which(DF.ast.dur$stage == stage),
                       colnames(DF.ast.dur) == "dur.uncertainty"])
  # Plot results.
  plot(density(dist.A_baseEmsian_D6_B12))
```

```
  # Save results.
  DF.ast[which(DF.ast$ID == "A-baseEmsian-D6"), 4] <-
    mean(dist.A_baseEmsian_D6_B12)  # mean
  DF.ast[which(DF.ast$ID == "A-baseEmsian-D6"), 5] <-
    sd(dist.A_baseEmsian_D6_B12) * 2  # 2 sigma


## ANCHOR: D5, BECKER 2012 ---------------------------------------------
------

# Using D5 as an anchor, determine the age and uncertainty of the Becker
2012
# Stage boundaries.

# Set the anchor point.
  anchor <- "D5"

# Create a new distribution for the base of the Lochkovian.
  # Set the Stage.
  stage <- "Lochkovian.below.D5D6.B12"
  # Sample the distribution for D5. Divide age.uncertainty by 2 to get 1
  # sigma.
  dist.A_baseLochkovian_D5_B12 <- rnorm(n,
    DF.ast.anchors[which(DF.ast.anchors$anchor == anchor),
                   colnames(DF.ast.anchors) == "age"],
    DF.ast.anchors[which(DF.ast.anchors$anchor == anchor),
                   colnames(DF.ast.anchors) == "age.uncertainty"] / 2) +
    # Sample the distribution of the Lochkovian duration below D5.
    runif(n,
          DF.ast.dur[which(DF.ast.dur$stage == stage),
                     colnames(DF.ast.dur) == "duration"] -
            DF.ast.dur[which(DF.ast.dur$stage == stage),
                       colnames(DF.ast.dur) == "dur.uncertainty"],
          DF.ast.dur[which(DF.ast.dur$stage == stage),
                     colnames(DF.ast.dur) == "duration"] +
            DF.ast.dur[which(DF.ast.dur$stage == stage),
                       colnames(DF.ast.dur) == "dur.uncertainty"])
  # Make a density plot of the new distribution.
  plot(density(dist.A_baseLochkovian_D5_B12))
  # Save results.
  DF.ast[which(DF.ast$ID == "A-baseLochkovian-D5"), 4] <-
    mean(dist.A_baseLochkovian_D5_B12)
  DF.ast[which(DF.ast$ID == "A-baseLochkovian-D5"), 5] <-
    sd(dist.A_baseLochkovian_D5_B12) * 2

# Create a new distribution for the base of the Pragian.
  stage <- "Lochkovian.above.D5D6.B12"
  # Sample the distribution for D5. Divide age.uncertainty by 2 to get 1
  # sigma.
  dist.A_basePragian_D5_B12 <- rnorm(n,
    DF.ast.anchors[which(DF.ast.anchors$anchor == anchor),
                   colnames(DF.ast.anchors) == "age"],
```

```
    DF.ast.anchors[which(DF.ast.anchors$anchor == anchor),
                   colnames(DF.ast.anchors) == "age.uncertainty"] / 2) -
    # Sample the distribution of the Pragian duration above D5.
    runif(n,
          DF.ast.dur[which(DF.ast.dur$stage == stage),
                     colnames(DF.ast.dur) == "duration"] -
            DF.ast.dur[which(DF.ast.dur$stage == stage),
                       colnames(DF.ast.dur) == "dur.uncertainty"],
          DF.ast.dur[which(DF.ast.dur$stage == stage),
                     colnames(DF.ast.dur) == "duration"] +
            DF.ast.dur[which(DF.ast.dur$stage == stage),
                       colnames(DF.ast.dur) == "dur.uncertainty"])
  # Make a density plot of the new distribution.
  plot(density(dist.A_basePragian_D5_B12))
  # Save results.
  DF.ast[which(DF.ast$ID == "A-basePragian-D5"), 4] <-
    mean(dist.A_basePragian_D5_B12)
  DF.ast[which(DF.ast$ID == "A-basePragian-D5"), 5] <-
    sd(dist.A_basePragian_D5_B12) * 2

# Sample dist.A_basePragian_D5_B12 and the duration of the Pragian to get
an age
# for the base of the Emsian
  stage <- "Pragian"
  dist.A_baseEmsian_D5_B12 <- sample(dist.A_basePragian_D5_B12,
                                     size = n,
                                     replace = TRUE,
                                     prob = dist.A_basePragian_D5_B12) -
    runif(n,
          DF.ast.dur[which(DF.ast.dur$stage == stage),
                     colnames(DF.ast.dur) == "duration"] -
            DF.ast.dur[which(DF.ast.dur$stage == stage),
                       colnames(DF.ast.dur) == "dur.uncertainty"],
          DF.ast.dur[which(DF.ast.dur$stage == stage),
                     colnames(DF.ast.dur) == "duration"] +
            DF.ast.dur[which(DF.ast.dur$stage == stage),
                       colnames(DF.ast.dur) == "dur.uncertainty"])
  # Plot results.
  plot(density(dist.A_baseEmsian_D5_B12))
  # Save results.
  DF.ast[which(DF.ast$ID == "A-baseEmsian-D5"), 4] <-
    mean(dist.A_baseEmsian_D5_B12)  # mean
  DF.ast[which(DF.ast$ID == "A-baseEmsian-D5"), 5] <-
    sd(dist.A_baseEmsian_D5_B12) * 2  # 2 sigma


## ANCHOR: D6, BECKER 2020 ------------------------------------------------
------

# Using D6 as an anchor, determine the age and uncertainty of the Becker
2020
# Stage boundaries.
```

```
# Set the anchor point.
  anchor <- "D6"

# Create a new distribution for the base of the Lochkovian.
  # Set the Stage.
  stage <- "Lochkovian.below.D5D6.B20"
  # Sample the distribution for D6. Divide age.uncertainty by 2 to get 1
  # sigma.
  dist.A_baseLochkovian_D6_B20 <- rnorm(n,
    DF.ast.anchors[which(DF.ast.anchors$anchor == anchor),
                   colnames(DF.ast.anchors) == "age"],
    DF.ast.anchors[which(DF.ast.anchors$anchor == anchor),
                   colnames(DF.ast.anchors) == "age.uncertainty"] / 2) +
    # Sample the distribution of the Lochkovian duration below D6.
    runif(n,
          DF.ast.dur[which(DF.ast.dur$stage == stage),
                     colnames(DF.ast.dur) == "duration"] -
            DF.ast.dur[which(DF.ast.dur$stage == stage),
                       colnames(DF.ast.dur) == "dur.uncertainty"],
          DF.ast.dur[which(DF.ast.dur$stage == stage),
                     colnames(DF.ast.dur) == "duration"] +
            DF.ast.dur[which(DF.ast.dur$stage == stage),
                       colnames(DF.ast.dur) == "dur.uncertainty"])
  # Make a density plot of the new distribution.
  plot(density(dist.A_baseLochkovian_D6_B20))
  # Save results.
  DF.ast[which(DF.ast$ID == "A-baseLochkovian-D6"), 6] <-
    mean(dist.A_baseLochkovian_D6_B20)
  DF.ast[which(DF.ast$ID == "A-baseLochkovian-D6"), 7] <-
    sd(dist.A_baseLochkovian_D6_B20) * 2

# Create a new distribution for the base of the Pragian.
  stage <- "Lochkovian.above.D5D6.B20"
  # Sample the distribution for D6. Divide age.uncertainty by 2 to get 1
  # sigma.
  dist.A_basePragian_D6_B20 <- rnorm(n,
    DF.ast.anchors[which(DF.ast.anchors$anchor == anchor),
                   colnames(DF.ast.anchors) == "age"],
    DF.ast.anchors[which(DF.ast.anchors$anchor == anchor),
                   colnames(DF.ast.anchors) == "age.uncertainty"] / 2) -
    # Sample the distribution of the Pragian duration above D6.
    runif(n,
          DF.ast.dur[which(DF.ast.dur$stage == stage),
                     colnames(DF.ast.dur) == "duration"] -
            DF.ast.dur[which(DF.ast.dur$stage == stage),
                       colnames(DF.ast.dur) == "dur.uncertainty"],
          DF.ast.dur[which(DF.ast.dur$stage == stage),
                     colnames(DF.ast.dur) == "duration"] +
            DF.ast.dur[which(DF.ast.dur$stage == stage),
                       colnames(DF.ast.dur) == "dur.uncertainty"])
  # Make a density plot of the new distribution.
```

```
  plot(density(dist.A_basePragian_D6_B20))
  # Save results.
  DF.ast[which(DF.ast$ID == "A-basePragian-D6"), 6] <-
    mean(dist.A_basePragian_D6_B20)
  DF.ast[which(DF.ast$ID == "A-basePragian-D6"), 7] <-
    sd(dist.A_basePragian_D6_B20) * 2

# Sample dist.A_basePragian_D6_B20 and the duration of the Pragian to get
an age
# for the base of the Emsian.
  stage <- "Pragian"
  dist.A_baseEmsian_D6_B20 <- sample(dist.A_basePragian_D6_B20,
                                     size = n,
                                     replace = TRUE,
                                     prob = dist.A_basePragian_D6_B20) -
    runif(n,
          DF.ast.dur[which(DF.ast.dur$stage == stage),
                     colnames(DF.ast.dur) == "duration"] -
            DF.ast.dur[which(DF.ast.dur$stage == stage),
                       colnames(DF.ast.dur) == "dur.uncertainty"],
          DF.ast.dur[which(DF.ast.dur$stage == stage),
                     colnames(DF.ast.dur) == "duration"] +
            DF.ast.dur[which(DF.ast.dur$stage == stage),
                       colnames(DF.ast.dur) == "dur.uncertainty"])
  # Plot results.
  plot(density(dist.A_baseEmsian_D6_B20))
  # Save results.
  DF.ast[which(DF.ast$ID == "A-baseEmsian-D6"), 6] <-
    mean(dist.A_baseEmsian_D6_B20)  # mean
  DF.ast[which(DF.ast$ID == "A-baseEmsian-D6"), 7] <-
    sd(dist.A_baseEmsian_D6_B20) * 2  # 2 sigma


## ANCHOR D5, BECKER 2020 ---------------------------------------------
------

# Using D5 as an anchor, determine the age and uncertainty of the Becker
2020
# Stage boundaries.

# Set the anchor point.
  anchor <- "D5"

# Create a new distribution for the base of the Lochkovian.
  # Set the Stage.
  stage <- "Lochkovian.below.D5D6.B20"
  # Sample the distribution for D5. Divide age.uncertainty by 2 to get 1
  # sigma.
  dist.A_baseLochkovian_D5_B20 <- rnorm(n,
    DF.ast.anchors[which(DF.ast.anchors$anchor == anchor),
                   colnames(DF.ast.anchors) == "age"],
    DF.ast.anchors[which(DF.ast.anchors$anchor == anchor),
```

```
                  colnames(DF.ast.anchors) == "age.uncertainty"] / 2) +
    # Sample the distribution of the Lochkovian duration below D5.
    runif(n,
          DF.ast.dur[which(DF.ast.dur$stage == stage),
                     colnames(DF.ast.dur) == "duration"] -
            DF.ast.dur[which(DF.ast.dur$stage == stage),
                       colnames(DF.ast.dur) == "dur.uncertainty"],
          DF.ast.dur[which(DF.ast.dur$stage == stage),
                     colnames(DF.ast.dur) == "duration"] +
            DF.ast.dur[which(DF.ast.dur$stage == stage),
                       colnames(DF.ast.dur) == "dur.uncertainty"])
  # Make a density plot of the new distribution.
  plot(density(dist.A_baseLochkovian_D5_B20))
  # Save results.
  DF.ast[which(DF.ast$ID == "A-baseLochkovian-D5"), 6] <-
    mean(dist.A_baseLochkovian_D5_B20)
  DF.ast[which(DF.ast$ID == "A-baseLochkovian-D5"), 7] <-
    sd(dist.A_baseLochkovian_D5_B20) * 2

# Create a new distribution for the base of the Pragian.
  stage <- "Lochkovian.above.D5D6.B20"
  # Sample the distribution for D5. Divide age.uncertainty by 2 to get 1
  # sigma.
  dist.A_basePragian_D5_B20 <- rnorm(n,
    DF.ast.anchors[which(DF.ast.anchors$anchor == anchor),
                   colnames(DF.ast.anchors) == "age"],
    DF.ast.anchors[which(DF.ast.anchors$anchor == anchor),
                   colnames(DF.ast.anchors) == "age.uncertainty"] / 2) -
    # Sample the distribution of the Pragian duration above D5.
    runif(n,
          DF.ast.dur[which(DF.ast.dur$stage == stage),
                     colnames(DF.ast.dur) == "duration"] -
            DF.ast.dur[which(DF.ast.dur$stage == stage),
                       colnames(DF.ast.dur) == "dur.uncertainty"],
          DF.ast.dur[which(DF.ast.dur$stage == stage),
                     colnames(DF.ast.dur) == "duration"] +
            DF.ast.dur[which(DF.ast.dur$stage == stage),
                       colnames(DF.ast.dur) == "dur.uncertainty"])
  # Make a density plot of the new distribution.
  plot(density(dist.A_basePragian_D5_B20))
  # Save results.
  DF.ast[which(DF.ast$ID == "A-basePragian-D5"), 6] <-
    mean(dist.A_basePragian_D5_B20)
  DF.ast[which(DF.ast$ID == "A-basePragian-D5"), 7] <-
    sd(dist.A_basePragian_D5_B20) * 2

# Sample dist.A_basePragian_D5_B20 and the duration of the Pragian to get
an age
# for the base of the Emsian.
  stage <- "Pragian"
  dist.A_baseEmsian_D5_B20 <- sample(dist.A_basePragian_D5_B20,
                                     size = n,
```

```
                                    replace = TRUE,
                                    prob = dist.A_basePragian_D5_B20) -
    runif(n,
          DF.ast.dur[which(DF.ast.dur$stage == stage),
                     colnames(DF.ast.dur) == "duration"] -
            DF.ast.dur[which(DF.ast.dur$stage == stage),
                       colnames(DF.ast.dur) == "dur.uncertainty"],
          DF.ast.dur[which(DF.ast.dur$stage == stage),
                     colnames(DF.ast.dur) == "duration"] +
            DF.ast.dur[which(DF.ast.dur$stage == stage),
                       colnames(DF.ast.dur) == "dur.uncertainty"])
  # Plot results.
  plot(density(dist.A_baseEmsian_D5_B20))
  # Save results.
  DF.ast[which(DF.ast$ID == "A-baseEmsian-D5"), 6] <-
    mean(dist.A_baseEmsian_D5_B20)  # mean
  DF.ast[which(DF.ast$ID == "A-baseEmsian-D5"), 7] <-
    sd(dist.A_baseEmsian_D5_B20) * 2  # 2 sigma


## SAVE DF.ast -----------------------------------------------------------
------

# Save DF.ast data frame as a .csv file.
  write.csv(DF.ast, file = "DF.ast.complete.csv")
```